From T2K to Hyper-Kamiokande : neutrino oscillation analysis and preparation of the time synchronization system

Lucile Mellet

Sorbonne Université

Thèse de doctorat

pour obtenir le grade de Docteur.e en Sciences de Sorbonne Université
Mention: Physique de l'Univers

École doctorale des Sciences de la Terre et de l'environnement et Physique de l'Univers, Paris - ED 560
Laboratoire de Physique Nucléaire et de Hautes Énergies - UMR 7585

De T2K à Hyper-Kamiokande : analyse d'oscillation des neutrinos et préparation du système de synchronisation en temps

présentée par

Lucile A.É. Mellet

Co-dirigée par
Boris Popov et Mathieu Guigue

Soutenue publiquement le 18 Septembre 2023 devant le jury composé de :

M. Dominique Duchesneau, D.R. CNRS au LAPP (Annecy)	**Rapporteur**
M. Laurent Simard, MCF Université Paris Saclay	**Rapporteur**
Mme. Asmaa Abada, Pr. Université Paris Saclay	**Examinatrice**
Mme. Delphine Hardin, Pr. Sorbonne Université	**Présidente du Jury**
M. Michel Abgrall, I.R. CNRS au SYRTE (Observatoire de Paris)	**Examinateur**
M. Boris Popov, D.R. CNRS au LPNHE	**Directeur de thèse**
M. Mathieu Guigue, MCF Sorbonne Université	**Co-encadrant**

Acknowledgements

It's not because it ends well that the road was easy. I could not have written this manuscript and performed the work it describes without help, guidance, and support from many people. Let me try to thank them here.

Je remercie tout d'abord mes directeurs de thèse, Mathieu et Boris pour m'avoir donné l'opportunité de découvrir la physique des neutrinos dès mon stage de M1 et celle de faire ma thèse dans ce domaine. Merci de m'avoir accompagnée durant cette période instable de pandémie. Contrairement à ce que dirait Boris, on n'est pas toujours d'accord mais on a réussi à faire tout le travail présenté dans cette thèse ensemble, et c'est ça qui compte. Plus largement, je remercie tout le groupe Neutrinos du LPNHE pour leurs conseils avisés à chacune de mes présentations. Merci à Claudio et Stefano pour leur relecture de certaines parties du manuscrit.

Je remercie également mon jury de soutenance pour leur relecture rigoureuse de mon manuscrit et leurs questions pertinentes.

I wish to thank the entire T2K collaboration for providing such a stimulating and friendly environment to learn to become a neutrino physics researcher. More specifically, I have to express my deep gratitude to the Oscillation Analysis conveners, past and present, Patrick, Clarence, Ciro, Ed, Andrea, and Benjamin, as well as the Analysis Steering Group conveners Christophe and Sara for advice, patience, encouragements and support. I, of course, have to mention Lukas (Berns), our P-Theta alive documentation! You are brilliant but always ready to explain everything from scratch to all new students, however basic our questions are, and you always encourage us and show us the good side of the mistakes we make. Thank you for that!
The oscillation analysis is a team effort, including numerous validations between fitters! I want to thank everyone involved for making this work fun and enjoyable, for understanding when someone needs a break, and for coping with time zone differences! Kenji, Noguchi-san, Henry, Jaiden and Denis, you were the best fellow analyzers I could have wanted, thanks!

Finally, I want to thank Kendall for the enthusiasm you always express and for trusting me with my first post-doc position. Looking forward to joining you and Sophie at MSU!

I thank the Hyper-Kamiokande collaboration for providing an equally interesting work environment, looking towards the future generation of neutrino oscillation experiments. Merci à tous mes collègues sur ce projet, y compris Vincent, que je n'ai pas encore mentionné.

A fundamental part of my life as a PhD student was the LPNHE life. Huge thank you to all the PhD students and post-docs I had the chance to share this time with. I cannot name you all without forgetting someone, so I won't. But all those lunches, coffee and 'goûter' breaks, and beer/cider evenings were amazing. We all support each other in a beautiful way by creating a space to complain about the PhD, share our interest for Physics, distract each other with everything BUT Physics and laugh stupidly. I don't see how one can complete a thesis without having this. Please preserve this atmosphere at LPNHE!
Merci Julianna pour ton template LaTeX et ton amitié.

Special thanks to my office mates! The first team Guy, Viet, and Sara, thank you for welcoming me in the lab and the office so warmly, in a middle of the pandemic! Chatting with you and sharing our frustrations and successes in real time was just what we needed. Your joy, enthusiasm and encouragements as well as your insights on any PhD dilemma that arose were just wonderful to have!
La seconde équipe, Dylan, Laura, et Léander, merci d'avoir contribué à l'environnement serein dont j'avais besoin pour écrire ce manuscrit et finir cette thèse sans trop de panique. Et merci de m'avoir supportée! Les thésards en dernière année ne sont pas toujours de très bonne compagnie ...

On ne fait pas une thèse sans un master! Un grand merci au passionnant master NPAC et à ses responsables Sorbonne: Delphine, pour avoir accepté le rôle de présidente de mon jury, et Éli pour tes encouragements depuis le M1, ton intelligence humaine et ta pédagogie. Thank you to all my NPAC classmates, COVID separated us at the end but spending that year along your side was great! En particulier, merci à Julien pour ta belle amitié.

Merci à tous ceux qui ont assisté à ma soutenance, votre soutien pendant ce moment stressant était crucial et célébrer cet accomplissement avec vous tous était un grand plaisir!

Je tiens à remercier absolument infiniment (jamais trop de superlatifs!!) mes parents Cécile et Philippe pour leur soutien sans faille et permanent depuis le premier jour, mais aussi pour leur intérêt profond pour la science et la connaissance qu'ils ont su me transmettre et qui fait certainement de moi une meilleure scientifique. Merci d'avoir toujours encouragé et alimenté ma façon de penser et ma soif de connaissances sans les formater.
Et enfin, un merci plus général à ma famille, ceux qui sont là pour moi dans les moments importants, depuis toujours, et avec qui on peut parler de tout et surtout **pas** de Physique, me rappelant qu'on n'est pas son métier, mais bien plus. Merci spécial à mes cousins/voisins pendant ma vie parisienne Mélanie, Thibault, Victoire et Théophile!

À mes parents,
À ma famille,

À la diversité des pensées,
et la bienveillance

Résumé substantiel

La Physique des particules est consacrée à l'étude du monde qui nous entoure et à la compréhension de phénomènes physiques observés à toutes les échelles, de l'infiniment petit des particules à l'infiniment grand de l'Univers. Ce domaine de recherche se concentre à chercher des réponses au niveau des constituants élémentaires et des interactions fondamentales. Il s'agit d'un domaine plutôt récent dont le support théorique est le Modèle Standard de la Physique des particules, formulé dans les années 70 dans sa version la plus complète. Son succès à prédire la découverte de nombreuses particules dans les décennies suivantes est indéniable. Cependant, certaines observations ne peuvent être expliquées par ce modèle qui ne semble pas tout à fait suffisant. Il reste des inconnues et des questions ouvertes laissant penser qu'il peut y avoir de la Physique à découvrir au delà du Modèle Standard.

Parmi les douze particules élémentaires du Modèle Standard, 3 sont des neutrinos. Ils existent en 3 saveurs correspondant aux trois familles de leptons : électronique, muonique et tauique. Bien qu'ils soient intégrés dans le Modèle Standard, les neutrinos ont des propriétés inexpliquées par celui-ci. Par exemple, le mécanisme d'acquisition de leur très faible masse, que l'on sait désormais non-nulle, implique, dans la plupart des scénarios, de nouvelles particules et/ou interactions. En effet, le Modèle Standard ne prévoit que des (anti-)neutrinos de chiralité gauche (droite) ce qui ne permet pas un couplage avec le boson de Higgs (et donc un terme de masse de Dirac) qui renverse la chiralité comme pour les autres particules. Entre autres interrogations spécifiques aux neutrinos, leur nature, Dirac ou Majorana n'est pas connue. En effet, en l'absence de charge électrique et de couleur, les neutrinos sont les seules particules élémentaires connues qui pourraient être de Majorana, c'est-à-dire être leur propre anti-particule. Cela fait de la physique des neutrinos un domaine de recherche enthousiasmant, touchant de près à des questions fondamentales sur la constitution de notre Univers, et avec un potentiel de découvertes passionnantes.

De plus, les propriétés des neutrinos en font des sondes très efficaces à de grandes échelles. En effet, leur très faibles masse et probabilité d'interaction (les neutrinos sont

uniquement sensibles à interaction faible) leur permet de voyager quasiment en ligne droite depuis les confins de l'Univers. Cela leur permet potentiellement de nous apporter des informations sur le très jeune Univers ainsi que sur des phénomènes astrophysiques tels que des explosions de Supernovae.
Cependant, c'est un autre phénomène spécifique aux neutrinos qui constitue le contexte de la majeure partie du travail de thèse présenté dans ce manuscrit. Il s'agit des oscillations de saveurs des neutrinos. La propagation et les interactions des neutrinos sont naturellement régies dans le cadre de la mécanique quantique. Il se trouve que les états propres de saveurs, par lesquels les neutrinos interagissent et donc peuvent être détectés, ne correspondent pas à leurs états propres de masse, par lesquels ils se propagent. En d'autres termes, chaque neutrino tel qu'il est produit ou qu'il interagit est en fait une superposition d'états de masses différentes. Ce qui se passe lors de la propagation peut être compris ainsi: les états de masses différentes vont avoir une vitesse différente, la proportion de chaque état va donc changer. Cela peut conduire, au moment de l'interaction à une saveur différente de celle de production du neutrino. C'est ce qu'on appelle l'oscillation de saveur. En réalité, le phénomène peut être plus compliqué, impliquant des interférences et des résonances notamment en prenant en compte les possibles interactions non-destructrices avec la matière pendant la propagation.

L'ensemble des propriétés des neutrinos ainsi que le formalisme des oscillations saveurs, appelé mécanisme de Pontecorvo, Maki, Nakagawa and Sakata (PMNS) en l'honneur des physiciens ayant participé à sa formulation à la fin des années 1960, sont décrits dans le Chapitre 1 de ce manuscrit. Un point de vue expérimental est pris et les différentes sources, modes d'interactions et méthodes de détections des neutrinos sont aussi détaillés. Un accent particulier est ensuite mis sur les possibilités de mesurer précisément les paramètres régissant l'oscillation des neutrinos et les meilleures contraintes actuelles sur ces valeurs sont données. En particulier, il est montré que la symétrie de Charge-Parité (CP) peut être violée dans le secteur leptonique et qu'un des paramètres d'oscillation est justement une phase de violation de CP : δ_{CP}. Si cette phase est mesurée non-nulle (modulo π) dans une expérience d'oscillation des neutrinos, alors cela signifierait qu'une des causes de l'asymétrie matière/anti-matière dans l'Univers, encore inexpliquée à ce jour, pourrait se trouver dans la production de particules du secteur leptonique. Cette découverte n'a pas encore été faite mais les contraintes actuelles sur l'oscillation des neutrinos favorisent le scénario d'une violation maximale à un niveau de confiance de presque 3σ. Cela explique l'engouement actuel de la communauté scientifique pour une mesure précise de δ_{CP}.

La première partie du travail présenté ici a été effectuée au sein de la collaboration internationale Tokai to Kamioka (T2K). Cette expérience est basée au Japon et per-

met d'étudier l'oscillation des neutrinos de manière précise avec un faisceau contrôlé de neutrinos. L'accélérateur J-PARC produit un faisceau alternativement de neutrinos ou d'anti-neutrinos muoniques par collision de protons sur une cible de graphite puis par désintégration des pions et kaons instables créés lors la collision. Un ensemble de détecteurs dit proches, à environ 280 m de la cible permet de caractériser le faisceau en terme de flux, composition, énergies et sections efficaces d'interaction, avant que le phénomène d'oscillation n'apparaisse. Cela permet de réduire les incertitudes sur la mesure finale. Un second détecteur, placé 2.5° hors de l'axe du faisceau et à 295 km de la cible, permet de détecter certains des neutrinos du faisceau après oscillation. L'expérience est conçue pour maximiser la probabilité d'oscillation au niveau du détecteur lointain. Ce détecteur à effet Cherenkov dans l'eau n'est autre que Super-Kamiokande (SK). La détection à SK est basée sur la reconstruction des anneaux de lumière Cherenkov produits par le lepton sortant de l'interaction à courant chargé du neutrino avec un nucléon de l'eau. Pour détecter cette lumière, les parois de la cuve d'eau sont couvertes de photo-multiplicateurs. Les détails techniques et justifications scientifiques pour chacun des éléments de cette expérience à large infrastructure font l'objet du Chapitre 2.

Un des projets que j'ai conduits était la participation à deux analyses d'oscillation principales dans T2K avec, pour la première, de nouveaux paramètres systématiques et, pour la seconde, de nouvelles données à SK représentant une augmentation de 9% des statistiques en mode neutrinos (par opposition au mode anti-neutrinos). La méthode générale d'analyse est décrite dans le Chapitre 3 ainsi qu'une discussion plus approfondie sur l'ajustement des données au détecteur lointain. Plusieurs logiciels d'analyse sont utilisés en parallèle. Parmi eux, P-Theta est celui que j'ai utilisé et qui est donc détaillé ici. Les nouveaux résultats produits pour cette thèse, qui ne sont pas encore des résultats officiels de la collaboration pour des raisons d'échelles de temps différentes entre ma thèse et les validations internes, sont présentés. Ils sont en cours de valorisation par la collaboration. En particulier, la complexité d'une telle analyse y compris en terme d'interprétation statistique et l'importance grandissante des effets systématiques sont soulignées. Les limites de l'analyse, avec un regard vers le futur sont aussi mises en avant.

Après avoir été introduit au chapitre précédent, le rôle crucial et complexe des effets systématiques est approfondi dans le Chapitre 4. En effet, des études dites de fausses données effectuées avec P-Theta pour l'analyse de l'année précédente (2021/2022) sont rapportées. Le modèle d'incertitudes sur les sections efficaces d'interaction de T2K est basé sur un choix de modèle théorique d'interaction et nucléaire. Cependant, ce choix n'est pas absolu car aucun modèle ne peut à ce jour prédire ni expliquer l'ensemble des données disponibles, toutes expériences confondues. Il convient donc de tester la

robustesse de l'analyse de T2K à un choix de modèle nominal erroné. Pour cela, les études de fausses données consistent à produire des données Monte-Carlo à partir de chaque modèle alternatif à tester. Ces jeux de données sont ensuite chacun à leur tour analysés selon le processus standard de T2K, au détecteur proche puis au détecteur lointain. Cela signifie qu'ils sont ajustés au modèle nominal. Le biais que cela crée sur les contraintes obtenues sur les paramètres d'oscillation est calculé. Si notre modèle d'effets systématiques est suffisamment complet, il absorbera les différences de modèle lors de l'analyse et donc ce biais sera faible. C'est la conclusion générale qui est trouvée. Néanmoins, le biais sur un paramètre, Δm^2, est un peu plus élevé et conduit la collaboration à ajouter a posteriori une incertitude sur ce paramètre au moyen d'un élargissement des intervalles de confiance par une convolution Gaussienne.

La seconde partie de cette thèse de doctorat se concentre de manière plus directe à préparer le futur des expériences d'oscillation des neutrinos. Elle a été effectuée dans le cadre de la collaboration internationale Hyper-Kamiokande (HK). HK sera non seulement un nouveau détecteur lointain pour l'étude des neutrinos de l'accélérateur de J-PARC mais aussi, le successeur complet de SK, c'est-à-dire un observatoire pour les neutrinos solaires, atmosphériques, astrophysiques ainsi que pour des études sur le temps de vie des nucléons. HK sera également un détecteur Cherenkov à eau et hors-axe. Il sera construit à la position symétrique à SK par rapport à la ligne de faisceau et devrait être mis en route en 2027. Bien que basé sur une technologie similaire à SK et donc éprouvée, HK fournira des possibilités de détections supérieures grâce à un volume de détection environ huit fois plus grand et à des performances améliorées de chacun de ces éléments. Les détails techniques, les buts scientifiques et les performances attendues de HK sont décrits dans le Chapitre 5.

Plus précisément, tous les sous-systèmes du détecteur sont imaginés et produits à nouveau, ce qui permet une amélioration globale de la détection. Un de ces éléments, crucial aux expériences de détection des neutrinos est le système de synchronisation d'horloges. Effectivement, une grande précision en temps est importante pour reconstruire le signal en coïncidence avec les nombreux photo-multiplicateurs, pour sélectionner les évènements venant du faisceau par rapport à un signal temporel de déclenchement envoyé par l'accélérateur, ainsi que pour caractériser des évènements de type astrophysique y compris en comparaison à d'autres expériences. Deux types de synchronisation sont en fait nécessaires: interne entre tous les éléments du détecteur et externe afin d'attribuer à chaque évènement détecté une heure et date universels UTC très précises. Le cahier des charges de HK en terme de précision temporelle, une courte revue des systèmes utilisés dans d'autres expériences de neutrinos, et une introduction au maintien de la stabilité

temporelle du point de vue utilisateur sont donnés dans le Chapitre 6.

Enfin, le travail accompli pendant cette thèse sur le développement de la génération d'un signal de fréquence temporel adéquat pour les besoins de HK est décrit dans le Chapitre 7. La caractérisation au laboratoire de chaque élément du système choisi, principalement d'une horloge atomique au Rubidium et d'un ensemble antenne et récepteur GNSS, et du système complet sont rapportés. Les performances attendues de stabilité, après une optimisation des méthodes de correction du signal et de l'intégration des informations GNSS, sont aussi discutées grâce à des simulations des signaux qui ont été conduites spécialement pour ce travail.

Une réflexion sur l'avenir des mesures des paramètres d'oscillation des neutrinos est développée en conclusion, avec un accent sur le besoin de méthodes diverses et de complémentarité entre les détecteurs et les expériences.

List of Figures

List of Tables

Contents

Preamble

The field of particle Physics aims at explaining the world around us, at all scales up to the Universe's scale, by looking for answers in the tiniest elementary constituents. This quite recent field of research has been successful in doing so with the Standard Model of particle Physics whose formulation was finalized in the 70's. However, there remains unknowns, open questions and observations which can not be solely understood within the Standard Model (SM) framework.

Neutrinos, which exist in three flavors matching lepton flavors (electron, muon and tau), are SM particles with such unexplained properties hinting at Physics beyond the Standard Model. For instance, the mechanism through which they gain their tiny yet non-zero masses is not fully understood and implies in most theories the presence of additional particles and/or interactions. Among other 'neutrino-mysteries', they could be the only elementary particles of Majorana Nature but this is yet undetermined.

Moreover, the properties of neutrinos make them a fantastic probe to understand larger scale interrogations about the Universe. Their weak interactions and tiny masses allow them to travel in quasi-straight lines potentially providing information on the early Universe as well as astrophysical events. Another phenomenon, which is the broad context of most of this thesis's work is the flavor oscillations of neutrinos. In the quantum mechanics framework, flavor eigenstates of neutrinos, through which they interact, do not correspond to their mass eigenstates through which they propagate. In other words, the flavor states that determine their interactions are a superposition of mass states. Mass eigenvalues being different, the propagation speed can be slightly different leading to a potentially different superposition of mass states after propagation. This can introduce a mixing of flavors and a different flavor state for the same neutrino at its production point and interaction point.

The properties of neutrinos as well as the formalism of this specific physics phenomenon are presented in Chapter 1, with a focus on experimental consequences and possibilities. In particular, it is shown that one of the parameters of the oscillations is a Charge-Parity

(CP) violating phase δ_{CP}. If this phase was measured to be non-zero (modulo π), this would mean that the leptonic sector participates in the matter/anti-matter asymmetry of the Universe, hence the strong interest of the community in this measurement.

The first part of the work presented in this thesis was performed within the international collaboration Tokai to Kamioka (T2K). It consists in a long-baseline neutrino oscillation experiment based in Japan, which studies flavor oscillations within a 600 MeV neutrino beam from the J-PARC accelerator, over a 295 km distance. The sophisticated sets of near detectors and the far detector Super-Kamiokande are described in details in Chapter 2.

The main oscillation analysis in the T2K experiment as well as the latest results are presented in Chapter 3, with a specific focus on the far detector fit, with the P-theta software. This Chapter aims at illustrating the complexity of such analysis, how crucial every step is and the statistical subtleties in the interpretation of results. It also introduces some of the limitation of the analysis in its current shape.

After having been introduced in the previous Chapter, the importance of the systematic parameters as well as the challenges due to their dependence with cross-section and nuclear models are extensively discussed in Chapter 4. More specifically, so-called Fake Data Studies performed with P-theta for the 2021/2022 T2K analysis are detailed together with their outcome.

A second part of this work focuses on the future of the neutrino program in Japan within the Hyper-Kamiokande international collaboration. This new detector, direct successor of Super-Kamiokande will be both the next generation experiment for accelerator and non-accelerator neutrino Phyics in Japan. It is described in Chapter 5.

More specifically, one of the technological sub-system essential to neutrino experiments is the timing system. Indeed, a high timing precision is needed in most cases to reconstruct the signals from neutrino interactions in the detector, to record events from the beam with respect to a time trigger from the accelerator facility, to characterize astrophysical events, and to perform coincidence with other experiments. Moreover, synchronization is needed between all parts of the detector in order to reconstruct consistent primary signals. A short review of existing timing systems in neutrino experiments as well as an introduction to time keeping from a user's point of view can be found in Chapter 6.

Finally, to build a timing system, a reliable time signal should be generated and distributed to the electronics of data acquisition. The development of the time generation part of

HK's new timing system is presented in Chapter 7. Characterization of each foreseen elements as well as the full generation system have been performed at the laboratory throughout this thesis. Simulations of expected frequency stability performance with optimized corrections based on the integration of GNSS signals in the system are also reported.

Chapter 1

Introduction to neutrinos oscillation physics

This first chapter aims at introducing neutrino physics and in particular neutrino oscillations so as to motivate the experiments that will be presented and the studies that were performed during this thesis.

Contents

1.1 Neutrinos: the ghost particle

Neutrinos are often referred to as the ghost particle in outreach communications. This is because, of all 12 elementary particles of the Standard Model (SM), there are the 3 most elusive ones. From their postulate in the 30's and their first experimental detection in 1956 up to nowadays, neutrinos have always been, and remain very challenging to grasp and detect. This is explained by their specific properties.

1.1.1 Neutrino properties

The Standard Model of elementary particles organizes very successfully the known elementary particles composing ordinary matter. It is visually summarized in figure 1.1. It consists in 12 elementary particles classified in 3 generations and 5 bosons (4 force carriers and the Higgs Boson). Among elementary particles, there are three neutrinos discriminated by their flavor (electron, muon or tau), matching the corresponding lepton flavor for each generation.

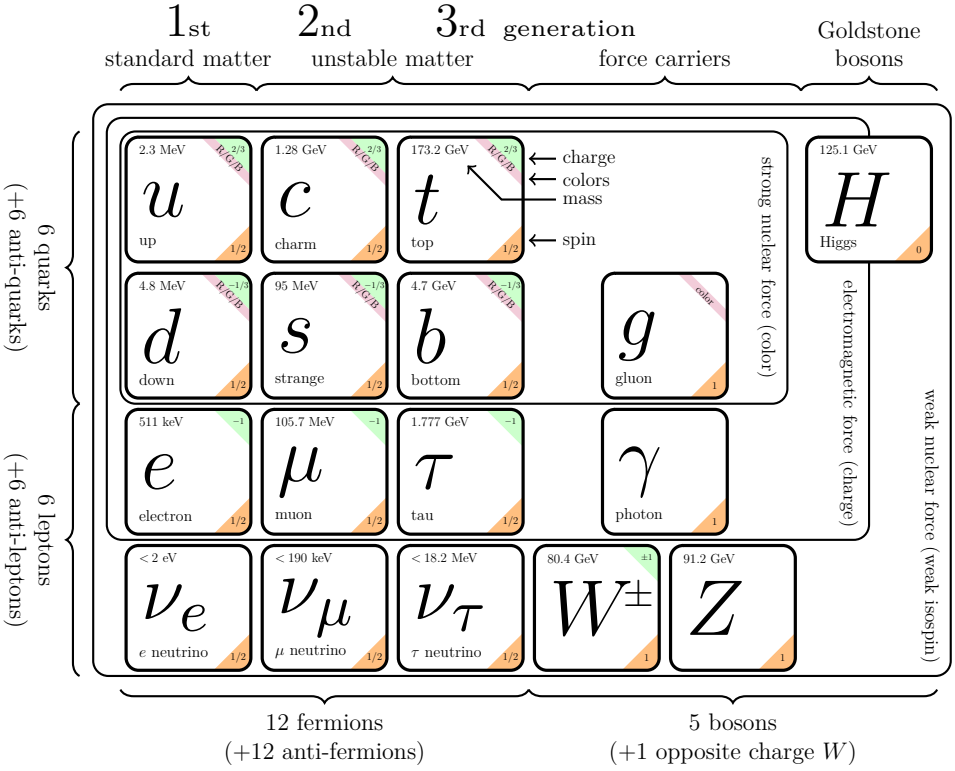

Figure 1.1. *The Standard Model of particle physics (adapted from [1])*

Flavor and mass bases

As it will be of great importance to explain the phenomenon of neutrino oscillations, the three flavors of neutrinos are eigenstates in the base of flavors, the relevant one for neutrino interactions. However, the flavor base does not correspond to the mass base, which is the one relevant for neutrino propagation and which has eigenstates 1, 2 and 3. So, it can be said that in terms of masses there is the neutrino 1, neutrino 2 and neutrino 3 and in terms of flavors there is the electron neutrino, the muon neutrino and the tau neutrino. There is no direct correspondence between them but a mixing, just like a change of base. The mixing between both bases is ruled by the PMNS (Pontecorvo, Maki, Nakagawa and Sakata) formalism which was first proposed for 2×2 bases by Z. Maki, M. Nakagawa and S. Sakata in 1962 [2] and by V. Gribov and B. Pontecorvo in 1969 [3] and then extended to 3 flavor and mass states in the 70's. The mixing matrix is following the PMNS formalism and by convention called U. If α denotes a flavor state (e, μ or τ) and i denotes a mass state (1, 2 or 3), the mixing at a specific moment can be written:

$$|\nu_\alpha\rangle = \sum_i U^*_{\alpha i} |\nu_i\rangle \tag{1.1}$$

Moreover, the PMNS matrix is built in such a way that it is unitary: $UU^\dagger = U^\dagger U = \mathbf{1}$. As there are three flavors of neutrinos in the Standard Model, confirmed by the width of the Z boson decay, the PMNS matrix can be presented as 3 rotation matrices in 2-flavors spaces. It is then parameterized by 3 mixing angles θ_{ij} between the 3 mass states: 1, 2, 3. A unitary 3×3 matrix has 9 degrees of freedom so that implies, in theory, 6 phases. It is important to note here that the nature of neutrinos is not known, meaning that they can be Dirac particles as any other SM particle but they could also be Majorana particles, meaning that they could be their own anti-particle. In the Dirac case, lepton and neutrino fields of each flavor α can be rewritten: $l_\alpha \to e^{i\phi_\alpha} l_\alpha$ and each neutrino field for each mass state i can also be rewritten: $\nu_i \to e^i \phi_i \nu_i$. This leaves the theory equivalent only if the PMNS matrix is redefined as $U_{\alpha i} \to e^{i(\phi_\alpha - \phi_i)} U_{\alpha i}$. Since there are 6 phases, there are only 5 independent $\phi^\alpha - \phi^i$ differences, so that 6 - 5 = 1 phase remains physical. The matrix is only parameterized by one CP symmetry violation phase δ_{CP} which would be equal to 0 in case of CP conservation. The CP operator changes a particle into its corresponding anti-particle with opposite parity. To take into account the case in which neutrinos are Majorana particles, two so-called Majorana CP violating phases are added. They can be added in a diagonal matrix P. The PMNS matrix is therefore written in the

following way, with s_{ij} denoting $\sin(\theta_{ij})$ and c_{ij} denoting $\cos(\theta_{ij})$:

$$\begin{aligned} U &= \begin{pmatrix} 1 & 0 & 0 \\ 0 & c_{23} & s_{23} \\ 0 & -s_{23} & c_{23} \end{pmatrix} \begin{pmatrix} c_{13} & 0 & s_{13}e^{-i\delta_{\mathrm{CP}}} \\ 0 & 1 & 0 \\ -s_{13}e^{i\delta_{\mathrm{CP}}} & 0 & c_{13} \end{pmatrix} \begin{pmatrix} c_{12} & s_{12} & 0 \\ -s_{12} & c_{12} & 0 \\ 0 & 0 & 1 \end{pmatrix} P \\ &= \begin{pmatrix} c_{12}c_{13} & s_{12}c_{13} & s_{13}e^{-i\delta_{\mathrm{CP}}} \\ -s_{12}c_{23} - c_{12}s_{13}s_{23}e^{i\delta_{\mathrm{CP}}} & c_{12}c_{23} - s_{12}s_{13}s_{23}e^{i\delta_{\mathrm{CP}}} & c_{13}s_{23} \\ s_{12}s_{23} - c_{12}s_{13}c_{23}e^{i\delta_{\mathrm{CP}}} & -c_{12}s_{23} - s_{12}s_{13}c_{23}e^{i\delta_{\mathrm{CP}}} & c_{13}c_{23} \end{pmatrix} P \end{aligned} \tag{1.2}$$

The PMNS mixing matrix, its parameters and the consequences of this mixing will be further detailed in section 1.2.

Charges and chirality

Neutrinos do not possess any electrical or color charge. However, (anti-)neutrinos have a -1 (+1) weak hypercharge and as a consequence they only interact through the weak interaction which contributes to their elusive nature as it will be further discussed in the next section. The corresponding electro-weak Lagrangian ruling the dynamics and kinematics of neutrinos is:

$$\begin{aligned} \mathscr{L}_{\mathrm{EW}} = &-\frac{1}{4}\sum_{i=1}^{3} F^i_{\mu\nu}F^{i\mu\nu} - \frac{1}{4}B_{\mu\nu}B^{\mu\nu} \\ &+ \bar{\psi}_L i\gamma^\mu D_\mu \psi_L + \bar{\psi}_R i\gamma^\mu D_\mu \psi_R \\ &+ (D_\mu\phi)^\dagger (D^\mu\phi) - \mu^2\phi^\dagger\phi - \lambda\left(\phi^\dagger\phi\right)^2 \\ &- y^j\left(\bar{\psi}_L\phi\psi_R + \bar{\psi}_R\phi^\dagger\psi_L\right), \end{aligned} \tag{1.3}$$

where, without going into mathematical details, the first term built from anti-symmetric gauge tensors describes the interaction of W bosons with B bosons; the second term describes the kinematics of such particles through interaction with the gauge covariant derivative D_μ (encoding variation of fields) with $\psi_L(\psi_R)$ the fermion field left (right)-hand component as well as the interaction between fermions and B and W bosons; the third term is the Higgs term where ϕ contains all Higgs scalar fields and the last term is the Yukawa coupling. After spontaneous symmetry breaking [4, 5], the two last terms provide the fermion Dirac mass through interaction with the Higgs field:

$$\mathscr{L}_{\mathrm{Dirac}} = \left(m\bar{\psi}_L\psi_R + m\bar{\psi}_R\psi_L\right). \tag{1.4}$$

Neutrinos in the Standard Model, however, are only postulated in one state of chirality: left-handed, and anti-neutrinos in a right-handed state.

Absolute masses

Their mass is so small that neutrinos were considered mass-less from the 30's, when Pauli postulated their existence [6] as an explanation to the missing energy in beta (β) decay spectra, up to the 60's when Pontecorvo suggested a mechanism of oscillation that would require a non-zero mass to explain solar neutrino observations [7]. Neutrino oscillations, which will be described in detail in section 1.2, were discovered in 1998 [8]. Since then, it is known that their mass can not be zero, however it has never been measured. The most stringent and recent upper limit on the effective electron anti-neutrino mass comes from the Karlsruhe Tritium Neutrino (KATRIN) experiment: $m_{\nu_e} < 0.8$ eV/c^2 at 90% confidence level [9]. The measured mass is never directly the neutrino masses of the mass states 1, 2 or 3 but an observable combination: $m_{\nu_e} = \sqrt{\sum_i |U_{ei}|^2 m_i^2}$. The KATRIN detector is a spectrometer that aims at measuring precisely the electron spectrum from tritium beta decay. The mass of the neutrino can be inferred from the end of the spectrum where electrons take most of the energy except for the known nuclear recoil (for that specific process) and the mass of the neutrino, which is at rest in the scenario of maximal electron energy. In that part of the spectrum, the neutrino mass is therefore the missing energy between the known released energy through this beta decay and the sum of the measured electron energy and the nuclear recoil. As a consequence, for the KATRIN experiment, the beta decay spectrum is measured, meaning that only the electron flavor is involved, the measured mass is therefore a combination of mass states projected on the electron flavor state. Apart from studying beta decay kinematics, mass limits on neutrinos can be inferred from cosmological observations. These limits are more stringent and directly set on the sum of mass states i but are cosmological model dependent and assume stability of the neutrino on cosmological scales. One of the most recent limit for the sum of masses is $\sum m_i < 0.42$ eV/c^2 at 95% confidence level [10]. The absolute mass of neutrinos remains an open question and an experimental challenge ahead of us.
Moreover, the particularly small mass of neutrinos can not be attributed to the Higgs mechanism as for all other massive particles. Indeed, as there are only left(right)-handed (anti-)neutrinos, and the Higgs field attributes masses through a change of chirality, this coupling is not possible with neutrinos in the Standard Model, ie Eq 1.4 is forbidden. One of the simplest theoretical solution to this is for instance see-saw mechanisms [11], and in particular the type-I see-saw which predicts a very heavy right-handed counter part of the neutrino: a sterile neutrino which does not interact in the Standard Model i.e.

through either strong, weak or electromagnetic forces. In that scenario, it is then possible to build a mass matrix from both standard Dirac mass terms of the form $m_{LR}\bar{\nu_L}\nu_R$ (ν is a neutrino field, L and R denote respectively left- and right-handed, and ^{C} the CP conjugate) and Majorana mass terms $M_{RR}\bar{\nu_R}\nu_R^C$ so that two masses appear (for each Standard Model neutrino mass state):

$$\left(\overline{\nu_L}\overline{\nu_R^c}\right)\begin{pmatrix} 0 & m_{LR} \\ m_{LR}^T & M_{RR} \end{pmatrix}\begin{pmatrix} \nu_L^c \\ \nu_R \end{pmatrix} \tag{1.5}$$

If one of the values (M_{RR}) for mass is very large, which is not forbidden for a sterile neutrino, then the other mass value (m_{LR}) is very small and an effective mass ($m_{LL} = -m_{LR}M_{RR}^{-1}m_{LR}^T$, with T denoting the transposed) for the left-handed standard neutrino can be found to correspond to the current limit on standard left-handed neutrino masses. Other more complicated see-saw mechanisms involve a heavy Higgs-triplet (Type-II see-saw) or additional neutrino singlets (double see-saw). These theories also often predict, but not necessarily, that the neutrino would be a Majorana particle, meaning that the neutrino and anti-neutrino of the Standard Model would actually be the same particle, in two states of chirality and that the Lepton number conservation, which is an accidental symmetry, would be broken. There are experimental searches ongoing in that direction with neutrino-less double beta decay experiments [12]. If it was observed it would be a signature of the Majorana nature of neutrinos.

Mass ordering

Whether the neutrino 3 is the highest or lowest mass state is not known yet and this open question is referred to as mass ordering or mass hierarchy. It is said that the ordering is either normal or inverted as illustrated in figure 1.2.

The mass ordering can be constrained by direct measurements of sum of masses and comparison with limits depending on the hypothesis (normal or inverted). It can also be determined through studying oscillations as it will be seen in section 1.2, or potentially through limits on neutrino-less double beta decay in certain scenarii.

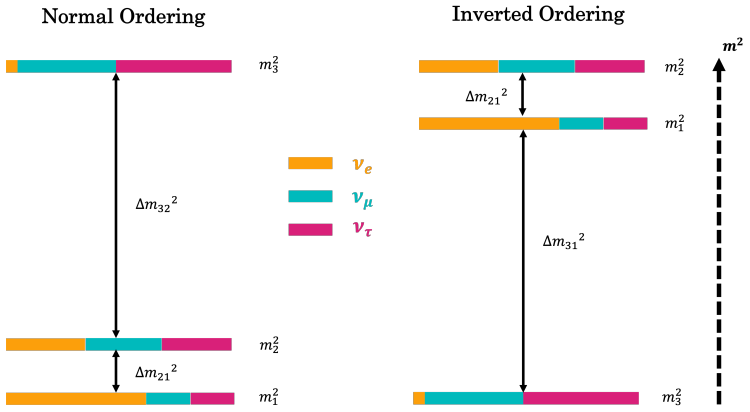

Figure 1.2. *Illustration of the two possible mass orderings for neutrinos as well as their flavor composition*

Conclusion

As a conclusion, all these properties lead to experimental challenges to detect such light, neutral and weakly interacting particles.

1.1.2 Interactions and detection

1.1.2.1 Neutrino interactions

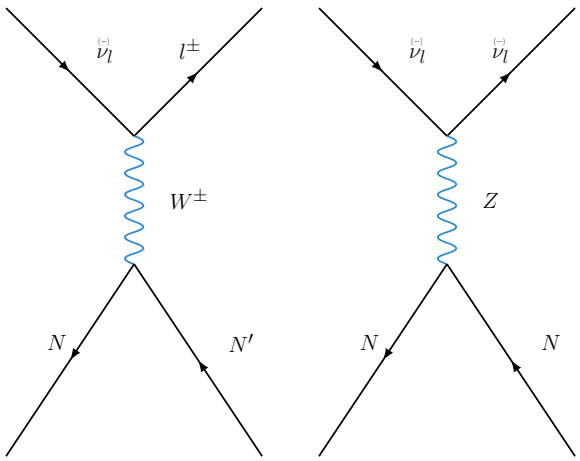

Figure 1.3. *Feynman diagrams of neutrino interaction with a nucleus, main charged current process (left) and neutral current scattering (right), l denotes any of the 3 flavors, and N a nucleon*

To be detected, neutrinos obviously need to interact with a detection medium. In fact, due to their properties, only the product of their interaction can be detected. Neutrino

detection can only be indirect. The weak interaction of neutrinos can happen either through charged current or neutral current, in an elastic or inelastic way, although elastic scattering will not leave any specific signal in most detectors. In particular, neutrino experiments will rely dominantly on neutrino interactions with nucleons more than leptons to obtain specific signals. One of the main charged current interactions is the quasi-elastic one where a neutrino interacts with a nucleon, producing a charged lepton in the final state. The Feynman diagram of this interaction is on the left-hand side of figure 1.3. It is often abbreviated CCQE for Charged Current Quasi Elastic. Neutral current interactions with nucleons are simple scatterings, a typical Feynman diagram can be found in the right-hand side of figure 1.3. Neutrino detection is not only difficult because it is indirect

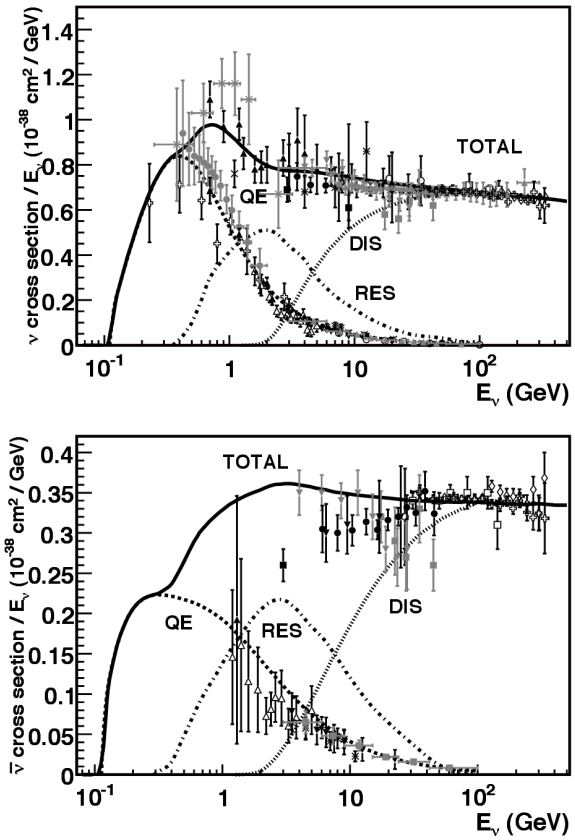

Figure 1.4. *Total cross-sections and breakdown by main interaction modes for Charged current divided by the energy for neutrinos (top) and anti-neutrinos (bottom) as a function of their energy, from [13]*

but also because the neutrino interaction probabilities, expressed in terms of cross-sections, are very small. The total cross-sections of neutrinos and anti-neutrinos for charged current are shown as a function of their energy in figure 1.4, respectively in the top and bottom plots. It can be seen that the cross-sections are of the order of 10^{-38}cm^2 per GeV for neutrinos and three times less for anti-neutrinos. It can also be seen that CCQE is the predominant interaction channel for neutrinos under an energy of about 1 GeV. Above,

interactions where a pion or more particles are produced through resonances such as resonant charge current (noted RES, diagram in figure 1.5, left plot) or deep inelastic scattering (noted DIS, diagram in figure 1.5, right plot) become more probable. One other possible interaction worth mentioning here, because it will be referred to in Chapter 4, is the so-called 2p2h (two particles, two holes, diagram in figure 1.6) or its generalization npnh (n being any integer) interaction. It consists in a CC interaction without pion in the final state such that, depending on the detection method it can easily be mistaken for a CCQE interaction. However its kinematic signature is different because the neutrino interacts with a nucleon which is itself bounded to others so that several nucleons are ejected from the nucleus during the primary interaction. As it is for energies below 10 GeV, it is estimated to be a second order background to CCQE interactions at the level of 15-30% [16] and therefore has to be taken into account in accurate neutrino interaction modeling.

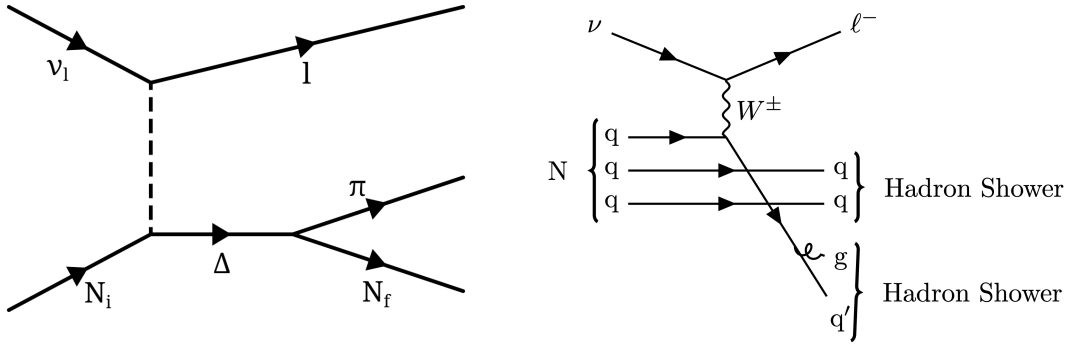

Figure 1.5. *Feynman diagrams of neutrino interaction with a nucleus, pion production resonant process from [14] (left) and deep inelastic scattering from [15] (right), l denotes any of the 3 flavors, N a nucleon, q a quark and g a gluon.*

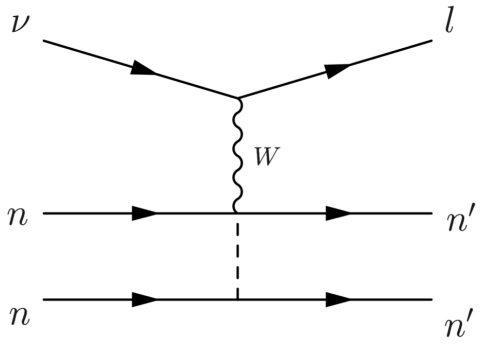

Figure 1.6. *Feynman diagram of neutrino interaction with a nucleus: 2p2h process from [17], l denotes any of the 3 flavors and n a nucleon*

It is worth stressing here the fact that these interactions are, for an experimentalist, primary interactions but do not fully cover what will be the final state visible in a particular detector. Depending on the detection method some of the outgoing particles may or may not be visible. Moreover, secondary or final state interactions can occur resulting in a different topology of events in the detector. For example, a nucleon can be reabsorbed, a muon can decay, a neutron can be captured, etc. Those scenarii need to be taken into account when analyzing experimental data.

1.1.2.2 Detection strategies

Making use of these interactions, neutrino physicists have designed different strategies of detection types. Most of them rely primarily on the detection of an outgoing charged lepton since the nucleus and nucleon generally do not have a large kinetic energy.

Cherenkov detectors

Although it is not historically the first used strategy, one can use water Cherenkov detectors to detect the charged lepton. Indeed, if the lepton energy is above the Cherenkov threshold (typically 160 MeV for a muon), or in other words if the lepton's velocity is higher than that of the light (c/n) in the medium (here water), then the wavefront emitted by the ionization on the particle path will become coherent, analogously to a sonic bang as schematized in figure 1.7. As a result, a cone with luminous surface will appear on the lepton's trajectory. The emission angle (angle inside the cone) ϑ will depend on the velocity v as well as the refractive index n of the medium in the following way:

$$\cos\vartheta = \frac{c}{nv}. \tag{1.6}$$

This cone of light will produce, projected in 2D, rings of light that can be reconstructed by coincidence between many photo-multipliers, including a measure of their luminosity, and studied to infer the properties of the charged particle detected. From the kinematic properties of the lepton, in case of a neutrino interaction, it is possible to make conclusions on the detected neutrino. As this is the detection method used in Super-Kamiokande, it will be further discussed in Chapter 2. The wavelength of such Cherenkov light in water is in the ultra-violet and visible blue range. This type of detection involves very large detector because of the small probability of interactions of neutrinos with nucleons. Water is the primary choice for such experiments as it is transparent so the Cherenkov rings can easily be detected and it is a straightforward material to supply and treat in comparison with chemical products.

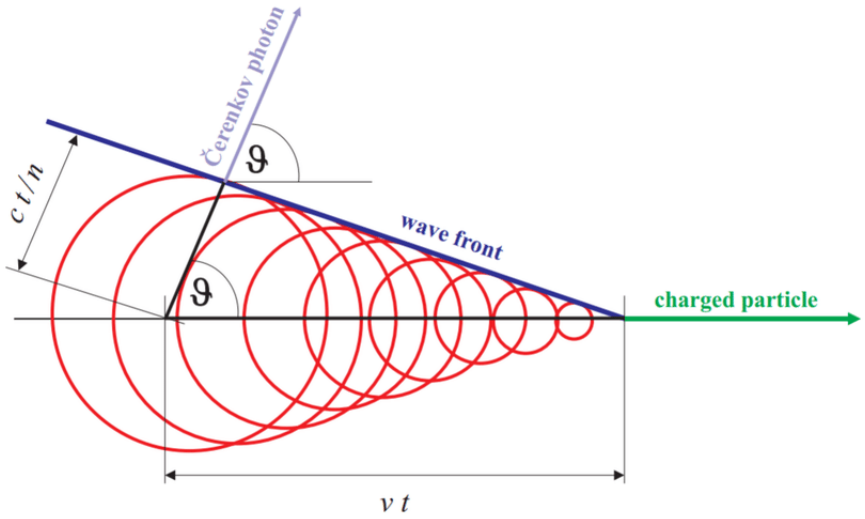

Figure 1.7. *Schematic of the constructive interference creating a Cherenkov light cone along a charged particle path, from [18]*

Other ionization processes

Any other type of experiment that relies on ionization can detect the charged lepton. We can cite here spark chambers that are designed such that when the gas inside the chamber is ionized by an outgoing lepton, an electrical field is applied and creates sparks along the lepton's trajectory. This is the method used to discover the muon neutrino in 1962 at the Brookhaven accelerator facility [19]. The gas is generally a noble gas. In that case it was neon. This experiment is one of the precursors of T2K as it produces a muon neutrino beam to study. Sources of neutrinos will be discussed further in the next section. We can also cite bubble chambers. Bubble chambers are filled with a super-heated liquid in a meta-stable phase, just below the boiling point. When a charged particle such as the lepton we want here to detect creates a ionization track, vaporization occurs and bubbles can be seen along the track. A magnetic field can be applied to bend trajectories and discriminate the sign of the particles charge. A notable example is the Gargamelle chamber which was operated at CERN between 1970 and 1979. It was filled with liquid Freon and had a 2 T magnetic field. Gargamelle provided the first observations of weak neutral current interactions with the discovery of muon neutrino scattering on both electrons [20] and hadrons [21]. This technology is still used nowadays to search for dark matter in the form of Weakly Interacting Massive Particles (WIMP) through nuclear recoil detection. Any type of scintillators is also a possibility, solid or liquid. In particular, Time Projection Chambers (TPC), relying primarily on ionization, and using also scintillation light have been extensively used as part of full sophisticated tracker systems. It is the case for the near detector ND280 of the T2K experiment as it will be presented in Chapter 2.

Neutron capture

The detection of the outgoing lepton can occur together with a detection of an outgoing neutron, in case of inverse beta decay:

$$\bar{\nu_e} + p^+ \rightarrow n + e^+ \tag{1.7}$$

Neutron capture signal can be seen in coincidence with scintillation light from the lepton. This is how the initial discovery of neutrino (actually electron anti-neutrino) was made in 1953 [22] at Hanford site and more importantly confirmed in 1956 [23] at the Savannah River nuclear plant. Fred Cowan and George Reines used alternating layers of liquid scintillator (toluene doped with terphenyl [24]) tanks and water tanks. The liquid scintillator allowed for the detection of the positron, through its track but more often through its annihilation with an electron into two gammas. The water tanks were doped with Cadmium Chloride so that the neutron could be captured by the Cadmium, leaving

the nucleus in an excited state:

$$n + {}^{108}\mathrm{Cd} \rightarrow {}^{109}\mathrm{Cd}^{*} \rightarrow {}^{109}\mathrm{Cd} + \gamma \tag{1.8}$$

The specific delayed signal (a few μs, 9 MeV) from the consequent de-excitation of the Cadmium triggered a new scintillation flash of light that could be measured by PMTs in coincidence with the positron signal allowing for a more stringent signature of a neutrino event.
Neutron capture can also be used in coincidence with Cherenkov light. This has been recently achieved in the water Cherenkov detector Super-Kamiokande by dissolving Gadolinium in the water [25] and will provide a better sensitivity to the $\bar{\nu_e}$ which have a smaller cross-section than ν_e.

Nuclear emulsions

Nuclear emulsions consist mostly, for use in particle physics, in silver bromide (AgBr) crystals in a gelatin film. When a ionizing particle deposits energy, it breaks the AgBr compound. The Ag^{+} released ions then go through a reduction process by absorbing an electron, and become Ag^{0} which is the metallic silver. After exposure to the beam of particles, the films of emulsion have to be developed using standard photographic procedures. In general, an organic reducing agent is used to take advantage of a chain reaction of reduction so as to reveal the track. The process is stopped when the desired contrast is obtained, changing the acidity of the medium. The film finally goes through different chemical baths in order to only contain in the end the track of silver grains, without being able to react anymore to energy deposits. For instance, this was the main part of the set of detectors used by the DONUT experiment at Fermilab to discover tau neutrinos through charged current and tracking of the outgoing tau lepton in 2000 [26]. The detector was placed after a proton beam dump to shield from as many backgrounds as possible, while still being exposed to the neutrinos produced by the decay of charmed quarks (produced in the collisions). Thick layers of nuclear emulsion were alternated with target material. A spectrometer was then placed to detect interaction products in the forward direction. It consisted in scintillators and wire-chambers, relying on ionization processes. A similar experiment set-up was used for the Oscillation Project with Emulsion-tRacking Apparatus (OPERA) for the first discovery of tau neutrino appearance in a muon neutrino beam between CERN and Gran Sasso laboratory in 2010 [27].

Radio-chemical detection strategies

An alternative approach to all the above is to use radio-chemical methods. It consists in having as a target material an element which will, after neutrino capture on one of its neutrons, become an unstable nucleus with a convenient half life-time. For example, the following reaction on Chlorine can be used:

$$\nu_e + {}^{37}_{17}\mathrm{Cl} \rightarrow e^- + {}^{37}_{18}\mathrm{Ar} \tag{1.9}$$

Argon 37 (^{37}Ar), which decays through electron capture, has a half-life of a little less than 35 days which is convenient. Indeed, one can leave the detector exposed to neutrinos for up to 100 days and then flush the ^{37}Ar out of the detector (which is quite easy because Argon is a noble gas). A Geiger counter can be used to count the amount of ^{37}Ar in the flushed gas, indirectly counting the number of neutrinos that have interacted. The value of half-life allows for a precise enough counting within reasonable time frames. Moreover, the neutrino capture threshold is quite low on Chlorine (about 0.8 MeV) so it allows for the detection of low energy neutrinos. This method was first used by Ray Davis in the 50's at Brookhaven and Savannah River nuclear reactors with negative results. It showed that indeed, anti-neutrinos from fission reaction cannot be captured in that way. More importantly, Davis, together with John Bahcall repeated that experiment in the Homestake Mine in South Dakota from the 60's to the 90's, giving the first evidence of the solar neutrinos problem in 1964 [28]. Indeed, Bahcall's theoretical calculations of the expected number of neutrinos from the Sun did not match the data where a significant deficit was observed. It was confirmed throughout the exposure of the detector until the final analyses in 1994 [29]. We now know, as will be discussed later, that this is an evidence of neutrino flavor oscillation. Due to the low energy of solar neutrinos, this experiment was only sensitive to one flavor: electron neutrinos.

As a conclusion, there are many ways to detect neutrinos but they are all indirect and challenging. They all offer sensitivity to different aspects and variables. In any case, they require ingenious technologies and careful management of background events.

1.1.3 Sources

An overview of neutrino properties and the strategies to detect them have been presented. But where can neutrinos come from ? This section aims at listing different sources of neutrinos and their relevant metrics.

1.1.3.1 Reactor neutrinos

As it has been seen before, electron anti-neutrinos are produced during beta decay. The most common natural radioactivity on Earth comes from Uranium (^{238}U, ^{235}U), Thorium (^{232}Th) and Potassium (^{40}K) that decay via the β^- process (inside the nucleus):

$$\underset{(udd)}{n} \rightarrow \underset{(uud)}{p} + e^- + \bar{\nu}_e \tag{1.10}$$

Those electron anti-neutrinos are quite numerous as their flux at the surface of Earth is of the order of $10^6 s^{-1}\text{cm}^{-2}$ but their energy is very low, of a few MeV (whereas the threshold for inverse β decay to detect them is 1.8 MeV), mostly under 3 MeV [30],[31].

However, the products of fission in nuclear plants (mostly Krypton and Baryum) undergo β^- decay as well and the yields are even larger. The typical rate for a standard modern power plant is about 10^{21}s^{-1} in all directions (in a 4π solid angle) [32] and their energies are a bit higher with an average of 4 MeV and can be up to 10 MeV. This is why they represent an interesting source of electron anti-neutrinos for physicists, and it is indeed how they were first detected as said before. Still nowadays many experiments use this flux of neutrinos to either study short length oscillations (as will be discussed in 1.2) or search for sterile neutrinos. We can cite RENO [33], Double CHOOZ [34], DayaBay [35],STEREO [36] and in the near future JUNO [37].

1.1.3.2 Solar neutrinos

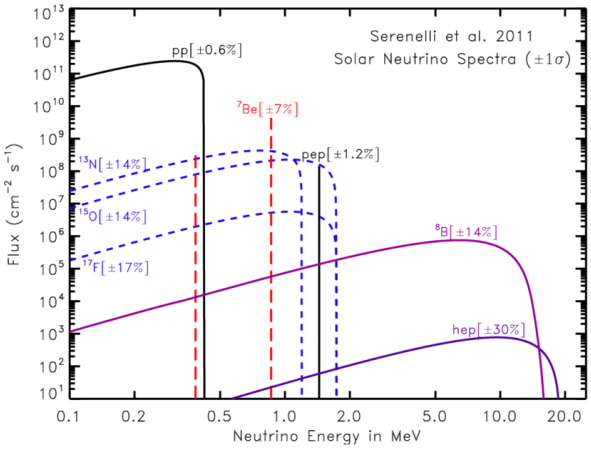

Figure 1.8. *Solar neutrino spectrum broken down by production processes, from [38]*

The thermonuclear reactions inside the core of the Sun also involve charged current weak interaction and so production of neutrinos; more specifically, electron neutrinos of also low energy (a few MeV). The received flux on the surface of Earth is of about $5 \times 10^{10}\text{s}^{-1}\text{cm}^{-2}$ maximum following Bahcall's model [39]. The break down of flux by

production process is displayed in figure 1.8. The main process is the chain reaction starting from proton-proton fusion. It produces more than 90% of all solar neutrinos, with 3 possible steps of ν production: pp-I, pp-II and pp-III. The detailed reactions and probability of each can be seen in figure 1.9 with different colors. The other emitted neutrinos come from the subdominant process called CNO for Carbon-Nitrogen-Oxygen (orange in the figure). In that process these heavier atoms act as catalysts for the fusion of 4 protons into Helium. Details are presented in the right part of figure 1.9.

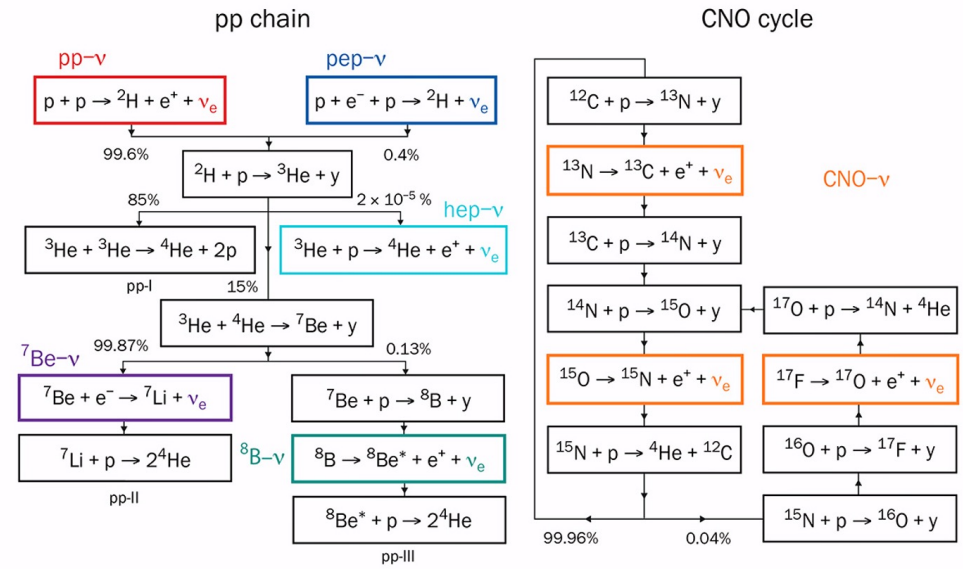

Figure 1.9. *Main electron neutrino production processes in the Sun core, from [40]*

1.1.3.3 Cosmic neutrinos

As neutrinos are emitted during fusion processes, all stars of the Universe are neutrino progenitors. More importantly, I want to mention here core collapse Supernovae (SN). Indeed, when a massive star undergoes gravitational collapse, 99% of the gravitational energy is released in the form of neutrinos of a few tens of MeV [41]. At the beginning of the implosion/explosion, a burst of about 10^{58} neutrinos is expelled in all directions during about 10 s only [42]. This represents a very specific signal that can be detected on Earth with current detectors if the supernova is inside our galaxy (The Milky Way) or nearby. It was indeed SN1987A, which collapsed in the Large Magellanic Cloud (a satellite galaxy to ours), that offered the first supernova burst neutrino detection in 1987, by three neutrino observatories: Kamioka [43], Irvine–Michigan–Brookhaven (IMB) detector [44], and Baksan [45]. Studying these bursts of neutrinos is very important to understand better the SN explosion mechanisms because they carry out most of its energy and their characteristics and history can say a lot about the environment inside the SN during the

core collapse. Moreover, because neutrinos interact only weakly and are very relativistic at these energies, they travel in straight line to us, and reach Earth about 3 h earlier than the photon signal in case of a nearby SN. This allows to infer the direction of incoming signals so as to be able to observe the transitory phenomenon earlier in time. This is an example of how valuable multi-messenger astronomy can be. Collecting as much information as possible with these neutrinos represents a technological challenge, especially in terms of precise timing and maximum rate of data taking as the signal lasts about 10 s as it can be seen in figure 1.10 which shows the time distribution of the SN87A detected signal. This will be discussed in Chapters 6, 7. As a note, the two neutrinos detected in the Mont Blanc experiment [46] are not trusted by the scientific community to be coming from the SN1987A supernova because of their unlikely time dispersion.

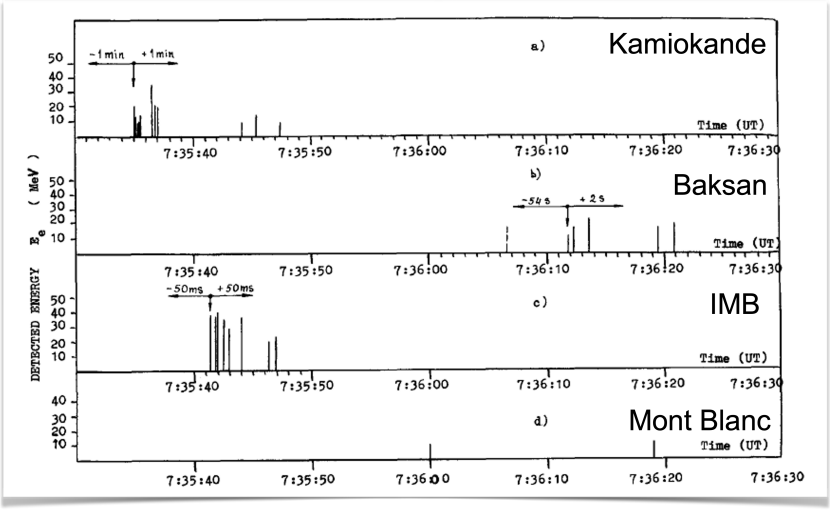

Figure 1.10. *Potential SN87 neutrino candidate events in Kamioka, IMB, Baksan, and Mont Blanc from [47]*

Supernovae explosions are very rare events in the galaxy (about one per 50 years in average). However, in the whole Universe it happens very often. Most of those neutrinos are not affected and reach us, forming a low flux of diffuse supernova neutrino background (DSNB). It has not yet been observed but future detectors may have the sensitivity to detect them in the next years. This will be discussed as well in Chapter 5.
As a note, in the Universe there are also non-relativistic ultra-low free streaming neutrinos, even if their detection is an enormous challenge that has not yet been achieved. They are relic neutrinos from the Big-Bang and were released at the time of neutrino decoupling, about 1s after the Big-Bang. Their energies are in the range of a few eV. They compose what is called the Cosmic Neutrino Background.
Finally, on the contrary, ultra-high energy neutrinos, above TeV, are produced in highly intense astrophysical events such as strong particle acceleration processes. This is the

case in the near environment of neutron stars or black holes. In particular, Active Galaxy Nuclei (AGN) and in their most extreme form quasars could produce neutrinos. Gamma Ray Bursts (GRB) are also potential progenitors of such neutrinos. The experiment IceCube is looking for such events [48] and has detected some candidate events even though the identification of their origin is a massive challenge.

1.1.3.4 Atmospheric neutrinos

Cosmic rays, mainly made of high energy protons hit the atmosphere constantly. Their collisions with the heavier nucleus of air molecules produce jets of particles including pions and kaons. These hadrons are unstable and decay very shortly after being produced. As there are about 10 times more pions than kaons that are produced in the atmosphere [49], we will focus on the example of charged pions. With a branching ratio of 99.99%, charged pions will decay into a muon and muon neutrino:

$$\pi^{\pm} \rightarrow \mu^{\pm} + \overset{(-)}{\nu}_{\mu}. \tag{1.11}$$

Muons themselves decay, with a longer lifetime of the order of the μs:

$$\mu^{+} \rightarrow e^{+} + \nu_e + \bar{\nu_{\mu}}, \tag{1.12}$$

$$\mu^{-} \rightarrow e^{-} + \bar{\nu_e} + \nu_{\mu}.$$

This results in the production of neutrinos of different flavors within these air showers, at an altitude of about 15 km. They are called atmospheric neutrinos and have a flux, at the surface of Earth of order 100 ν $\mathrm{m}^{-2}\mathrm{s}^{-1}\mathrm{sr}^{-1}$ depending on their energy which ranges from 100 MeV to 10 TeV [50]. As usual, those neutrinos can go through the Earth without interacting and so they are detectable in all directions.

1.1.3.5 Accelerator neutrinos

The same process of neutrino production as for atmospheric neutrinos can be provoked and controlled in accelerator facilities in order to create a (muon) neutrino beam. Indeed, a primary proton beam can be produced and directed towards a long target, in general mainly made of carbon (graphite target). The collisions produce charged hadrons such as pions which will decay within an appropriately designed decay volume, into neutrinos. Because of the incoming energy and directionnality of the protons, the decay will be Lorentz boosted so that neutrinos are mostly emitted forward, creating a neutrino beam. Hadrons of all sign of charge are produced but magnets in the decay volume can allow to deflect one sign and focus the other, letting the operators choose whether to produce a neutrino or anti-neutrino beam. The proton beam after the target is dumped. As it

has been seen previously with Eq. 1.11 and Eq. 1.12, the (anti-)neutrinos will be mostly muon flavored, with a small electron contamination. Currently operating accelerators such as the J-PARC one, in Tokai, Japan, are able to produce about 10^7 ν cm^{-2}s^{-1} in the direction of the beam [51], with energy of the order of several hundreds of MeV.
The first neutrino beam was produced at the Alternating Gradient Synchrotron (AGS) facility in Brookhaven laboratory (Long Island, New York, US) [52]. It allowed for the discovery of the muon neutrino in 1962. However, the pions and kaons (secondary mesons) in the decay volume were not focused which limited its final flux of neutrinos considerably. The first focused neutrino beam was then built at CERN in the 60's, and since then neutrino beam facilities all follow this principle. Nowadays, accelerator neutrino experiments, mainly T2K and NOνA are taking data and their direct successors are being built, namely Hyper-Kamiokande (HK) and DUNE. T2K and HK will be described in chapters 2 and 5 respectively.

1.2 Flavor oscillations formalism

After the above general introduction to neutrino properties and detection challenges, this section will focus on describing the phenomenon of neutrino flavor oscillations which is relevant to the scope of this thesis.

1.2.1 In vacuum

As it has been stated in section 1.1.1, each neutrino flavor is a coherent superposition of mass eigenstates as written in Eq. 1.1. A neutrino propagates as a superposition of flavor and mass states:

$$|\nu_\alpha(t)\rangle = \sum_i U^*_{\alpha i} e^{-iE_i t} |\nu_i\rangle \,, \tag{1.13}$$

E_i being the energy of a mass state i: $E_i = \sqrt{p_i^2 + m_i^2}$. Natural units are used here: $\hbar = c = 1$. In the case of ultra-relativistic neutrinos, which is almost always the case, $m_i \ll p_i$ and $p_i \approx E$ with E the neutrino total energy. This way, the probability of the propagating neutrino, originally in an α flavor state to interact as a certain β flavor state can be inferred by projecting the propagating neutrino onto a pure ν_β state. Using the approximation of plane waves to simplify the derivation, the following formula can be obtained:

$$P\left(\nu_\alpha \to \nu_\beta\right) = \left|\left\langle \nu_\beta \mid \nu(t) \right\rangle\right|^2 = \left|\sum_i U_{\beta i} U^*_{\alpha i} e^{-iE_i t}\right|^2 \tag{1.14}$$

This is the flavor oscillation probability. Indeed, this phenomenon, inherent to the quantum properties of neutrinos, allows for a neutrino of a certain flavor to become,

after propagation a neutrino of a different flavor. Using all the previous equations, this probability can be developed as:

$$\begin{aligned} P\left(\nu_\alpha \to \nu_\beta\right) = \delta_{\alpha\beta} - 4\sum_{i<j} \mathrm{Re}\left[U_{\alpha i}U^*_{\beta i}U^*_{\alpha j}U_{\beta j}\right] \sin^2\left(\frac{\Delta m^2_{ji}L}{4E}\right) \\ + 2\sum_{i<j} \mathrm{Im}\left[U_{\alpha i}U^*_{\beta i}U^*_{\alpha j}U_{\beta j}\right] \sin\left(\frac{\Delta m^2_{ji}L}{2E}\right) \end{aligned} \tag{1.15}$$

The length of propagation replaces the time of propagation using natural units where the speed of light $c = 1$, still in the ultra-relativistic approximation. The third term containing an imaginary part has an opposite sign for anti-neutrinos and U^* and U are exchanged. From Eq 1.15, it can be seen that the oscillation parameters are the following:

- The 3 mixing angles θ_{ij}
- The 2 differences of squared masses between mass eigenstates $\Delta m^2_{ij} = m^2_i - m^2_j$
- One single Dirac CP violating phase δ_{CP} because only pairs of UU^* appear in the oscillation probability and the Majorana matrix P is diagonal so that the Majorana phases cancel out in this calculation

As a note on vocabulary throughout this manuscript, oscillation probabilities are referred as follows:

- $P\left(\nu_\alpha \to \nu_\beta\right)$ is the appearance probability of a flavor β neutrino from a flavor α neutrino.
- $P\left(\nu_\alpha \to \nu_\alpha\right)$ is the survival probability of a flavor α neutrino.
- $1 - P\left(\nu_\alpha \to \nu_\alpha\right)$ is the disappearance probability of a flavor α neutrino.

The oscillation probability also depends on the ratio L/E of the length of propagation over the neutrino energy E as illustrated in figure 1.11 which shows KAMLAND results [53] with neutrino reactors with different powers and distances to the detector.

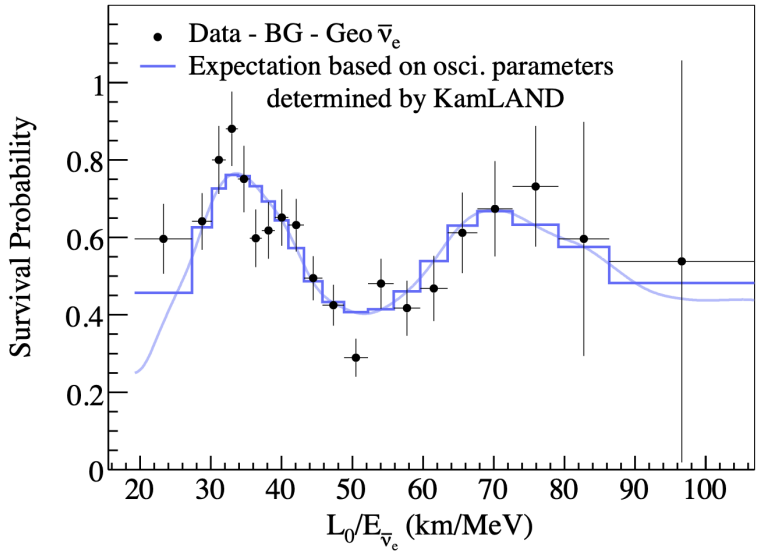

Figure 1.11. *Dependence of survival probability of electron anti-neutrino with the ratio L/E, from [53]*

1.2.2 In matter

This formalism was for neutrino propagation in vacuum. However, neutrinos can interact with matter along their path. They can all interact through neutral current scattering, and additionally electron neutrino can interact through charged current. When not destructive, this will affect the neutrino mixing. To take this into account in the oscillation formalism, one needs to add terms of interaction to the Hamiltonian of propagation:

$$V_{\mathrm{CC},\alpha} = \begin{cases} \pm\sqrt{2}G_F n_e(x) & \alpha = e \\ 0 & \alpha = \mu,\tau \end{cases}, \quad V_{\mathrm{NC},\alpha} = \mp\frac{G_F}{\sqrt{2}} n_n(x) \quad (\alpha = e,\mu,\tau) \tag{1.16}$$

In the above Eq 1.16, G_F is the Fermi constant and $n_e(x)$, $n_n(x)$ are respectively the densities of electron and neutron in the medium as a function of their spatial position. The signs are for either neutrinos or anti-neutrinos. It is then possible to re-write the eigenstates and effective mixing parameters as a function of the Fermi constant, the medium densities and the vacuum parameters. Doing so, it is possible to obtain the 2 flavor case matter mixing angle θ_m expressed in that way [54]:

$$\sin 2\theta_m = \frac{\sin 2\theta}{\sqrt{\left(1 \mp \frac{n_e}{n_{\mathrm{res}}}\right)^2 \cos^2 2\theta + \sin^2 2\theta}} \tag{1.17}$$

with $n_{\mathrm{res}} = \frac{\Delta m^2 \cos 2\theta}{2\sqrt{2}G_F E}$. A resonant value of electron density n_{res} appears, at which the mixing will be maximum regardless of the value of the vacuum mixing angle. For

anti-neutrinos, the resonant value is $-n_{\text{res}}$ since the resonance condition is in that case $\Delta m^2 \cos 2\theta < 0$. The effect is referred to as the MSW (Mikheev-Smirnov-Wolfenstein) effect [54, 56] and is particularly studied inside the sun and supernovae.
Taking matter effects into account is very important, especially on long distance of propagation and when the medium is dense. It makes the expressions of oscillation or survival probability heavier but the parameters and the structure of the formalism remain unchanged. For relatively short distance such as when studying neutrinos from reactor or accelerator, it is perfectly justified to consider the electron and neutron densities constant. However, when looking at neutrinos through the Earth such as for atmospheric neutrinos in upward directions, it is necessary to use a model of the Earth density layers. The commonly used model is the Primary Reference Earth Model (PREM) [57]. The study is also done the other way around, using current knowledge on neutrino oscillations to infer information on the density profile of the Earth at inaccessible levels [58].

1.2.3 Constraints on oscillation parameters

Most recent global constraints

Table 1.1. *Current constraints on oscillation parameters from [59]*

Parameter	Sources	Values
$\sin^2(\theta_{12})$	Sun + reactors (KAMLAND)	$0.307^{+0.013}_{-0.012}$
$\sin^2(\theta_{23})$	Accelerator (LBNO experiments)	NO 0.546 ± 0.021 IO 0.539 ± 0.022
Δm^2_{32} (NO) Δm^2_{31} (IO)	Accelerator (LBNO experiments)	$(+2.453 \pm 0.033)10^{-3}\text{eV}^2$ $(-2.536 \pm 0.034)10^{-3}\text{eV}^2$
$\sin^2(\theta_{13})$	Reactors	$(2.20 \pm 0.007)10^{-2}$
δ_{CP}/π	Accelerator (LBNO experiments)	$1.36^{+0.20}_{-0.16}$
Δm^2_{12}	Sun	$(7.53 \pm 0.018)10^{-5}\text{eV}^2$

Given the flavor oscillation formalism, studying various sources of neutrinos at different distances can allow to have sensitivity to different oscillation parameters. Indeed, depending on the ratio L/E as well as the flavors involved and whether we are measuring the disappearance or appearance of a certain flavor, the leading term will have dependence on different parameters. Combining all types of experiment's results, the Particle Data Group publishes each year the current best knowledge on all 6 oscillation parameters as is summarized in table 1.1 where uncertainties are at 68% level [59]. LBNO stands for long baseline neutrino oscillations and NO/IO stands for Normal/Inverted mass Ordering. It is important to notice, from the 1σ errors quoted, that CP violation has not yet been discovered: the δ_{CP}/π value is still compatible with the conservation of CP ($\delta_{CP}/\pi = 1$ or 0) at the level of discovery 5σ. Moreover, the octant of $\sin^2(\theta_{23})$ (whether it is more or less than 0.5) is not known. Finally, it can be observed that the so-called reactor mixing angle ($\sin^2(\theta_{13})$) is the most constrained parameter, which explains why a lot of effort is now put in constraining the other parameters at the same level.

Constraining the 1-3 sector parameters

As a consequence of the universal CPT symmetry, $P(\nu_\alpha \to \nu_\alpha) = P(\bar{\nu_\alpha} \to \bar{\nu_\alpha})$. The survival probability of electron neutrinos can be written in vacuum and in the 3-flavor mixing case as:

$$\begin{aligned} P(\nu_e \to \nu_e) = P(\bar{\nu}_e \to \bar{\nu}_e) = 1 &- \cos^4(\theta_{13}) \sin^2(2\theta_{12}) \sin^2\left(\Delta m^2_{21} L/4E\right) \\ &- \cos^2(\theta_{12}) \sin^2(2\theta_{13}) \sin^2\left(\Delta m^2_{31} L/4E\right) \\ &- \sin^2(\theta_{12}) \sin^2(2\theta_{13}) \sin^2\left(\Delta m^2_{32} L/4E\right) \end{aligned} \tag{1.18}$$

In the case of reactor anti-neutrinos ($\sim$ MeV), for a short baseline oscillation experiment with a detector at a small distance L ($<$ a few km), the terms in Δm^2_{21} can be neglected. Moreover, it can be approximated that $\Delta m^2_{31} \approx \Delta m^2_{32}$ (see figure 1.2). The dominant term in reactor electron anti-neutrino disappearance experiment is therefore:

$$P(\bar{\nu}_e \to \bar{\nu}_e) = 1 - \sin^2(2\theta_{13}) \sin^2\left(\Delta m^2_{31} L/4E\right), \tag{1.19}$$

hence a good sensitivity to θ_{13}.

Constraining the 1-2 sector parameters

On the contrary, the survival probability of the solar electron neutrinos, with same energy range and still neglecting matter effects, can be approximated as follows. Because they travel on very long distances, oscillation terms in $\sin(\frac{\Delta m^2_{32} L}{4E})$ are averaged over the propagation and can be neglected. Same for those in $\sin(\frac{\Delta m^2_{13} L}{4E})$ since they are the same

order of magnitude. Moreover, since θ_{13} is small compared to the two other mixing angles, terms in $\sin(\theta_{13})$ are suppressed and $\cos(\theta_{13})$ can be approximated to 1. What is left is a two-flavor mixing 1-2:

$$P\left(\bar{\nu}_e \to \bar{\nu}_e\right) = 1 - \sin^2\left(2\theta_{12}\right)\sin^2\left(\Delta m^2_{21} L/4E\right) \tag{1.20}$$

This is why the sector 1-2 is called the solar sector as measuring electron neutrino disappearance in solar neutrinos gives the best sensitivity to these 1-2 parameters.

Constraining the 3-2 sector parameters

As for the 3-2 parameters, they are best constrained in atmospheric or accelerator muon disappearance and electron appearance measurements. For example in vacuum, electron appearance probability can be written in 4 terms:

$$\begin{aligned} P\left(\nu_\mu \to \nu_e\right) &= P1 + P2 + P3 + P4 \\ P1 &= \sin^2\left(\theta_{23}\right)\sin^2\left(2\theta_{13}\right)\sin^2\left(\Delta m^2_{32} L/4E\right) \\ P2 &= \cos^2\left(\theta_{23}\right)\sin^2\left(2\theta_{13}\right)\sin^2\left(\Delta m^2_{21} L/4E\right) \\ P3 &= \mp J \sin\left(\delta_{CP}\right)\sin\left(\Delta m^2_{32} L/4E\right) \\ P4 &= J \cos\left(\delta_{CP}\right)\cos\left(\Delta m^2_{32} L/4E\right) \end{aligned} \tag{1.21}$$

where:

$$\begin{aligned} J = &\cos\left(\theta_{13}\right)\sin\left(2\theta_{12}\right)\sin\left(2\theta_{13}\right)\sin\left(2\theta_{23}\right) \times \\ &\sin\left(\Delta m^2_{32} L/4E\right)\sin\left(\Delta m^2_{21} L/4E\right) \end{aligned} \tag{1.22}$$

From Eq 1.21, it can be seen that the 3-2 parameters can be accessed.

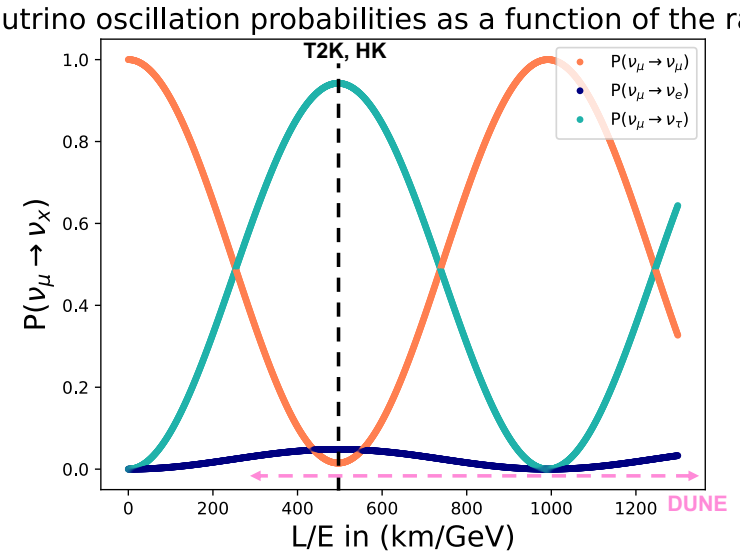

Figure 1.12. *Oscillation probabilities in a muon neutrino beam as a function of the ratio L/E, each component computed in the 2-flavors approximation*

Analyses are generally based on global simultaneous fit of all parameters, studying the shape of neutrino spectra as a function of the physical parameters of the experiment, mostly the ratio L/E and broken down by flavor. Focusing on LBNO experiments, figure 1.12 shows the survival probability of muon neutrinos and the appearance probabilities of electron and tau neutrinos in a muon neutrino beam, as a function of the ratio L/E. It can be seen that the first maximum of oscillation is located at L/E= 500 km/GeV which corresponds to most of the neutrinos in the design of the T2K and HK experiment described in Chapters 2 and 5 respectively. The larger range of the future experiment DUNE which will be briefly mentioned in Chapters 2, 6 is also shown. It can be noticed that most oscillating muon neutrinos oscillate to the tau flavor. This plot also allows to visualize better the oscillation probabilities, for instance it can be understood that the Δm^2 parameters will affect the period of oscillations whereas the $\sin^2\theta$ are changing the amplitude of oscillations.

Focus on constraining δ_{CP}

As Eq.1.21 shows, the CP violation phase is also accessible in atmospheric and LBNO experiments. Even if global analyses are always favored as they allow to extract all possible information from the data, especially since parameters are entangled, the sensitivity to δ_{CP} can be understood in the following way: The CP symmetry violation phase appears in the CP-odd term P3 of Eq.1.21. If θ_{13} had been close to 0 as it was first thought possible (only an upper limit was defined), it can be seen that the CP-odd term would be very suppresses and δ_{CP} would be almost impossible to measure. Fortunately, we now

know θ_{13} is large enough for hoping to measure the CP violation. In that case, it can be more directly accessed by computing the asymmetry $A_{\mu e}$ of electron appearance in muon neutrino and anti-neutrino beams. It is proportional to $sin(\delta_{CP})$:

$$A_{\mu e} \equiv \frac{P(\nu_\mu \to \nu_e) - P(\bar{\nu}_\mu \to \bar{\nu}_e)}{P(\nu_\mu \to \nu_e) + P(\bar{\nu}_\mu \to \bar{\nu}_e)} \simeq -\frac{\cos\theta_{23}\sin 2\theta_{12}}{\sin\theta_{23}\sin\theta_{13}} \sin\left(\frac{\Delta m^2_{21} L}{4E}\right) \sin\delta_{\mathrm{CP}} \tag{1.23}$$

Let's focus on oscillations from muon flavor to electron flavor as it is the targeted phenomenon in LBNO experiments (tau leptons being challenging to detect as it has been discussed in section 1.1.2.2 and will be reminded in section 2.4.2). The asymmetry between neutrino and anti-neutrino in that context gives the cleanest measurement of δ_{CP} possible for now. This asymmetry has been given in Eq. 1.23 but its denominator can also be expressed in terms of the Jarlskog invariant [60]. It is named after the Swedish physicist who first constructed it: Cecilia Jarlskog and is an invariant with respect to the choice of parameterization of the PMNS matrix. For this reason it is a very convenient quantity for theorists to make connections with the experimental results. With the usual parameterization, it is possible to write:

$$P(\nu_\mu \to \nu_e) - P(\bar{\nu}_\mu \to \bar{\nu}_e) = 16 J_{Jarlskog} \sin\left(\frac{\Delta m^2_{21} L}{4E}\right) \sin\left(\frac{\Delta m^2_{31} L}{4E}\right) \sin\left(\frac{\Delta m^2_{32} L}{4E}\right) \tag{1.24}$$

where the Jarlskog invariant $J_{Jarlskog}$ is extracted from the PMNS matrix elements U_{in}:

$$\begin{aligned} J_{Jarlskog} &= \mathrm{Im}\left[U_{e1} U^*_{\mu 1} U^*_{e2} U_{\mu 2}\right] \\ &= \frac{1}{8}\cos\theta_{13}\sin 2\theta_{12}\sin 2\theta_{13}\sin 2\theta_{23}\sin\delta_{\mathrm{CP}} \end{aligned} \tag{1.25}$$

From these expressions, additional conditions to the measurement of δ_{CP} can be seen. Sines of all three mixing angles are involved so none of these angles should be zero nor π to have a non-vanishing asymmetry term. Moreover, all mass states must have different masses otherwise, one of the $\frac{\Delta m^2_{ij} L}{4E}$ would also cancel the asymmetry term.
It has also been seen in section 1.2.2 that matter effects can change the ratio of flavors after propagation and enhance an asymmetry because only electron can be found in ordinary matter (no muons or taus). As a result, from the matter potential equations it can be deduced that muon flavor to electron flavor oscillations can be enhanced for neutrinos and suppressed for anti-neutrinos in normal ordering or the other way around in inverted ordering. One solution to disentangle these so-called matter effects from CP violation is to design an experiment with baseline and energy chosen so as to target the second maximum of oscillation. In that case, as can be deduced from Eq.1.23 and visually noticed in figure 1.13, the asymmetry is enhanced compared to the first maximum for the same neutrino energy. Finally, depending on the baseline, the mass hierarchy can

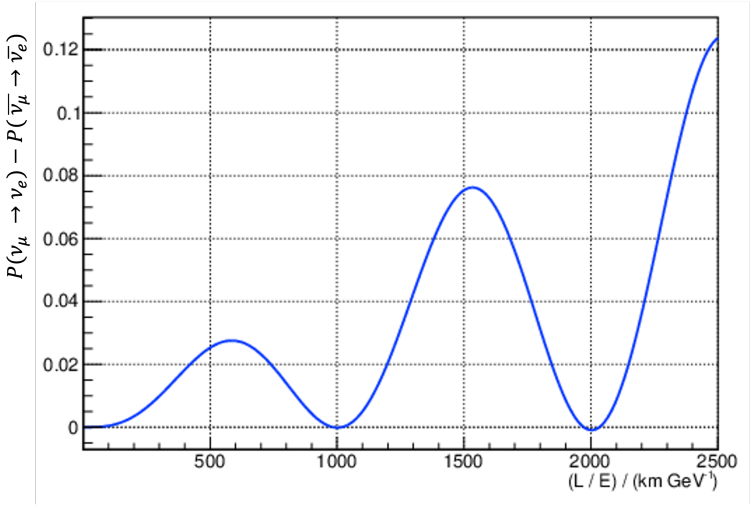

Figure 1.13. *Electron neutrino appearance asymmetry as a function of the L/E ratio, from [61]*

also be degenerated with CP violation as can be seen in figure 1.14 for a neutrino energy around 600 MeV and a baseline of 295 km which are the experimental conditions of the T2K experiment. This plot shows the number of anti-neutrino electron-like candidates as function of the neutrino ones for both mass ordering (NO: solid lines, IO: dashed lines), four different values of $sin(\theta_{23})$ (4 colors) and different values of δ_{CP} around the ellipses. Indeed, it can be observed that for a single point in that space, there is often two possibilities for the δ_{CP} value depending on the mass ordering hypothesis as the solid line and dashed line ellipses are superimposed and slightly shifted.

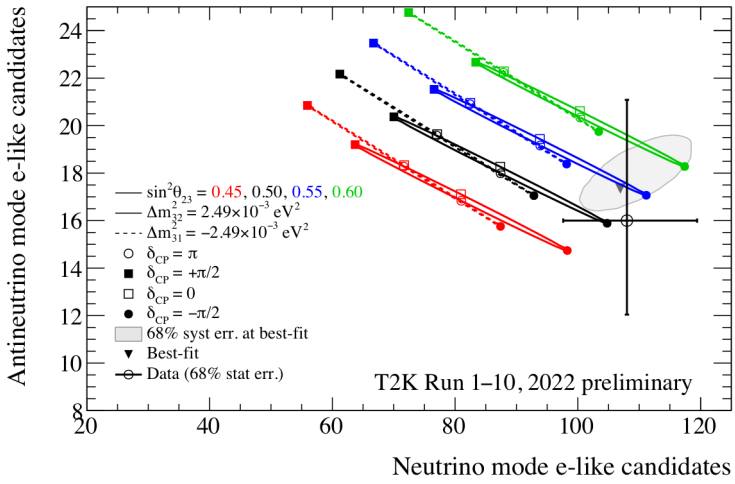

Figure 1.14. *Bi-probability plot for T2K analysis 2021, showing the number of anti-neutrino electron-like candidates as function of the neutrino ones for both mass ordering and several δ_{CP} and $sin^2(\theta_{23})$ values, source: T2K collaboration (https://t2k.org).*

This final point illustrates the need for a diversity of complementary high precision experimental set-ups in order to combine sensitivities to different entangled aspects.

1.3 Why studying neutrinos ?

As said before, neutrinos are an excellent probe to many phenomena in the Universe. Their absolute masses for instance, although constrained but unknown for now, imply that the Standard Model of particle physics is not sufficient and needs to be extended in a way or another. Neutrinos are the first particles to have decoupled after the Big Bang and so could be a probe to study the early universe if this neutrino background can one day be measured. We have also mentioned that neutrinos are massively emitted in extreme astrophysical events and could therefore help us understand better those phenomena. This thesis however is essentially about neutrino oscillations and those are ruled by 6 parameters and are impacted by the unknown mass ordering (the sign of the Δm^2_{32} and Δm^2_{31} parameters). Observing neutrino oscillation means observing the entangle effect of all these parameters and unknown even if we have seen that different experimental designs can offer targeted sensitivity to some parameters. Therefore, it is crucial to enter an era of precision measurements of those parameters to be able to answer more fundamental questions. Indeed, the mass ordering and more importantly the CP violation in the leptonic sector of the Standard Model have implications in theory, in particular their determination may confirm or exclude theories of flavor symmetry up to the Grand Unified Theory (GUT) context, see-saw mechanisms and leptogenesis models. The baryon asymmetry between matter and anti-matter remains of unknown origin, with the very simple and essential question of how it is possible that there is still non-annihilated matter in the Universe. An asymmetry at the level of particle production could explain this. In particular for leptons as the CP symmetry violation for quarks is known to be very small. The CP violation among light (Standard Model) neutrinos would not be enough to explain the amount of matter in the Universe but its existence would make more general asymmetric leptogenesis models involving heavy sterile neutrinos more plausible.
Measuring precisely those effects is tricky. Indeed, when studying neutrino oscillations, the raw observables are basically ratios of numbers of neutrinos between flavors and neutrino/anti-neutrino ratios, as a function of kinematic variables. Many things can cause the same effect in these observables. Using a neutrino beam from a dedicated accelerator and a set of near and far detectors as in long baseline neutrino oscillation (LBNO) experiments allows to control better systematic effects that would change ratios in flavor. For instance, it allows to know the proportion of electron neutrino contamination in a muon neutrino beam and to measure separately neutrino and anti-neutrino oscillations

and refine flux and cross-section models used in the analysis. A very careful management of systematic uncertainties is crucial.

1.4 Conclusion

Throughout this introductory chapter, the properties and sources of neutrinos have been presented, focusing slightly more on flavor oscillations in accelerator neutrino beams as this will be the overall context of this thesis manuscript, as well as the reasons why we study them so carefully. The combination of the high scientific interests in studying neutrinos, driven by the cross-section between neutrinos and fundamental questions about our Universe, and the difficulty in detecting them is also illustrated by the number of Physics Nobel prizes that have been attributed for discoveries on neutrinos. We can cite here the 1995 prize to F.Reines for the first detection of neutrino, the 1988 prize to L.M.Lederman, M.Schwartz and J.Steinberger for the muon neutrino beam technique and the muon neutrino detection, the 2002 prize to M.Koshiba and R.Davis for astrophysical neutrino studies (solar and 1987 supernovae burst detection) and the 2015 prize to A.McDonald and T.Kajita for neutrino flavor oscillations.
More generally speaking, this chapter aimed at extensively discussing the experimental challenges and precision requirements to motivate the research performed for this thesis.

Chapter 2

The Tokai to Kamioka (T2K) experiment

This chapter will describe the Tokai to Kamioka (T2K) experiment which is the context of the work presented in this manuscript. It mainly consists in the production of a neutrino beam, a set of near detectors and a far detector. Each of these elements will be described.

Contents

2.1 Overview of the T2K experiment

Tokai to Kamioka (T2K, [62]) is a long-baseline neutrino oscillation (LBNO) experiment that studies flavour oscillation of a muon-neutrino beam between the Japan Proton Accelerator Complex (J-PARC) in Tokai (Ibaraki prefecture, Japan) and the Super-Kamiokande (SK) detector in Kamioka (Gifu prefecture, Japan). A diagram of the overall experimental setup can be found in figure 2.1.

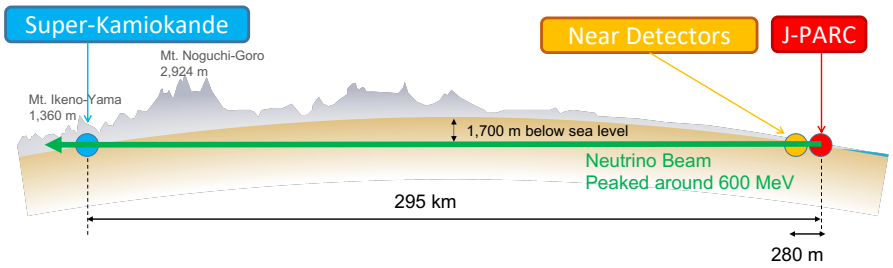

Figure 2.1. *Cross-section of the T2K experiment baseline, source: T2K collaboration (https://t2k.org).*

The idea of producing muon neutrino beams to study neutrino comes from the late 50's and lead to the discovery of the muon neutrino in 1962 as said in Chapter 1. In the 90's this idea was revisited when flavour oscillations were actively searched for. This is the context in which LBNO experiments have been designed. It is possible to differentiate three LBNO experiment generations. The first generation aimed at confirming the neutrino oscillation discovery of 1998 [8] with atmospheric neutrinos by Super-Kamiokande. The two main experiments were then the KEK to Kamioka (K2K [63]) experiment and the Main Injector Neutrino Oscillation Search (MINOS [64]) experiment. K2K was using a 12 GeV proton beam from the KEK facility in Tsukuba (Ibaraki prefecture, Japan) to produce a muon neutrino beam with an energy of 1.3 GeV. It was looking for oscillations between its near detector, a 1 kton water Cherenkov detector located 300 m downstream on the beam-line, and the Super-Kamiokande 50 kton water Cherenkov detector. It used a 250 km baseline and operated between 1999 and 2004. It came very close to confirm the 1998 oscillation discovery with a 4σ significance on muon-neutrino disappearance observation [65]. With the same overall physics goals, MINOS started taking data in 2005 and, thanks to various upgrades, continued to do so until 2016. Located in the US, it used the very energetic 120 GeV proton beam from the Neutrinos at the Main Injector (NuMI) project at Fermilab (Illinois, U.S.) to produce a neutrino beam of 3 GeV in average. It used also a far scintillator detector in Minnesota after a 735 km baseline.

These first generation experiments were not fully optimized, and although they brought proofs of concept and interesting secondary results, they did not fulfill their primary physics purpose in terms of discovery at 5σ. To do so, their successors were proposed and built, T2K and the NuMI Off-Axis Electron Neutrino Appearance (NOνA [66]) for respectively K2K and MINOS. T2K started taking data in March 2010. By that time, the idea was to study precisely flavour oscillation parameters. In particular, the question that arose was whether $\sin^2\theta_{13}$ was non-zero or not. K2K was not optimized for precision measurements. For instance, the near detector was not specifically designed for all the necessary flux and cross-section measurements and the average of the wide range of neutrino energies produced was 1.3 GeV, when, for a 250 km baseline, the maximum of oscillation is around 500 MeV. To improve the sensitivity of the experiment, T2K was built together with a sophisticated set of near detectors that will be described in section 2.3. Moreover, a medium-energy neutrino beam at J-PARC was inaugurated (described

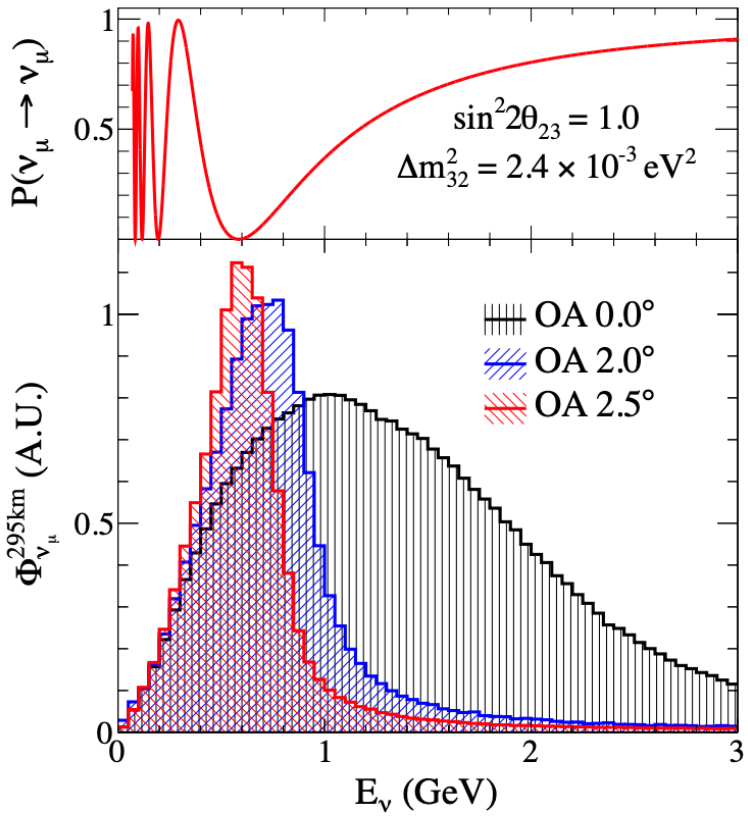

Figure 2.2. *ν_μ survival probability (top) and T2K flux (left) for various off-axis angles for the T2K baseline (295 km) and fixed values of the oscillation parameters, from [51]*

in section 2.2) instead of using the KEK higher energy one. In combination, the off-axis strategy was implemented for the first time. It consists in locating some of the near detectors and the far detector, not directly on the beam axis but at a shifted position. Indeed, as detailed in Chapter 1, muon neutrinos in an accelerator beam mainly come

from pion disintegration and their energy can be written as:

$$E_\nu = \frac{m_\pi^2 - m_\mu^2}{2(E_\pi - p_\pi \cos\theta)}, \tag{2.1}$$

where m_π and m_μ are the pion and muon masses, E_π is the pion energy, p_π its momentum and θ is the angle between the pion direction before disintegration and the neutrino direction, in the laboratory frame. As illustrated in figure 2.2 for T2K, the neutrino energy is less dependent on the pion energy when neutrinos are emitted at a large angle θ. As a result, the neutrino spectrum on the beam axis is wide, whereas, it is more peaked around a certain value when observed at a certain off-axis angle. With an estimate of the oscillation parameters values, it is possible to optimize the off-axis angle at which the detectors should be placed so that the mean neutrino energy corresponds to the oscillation maximum at a given baseline. As a result, T2K is designed with a 295 km baseline and an off-axis angle of 2.5°, selecting a mean neutrino energy of 600 MeV. This energy also presents the advantage to fall into the region where CCQE interactions with water are dominating the neutrino cross-section, making measurements cleaner and nuclear interaction modeling easier. The off-axis angle experimental configuration, because of kinematics effects, also selects 2-bodies decays components of the neutrino beam as opposed to 3-bodies decays. This reduces the intrinsic electron neutrino background in the beam since electron-neutrino contamination comes from muon and positive kaon 3-bodies decays. NOνA, which started taking data a bit later than T2K, in 2014, has also implemented the off-axis configuration (0.8°) on a 810 km baseline.

T2K was very successful since the beginning, providing the first significant constraint on θ_{13}, claiming it is non-zero with a 90% confidence level in 2011 [67], improving the former leading limit set by Chooz (département des Ardennes, France), a short baseline reactor neutrino oscillation experiment in 2003 [68] . T2K's result was followed shortly after by the Chooz successor, Double Chooz, in 2012 [69]. Today, the precision measurement is led by the Daya Bay experiment in China [35].
After that first result, T2K physics goals shifted a bit as the non-zero value of θ_{13} opened the door to CP phase measurements and mass ordering evaluation.
With an optimized design to look for electron-neutrino appearance and muon-neutrino disappearance and the possibility, since 2014, to run with either a neutrino or anti-neutrino beam, T2K has already achieved a lot. It is currently an international collaboration over 14 countries, 76 institutes and with about 500 collaborators. As depicted in figure 2.3, as of today (2023) T2K has collected 11 runs of data with a beam delivering 2.1428×10^{21} and 1.634556×10^{21} protons on target (POT) respectively in neutrino and anti-neutrino modes. This corresponds for instance to about 400 muon neutrinos and 110 electron

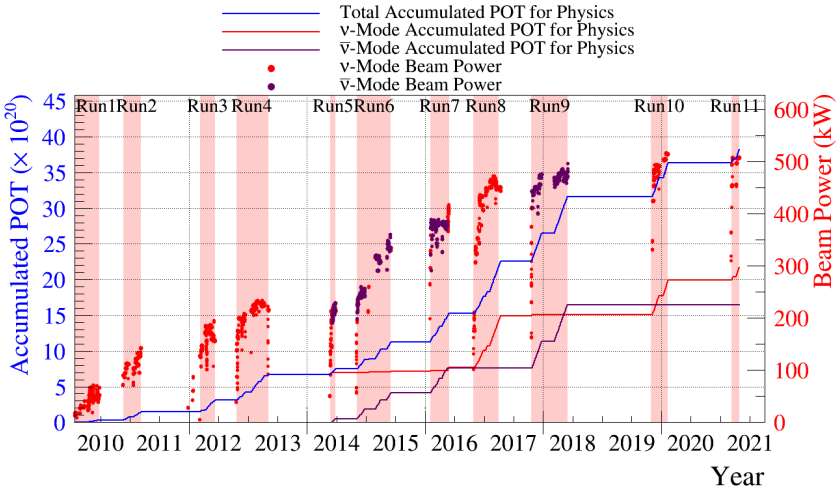

Figure 2.3. *Accumulated POT and beam power as a function of run years, source: T2K collaboration (https://t2k.org).*

neutrinos detected at SK (detailed breakdown will be given in section 2.4.1). Mainly, this has allowed T2K to constrain precisely the atmospheric oscillation parameters but, more importantly, to lead δ_{CP} measurements with an exclusion of CP conservation at almost 3σ in 2020 [70]. T2K will aim at improving these constraints until the end of operation of SK, when its successor Hyper-Kamiokande (HK) will take over.
Indeed, going further in this direction will be the main goal of the future 3rd generation LBNO experiments, HK, DUNE ([71]), and later ESSnuSB [72].

2.2 The beam

The J-PARC accelerator chain is made of 3 main components. The first one is a linear accelerator (LINAC) which serves as an injection system. It accelerates H^- ions up to 400 MeV with a pulse width of 500 μs until they are injected into the second part: the Rapid Cycling Synchrotron (RCS). When injected into the RCS, ions are charge-stripped thanks to carbon foils, converting the ion beam bunches into proton bunches. These are accelerated to 3 GeV at a repetition rate of 25 Hz. At the end of this step, the beam line separates in two. Most of the beam bunches are sent to the Materials and Life science Facility (MLF) to generate intense neutron/muon beams, but some of them are injected into a third part of the accelerator chain: the Main Ring synchrotron (MR). This last part will accelerate the protons to 30 GeV which is the necessary energy to produce the intended neutrino beam. At this point, there are 8 proton bunches of 58 ns each separated by 598 ns gaps per cycle. There is one cycle every 2.48 s (referred to as repetition rate). These 30 GeV protons are then extracted, their trajectory is directed towards SK in an

arc section, using 3 pairs of supra-conducting magnets. After the beam-line is bent, it is focused thanks to both dipole and quadrupoles magnets so as to hit the target in the center. The collision of the proton beam with the target produces secondary particles such as pions and kaons which decay into leptons and neutrinos as explained in section 1.1.3.4. The overall scheme of the setup after extraction of the 30 GeV proton beam is displayed in figure 2.4. The MR accelerator was designed to be run with a power of 750 kW but has achieved 'only' 515 kW. In 2023, it is currently restarting after an upgrade to be able to reach the target power. The T2K target station is located 12 m underground

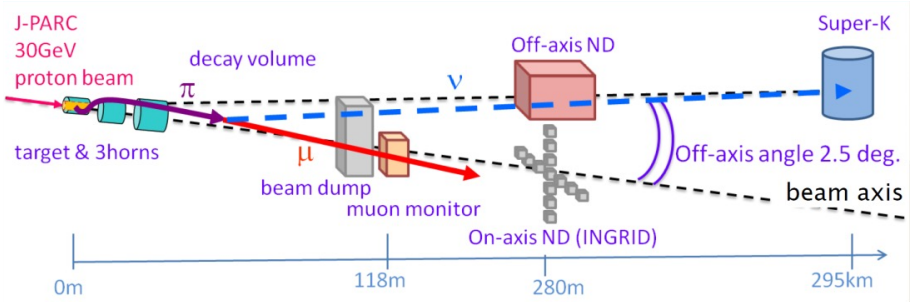

Figure 2.4. *Scheme of the J-PARC neutrino beam-line, source: T2K collaboration (https://t2k.org).*

according to the direction of the beam as can be seen in figure 2.4. It consists, upstream of the target, in a graphite collimator which focuses proton towards the target, as well an optical transition radiation monitor (OTR) to monitor the proton beam profile. The target itself is a 91.4 cm long, 2.6 cm diameter and 1.8 g/cm^3 dense graphite cylinder. The choice of carbon allows to produce the intended secondary particles without being damaged too fast by the energy deposit of the beam, as would material with a higher Z, such as metals. To avoid melting down, the target is cooled by gaseous Helium. The vacuum region upstream of the target is separated from the Helium vessel by a titanium foil. After the target there is a 96 m decay volume. Before decaying, the (mainly) pions need to be focused along the beam axis so that the inferred neutrino beam does not diverge too much. Indeed, neutrinos can not be focused. To achieve this, three horn systems are used and the first one surrounds the target. The sign of the horn current can be chosen so as to focus either positive or negative pions, resulting in respectively a neutrino or anti-neutrino beam. The horn current value has been 250 kA up to now but is designed to reach 320 kA in the nearest future. The example of the production of a neutrino beam, called Forward Horn Current (FHC) mode is shown in figure 2.5. The anti-neutrino mode is referred to as Reverse Horn Current (RHC) mode.
After the decay volume, a 75 tons graphite (1.7 g/cm^3) beam dump is placed to stop all the produced muons as well as hadrons below 5 GeV without impacting the neutrino

beam. The beam dump dimensions are: 3.174m×1.94m×4.69 m (length×width×height).

As shortly mentioned previously in this section, the beam-line is currently going through an upgrade. The current 'repetition rate' will be almost doubled to 1 spill every 1.36 s by upgrading the magnet power supplies, the radio-frequency (RF) systems, and injection/extraction devices. This will allow to increase the number of protons per bunch by 30% going from 2.6×10^{14} to 3.2×10^{14}. It is foreseen to reach a beam power of 1-1.3 MW after all upgrades by 2028.

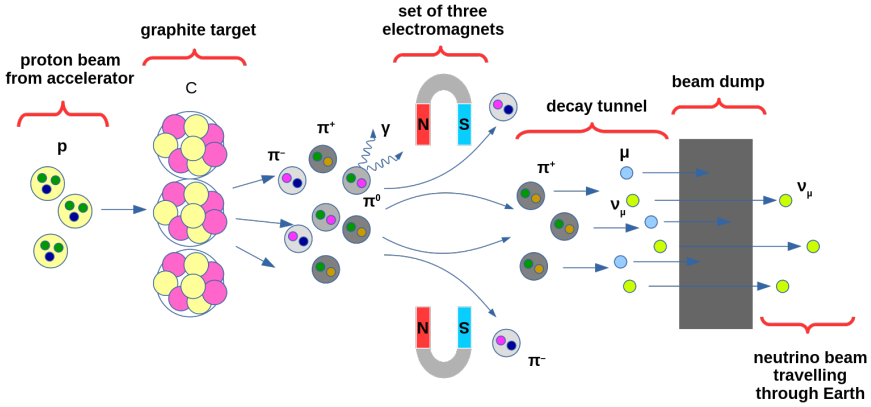

Figure 2.5. *Scheme of the muon-neutrinos beam production at J-PARC, source: wikipedia (*https : //en.wikipedia.org/wiki/T2K_experiment*)*

2.3 The near detectors

The different near detectors can be separated into two categories according to their positions with respect to the beam: on-axis and off-axis detectors. As it has been described in section 2.1, the off-axis strategy is used for the far detector to enhance the oscillation signal. Indeed, as reminded in figure 2.6, the flux peak of J-PARC neutrinos at the chosen angle of 2.5° corresponds to the maximum oscillation probability (minimum of the survival probability) of muon neutrinos for the T2K baseline (295 km). To constrain the flux and cross-section of (anti-)neutrinos in the same conditions, in particular in terms of energy, it is very valuable to have a set of near detectors at the same off-axis angle. However, the T2K experiment also relies on on-axis near detectors to characterize the beam position and the hadron production.

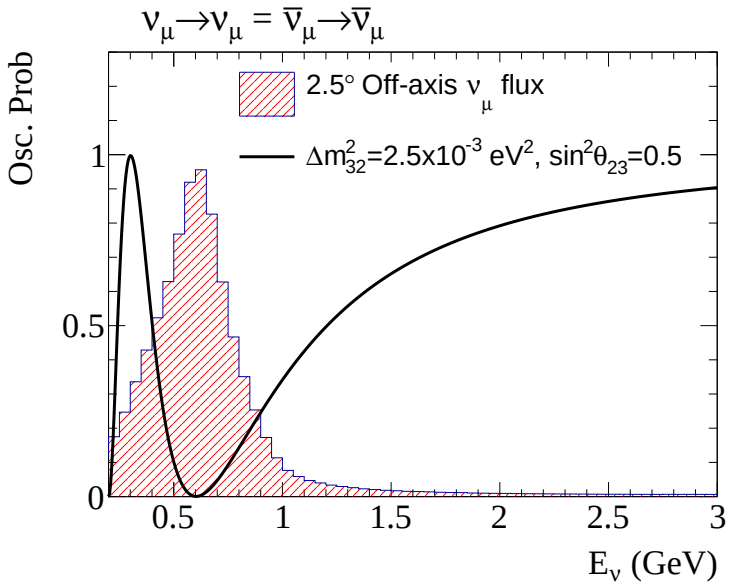

Figure 2.6. *ν_μ survival probability and T2K flux overlaid for the T2K baseline (295 km) and fixed values of the oscillation parameters, source: T2K collaboration (https://t2k.org).*

2.3.1 On-axis near detectors

Downstream of the T2K target and decay volume, the first on-axis detector is the MUon MONitor (MUMON). It is an array of ionization chambers and semi-conductor detectors that allow to monitor the muon profile from detected those above 5 GeV that passed through the beam dump. This helps monitoring the beam direction from the muon distribution within 0.25 mrad as well as the beam intensity with a 3% precision.
The second on-axis near detector is the Interactive Neutrino GRID (INGRID [73]) which is located 280 m after the target. As opposed to the MUMON, INGRID is intended to monitor the neutrino beam directly by detecting the outgoing particles of neutrino interactions. The detector is arranged in a cross configuration as can be seen from the side in the left part of figure 2.7. This cross consists of two lines of 7 modules which do not cross physically (the vertical and horizontal lines are not on the same plane). Each module is a cube of a bit less than 1.5 m length, resulting in a cross of dimensions 10x10 m which is consistent with the spatial spreading of the beam (at 1σ) of 5 m at this distance from the target. Additionally, there are two off-axis modules placed in diagonal with respect to the cross, to monitor the asymmetry of the beam. Each module is made of a sandwich structure of nine iron plates acting as target for neutrino interactions and 11 scintillator planes used to track the outgoing particles trajectories. The module lines are surrounded by scintillator planes used to veto particles coming from outside. The horizontal and vertical beam profiles are reconstructed from the number of observed events in each module and the beam center is measured from the center of these profiles. The

detector is calibrated with cosmic ray data. INGRID mainly detects muons from the unoscillated muon neutrinos interactions since the iron plates absorb the pions and protons, not allowing the tracker to reconstruct their trajectories. To remedy this, a different additional module has been placed at the center of the beam, in the gap between the horizontal and vertical INGRID module lines. It consists of scintillator planes surrounded by veto planes, without the iron layers and with optimized scintillators dimensions for proton tracking. It is called the INGRID Proton Module and helps differentiating neutrino interaction types.

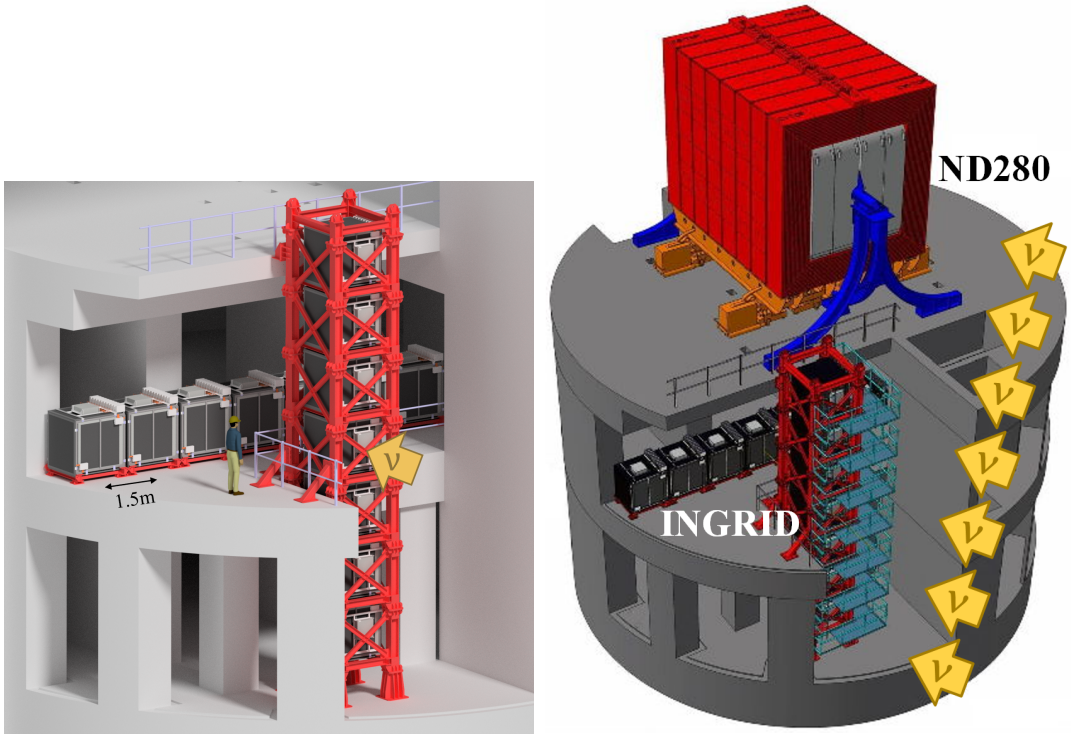

Figure 2.7. *Scheme of the INGRID detector (left) and of the full off-axis detectors set (right), source T2K collaboration (https://t2k.org).*

2.3.2 Off-axis near detectors

T2K only has a very complete set of off-axis near detectors, at 2.5° just like SK. They are called ND280 for Near Detector, at 280 m from the target. As said above, the spreading of the beam is only a few meters at this stage along the baseline and so, ND280 is actually physically close to INGRID, in the same facility, as it can be seen in the right plot of figure 2.7. Being exposed to the neutrino beam in the same conditions as SK, ND280 has several purposes. It is designed to measure the flux, energy spectrum and ν_e contamination of the beam at that specific off-axis angle. It is also designed to perform

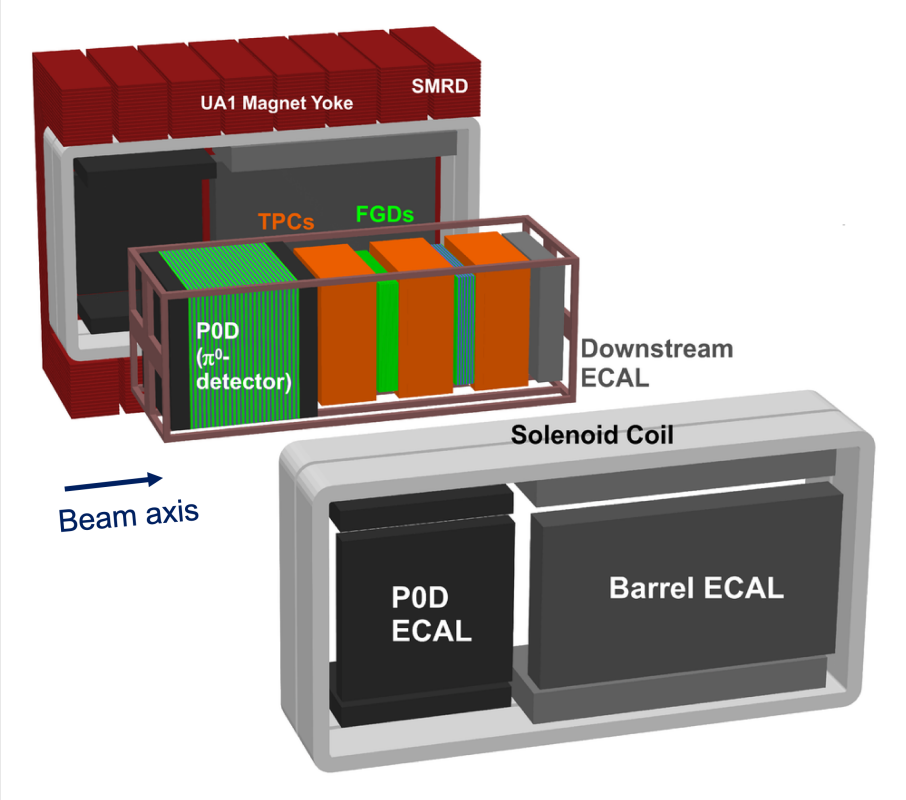

Figure 2.8. *Scheme of the current configuration of the ND280 detectors (before 2023 upgrade), source: T2K collaboration (https://t2k.org).*

precise cross-section measurements of ν_μ, $\bar{\nu_\mu}$, and $\overset{(-)}{\nu_e}$ on Carbon and Oxygen, including broken down by specific interaction modes. To that end, ND280 consists of [74]:

- A π^0 detector (P∅D)
- Three time projection chambers (TPC), part of the tracker
- Two fine grained detectors (FGD), part of the tracker
- An electromagnetic calorimeter (ECAL)
- A scintillator muon range detector (SMRD)

All these elements are arranged as shown in figure 2.8, inside a magnet yoke (0.2 T) reused from the UA1/NOMAD experiments at CERN and a solenoid coil so that particle signs can be determined. The middle part of the detector, containing the P∅D, TPCs, and FGDs, is framed by a metallic structure, referred to as the basket, with dimensions $6.5 \times 2.6 \times 2.5 m^3$ (length × width × height). The performance of this set of near detectors that is going to be described allows T2K to constrain flux and cross-sections uncertainties at a level of about 3-5%.

P∅D

One of the main backgrounds at SK comes from the decay of neutral pion (mean lifetime of 8.43×10^{-17} s [59]) into two photons, mimicking an electron ring. This neutral pion comes mainly from coherent neutral current pion production processes on water such as:

$$\nu + N \rightarrow N + \nu + \pi^0, \tag{2.2}$$

with N a nucleon. To quantify this background, the near detector set contains a dedicated detector: the P∅D. The configuration of that detector can be seen in figure 2.9. It consists mainly of alternating layers of water bags (28 mm thick) and brass sheets (1.5 mm thick) with scintillator layers. There are in total 50 water layers and 40 scintillator layers, called P∅D Module. This sandwich configuration is separated into an "upstream water target" and a "central water target" sections. The P∅D can be operated both with filled or empty water bags, allowing to isolate the measurement of π^0 production cross-section on water which is especially relevant for interactions at SK. Each scintillator layer is made of two perpendicular arrays of triangular scintillator bars, 134 vertical and 126 horizontal ones. These bars are doped polystyrene scintillator bars coated with T_iO_2 to reflect escaping light, as well as a wave length shifter. In addition to these water target sections, as it can be noticed in figure 2.9, the most upstream and downstream part of the detector are made of electromagnetic calorimeters layers. They consist of 7 scintillator layers alternated with lead sheets. This has the double purpose of containing electromagnetic showers and acting as a veto volume for particles from interactions outside the P∅D. The detector has been successful in measuring this background and found results compatible with simulations [75].

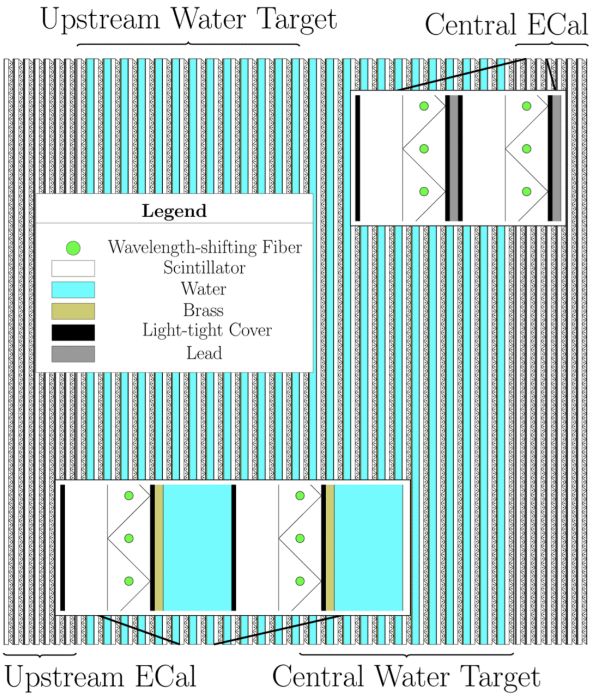

Figure 2.9. *Diagram of the π^0 detector (P∅D) [62].*

TPCs

The TPCs, together with the FGDs are the tracker part of the detector. They are alternated since the main interaction that needs to be characterized is the CCQE one, and the TPCs are adapted to detect the outgoing leptons whereas the FGDs are more adapted for detecting the ejected nucleon. This sandwich configuration allows to reconstruct tracks from both types of particles. Each TPC module is 1 m long along the beam direction and each side in the perpendicular plane is approximately 2.5 m long. It is surrounded by a field cage ensuring the uniformity of the electric field for electron drift. The electric field is perpendicular to the beam direction. The TPCs are vertical and each of them is filled with 3000 L of a specific optimized gas mixture: $Ar/CF_4/iC_4H_{10}$ (95/3/2). It has been chosen because the drift velocity is quite fast, around 7.9 cm/μs for an electric field of 280V/cm and the transverse spreading is low with a diffusion coefficient of about 250 $\mu m/cm^{1/2}$ in the 0.2 T magnetic field. Indeed, this allows to reconstruct the particles sign and momentum precisely as when they pass through the TPC, they ionize the gas, and thanks to the electric field applied, the electrons drift toward the side of the TPC where the anode and readout planes are. The particle identification (PID) is performed through energy deposit measurements (dE/dx), using the Bethe-Block formula [76] with the reconstructed kinematics of the particle. The anode readout plane is made of 12 bulk MicroMegas (micro-mesh gaseous detector) modules and there are two readout planes per TPC. These planes provide a 2D mapping of the trajectory. The third dimension is

computed from the drift time. The incoming electrons induce an electronic cascade in the gaseous part, amplifying the detectable signal. With this technology, T2K's TPCs have demonstrated an energy resolution better than 8%, allowing to distinguish muons from electrons by more than 3σ, and a spatial resolution between 600 μm and 1.2 mm depending on the track's orientation.

FGDs

Two FGDs are sandwiched between the TPCs as it can be seen in figure 2.8. They provide a target mass for neutrino interactions detected in the TPCs and complete these TPCs to be a full tracker. The two FGDs are slightly different. One of them, referred to as FGD1 is a pure scintillator whereas the second one, FGD2, is made of alternating layers of water and scintillator, providing additional information on neutrino-water interaction cross-sections to the P∅D measurements. Each FGD has outer dimensions of $2300 \times 2400 \times 365\text{mm}^3$ with 1.1 tons of target and the scintillator material used is also polystyrene bars with T_iO_2 coating and wave-length shifter as for the P∅D. FGD consists of 30 layers of 102 bars, each layer being orthogonal to the previous one, allowing for 2D particle track reconstructions. FGD2 is made of 14 such layers. After every set of two orthogonal layers, there is a 2.5 cm thick water layer at sub-atmospheric pressure. Both FGDs are contained in a black box with photo-sensors to readout the scintillator signals. FGD can not distinguish muons from pions due to similar energy deposits (similarly as in the TPCs) but they are very efficient for pion/proton discrimination, making them complementary to the TPCs performance.

ECAL

The electromagnetic calorimeter detector is surrounding the middle, or inner part of ND280 containing the TPCs, FGDs and the P∅D. Its role is to detect and measure the energy of photons as well as charged particles escaping the inner detectors so as to complete the tracking system and collect as much information as possible on the interactions that happened. The photon detection is crucial to the reconstruction of neutral pion production together with the P∅D. As it can be seen in figure 2.8, the ECAL is made of 13 modules in three different sections: the Barrel ECAL, the Dowstream ECAL and the P∅D ECAL. Each ECAL module is made of the same type of scintillator already described for the P∅D and the FGD, with 34 layers of 50 scintillator bars. Each layer is shifted by 90° from the previous one, allowing for 3D reconstruction. They are also separated by 1.75 mm thick lead sheets. First, 6 of the 13 modules make up the Barrel ECAL, covering four sides of the inner tracker of ND280 (TPCs+FGDs): the plane parallel to the beam axis and the top and bottom planes referring to the orientation of

the diagram in figure 2.8. Six other modules make the P∅D ECAL which surrounds the four sides of the P∅D in the same way the Barrel ECAL surrounds the tracker. It has a reduced granularity with respect to the other two ECAL and is used as a veto for entering particles and tag muons and photons that escape the P∅D without being reconstructed. The last module serves as the Downstream ECAL covering the downstream exit of the tracker system, perpendicular to the beam axis.

SMRD

The last part of ND280 that has not yet been described is the side muon range detector (SMRD). It is a scintillator detector placed within the 1.7 cm air gaps between the UA1 magnet yoke 4.8 cm thick steel plates. It consists of 440 scintillator modules arranged in 3 layers. They are made of extruded polystyrene and dimethylacetamide with admixtures of POPOP and para-terphenyl for coating, with embedded wavelength shifting fibers and Multi-Pixel Photon Counter (MPPC) read-outs [77]. The SMRD is used to measure the momentum of muons emitted at large angles with respect to the beam axis, escaping ND280. It is also participating in the rejection of cosmic rays and events from interactions outside the detector volume.

WAGASCI and BabyMIND

The WAGASCI experiment [78] is more an independent project than a T2K near detector as it is not directly used in the near detector analysis yet. It has, however, been designed to perform cross-section measurements for the T2K experiment, is located in the near detector complex (at 280 m from the T2K target) and is exposed to the same neutrino beam. It was added at a later stage to T2K and produced first results in 2019. It aims to perform a study of neutrino-nucleus interactions at the J-PARC accelerator in Japan with a new fine-grained neutrino detector (WAGASCI module) coupled with muon range detectors (WallMRD and BabyMIND). The configuration is shown in figure 2.10. It is located at a different off-axis angle than ND280 and SK, at 1.5° which allows for model-independent extraction of the cross-section for narrow energy by combination and comparison with ND280 measurements. WAGASCI stands for WAter Grid And SCIntillator meaning measurements of interaction in both target materials (water and C-H, 80:20 proportions) are performed. WAGASCI is made of 4 blocks $1 \times 1 \times 0.5\text{m}^3$ filled with water and hydrocarbon in an alternating configuration [79]. The blocks are instrumented with plastic scintillator bars in a grid-like structure allowing 3D track reconstruction. It is surrounded by muon spectrometers to measure the momentum of muons outgoing the neutrino interactions in the target material. To this end, two muon range detectors (MRD) are placed on the WAGASCI sides parallel to the beam axis, as it can be seen in

figure 2.10 and are called 'Wall MRD'. In addition, a downstream muon spectrometer, called BabyMIND (Magnetized Iron Neutrino Detector, [80]) has been added. Both types of spectrometers consist of several plates of steel 3 cm thick, interleaved with plastic scintillator detector modules but BabyMIND is a magnetized detector which resolves the poor momentum resolution of MRD for low energy muons (below 500 MeV) and allows for a 90% charge identification efficiency. BabyMIND consists of 33 magnetized metal plates alternated with 18 scintillator modules that measure the position of hits along the spectrometer and the curvature of the track in a 1.5 T magnetic field.

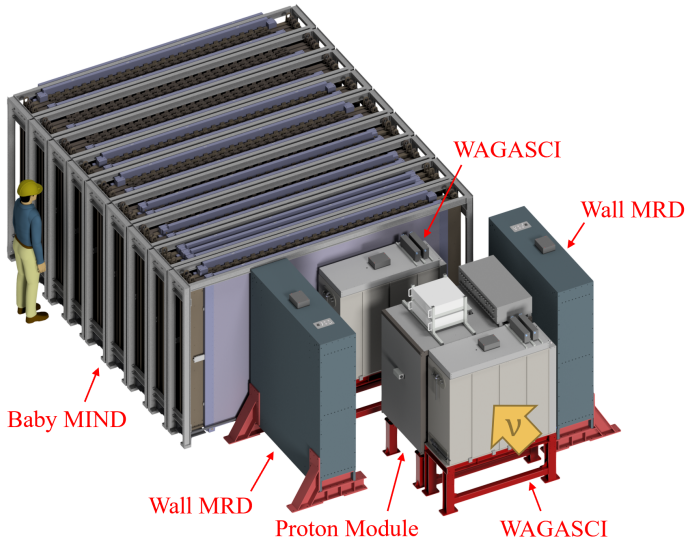

Figure 2.10. *Diagram of the WAGASCI and BABYMIND near detectors, source: T2K collaboration (https://t2k.org).*

2.3.3 The upgrade of ND280

The middle/inner part of ND280 is currently being upgraded [81] and the installation should be completed by the end of the year (2023). More precisely, the P∅D will be removed and the space will be filled with two new types of detectors: two High-Angle TPCs (HA-TPC) sandwiching a Super-Fine Grained Detector (SFGD) as shown in figure 2.11, and surrounded by a time of flight detector. The goal is to reduce cross-section systematic uncertainties for the next and last phase of data taking in T2K, referred to as T2K-II and corresponding to operation with the upgraded beam power. The upgraded near detector will still be in operation for Hyper-Kamiokande, hence the necessity to obtain the best performance possible to ensure the longevity of the near detector complex. The upgrade aims at improving the detection efficiency, in particular for low momentum or high-angle particles.

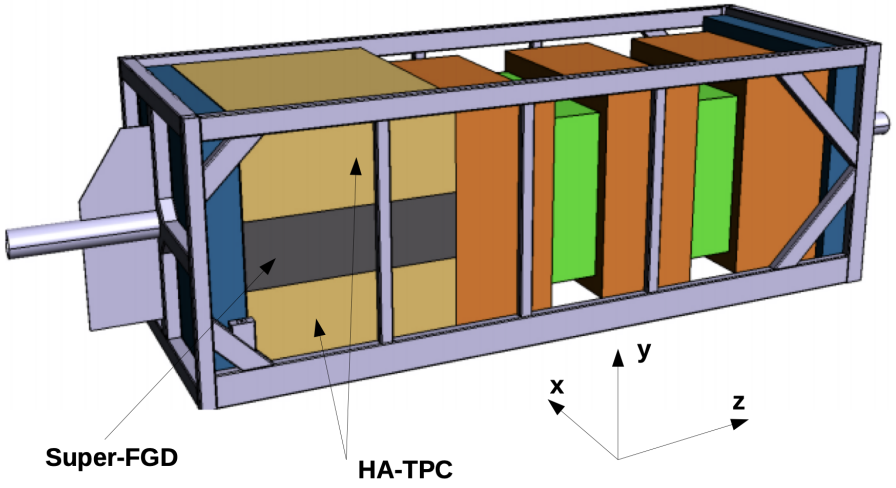

Figure 2.11. *Diagram of the part of ND280 being upgraded [81].*

High-Angle TPCs

TPCs are very valuable is ND280 as they can be used to perform 3D track reconstruction, energy and momentum measurements as well as PID. Since their performance in ND280 have been very satisfying so far, it was decided to add two similar TPCs on the top and bottom sides of the new tracker part, in order to reconstructed higher-angle outgoing particles. They are based on the same technology as the existent TPCs with two major novelties: the Micromegas readout detectors will use the "resistive bulk" technique that naturally introduces a spreading of the charge deposit on the anode plane, reducing the risk of sparks and improving the spatial resolution, and the field cage will be built in such a way that the fiducial volume is maximized.
Each end-plate of the new TPCs will be instrumented with eight Micromegas charge readout modules. The anode, segmented in pads, is covered by a foil of insulating material, which has a thin resistive layer on its top side, made of Diamond-Like Carbon (DLC), and an insulator layer. The resistive layer acts like a 2-D RC network and the charge deposited by the avalanche induces a signal also on the adjacent pads with a Gaussian behavior. This additional information on the adjacent pads provides a better spatial resolution. Moreover, the intensity of signal in each pad is reduced, resulting in less sparks or saturation of the detection signal. The comparison of technology with the standard Micromegas used in the vertical TPCs is illustrated in figure 2.12. These new Micromegas detectors are referred to as Encapsulated Resistive Anode Micromegas (ERAM).

In addition, a new field cage has been designed for the HA-TPC. The cage box walls (four lateral sides) consist of a single sandwich structure including a core made of Aramid honeycomb (25mm thick) and of two laminate skins (approx. 2mm thick) on opposite

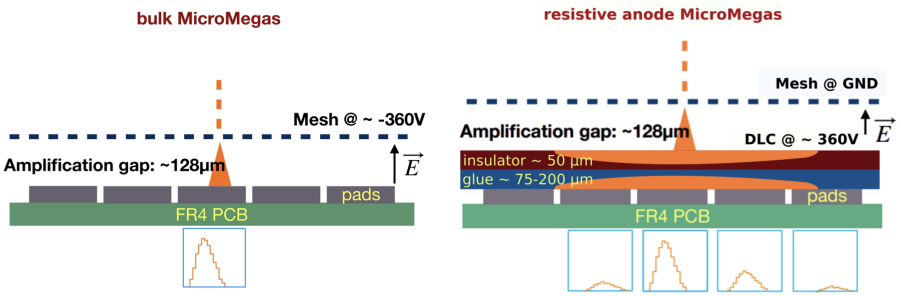

Figure 2.12. *Schematic of the standard bulk Micromegas technology (left) and the new resistive Micromegas (right), from [82]*

sides of the core. The main field forming element is a Kapton foil (40 μm thick) covered by Copper strips (5 μm thick) on both sides. The composite sandwich structure and the choice of material allow for a larger volume inside the cage while full-filling the electric field uniformity requirements. Its overall dimensions will be 1865×2000×820 mm^3.
HA-TPCs prototypes have been tested in several test beams campaign at the DESY facility ([83]) in Hamburg, Germany: [82, 84] and at CERN [85]. Thanks to these studies, it has been showed that such technology allows to achieve all requirements, including an energy deposit (dE/dx) resolution smaller than 10%, and a spatial resolution better than 800 μm [84].

SFGD

One main limitation of the FGDs structure of long perpendicular scintillator bars is that the trajectory of particles passing through the detector along one bar, or having low momentum, hence short tracks, is not easily reconstructed. To improve the detection of such particles in ND280, the SFGD will have a full 3D structure [86]. It is made of 192 cubes in width, 56 in height and 184 in length for a total of 1,978,368 individual cubes. Each 10 mm size scintillator cube is made of polystyrene doped with 1.5% of paraterphenyl (PTP) and 0.01% of 1,4-bis benzene (POPOP) and has been drilled to have three orthogonal through holes of 1.5 mm diameter. Through these holes, cubes will be traversed by a 3D net of wave-length shifter (WLS) fibers (1 mm diameter), carrying the scintillation signals to the read-out plates instrumenting the sides of the detector. The overall structure can be seen in figure 2.13. The readout will be made by 1.3 mm sized Multi-Pixel Photon Counter (MPPCs) of the same type as those in the current FGDs, interfaced with the fibers end-points. The SFGD will be able to reconstruct well low-momentum hadron production in hydrocarbon and to detect neutrons, allowing to extend ND280 sensitivity to anti-neutrino interactions on hydrogen. The fiducial volume is expected to be 1.9 tons. The SFGD's very fine grained structure will allow to lower the

hadron momentum detection threshold. For instance for protons, the current threshold is 450 MeV/c and is estimated to be reduced to 300 MeV/c in the SFGD. One example of measurement that could be benefiting from this is the following. The shape of the "transverse boosting angle", δ_{α_T} (angle in the kinematic imbalance, see [87] for more details), has been shown to be particularly sensitive to nucleon final state interactions (FSI). As it can be seen in figure 2.14, the effect of FSI is not visible with the FGDs but could be studied with the SFGD [88].

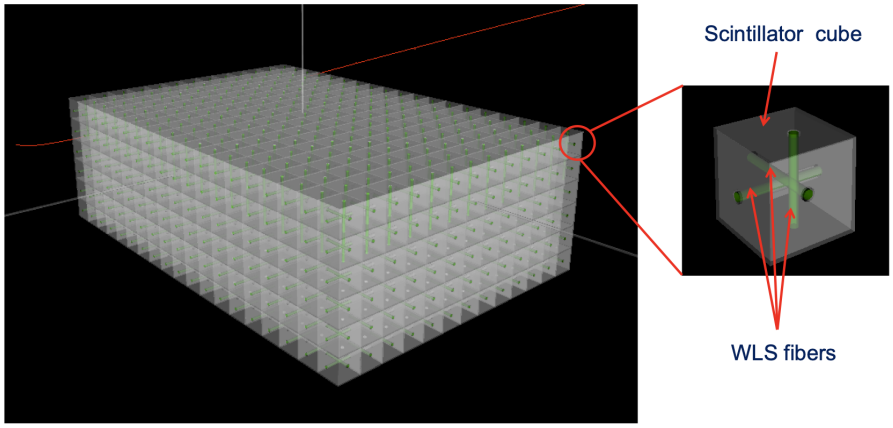

Figure 2.13. *Schematic concept of the SuperFGD structure [81].*

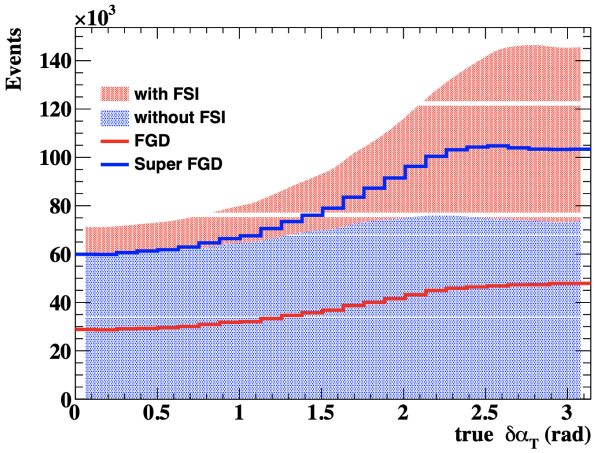

Figure 2.14. *Simulation of the distributions of δ_{α_T} with (red areas) and without (blue areas) final state interactions for all CC0pion interactions, overlaid with the total simulated distributions that could be seen in the current FGDs (red) and the new SFGD (blue), from [88]*

Time of Flight (TOF) detector

A time resolution better than 500 ps is required to determine the flight direction of charged particles unambiguously at the scale of ND280. Moreover, even better time resolution would improve the particle identification, especially the protons/positrons and muons/electrons in the energy ranges 0.1-0.3 GeV and 1-2 GeV respectively which cannot be achieved with ionisation energy loss only. To that end, the new tracker (HA-TPCs + SFGD) will be surrounded by 6 plastic scintillator bars (2 m long along the beam axis, 2.3 m long perpendicularly) coupled with large-area silicon-photo-multiplier MPPC sensors in a configuration that is schematized in figure 2.15. This set of scintillators is referred to as the TOF detector. It is expected to achieve a 150 ps time resolution.

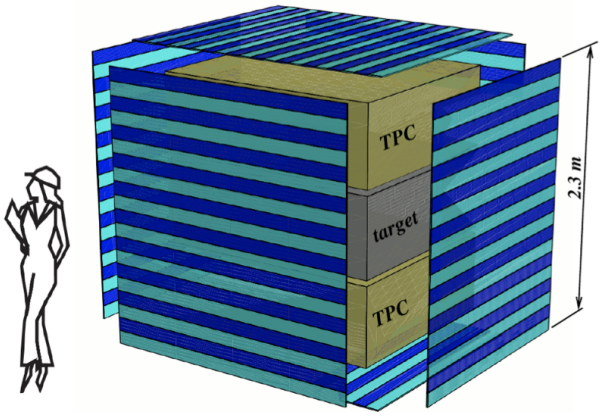

Figure 2.15. *Schematized view of the 6 scintillator planes of the TOF around the new tracker system for the ND280 upgrade, from [81]*

Conclusion

The upgrade of ND280 consists in building three new detectors with improved technologies. The main goal is to increase statistics and detection efficiency at the near detector in order to obtain better constraints for the oscillation analysis. As it can be noticed in figure 2.16, this particular combination of new near detector trackers is expected to more than double the efficiency in some angular regions and perform more homogeneously in angles than the current tracker. All elements of the upgrade are under their final stage of completion, have been tested in various test beams, and are expected to allow cross-section uncertainties to reach a level of 2-3% when we will enter the Hyper-Kamiokande era.

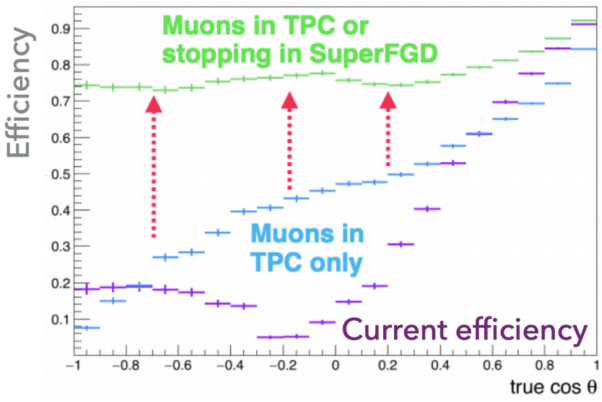

Figure 2.16. *Detection efficiency as a function of the outgoing lepton* $\cos\theta$ *with respect to the beam axis, in purple the current ND280 efficiency, in blue the expected one with the addition of two HA-TPCs, and in green the one with the full upgraded detector, from [89].*

2.4 Detection at the end of the chosen T2K baseline

2.4.1 Super-Kamiokande

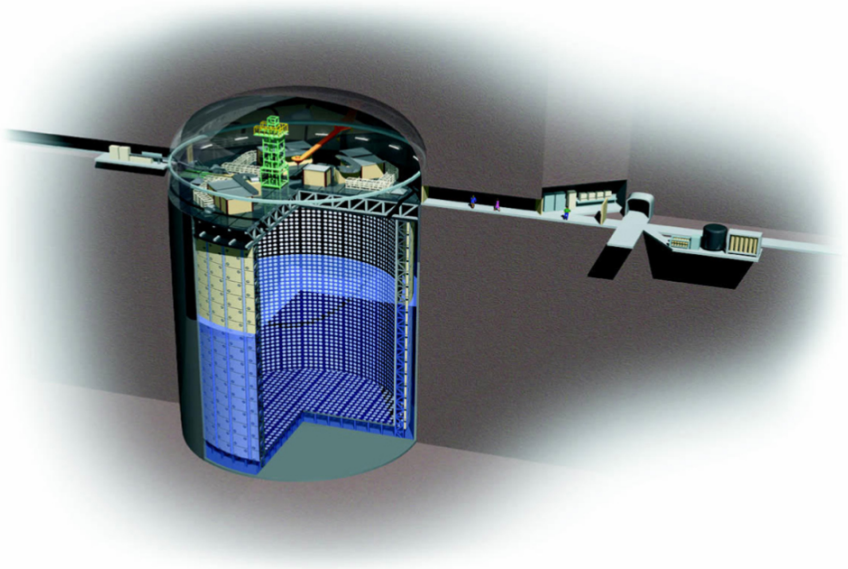

Figure 2.17. *Illustration of the Super-Kamiokande detector, source: T2K collaboration (https://t2k.org).*

Super-Kamiokande (SK) [90] is the off-axis water Cherenkov far detector of the T2K experiment. But, it is also a stand-alone detector and collaboration for non-accelerator neutrino and other searches. Indeed, SK is the successor of the Kamiokande detector. KamiokaNDE (Kamioka Nucleon Decay Experiment) started taking data in 1983, with a

water Cherenkov detector in the Mozumi mine where the current SK detector is located (in a different pit). Its first physics goal was to look for hints of Grand Unified theory through observation of nucleon decay. It consisted of a 16 m diameter and a 16 m height cylinder filled with 3,000 tons of pure water and instrumented with about 1,000 50 cm diameter photo-multiplier tubes (PMTs). It was operated as such until 1986, when it underwent a significant upgrade of its electronics and purification system as well as the addition of an instrumented outer detector to act as a veto for incoming charged particles. These upgrades allowed to lower the threshold of detection, making it suitable for neutrino detection, in particular solar neutrinos. Shortly after, it was renamed Kamioka Neutrino Detection Experiment, leaving the acronym unchanged. The experiment was successful in confirming the so-called solar neutrino problem, saw a deficit in atmospheric muon neutrinos (without enough statistics to claim a discovery) and detected neutrinos from a supernovae explosion (SN 1987A) in 1987 ([43]) as described in section 1.1.3. It continued taking data until 1995. In April 1996, its successor SK, which was being built since 1991, started taking data. A diagram of SK's detector can be found in figure 2.17. It is based on the same technology as KamiokaNDE.

SK [90] is a 42 m high cylindrical tank with a diameter of 39 m and filled with 50,000 tons of ultra pure water. It is located under an over-burden of about 1000 m, providing shielding from cosmic/atmospheric muons below 1.3 TeV. It is separated into an inner volume, the main detection one, and an outer veto volume. The inner volume has a 33.8 m diameter for a 36.2 m height. The inner detector (ID) walls are covered by more than 11,000 50cm diameter hemispherical PMTs from the Hamamatsu company (Hamamatsu Photonics K.K R3600). A stainless-steel framework of thickness 55 cm supports the PMTs and separates the ID from the outer detector (OD, about 2-2.5 m from the outer wall of the tank). The OD walls are instrumented with a little less than 2000 20 cm diameter PMTs from the same brand. To maximize water transparency and minimize backgrounds due to natural radioactivity, the water used to fill the detector tank is highly purified by a multi-step system including filtration, reverse osmosis (RO) and de-gasification and its level of purity is maintained through re-circulation in that system at a rate of about 30 tons per hour. The air in the tank complex is also frequently recycled. The water is maintained at a temperature around 12°C which has been optimized to reduce the dark rate in PMTs.

In 1999, K2K experiment started and SK was its far detector. In July 2001, SK was shut down and emptied so as to be upgraded, including replacing faulty PMT tubes. However, the implosion of one PMT, during the refill of the tank, induced a cascade implosion and about 53% of PMTs were damaged. Following that incident, PMTs have been covered in fibre-reinforced plastic and acrylic to protect them from shock-waves. In 2006, the full intended coverage in PMTs was restored. Finally, in 2010, the T2K experiment started

shooting a neutrino beam to SK.
On top of being the far detector for T2K, SK has had the same physics goals at its predecessor. It can be noted that it has been successful in discovering atmospheric neutrino oscilations in 1998 [8], solar neutrino oscillations in 2001 [91] (in parallel with the SNO experiment [92]), and set world-leading limits on nucleon decay, and in particular proton decay in 2012 [93, 94]. All signals seen by the PMTs can not be recorded as the amount of data would ramp up very fast. As a result only potential neutrino events are kept thanks to a loose selection based on the number of hit PMTs, the time window into which the clustered hits have been observed and the primary roughly reconstructed vertex position. Such low energy events as solar neutrinos and potential proton decay products are selected by specific separated levels of triggers.

2.4.2 Reconstruction of beam neutrino events for T2K

In this section, we will focus on the reconstruction of beam neutrino events which is relevant to the T2K experiment. As a reminder, neutrinos from the beam have an average energy of 600 MeV, which means that tau neutrinos, which are most of the oscillated neutrinos, can not be detected in SK, the mass of a tau lepton being 1.7 GeV/c^2. The events from the beam neutrinos are selected in a time window [-2, +10] μs around the expected arrival time of the leading edge of beam spill, given by the signal trigger from J-PARC (neutrino have an approximate time of flight of 1 ms from J-PARC to SK). Since 2017, an algorithm with improved performance, called fiTQun [95, 96], is used for the event selection and reconstruction. The previous reconstruction algorithm, which is called APFit [97] and was introduced at the very beginning of the Super-Kamiokande experiment, was a single-iteration fitter based on the time and charge information of hit PMTs. It was determining sequentially the vertex position, the number and direction of rings, and the particle type and momentum. fiTQun performs a global simultaneous fit based on likelihoods functions with probability density functions for the two raw measured variables: the charge q_i and time t_i of each PMT hit as follows:

$$L(\mathbf{x}) = \prod_{j}^{\text{unhit}} P_j(\text{ unhit } \mid \mathbf{x}) \prod_{i}^{\text{hit}} \{1 - P_i(\text{ unhit } \mid \mathbf{x})\} f_q(q_i \mid \mathbf{x}) f_t(t_i \mid \mathbf{x}) \tag{2.3}$$

where $\mathbf{x}$ is a vector containing all seven reconstructed variables: vertex position, time of the interaction, zenith and azimuth angles of the direction and the momentum; and with the first product running on unhit PMTs and the second one on hit PMTs. This likelihood is based on a model from the MiniBooNE collaboration [98]. This likelihood is maximized so as to find the most probable kinematics of the detected particle. In practice, that is done by minimizing the negative log likelihood by varying all the fit parameters

simultaneously using MINUIT. This likelihood calculation is performed by seeding the vextex position parameters with likely values extracted from a pre-fitter algorithm in order to avoid local minima of the likelihood function. fiTQun performs this fit many times for many scenarios in terms of number of rings and PID (event topology) in order to find the best fit for all variables. In that sense, the PID is done in a complicated integrated fit. However, the basic principle to identify an electron from a muon is the following: the shape, intensity and spatial spreading of the Cherenkov rings is different. Indeed, as

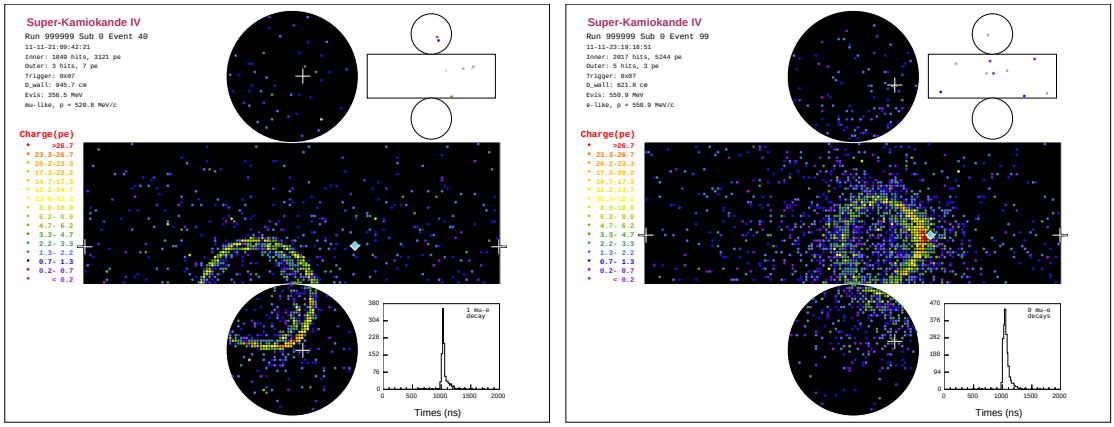

Figure 2.18. *Display of a simulated μ-like event (left) and an e-like event (right) in SK, source: T2K collaboration (https://t2k.org).*

shown in figure 2.18 with simulated Monte-Carlo (MC) events reconstructed by fiTQun, an electron ring will be fuzzier due to electron scattering in water (right-hand plot) compared to sharper rings for muons (left-hand plot). The vertex position resolution, defined as the 68.3 percentile, is 19.5 cm for electrons and 17.5 cm for muons. The angular resolutions for the particle direction, defined in the same way, are 2.6° and 1.8° for electrons and muons respectively. The mis-identification between electron and muons is, in the most simple cases, under 0.5%.

The observed neutrino interaction events from the T2K beam are categorized in 6 different samples using cuts on reconstructed variables, after the fiTQun fit. In the MC, the interaction category (modes) is known, however it can not be reconstructed for the data, only the event topology can be selected. These interaction categories will be detailed in section 3.1.2.3, but from figure 2.19, where the expected flux broken-down by neutrino interaction category are overlaid with T2K flux at SK, it can be seen that T2K has been optimized to mostly observe CCQE interactions. This allows for cleaner signals and an easier kinematic reconstruction. The current 6 T2K samples are the following:

- 1-ring electron-like neutrino event: 1Re FHC or ν_e1R
- 1-ring muon-like neutrino event: 1Rμ FHC or ν_μ1R
- 1-ring electron-like anti-neutrino event: 1Re RHC or $\bar{\nu_e}$1R

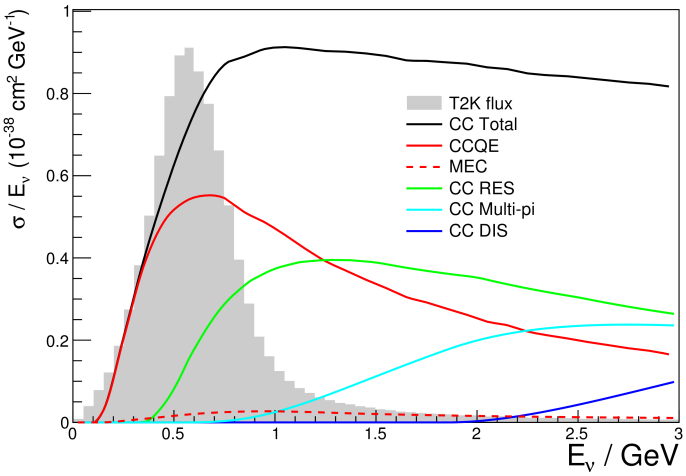

Figure 2.19. *T2K flux overlaid with neutrino cross-sections on water broken-down by interaction modes, source: T2K collaboration (https://t2k.org).*

- 1-ring muon-like anti-neutrino event: 1Rμ RHC or $\bar{\nu_\mu}$1R
- 1-ring electron-like neutrino event with 1 decay electron: 1Re1de or ν_e1R1de
- muon-like neutrino event with 1 or 2 decay electrons: numucc1pi or $\nu_\mu$cc1π

The two last categories are sometimes abusively called multi-ring samples, as the decay electrons are producing a visible ring (when detected) but that happens with a delay and needs to be distinguished from simultaneous multi-ring topologies. The decay electron comes from the decay of a pion produced by a resonance as part of the neutrino interaction which itself produces a muon, decaying into an electron. In general, the energies are low enough that only the electron ring is visible. To reconstruct all samples, a first set of cuts is applied. The arrival time must be within the trigger window as described above, the visible energy must be higher than 30 MeV, there must not be simultaneous hits in the OD (less than 16 hits), and the events must be fully contained within the fiducial volume. To ensure this, taking into account the coverage by the PMTs, the distance to the nearest wall (*wall*) must be larger than 50 cm and the distance to the wall in the particle's direction (*towall*) must be larger than 1.5 m. After that, the selections cuts are the following, neutrino and anti-neutrino can not be distinguished and depend on the beam mode:

Single ring electron events

- Additional "fully-contained" cut: (*wall*)$>$ 80 cm and (*towall*) $>$ 170 cm
- Only one ring is identified by fiTQun , even in the multi-ring part of fitter

- An electron ring is the favored scenario by fiTQun: $\ln(L_e/L_\mu) > 0.2 \times p_e$, where $\ln L_e$ is the fiTQun single-ring e-like log likelihood, $\ln L_\mu$ single-ring μ-like log likelihood, and p_e reconstructed electron momentum of single-ring e-like hypothesis in MeV
- The visible energy is greater than 100 MeV
- There are no decay electrons detected
- The reconstructed neutrino energy is smaller than 1250 MeV
- The π^0 hypothesis is rejected: $\ln(L_{\pi^0}/L_e) < 175 - 0.875 \times m_{\pi^0}$ where $\ln L_{\pi^0}$ is the likelihood from the dedicated π^0 fiTQun fit and m_{π^0} is the fitted neutral pion mass in MeV

Single ring electron event with one decay electron

- Additional "fully-contained" cut: $(wall)$> 50 cm and $(towall)$ > 270 cm
- Only one ring is identified by fiTQun, even in the multi-ring part of fitter
- An electron ring is the favored scenario by fiTQun: $\ln(L_e/L_\mu) > 0.2 \times p_e$, where $\ln L_e$ is the fiTQun single-ring e-like log likelihood, $\ln L_\mu$ single-ring μ-like log likelihood, and p_e reconstructed electron momentum of single-ring e-like hypothesis in MeV
- The visible energy is greater than 100 MeV
- There is one decay electron detected (hence 2 sub-events within the event)
- The reconstructed neutrino energy is smaller than 1250 MeV
- The π^0 hypothesis is rejected: $\ln(L_{\pi^0}/L_e) < 175 - 0.875 \times m_{\pi^0}$ where $\ln L_{\pi^0}$ is the likelihood from the dedicated π^0 fiTQun fit and m_{π^0} is the fitted neutral pion mass in MeV

Single ring muon event

- Additional "fully-contained" cut: $(wall)$> 50 cm and $(towall)$ > 250 cm
- Only one ring is identified by fiTQun, even in the multi-ring part of fitter
- A muon ring is the favored scenario by fiTQun: $\ln(L_e/L_\mu) < 0.2 \times p_e$, where $\ln L_e$ is the fiTQun single-ring e-like log likelihood, $\ln L_\mu$ single-ring μ-like log likelihood, and p_e reconstructed electron momentum of single-ring e-like hypothesis in MeV
- The reconstructed muon momentum is greater than 200 MeV/c

- There is zero or one decay electron detected (hence 1 or 2 sub-events within the event)
- The π^+ hypothesis is rejected: $\ln(L_{\pi^+}/L_\mu) < 0.15 \times p_\mu$ where $\ln L_{\pi^+}$ is the likelihood from the dedicated π^+ fiTQun fit and p_μ is the reconstructed muon momentum in MeV/c

Multi-ring muon event numucc1pi

The selection for this sample is a bit more complicated but essentially the flow is:

- Additional "fully-contained" cut: $(wall)$> 80 cm (50 cm) for 1 (2-respectively) decay electrons and $(towall)$ > 200 cm
- More than one ring is identified by fiTQun **or** more than 1 decay electron is identified: 1-3 rings possible
- No electron ring or $\pi^-\pi^+$ ring is identified in the primary ring cluster (not the delayed decay electron rings)
- One muon ring (mandatory) and possibly 1 π^+ ring are the identified by fiTQun
- There is one or two decay electrons detected (should be two but one can be missed due to pion secondary interactions, separated into two sub-categories)

Even if it is not yet used for the beam sample selection, in August 2020, the SK collaboration has begun to dissolve 13 tons of encapsulated Gadolinium ($Gd_2(SO_4)_3 \cdot 8H_2O$), roughly 10% of the final target concentration [25] which will be reached in a few years from now. The already dissolved concentration of Gd corresponds to a 50% neutron capture efficiency. As explained in section 1.1.2.2, this allows to enhance electron anti-neutrino detection as the neutron capture produces a specific signal. This is very useful since neutrino and anti-neutrinos can not be distinguished in SK. It is of particular use for the detection of both supernova bursts and relic neutrinos which are hard to detect because of their relatively low energies. As it can be seen in figure 2.20, up to 3 rings, the two last after a delay of between a few tens to a few hundreds of μs depending on the Gadolinium concentration and the neutron's energy. There are two main Gadolinium isotopes: ^{157}Gd and ^{155}Gd which produce respectively gamma rays of 7.9 and 8.5 MeV [99].

Note again that SK is not only T2K's far detector but also a standalone experiment for solar and atmospheric neutrinos. It also aims at constraining nucleon decay and detecting neutrinos from both supernovae bursts and diffuse background. This is even more the case since the Gadolinium addition which enhances the neutron tagging performance of the detector. These various physics goals will be more detailed in Chapter 5 in the context of the next generation detector Hyper-Kamiokande (HK).

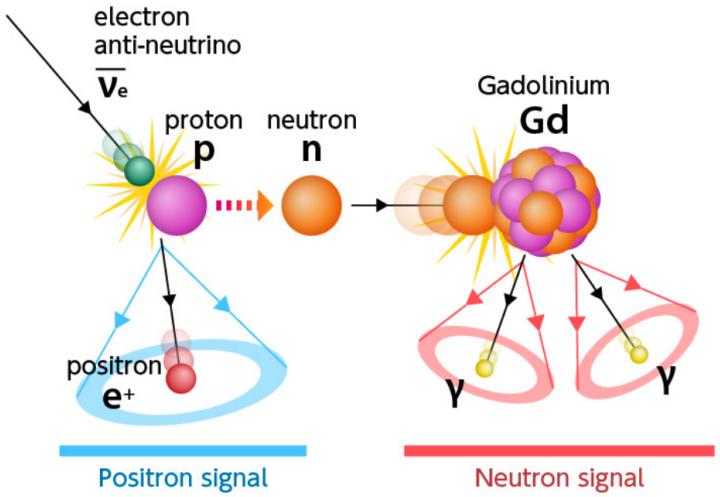

Figure 2.20. *Illustration of the electron anti-neutrino signal with neutron capture in the Super-Kamiokande detector, diagram taken from [100]*

2.5 Conclusion

It can be said as a conclusion that T2K is a very sophisticated experiment including several different detectors and dedicated external measurements. All of these items are built upon the experience from precursor experiments. As it will be shown in Chapter 3, the precision measurements of neutrino oscillation parameters for which T2K has been optimized require an equally sophisticated analysis process.

Chapter 3

Oscillation analysis in T2K

This chapter is dedicated to the oscillation analysis in T2K, with a specific focus on the far detector final analysis with the P-Theta software. It will describe the general principle, the P-Theta analysis method, and the result of the analysis performed for this thesis with new data at the far detector, from the so-called Run 11.

Contents

3.1 Analysis pipeline

3.1.1 Principle

Once the data at both near and far detectors are collected and reconstructed, the oscillation analysis can begin. The general principle consists in doing a statistical analysis of the neutrino flux composition as observed at both sites. As described in the previous section, events are separated into 6 samples and information such as position and kinematics are estimated for each event. Data can then be binned in these different variables to obtain reconstructed neutrino spectra observed in the detectors. The spectra at the far detector can be inferred from those at the near detector given the value of oscillation parameters. Thus, knowing the observed spectra at both detector sites, it is possible to constrain those parameters. Of course, many other elements and uncertainties need to be added to the analysis. In practice it is a little bit more indirect. A visual summary of the analysis can be found in figure 3.1.

To constrain the oscillation parameters, one needs to compare what is expected at the far detector for many oscillation parameters values with what is observed. More precisely, what are compared are spectra of neutrino as a function of their reconstructed kinematics variables, for simplicity here, the example of the neutrino energy E_ν can be used. This means using a model. This model has to be composed of a flux model $\Phi(E_\nu)$, a cross-section model $\sigma(E_\nu)$ and an oscillation model giving a probability $P(\nu_\alpha \to \nu_\beta)$, α and β being leptonic flavors. When looking at disappearance, $\alpha = \beta$. When looking at appearance, one has to add the appearance component to the survival component of the initial contamination. For a particular bin in energy centered on E_ν, one can write the number of expected events $N_{pred}(E_\nu)$, in the case of disappearance namely in the case of muon neutrinos in T2K, as: $N_{pred}(E_\nu) = P(\nu_\mu \to \nu_\mu) \times \Phi(E_\nu) \times \sigma(E_\nu)$. Those models are mainly built from the near detector inputs; as well as some external measurements.

Flux

Concerning flux, the near detectors, in particular INGRID, provide direct measurements of flux as well as measurements of the product $\Phi \times \sigma$. In addition, the NA61/SHINE experiment at CERN [101] takes data with the proton beam hitting a T2K replica target so that the hadron production can be measured with a dedicated detector. Those additional hadron yields measurements are passed on to the analysis to re-weight the Monte-Carlo simulation of the T2K experiment [51] but also used to assess uncertainties on flux predictions at the far detector. The uncertainties on flux are also evaluated using these measurements.

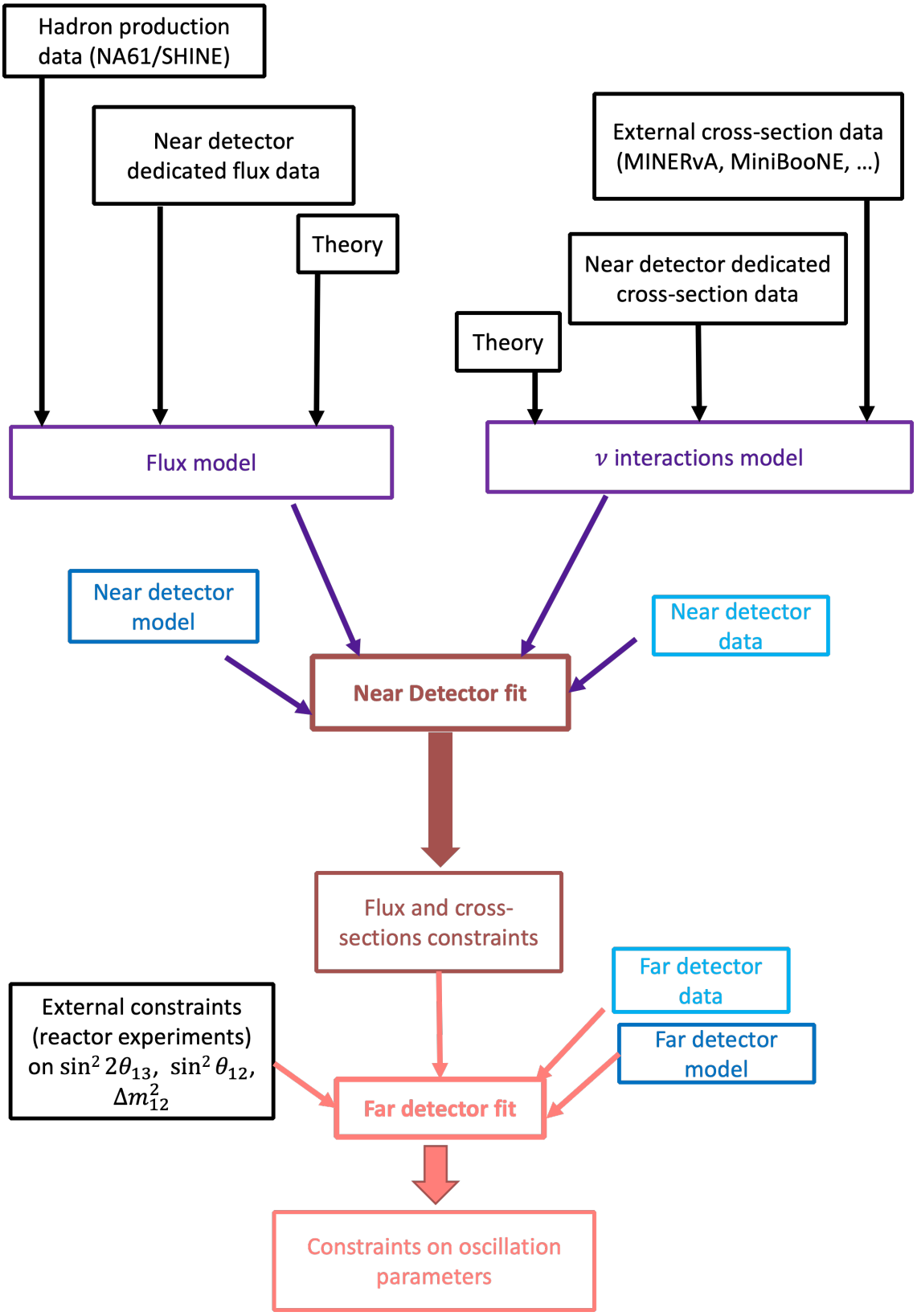

Figure 3.1. *Schematic summary of the ν oscillation analysis principle in T2K*

Cross-section

For cross-section, the near detectors of T2K perform a number of cross-section measurements on different types of targets thanks to the complexity of the detectors set. Such measurements especially on Oxygen and Hydrogen inform on the probability of interaction at the far detector. Together with external data mainly from bubble chambers experiments, MINERvA (Main Injector Neutrino ExpeRiment to study v-A interactions,[102, 103]) and MiniBooNE (Mini Booster Neutrino Experiment [104]), those measurements are used to build the nominal T2K cross-section model (described here [105], [106]). Similarly, some uncertainties are evaluated using data-driven methods.

Other inputs

Finally, the oscillation probability formalism is the one presented in Chapter 1, taking into account matter effects. The density of matter has been estimated to be the constant $\rho = 2.6$ g.cm^{-3} along the baseline. Indeed, T2K accelerator neutrinos only traverse the upper crust of the Earth.

Near detector fit

A first fit of the full model (through MonteCarlo events) to the near detector data is performed at the level of the near detector, taking into account uncertainties on the external data and the models. This fit is currently performed in a framework named Beam And ND280 Flux extrapolation task Force (BANFF) which consists in finding the best values mostly of cross-section parameters thanks to a maximization of a global likelihood using the MINUIT package [107] within ROOT [108]. The likelihood is built from Poisson distributions of events in bins (in momentum and angle of the detected lepton with respect to the beam axis) and from penalty terms for the nuisance parameters. It outputs several items needed for the next step of the analysis such as constraints on the flux and cross-sections as well as post-fit and covariance values for the systematic parameters. Those systematic parameters contain the uncertainties on flux and cross-section of which prior values were given by the model's tuning to external data. Uncertainties on the near detectors model are taken into account in the fit as well. The reduction of uncertainties on flux and interaction cross-sections can clearly be seen in figure 3.2 which shows the error bands on analysis samples spectra for this type of parameters. The difference between errors before the fit (red) and after the ND fit (blue) illustrates the crucial role of the near detector in the precision of T2K measurements. A new optimized fitter, called GUNDAM is currently being validated and works on the same principle, but it is not yet used for the official analysis.

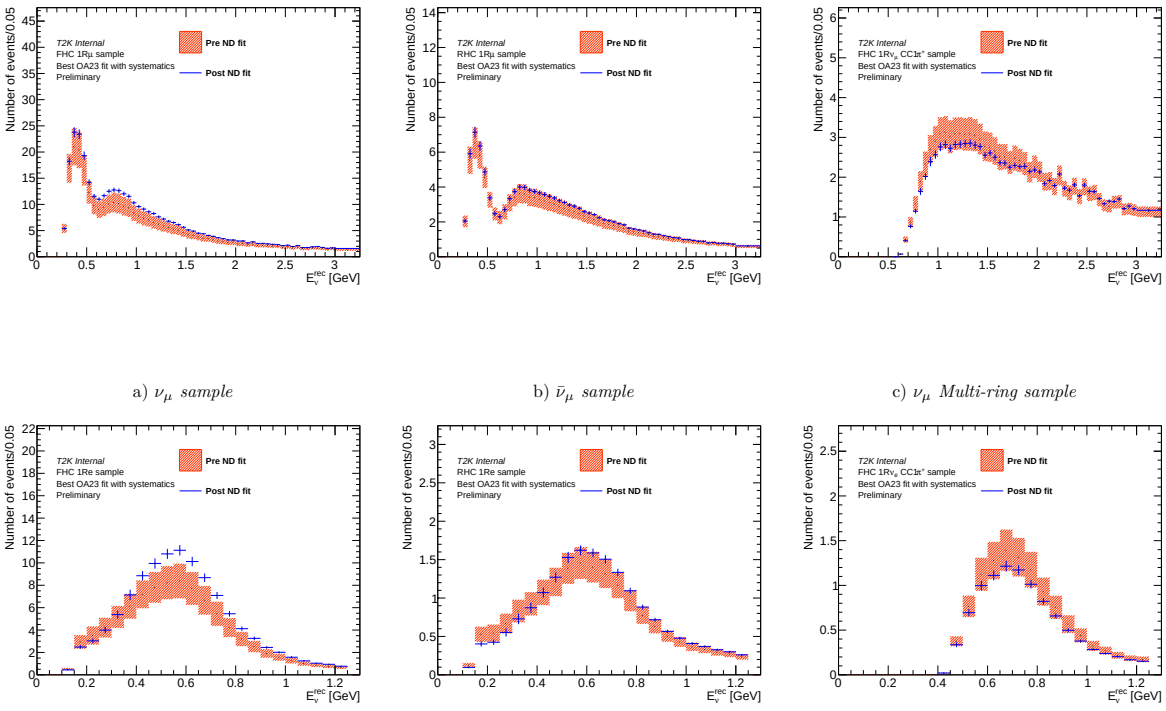

a) ν_μ *sample* b) $\bar{\nu}_\mu$ *sample* c) ν_μ *Multi-ring sample*

d) ν_e *sample* e) $\bar{\nu}_e$ *sample* f) ν_e *1 d.e. sample*

Figure 3.2. *Comparison of the error bands on spectra (broken down by SK samples) before the ND fit (red areas) and after the ND fit (blue error bars) for flux and cross-section parameters.*

Far detector fit

The final step is the far detector fit from which the constraints on oscillation parameters will come. It is performed by three different fitters that compare results for cross-checks and validation. Those fitters will be described in the next sections 3.1.2 and 3.1.3. The principle is however the same for all. The far detector predicted spectra are fitted to the data ones. Spectra are predicted from MonteCarlo (MC) events from the SK collaboration and built with the nominal T2K flux and cross-section models. From likelihood calculations (simultaneous or not depending on fitters) between predicted and observed spectra, constraints on parameters of interests are inferred given the estimated uncertainties. The nuisance parameters are mainly categorized in 3 types of systematic parameters: flux and cross-section which are outputs of the BANFF fit and detector uncertainties which are estimated from atmospheric neutrino data taken in the Super-Kamiokande detector. The parameters of interest can be any of the three parameters that we are trying to measure precisely with T2K: δ_{CP}, $\sin^2\theta_{23}$, and Δm^2_{32} as well as $\sin^2\theta_{13}$ which is varied inside a strong prior from reactor $\bar{\nu_e}$ disappearance experiments (DayaBay [35], Double-Chooz [34], Reno [33], ...) which have a targeted sensitivity to its value. The mass hierarchy is also a parameter of interest as the results of the fit are always reported in both cases of hierarchy. However, the two remaining oscillation parameters $\sin\theta_{12}$ and Δm^2_{12} are considered as nuisance parameters and systematically marginalized over as such because T2K sensitivity to them is way below that of other experiments, especially solar neutrino data and KamLAND (Kamioka Liquid-scintillator Anti-Neutrino Detector) data [109]. T2K's baseline value and range of neutrino energies do not allow for an optimal measurement for these two parameters as it has been extensively discussed in Chapter 1.

3.1.2 P-Theta software

P-Theta is the fitter that I used for the analysis. It is named after the kinematics variables that it uses to bin the data and MC events: p, the momentum of the outgoing charged lepton (product of the neutrino interaction in the SK detector) and θ, the angle between the outgoing lepton momentum and the neutrino beam axis. It is a quite flexible framework based on the analysis method presented in the previous section. Its working principle will be detailed here and is summarized in figure 3.3.

3.1.2.1 The likelihood calculation

As said before, the overall process relies on a likelihood calculation. Predicted spectra are built for many values (throws) of nuisance parameters and marginalized over, and neutrino oscillations are applied to them. One can vary the oscillations parameters values used to build the predicted spectra and fit them all to data. Doing so, one can compute

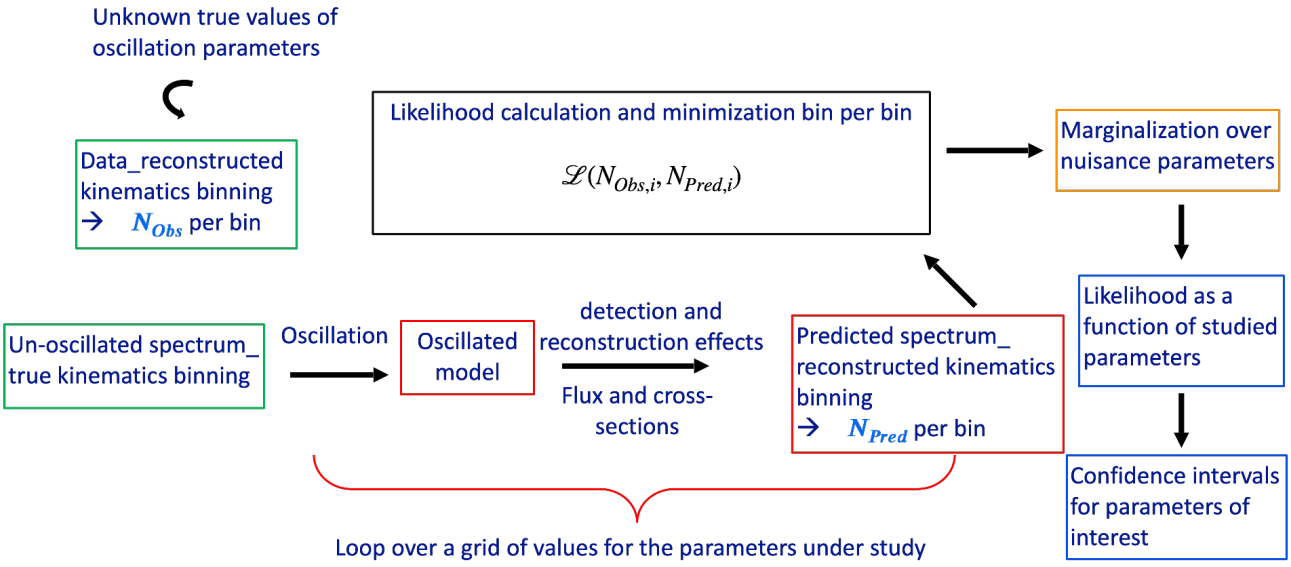

Figure 3.3. *Schematic summary of the P-Theta analysis framework*

the likelihood for each fit. The total likelihood can be expressed in the following way, where s runs over all 6 data samples, N_s^{obs} is the observed number of events at SK for sample s, x_s^{obs} contains the associated kinematics variables, o the oscillation parameters, f the nuisance parameters and $\mathcal{L}$ is the total likelihood in which the nuisance parameter term can be factorized:

$$\mathcal{L}(\left\{N_s^{obs}, x_s^{obs}\right\}_{\forall s}, o, f) = \prod_{s \in samples} [\mathcal{L}_s(N_s^{obs}, x_s^{obs}, o, f)] \times \mathcal{L}_{syst}(f) \tag{3.1}$$

It is a bin per bin calculation, so the total likelihood is the sum over all bins in reconstructed kinematic variables of the likelihood per bin i $\mathcal{L}_i$. The likelihood of N^{obs} in each bin i is computed against the model predicting N^{pred} events and is associated to a probability following a Poisson law. For each bin i we have:

$$Probability(N_{obs}) = \frac{N_{pred}^{N_{obs}}}{N_{obs}!} e^{-N_{pred}} \tag{3.2}$$

The quantity that will be minimized in the analysis is $-ln(\mathcal{L})$ for convenience and easier convergence of the minimizer. We can derive the implemented calculation easily:

$$ln(\mathcal{L}(N_{obs})) = N_{obs} \times ln(N_{pred}) - ln(N_{obs}!) - N_{pred} \tag{3.3}$$

Using the Stirling formula:

$$\begin{aligned} ln(\mathcal{L}(N_{obs})) &= N_{obs} \times ln(N_{pred}) - N_{obs} \times ln(N_{obs}) + N_{obs} - N_{pred} \\ &= (N_{obs} - N_{pred}) - N_{obs} \times ln(\frac{N_{obs}}{N_{pred}}) \\ -ln(\mathcal{L}(N_{obs})) &= (N_{pred} - N_{obs}) + N_{obs} \times ln(\frac{N_{obs}}{N_{pred}}) \end{aligned} \tag{3.4}$$

3.1.2.2 The P-Theta binning

The binning used for all electron-flavored samples is $\mathrm{P} - \theta$ whereas the binning used for 1-ring muon-flavored samples is $E_{\mathrm{rec}} - \theta$, E_{rec} being the reconstructed energy of the neutrino, and only E_{rec} is used for the new multi-ring muon-like with one pion sample (numucc1pi). E_{rec} is the reconstructed energy of the neutrino, θ is the angle between the produced charged lepton direction and the beam direction, and P is the momentum of the lepton. This binning has been optimized according to the number of detected events in each bin and the precision of reconstruction for the theta angle in each topology. The detailed breakdown of P-Theta binning can be found in Table 3.1. A different binning is

Table 3.1. *P-Theta binning*

Range	Size of a bin	Number of bins
Momentum		
0-1500 MeV/c	100 MeV/c	15
Angle θ for e-flavored events		
0-140°	10°	14
140-180°	40°	1
Angle θ for μ-flavored events		
0-100°	20°	5
100-180°	80°	1
E_{rec} for μ-flavored events		
0-3 GeV	50 MeV	60
3-4 GeV	250 MeV	4
4-6 GeV	500 MeV	4
6-10 GeV	1 GeV	4
10-30 GeV	20 GeV	1
E_{rec} for e-flavored events		
0-1.25 GeV	50 MeV	25

used for the true energy of neutrinos in MC events and can be found in Table 3.2.

Table 3.2. *P-Theta μ E true binning*

Range	Size of a bin	Number of bins
True E for μ-flavored events		
0-0.3 GeV	50 MeV	6
0.3-0.9 GeV	20 MeV	30
0.9-1.2 GeV	50 MeV	6
1.2-2.4 GeV	100 MeV	12
2.4-3.4 GeV	200 MeV	5
3.4-30 GeV	depends on bins	5

3.1.2.3 The interaction categories

In P-Theta, on top of the categorization of events into the 6 analysis samples, neutrino interactions modes are defined for the MC events to allow for systematic parameters to be specific to an interaction process. The 13 categories of interaction are the following:

- Charged-current quasi-elastic interactions (CC QE)
- 2p2h, charged-current interactions (CC MEC)
- Charged-current resonant production of a single charged pion (CC 1PIC)
- Charged-current resonant production of a single neutral pion (CC 1PI0)
- Charged-current coherent pion production (CC COH)
- Charged-current multi pion production (CC multi-π)
- Charged-current deep inelastic scattering (CC DIS)
- Miscellaneous charged-current processes (CC Misc)
- Neutral current with production of a single neutral pion (NC 1PI0)
- Neutral current with production of a single charged pion (NC 1PIC)
- Neutral current coherent
- Neutral current induced single photon production (NC1γ)
- Other neutral current interactions (NC other)

3.1.2.4 Introduction to nuisance parameters treatment

As said before, the nuisance parameters are marginalized over in P-Theta analysis. As a standard, 100 000 throws of those parameters values among their prior distributions are used. An analysis is never run with more than 2 parameters of interests (2D-likelihood).

3.1.2.5 Nuisance oscillation parameters

When an oscillation parameter is treated as a nuisance parameter, throws are drawn in a uniform prior over a range of definition, except for $\sin^2 2\theta_{13}$ when the so-called reactor constraints (prior distribution from more sensitive experiments) are applied (which can be turned on or off thanks to P-Theta flexibility). In that case, the prior is Gaussian. The same thing is applied to $\sin^2\theta_{12}$ and Δm^2_{21} which are not constrained well by T2K but much better by reactor and solar neutrino experiments.

3.1.2.6 Re-normalization parameters

The other nuisance parameters, the systematic uncertainties, can be separated into different categories. First, the 50 beam flux parameters are passed on to P-Theta's framework through the *ROOT*© file containing the nominal values, pre-fit and post-fit values from the BANFF as well as a covariance matrix. Those parameters are applied in P-Theta as simple reweighting factors of the number of events per bin, on a sub-set of energy ranges, like a re-normalization. Their priors are Gaussian and are drawn inside a range of $\pm 5\sigma$ around their nominal value.
This is also how we apply the 61 SK detector systematic parameters, the difference being that they come from a separate SK detector matrix provided by the T2K sub-group T2K-SK which works with atmospheric neutrino data. As described in the previous section, the fit from the near detector outputs, through the BANFF file, constrains on flux but also on cross-sections for the different modes of neutrino interaction. 14 of those cross-section parameters are normalization parameters applied in P-Theta in the same way as flux and detector ones.

3.1.2.7 Response function parameters

The 40 other cross-section parameters are applied using response functions (RF). This means that the effect they can have on the number of events can differ from one bin to another and is encoded in response functions that are evaluated on the MC events for

a few values and are then interpolated via cubic splines. These RF are created for all reconstructed bins, true bins, interaction mode and flavor change type (i.e.: $\nu_\mu \rightarrow \nu_e$) from the MC events. When they are applied, the effect of all relevant RF is summed. An example of response function can be found in figure 3.4. This allows for parameters to change the shape of events distribution and as a result such parameters are said to be shape parameters. The priors are Gaussian for all parameters that are constrained by the near detector fit, which is the case for all except the specific 2p2h energy dependent ones. The full list of cross-section parameters is available in Appendix A.

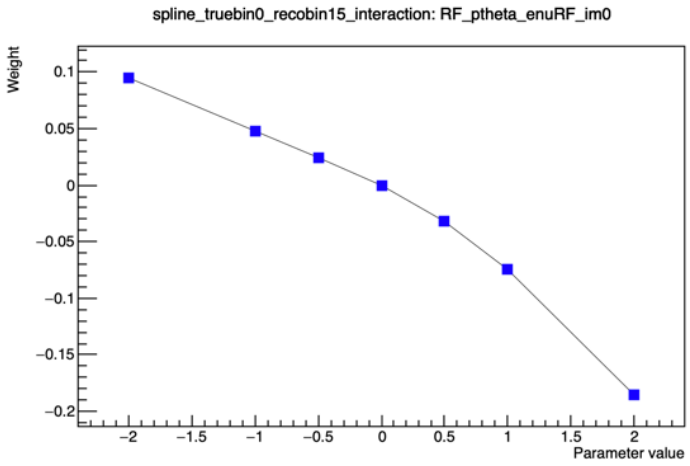

Figure 3.4. *Example of a response function in the P-Theta analysis for the Optical potential on Oxygen for neutrinos parameter, CCQE interaction, ν_μ event, true energy bin between 0 and 0.4 GeV and reconstructed energy bin between 0.75 and 0.80 GeV*

3.1.2.8 Additive response function parameters

There are 3 systematic parameters that are applied in a different way: the nucleon removal energy (E_b) uncertainty for both neutrinos and anti-neutrinos and the momentum scale factor ($p-scale$). The first two are cross-section parameters constrained by BANFF, the last one is estimated by the T2K-SK group and concerns a scaling of the momentum calibration at the far detector. They are implemented in P-Theta in such a way that they not only reweight each bin in a different way like RF can, but account for migration of events in between bins, including empty ones where a multiplication factor would have no effect. This was found to be an issue for those 3 parameters and the implementation is internally named Additive response functions (AddRF).

3.1.2.9 Conclusion on nuisance parameters

There are 2 other re-normalization factors which lead to a total of 170 systematic parameters applied to the far detector fit in P-Theta. At the near detector there are more

because, for instance the interaction volume contains Carbon in some ND detectors which is not the case in the pure water of SK. To give orders of magnitude, a full breakdown of the errors in % is given in Table 3.3 for the 2023 analysis described in section 3.3.2. This table also illustrates the crucial role of the near detectors (ND): it can be read that the flux errors and cross-sections (noted Xsec) errors constrained by the ND are for most samples larger alone than the combined errors on both noted 'Flux+Xsec (ND constr)'. This is because the near detectors data allow us to constrain both flux and cross-section in a correlated way, thus constraining directly the product of the two categories of errors.

Table 3.3. *Uncertainties on the number of events broken down by SK samples and by error sources, the uncertainty on the ratio of neutrino and anti-neutrino is also given in the last column.*

Error source (units: %)	1R FHC e	1R FHC μ	1R RHC e	1R RHC μ	MR e CC1π^+	MR μ CC1π^+	ratio e FHC/RHC
BeamFlux	2.8	2.8	3.0	2.9	2.9	2.9	2.2
Xsec (ND constr)	3.8	3.6	3.5	3.5	4.3	3.0	2.4
Flux+Xsec (ND constr)	2.9	2.8	2.7	2.6	3.7	2.2	2.3
2p2h shape O only	0.1	0.3	0.1	0.1	0.0	0.0	0.0
2p2h Edep	0.2	0.5	0.2	0.5	0.0	0.1	0.2
IsoBkg low-p_π	0.1	0.3	2.1	2.3	0.1	0.9	1.9
$\sigma(\nu_\mu)/\sigma(\nu_e)$, $\sigma(\bar{\nu})/\sigma(\nu)$	2.6	0.0	1.5	0.0	2.6	0.0	3.1
NC γ	1.2	0.0	2.1	0.0	0.0	0.0	0.8
NC Other	0.2	0.2	0.4	0.2	0.9	1.0	0.2
Flux+Xsec (all)	4.1	2.8	4.3	3.5	4.6	2.6	4.4
SK	2.7	1.4	5.1	3.6	4.3	2.9	4.0
Total All	4.9	3.2	6.7	5.0	6.3	3.9	5.9

3.1.2.10 Model's spectra

Finally, to complete the model that is fitted to data in the likelihood minimization, predicted spectra need to be built. They are called internally PDF for 'probability density functions' and are built from MC events, with systematic parameters at their ND post-fit value and oscillations applied. For validation, they can be evaluated also at the parameter's nominal or pre-fit values.

3.1.2.11 Statistical treatment in the analysis

Bayesian and frequentist approaches

Roughly speaking, there are two approaches to statistical analyses. The frequentist approach consists in attributing a probability to having obtained this set of data, given

a hypothesis. This can be done for several hypotheses and multiple data sets, in order to obtain confidence levels on the hypotheses. It is purely data-driven, without prior knowledge or assumptions.
In the Bayesian approach, what is being assessed is the probability of a certain hypothesis, given the data. In that case, the data can be considered with a prior probability density which contains assumptions, external or prior data analysis results. It allows to conclude with credible intervals for the hypothesis, knowing the data. The Bayes theorem is often written the following way:

$$\mathrm{P}(\mathrm{A}|\mathrm{B}) = \frac{\mathrm{P}(\mathrm{B}|\mathrm{A})\,\mathrm{P}(\mathrm{A})}{P(B)}, \tag{3.5}$$

where $\mathrm{P}(\mathrm{A}|\mathrm{B})$ is the conditional probability of event A occurring given that event B is true (also called the posterior probability of A given B), and vice versa for $\mathrm{P}(\mathrm{B}|\mathrm{A})$. $\mathrm{P}(\mathrm{A})$ is the probability of observing A without conditions, it is the prior probability.
For instance in neutrino physics, in a frequentist approach, we would say that an experiment has excluded CP conservation at a X% confidence level, whereas the conclusion of a Bayesian analysis would be that conservation of CP hypothesis is outside the X% credible interval. P-Theta is said to be semi-frequentist in the sense that it takes prior knowledge, in particular from the ND fit, into account and proceeds to a marginalization of the nuisance parameters but then, the analysis is frequentist and produces confidence levels for the parameters-of-interest values.

Marginalizing and profiling

Moreover, the analysis treatment of nuisance parameters consists in marginalizing them. It means taking the average likelihood over all obtained values from nuisance parameters throws. This choice is made because it is a more complete way of taking systematic parameters into account as opposed to the other method which is profiling. When using profiling, one takes only the minimal likelihood, meaning in a way that one selects the set of nuisance parameter values that minimizes the likelihood and consider this as the nuisance parameters best values. Marginalization is therefore more conservative. However, for specific studies, for instance at higher statistics, P-Theta framework's flexibility allows the use of profiling.

Feldman-Cousins studies

A final specific statistical treatment that is performed in P-Theta is a so-called Feldman-Cousins fit. It refers to a publication by Gary J. Feldman and Robert D. Cousins in

1998 [110]. Its goal is to provide confidence intervals without the assumption that the posterior is Gaussian which historically was noticed in counting experiments with few events. This is of particular importance for δ_{CP} for which the discovery of violation of the CP symmetry is fully based on the power to exclude the value 0. Under the Gaussian assumption, the confidence levels coverage correspondence with $\Delta\chi^2$ values has been tabulated and is the one shown in Table 3.4. However, if the posterior distribution is

Table 3.4. *$\Delta\chi^2$ values for standard confidence levels under the Gaussian assumption*

Coverage in %	Usual name	$\Delta\chi^2$ for 1D	$\Delta\chi^2$ for 2D
68.3	1σ	1	2.3
90	90 %	2.71	4.61
95.45	2σ	4	6.18
99.73	3σ	9	11.62

non-gaussian, taking those values of $\Delta\chi^2$ to build the confidence intervals might lead to under or over-coverage. This is the case for δ_{CP} because it is periodic and for now still not strongly constrained. To avoid this, Dr Feldman and Dr Cousins suggested the following method. Let's say that we want to obtain "true" confidence level (with the proper coverage) for δ_{CP}. Once the best fit values of the parameters of interest have been estimated in our analysis; many "toy experiments" from MC events can be produced with different throws for the nuisance parameters as usual. For oscillation parameters, all but δ_{CP} can be drawn for each toy from the posterior distribution of the standard analysis. δ_{CP} value for the toys is fixed; it is their true δ_{CP} value. Then, we perform the fit for all toys and compute a 1D likelihood for the analysis estimated δ_{CP}, marginalizing over the other oscillation parameters as if we were performing the analysis to constrain the δ_{CP} value. We can, by counting the number of toys around the true value (which is necessarily the best fit point of this fit, or very close) build the interval that indeed contains the desired coverage (in %). It can be built in a symmetric way, ordering the toy experiments with a likelihood test. This confidence interval will be expressed in terms of its critical $\Delta\chi^2$ above which the interval would contain more than the desired coverage. If we do this for some key values of δ_{CP} and then make an interpolation, we can obtain the curve of the critical $\Delta\chi^2$ as a function of the true value of δ_{CP}. In general this is done at least for 1σ and 3σ levels. This can then be used to conclude on different hypothesis. The drawback of the method is that it is computationally heavy, given the number of toy experiments and so of fits, that it requires (about 50,000 per δ_{CP} true value, with 10 true values).
Although it is less critical from the physics conclusion point of view, this can also be performed for $\sin^2\theta_{23}$ and even in the 2D space $\sin^2\theta_{23}$ / δ_{CP}.
The treatment of systematic parameters in a Feldman-Cousins study is the result of a choice among several possibilities. In P-Theta, it has been chosen to throw their values

from the post-fit distributions. This is called the a posteriori Highland-Cousins method. This method offers a better treatment of systematic effects as the ones in which they are fixed to a value (either pre or post fit best values). Additionally, throwing from a posterior distribution infers a more accurate coverage as it is as close as possible to the data. However, this is the most conservative approach. One caveat here is that in the T2K analysis, we currently throw systematics from the near detector (ND) post fit distributions, not the final far detector post fit distributions. In that sense, it is not fully a Highland-Cousins method.

3.1.3 Other far detector fitting software

As said before, there are two other fitters and the T2K published constraints on oscillation parameters are always a result of cross-validations between all three, or at the very minimum between two. The ValOR (VALencia-Oxford-Rutherford) fitter has a very similar approach to that of P-Theta in the sense that it is a semi-frequentist statistical analysis, based on minimization of likelihood and marginalization of the nuisance parameters. However the choice of variables for the spectra's binning is different. ValOR bins the data and MC events in reconstructed neutrino energy and reconstructed lepton angle with respect to the beam axis. The third fitter is a little bit more different. Its name is MaCh3 which stands for Markov Chain, three flavors. It uses a Markov Chain MonteCarlo with a Metropolis Hastings algorithm to perform a simultaneous near detector and far detector fit. Its statistical approach is fully Bayesian. MaCh3 choice of binning is that of the BANFF for near detector data and 1D reconstructed neutrino energy for the SK data.

3.2 New features since 2020

When I joined the oscillation analysis, the analysis was being updated with new features. Here is a description of the main ones impacting the analysis pipeline at the far detector.

3.2.1 Multi-ring sample

As stated in Chapter 2, the data is separated into 6 samples for the analysis. Before 2020, there were actually only 5 samples. The 6th one, the muon multi-ring sample (numucc1pi or $\nu_\mu$cc1π) is a new feature for this analysis. It was motivated by increasing statistics significantly in muon-like events (40%), so in the disappearance channel, making full use of our selection capabilities at the far detector. The impact on fitting results were not found to be important though a small improvement in Δm^2_{32} was found.

3.2.2 New cross-section systematics

As a consequence of an update of the cross-section model, a number of new systematic parameters was introduced. I participated in implementing them in P-Theta. Among the list given in Appendix A, 28 parameters are new. In addition, 13 detector systematics were introduced specifically to account for the selection of the new muon-mike multi-ring sample. Moreover, P-Theta moved to a new system of units for the systematic parameters, called 'natural units' as opposed to the previous system which was using physics units, confusing when computing values at N sigma from the nominal value. I implemented this new unit system in P-Theta's treatment of systematics.

3.2.3 New removal energy treatment

Among all parameters, one was given a slightly new treatment in the analysis. The removal energy (E_b) value of the nucleon that interacted with the neutrino in the far detector is a sensitive parameter that needs to be evaluated in the analysis. Indeed, it impacts both the prediction and the reconstruction as the final state kinematics depends on it. As a result, the removal energy is present in a non-trivial way in the reconstruction formula of the neutrino energy under the CCQE hypothesis:

$$E_{rec}^{CCQE} = \frac{m_p^2 - (m_n - E_b)^2 - m_l^2 + 2(m_n - E_b)E_l}{2(m_n - E_b - E_l + p_l \cos\theta_l)} \tag{3.6}$$

In formula 3.6, the indices l denote the outgoing lepton, p the proton and n the neutron. Note that this formula assumes the nucleon at rest, which is , in general, not the case. We however use this value as an observable correlated to the true neutrino energy. The analysis is performed by predicting this observable from the reconstructed Monte Carlo and comparing it to the observed values. It is also important to note that this formula is only valid for single-ring events where there is not any resonance and pion production involved. In the case of the 1Re1de and numucc1pi samples, the formula used does not involve the removal energy and is:

$$E_\nu^{\text{rec}} = \frac{\left(M_{\Delta^{++}}^2 - M_p^2 - m_x^2\right)/2 + M_p E_l}{M_p - E_l + p\cos\theta} \tag{3.7}$$

where $M_{\Delta^{++}}$ is the mass of the resonant delta and m_x is the charged pion mass for the numucc1pi sample or the electron mass for the 1Re1de sample. The current cross-section model used in the T2K analysis is the spectral function one, with a nominal value for Oxygen 16 of $E_b = 27$ MeV. Even though this cross-section model was chosen carefully to add the level of detail needed for the analysis without becoming computationally too

heavy, it is not an absolute choice. There is currently no "perfect" cross-section model that reproduces all experimental data. To cover this, a systematic uncertainty is associated to the E_b parameter. However, the spectral function model does not predict any dependence of E_b on the kinematics of the interaction. Another model, the relativistic Mean-field model (RMF) does predict a strong 3-momentum transfer ($Q_3 = \sqrt{p_\nu^2 + p_l^2 + p_\nu p_l \cos\theta}$) dependence; and this scenario is favored by external electron scattering data as well [**escatdata**, **TN414**]. This was the motivation to add a Q_3 dependence to the uncertainty on E_b in order to allow for this freedom to be absorbed by the systematics treatment. I therefore implemented this possibility at the level of the far detector, in P-Theta. The ideal implementation would have been to be able to create 2D splines for both the Q_3 dependence and the usual E_b uncertainty, but we started with a simpler implementation and for reasons that will be explained later, no sophistication was then pursued. It was decided to proceed with the following implementation. The Q_3 dependent part was not allowed to vary during the fit as part of the uncertainty on the removal energy value but was fixed, according to the preferred value by the near detector fit. In more details, this Q_3 dependence translates into a shift of the removal energy, linear to Q_3 in the following way:

$$\Delta_{E_b} = \alpha \ (m \times Q_3 + c) \tag{3.8}$$

where m and c are constant estimated by dedicated fit studies and α is the strength of the correction (between 0 and 1). m was set to 0.056 (no units) and c to -41.6 MeV. It is the α parameter that is fixed, instead of being varied as a systematic parameter. As can be seen from the distribution of Q_3 values in the MC events in figure 3.5, this E_b shift can potentially be large, up to -13.6 MeV for $Q_3 = 500$ MeV (the most frequent value in the MC events) and α at its extreme value 1. The impact of this E_b shift on the samples spectra has been established for various values of α: 0.25, 0.50 and 0.75 and a graphic representation of it for the 1Rν_μ sample can be found in figure 3.6 where the ratio to the nominal spectrum (i.e.: $\alpha = 0$) is plotted as a function of the neutrino reconstructed energy. The impact is relatively small. This effect was validated against a similar study in the MaCh3 fitter, validating the implementation I made in P-Theta. More importantly, the near detector fit allows for the α parameter to vary and the result gives a strong constraint on α, setting it to 0. This means that T2K data completely disfavor the scenario of a Q_3 dependent shift of E_b. This is in contradiction with external data. An explanation could be that we already have in the analysis correlated systematic parameters such as the optical potential or Pauli blocking related systematics, which have a similar impact and so absorb the freedom that was intended to be given to the α parameter. In any case, because the strongly preferred value of α by T2K data was 0, it was decided that it would be fixed to 0 for this year's analysis and more understanding was needed from the neutrino interaction working group (NIWG) to pursue the implementation and understand the

difference with external data. The effect of using another value of α will be discussed in Chapter 4.

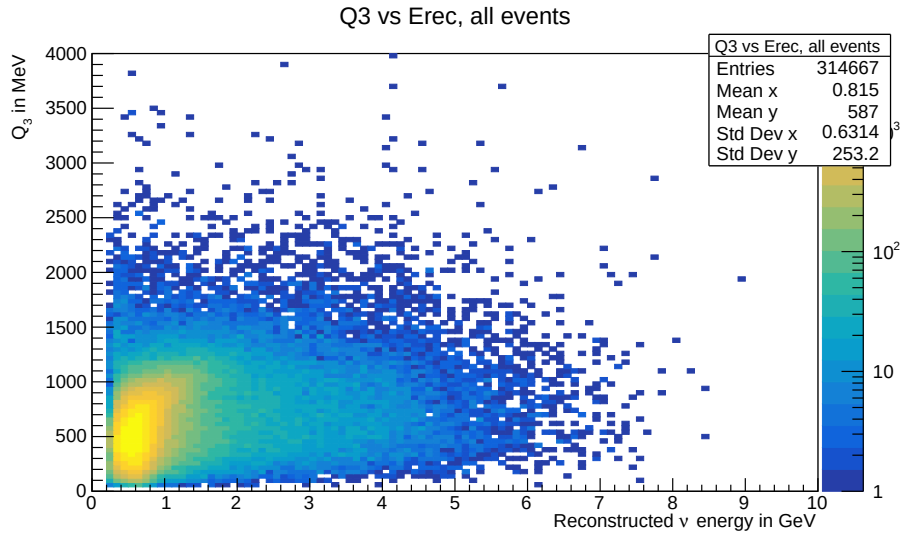

Figure 3.5. *Distribution of Q_3 values as a function of neutrino reconstructed energy for the $1R\nu_\mu$ sample, CCQE interaction only*

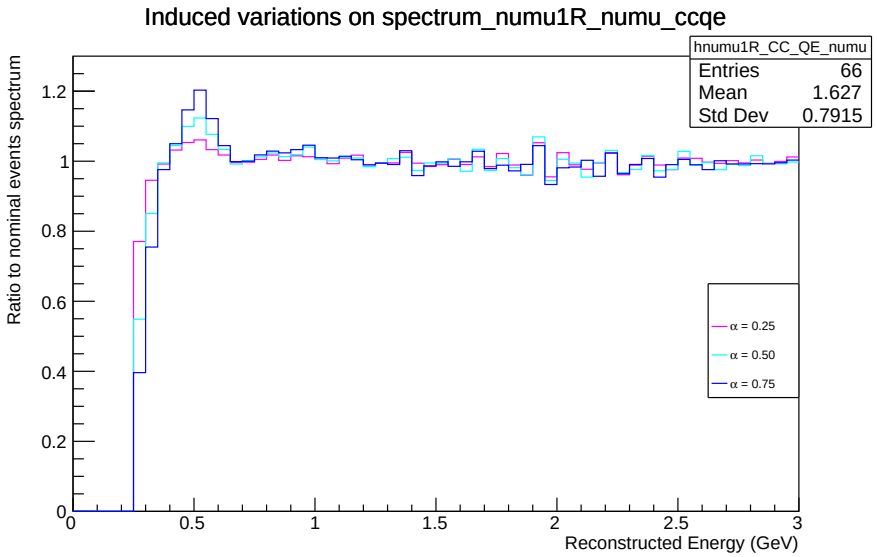

Figure 3.6. *Ratios to nominal spectrum for various values of α for 1Rν_μ, CCQE*

3.3 Results

3.3.1 2021 Analysis

In this section, the so-called 'Oscillation Analysis 2021' or OA21 will be briefly presented. It consists in the new analysis features being used without new data. The near detector data used is from run 2-9 until ND280 was turned off; the last data taking happened in 2018. The far detector data used is from run 1-10 (up to 2020). The corresponding beam power breakdown in beam modes (neutrino or anti-neutrino) and accumulated Protons On target (POT) has been shown in figure 2.3.

The results of OA21, in the form of best fit values and 1σ errors on the parameters constrained by T2K are summarized in Table 3.6. The corresponding χ^2 values directly from the fit, as well as the ones re-scaled to put the best fit χ^2 at 0 are also given. As explained in detail in the previous sections, P-Theta analysis is using marginalizing over nuisance parameters to obtain constraints on parameters, in either 1D or 2D spaces. However, a global fit is also performed by the Minuit gradient from ROOT so as to obtain best fit values. This is the result from this additional last step that is shown in Table 3.6. 'T2K only' means without reactor constraints on the 1-3 mixing angle. Indeed, as said in section 3.1, by default T2K analysis takes advantage of the accurate already existing constraints on $\sin^2(2\theta_{13})$. To do so, values of $\sin^2(2\theta_{13})$ during the fit are thrown from a gaussian prior with mean the external best value and with σ the external 1σ error. These values can be found in Table 3.5. However, the T2K oscillation analysis results are

generally also presented without using that constraint in order to evaluate T2K sensitivity to it as well as how it would change the constraints on the other parameters. Full details of the OA21 results are not provided since a similar analysis with a statistical update (far detector data) was a part of this thesis's work and is presented in the rest of this Chapter.

Table 3.5. *Prior values for* $\sin^2(2\theta_{13})$ *from [111]*

	mean	1σ
$\sin^2(2\theta_{13})$	0.08606400	0.00267680

Table 3.6. *Best fit values and* 1σ *errors on the parameters constrained by T2K, results of the oscillation analysis 2021*

Parameter	Best fit			
Data	T2K only		T2K + reactor	
Hierarchy	Normal	Inverted	Normal	Inverted
$\sin^2(2\theta_{13})$	0.103	0.114	0.0861	0.0865
$\sin^2(\theta_{13})/10^{-3}$	$26.6^{+2.8}_{-5.8}$	$29.3^{+3.1}_{-6.1}$	$22.0^{+0.76}_{-0.6}$	$22.1^{+0.74}_{-0.63}$
δ_{CP}	$-2.25^{+1.39}_{-0.75}$	$-1.25^{+0.69}_{-0.91}$	$-2.18^{+1.22}_{-0.47}$	$-1.37^{+0.52}_{-0.68}$
Δm^2_{32} (NH)/$\lvert\Delta m^2_{31}\rvert$ (IH) $[10^{-3}$ eV^2/c$^4]$	$2.506^{+0.048}_{-0.058}$	$2.474^{+0.049}_{-0.056}$	$2.506^{+0.047}_{-0.059}$	$2.473^{+0.051}_{-0.054}$
$\sin^2(\theta_{23})$	$0.466^{+0.106}_{-0.015}$	$0.465^{+0.103}_{-0.015}$	$0.559^{+0.018}_{-0.078}$	$0.560^{+0.019}_{-0.041}$
$-2\ln L$	651.433	652.254	651.584	653.222
$-2\Delta\ln L$	0	0.821	0	1.638

T2K Run 1-10, preliminary

3.3.2 Following statistical update

3.3.2.1 Generalities

This section will present and discuss the results of the oscillation analysis including the Run 11 far detector data set. It consists in an increase of 9% in the FHC POT (neutrino mode), that was taken during Spring 2021. No major new features were added to the analysis, hence it is called a statistical update. It is referred to as either OA23 or Run 11 statistical update. I was the main P-Theta analyzer for this update. It is important to note here that these results are not the T2K official results due to incompatibilities of time-lines.

Before looking at the data fit, we validate the analysis in many steps. One part of this validation is to obtain agreement with the other fitters, or for the current analysis with MaCh3 at least, at the level of event rates without systematic parameters applied, then with each group of systematics applied one by one, as well as in terms of systematic

parameters response. After these first validations, so-called Asimov fits are performed. They consist in fitting Monte-Carlo events with a defined set of oscillation parameters. In most cases, for this analysis the Asimov A22 set is used which corresponds to the values published in the Particle Data Group booklet 2022 [111] for parameters not well constrained by T2K and to T2K best fit points from the previous analysis for the others. An alternative set called B22 is sometimes used and modifies A22 in such a way that the CP symmetry is conserved and the $\sin^2\theta_{23}$ mixing is minimized. The exact value used can be found in Table 3.7. Sensitivity plots of the T2K analysis for MC events at both

Parameter	Asimov A22	Asimov B22
δ_{cp}	-1.601	0.0
$\sin^2\theta_{13}$	0.0220	0.0220
$\sin^2\theta_{23}$	0.561	0.45
$\sin^2\theta_{12}$	0.307	0.307
$\lvert\Delta m^2_{23}\rvert$ (eV^2)	2.494×10^{-3}	2.494×10^{-3}
$\lvert\Delta m^2_{12}\rvert$ (eV^2)	7.53×10^{-5}	7.53×10^{-5}

Table 3.7. *Sets of oscillation parameter values used to produce simulated data for sensitivity studies*

A22 and B22 oscillation parameters sets can be found in figure 3.7. The above mentioned modifications to δ_{CP} and $\sin^2\theta_{23}$ to build B22 from A22 are clearly visible respectively in the left and right plots.

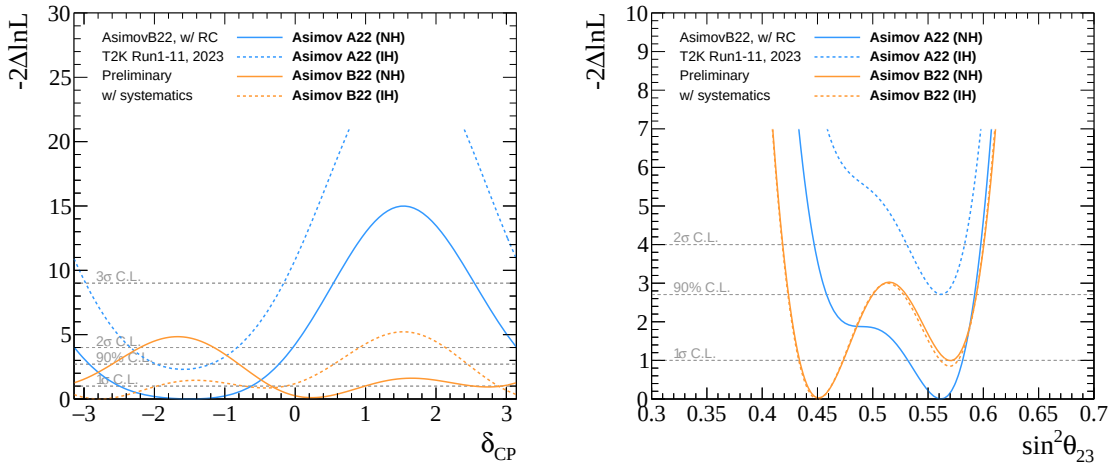

Figure 3.7. *Sensitivity plots of the T2K analysis for MC events at both A22 and B22 oscillation parameters for δ_{CP} (left) and $\sin^2\theta_{23}$ (right)*

3.3.2.2 Predicted distributions of events and background

Using the A22 Asimov set of MC events, distributions of events in the reconstructed neutrino momentum/lepton angle plane or the reconstructed neutrino energy/lepton angle depending on the sample analysis binning can be plotted for different interaction category or oscillation channels. Figures 3.8, 3.9, 3.10, 3.11, 3.12 show these distributions for, respectively, samples ν_e1R, $\bar{\nu_e}$1R, ν_e1R1de, ν_μ1R, $\bar{\nu_\mu}$1R. Note that the color scales are different for each plot. Such distributions are not shown for the new numucc1pi sample as, when a new sample is introduced, we always start with the simplest analysis which is an Erec binning only. For the electron samples, figure 3.8, 3.9, 3.10, true muon events, non-oscillated electron events, wrong sign (eg: anti-neutrino for the neutrino mode) events and neutral current events are considered as background for the electron flavor appearance signal. For muon samples, figures 3.11, 3.12, the background categories shown here are neutral current and wrong sign components. In both cases, it can be seen that these kinematics distributions can be used as an additional background identification. This is why the scattering angle θ is used in the analysis binning, providing power to distinguish these events in the full fit.

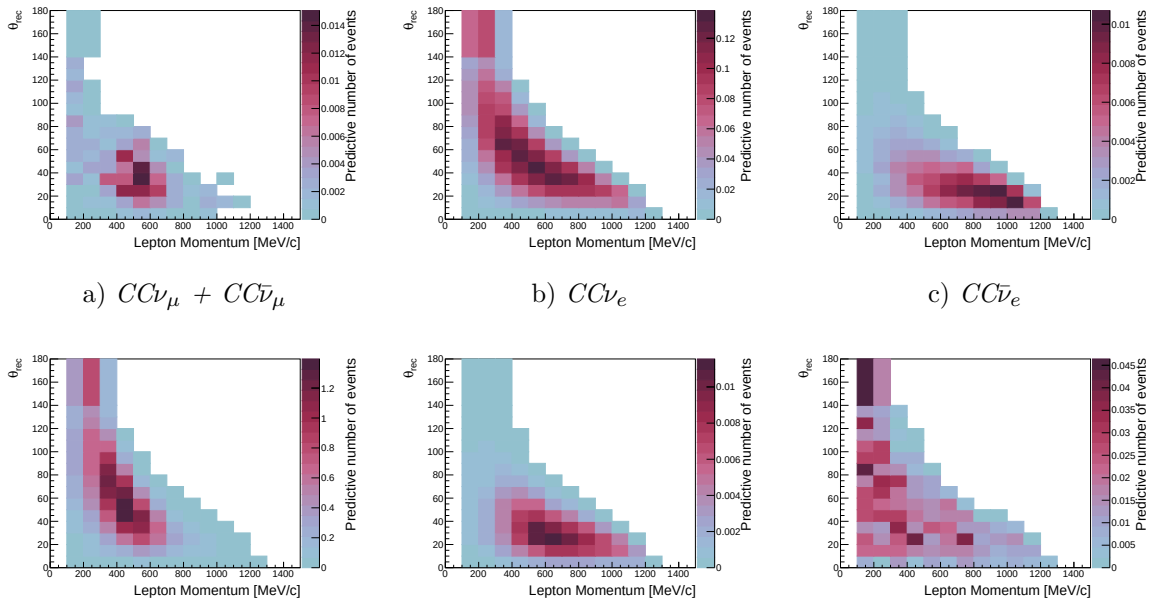

a) $CC\nu_\mu$ + $CC\bar{\nu}_\mu$ b) $CC\nu_e$ c) $CC\bar{\nu}_e$

d) *Osc.* $CC\nu_e$ e) *Osc.* $CC\bar{\nu}_e$ f) *NC*

Figure 3.8. *Distributions of the lepton momentum and angle (in degrees) for the FHC 1Re-like samples for the signal (3.8d) and the five background categories. These figures assumes the oscillation parameters set A22 listed in Table 3.7. The color indicates the expected number of events (normalized).*

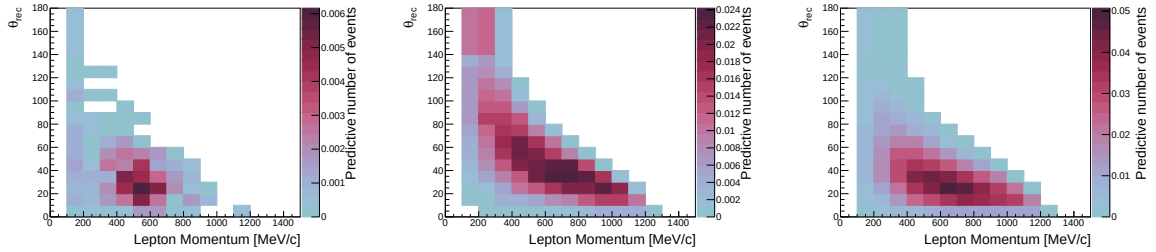

a) $CC\nu_\mu$ + $CC\bar{\nu}_\mu$ b) $CC\nu_e$ c) $CC\bar{\nu}_e$

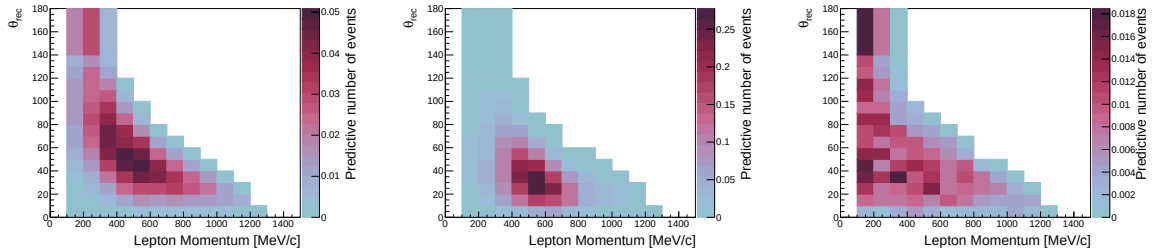

d) *Osc.* $CC\nu_e$ e) *Osc.* $CC\bar{\nu}_e$ f) *NC*

Figure 3.9. *Distributions of the lepton momentum and angle (in degrees) for the RHC 1Re-like samples for the signal (3.9e) and the five background categories. This figures assumes the oscillation parameters set A22 listed in Table 3.7. The color indicates the expected number of events (normalized).*

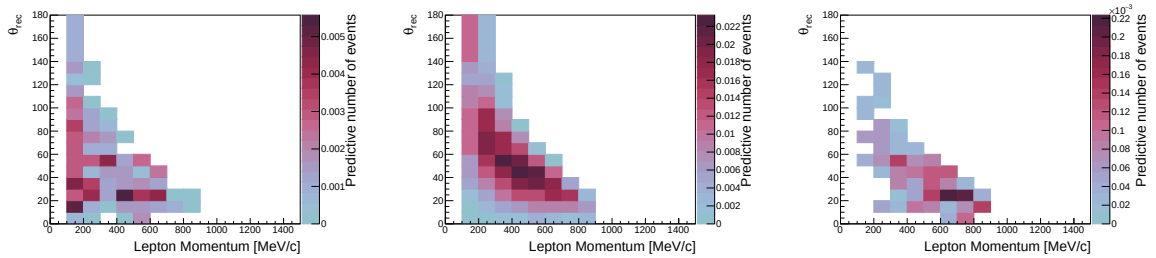

a) $CC\nu_\mu$ + $CC\bar{\nu}_\mu$ b) $CC\nu_e$ c) $CC\bar{\nu}_e$

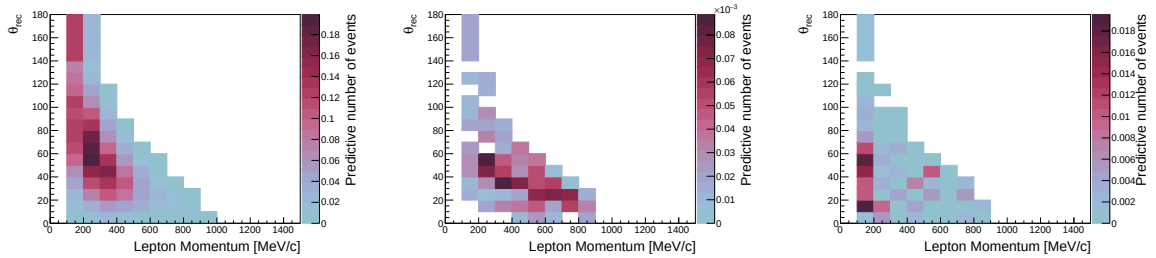

d) *Osc.* $CC\nu_e$ e) *Osc.* $CC\bar{\nu}_e$ f) *NC*

Figure 3.10. *Distributions of the lepton momentum and angle (in degrees) for the FHC 1R ν_e CC1π sample for the signal (3.10d) and the five background categories. This figures assumes the oscillation parameters set A22 listed in Table 3.7. The color indicates the expected number of events (normalized).*

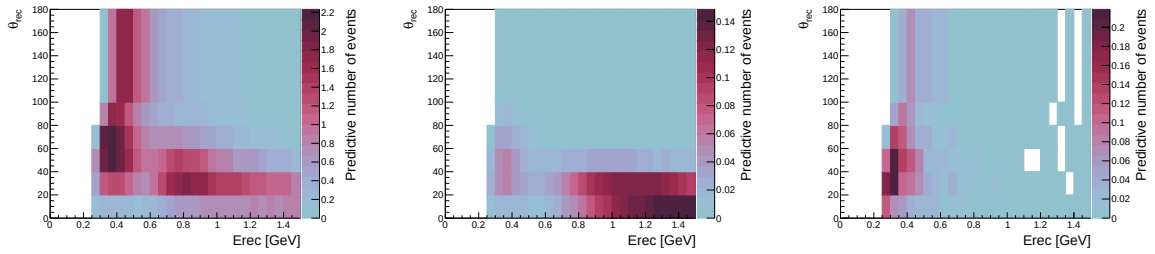

a) $CC\nu_\mu$ b) $CC\bar{\nu}_\mu$ c) NC

Figure 3.11. *Distributions of the lepton momentum and angle (in degrees) for the FHC 1Rμ-like samples for the CC signal (3.11a, 3.11b) and NC background (3.11c) categories. These figures assume the oscillation parameters set A22 listed in Table 3.7. The color indicates the expected number of events (normalized).*

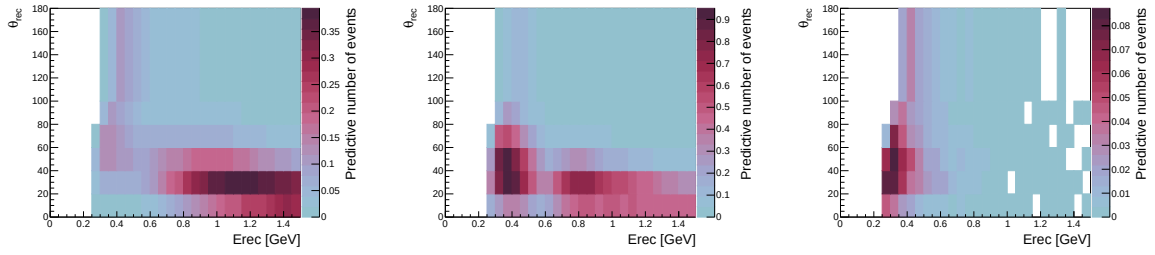

a) $CC\nu_\mu$ b) $CC\bar{\nu}_\mu$ c) NC

Figure 3.12. *Distributions of the lepton momentum and angle (in degrees) for the RHC 1Rμ-like samples for the CC signal (3.12a, 3.12b) and NC background (3.12c) categories. These figures assume the oscillation parameters set A22 listed in Table 3.7. The color indicates the expected number of events (normalized).*

3.3.2.3 New inputs for the statistical updates

The analysis, on top of using new SK data, is not completely similar to OA21 as it has two new features. The first one is that the cut to select decay electrons applied when building the SK samples has been modified. This is in relation with Run11 being the first run of data since the addition of Gadolinium. Even if the neutron tagging data is not yet integrated in the oscillation analysis, the cut has been made more sophisticated in order to separate more clearly tagged-neutrons from decay electrons. This has been achieved by adding a cut on the number of hits in 50 ns time window. The second, more impactful change is a new SK detector systematic error matrix. This matrix is given to the oscillation analyzers by a dedicated T2K-SK group which is in charge, among other things, to build the error model for the detection effect at SK. The evaluated errors, separated in the 6 analysis samples is propagated to the analysis through a covariance error matrix. For OA21, the introduction of new sample $\nu_\mu$cc1π in the error matrix was not fully achieved: the correlations with other samples could not be added in due time. For the statistical update, the full correlations have been added. Finally, the pipeline for the production of this matrix has been modified in such a way that an intermediate binning was removed. This resulted in reducing significantly the errors on ν_e1R1de sample (from 13.3% to 4.3% error values).
Sensitivity studies (standard P-Theta analysis run with a set of MC events) at Asimov A22 are shown in figure 3.13 for different sets of inputs so as to evaluate which new feature has the most impact on the analysis and will cause the most differences with OA21 results. The purple curve is the OA21 sensitivity, the orange curve is this OA23 sensitivity, the green curve is OA23 sensitivity with the previous SK detector error matrix, and the blue curve is this OA23 sensitivity without the Run 11 POT. This way, comparing the purple curve to the green curve allows to see the combined impact of the additional data (POT) and the new decay electron cut. Going from the blue to the orange curves allows to isolate the effect of the new data. The comparison of the green curve to the orange one shows the impact of the new SK detector error matrix only. This is shown for the main 3 parameters constrained by T2K: δ_{CP} (left), $\sin^2\theta_{23}$ (right), and Δm^2 (bottom). It can be concluded that the impact on Δm^2 is mild and mostly visible for the inverted ordering. The best value (minimal χ^2) is slightly shifted towards higher values and the sensitivity is improved. The cause is equally shared by the increase of POT and the new detector matrix. This impact could be the result of the largest impact seen on $\sin^2\theta_{23}$ since those two parameters are highly correlated. The sensitivity to the octant is higher and the minimal χ^2 in 1D distributions seems very slightly shifted towards higher values as well. Again it can be said that the increase of sensitivity is more or less equally due to the new SK matrix and the new data although the matrix has a bit larger impact in normal ordering. Finally, the δ_{CP} sensitivity, which is the most crucial one in terms of physics

analysis as it has been discussed in Chapter 1, is improved by a bit more than 1 unit of χ^2, in particular the ability to reject the wrong sign of the phase. For this parameter, the addition of data has the largest impact even-though the impact of the new detector error matrix is non-negligible. The impact of the matrix can be explained in that it reduces significantly the error on an electron appearance sample, compared to errors on muon-like samples, which enhances sensitivity to the atmospheric oscillation parameters and CP violation as shown in Chapter 1.

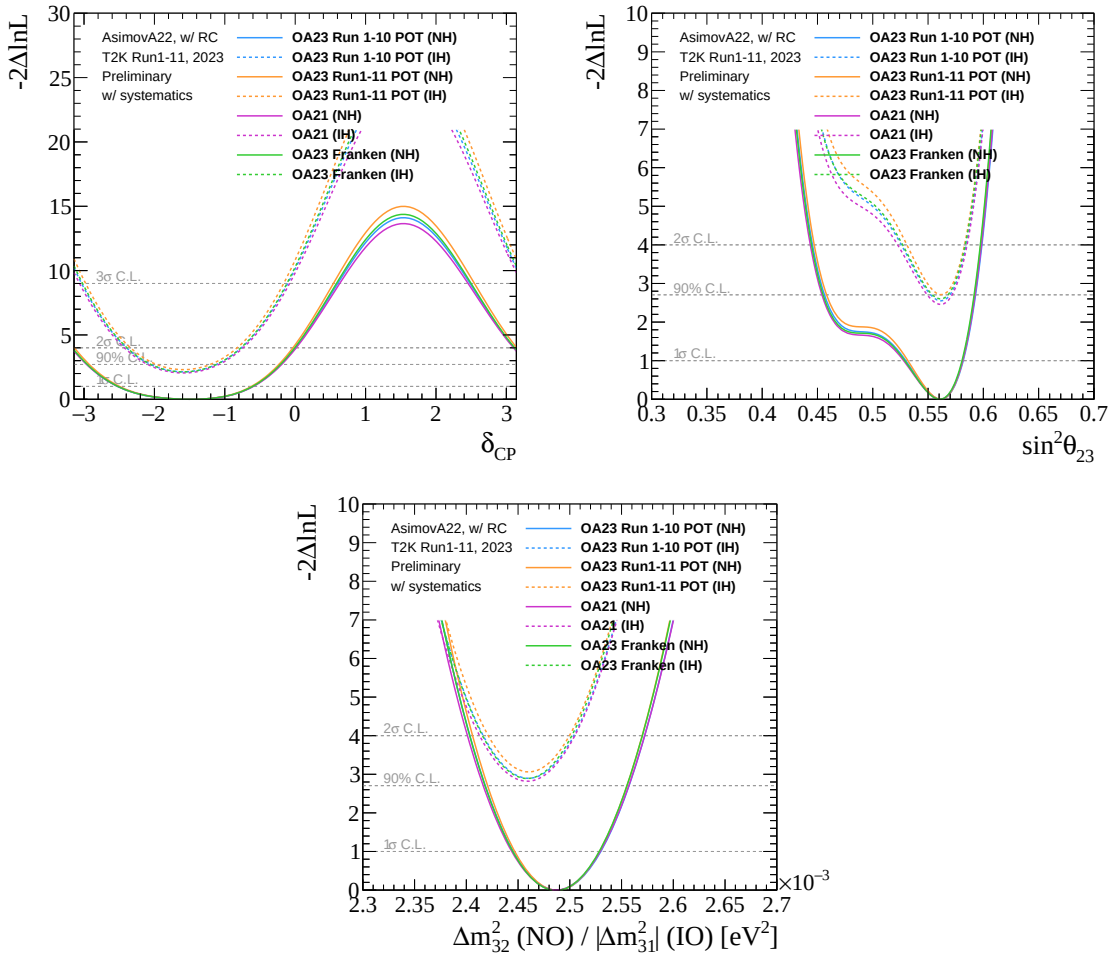

Figure 3.13. *Sensitivity plots at A22, with reactor constraints and with systematic parameters, for δ_{CP} (left), $\sin^2\theta_{23}$ (right), and Δm^2 (bottom) adding the Statistical update specific items one by one. The purple curve is the OA21 sensitivity, the orange curve is this OA23 sensitivity, the green curve is OA23 sensitivity with the previous SK detector error matrix, and the blue curve is this OA23 sensitivity without the Run 11 POT*

3.3.2.4 Data distributions

When opening the data, before performing the analysis, one useful cross-check is to look at the distribution of data points as a function of the reconstructed kinematic variables.

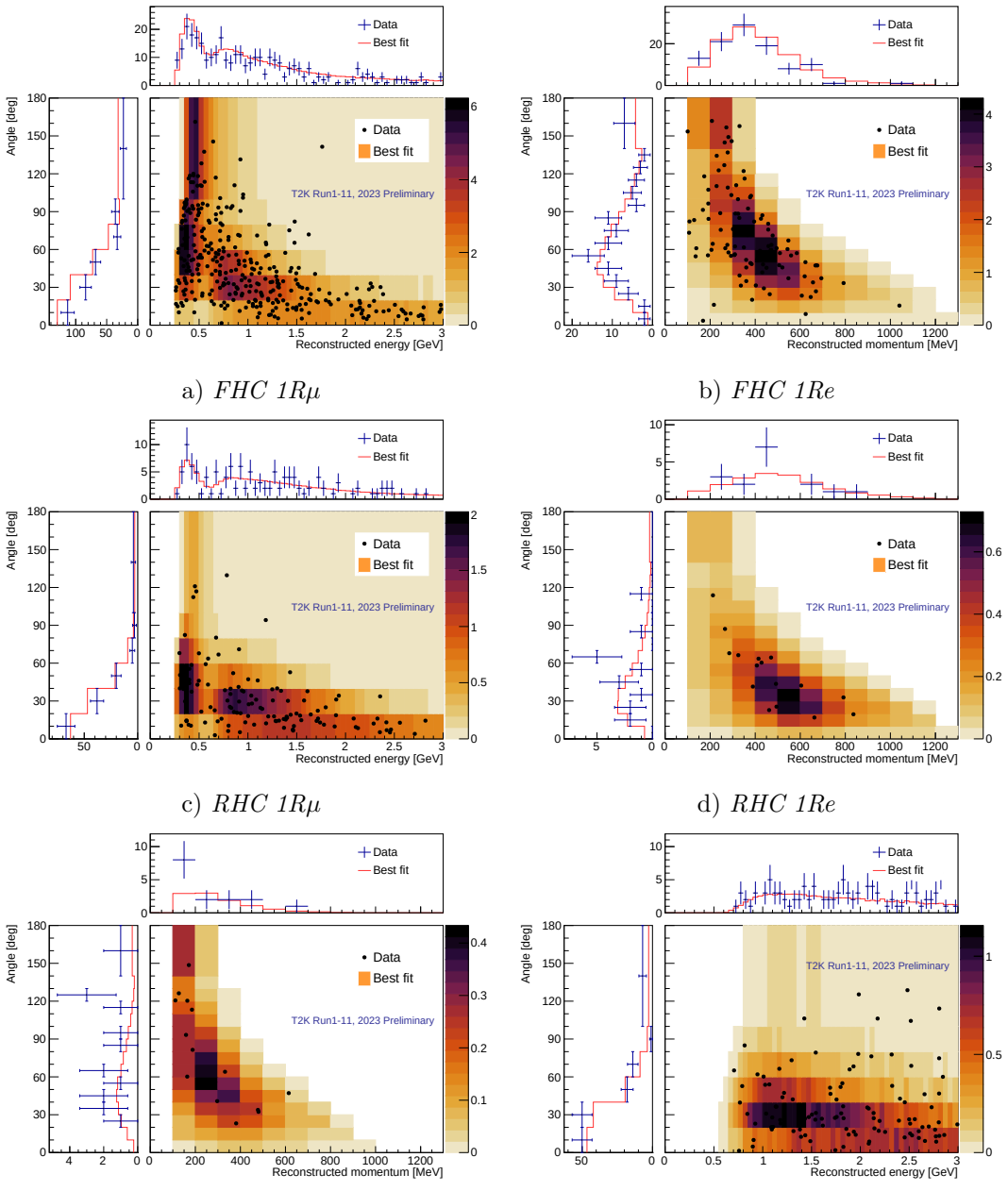

a) *FHC 1Rμ* b) *FHC 1Re*

c) *RHC 1Rμ* d) *RHC 1Re*

e) *FHC 1R* ν_e *CC1π* f) *FHC MR* $\nu_\mu CC1\pi^+$

Figure 3.14. *Events of the runs 1–11 data set for the six samples reconstructed in 2D (note that numucc1π is analyzed in 1D only). The color scale shows the expected number of events (normalized) for the result of best-fit with oscillation parameters set at their best-fit values and systematic parameters at their best ND-fit values. The error bars represent the 68% confidence interval for the mean of a Poisson distribution given the observed data point (calculated using the quantile function of a gamma distribution with unit shape parameter). For bins where the expected number of events is 0, no error bars are shown.*

The chosen kinematic variables, by sample, are the ones used for the analysis and described in section 3.1. Figure 3.14 shows the data (black dots), broken down by samples, and overlaid on a 2D histogram of the distribution of MC events at best fit for comparison with expectation in the 2D planes $E_{rec} - \theta$ or $p_l - \theta$ depending on the samples (same quantities as described before). The best fit is not known before analysis of course, but it can be added a posteriori to this comparison. Internally, a first check with last year's best fit was performed. The figure also shows the overlaid data/expectation histograms in 1D projections on the side and the top. Note that the $\nu_\mu$cc1π sample is shown here in 2D but is currently analyzed in 1D only (reconstructed neutrino energy). Overall, it can be seen that the data distributions are in very good agreement with the predictions.

3.3.2.5 Main results

With systematic parameters

The analysis of all T2K data including the new set of data from Run 11 was performed applying all systematic parameters, using the so-called reactor constraint, all 6 SK analysis samples and assuming both, separately, mass orderings. 100 000 throws were used for both systematics and oscillation parameters. As said before, a distinct global fit was performed so as to assess the best fit values. The result of this global fit is given in Table 3.8. The asymmetric errors are computed from the standard analysis (with marginalization), using the best fit point distance to the 1σ interval limits in most cases, except for $\sin^2(\theta_{23})$ in Normal Ordering where the 90% C.L. interval is used because the 1σ interval is split in two regions. For both δ_{CP} and $\sin^2(\theta_{23})$, Feldman-Cousins studies (described in 3.3.2.7) results are used to compute the errors.

An MC-data set at the best fit points in normal ordering (which is the global best fit scenario) is built from these values and put through the standard analysis in P-Theta in order to compare the sensitivity at these particular values with the data fit. The obtained 1D likelihood curves for the 4 parameters that T2K is mostly sensitive for, namely Δm^2 (top left), $\sin\theta_{23}$ (top right), δ_{CP} (bottom left), and $\sin\theta_{13}$ (bottom right), are presented in figure 3.15. The two possible mass orderings are shown: normal ordering (solid lines) and inverted ordering (dashed lines). It can be seen that for $\sin\theta_{13}$ the data fit (orange) and sensitivity (blue) match perfectly. This can be explained by the fact that it is already very constrained by the reactor constraints and therefore does not have much freedom in the T2K analysis. Another thing to notice is that the constraint on δ_{CP} from the data is stronger than that of the sensitivity. This is a feature that has also been observed in the past. It means that the asymmetry between neutrino and anti-neutrinos seen in the data is larger than what is expected at this value of maximal CP violation. This can be due to a bias in one of the many steps of the analysis but all are developed and checked

Table 3.8. *Best fit values for the OA23 analysis with reactor constraints, global best fit is in normal ordering*

	Normal ordering	Inverted ordering
$\sin^2(\theta_{13})/10^{-3}$	$(21.9^{+0.9}_{-0.5})$	$(22.0^{+1.0}_{-0.4})$
δ_{CP}	$-2.08^{+1.33}_{-0.61}$	$-1.41^{+0.64}_{-0.82}$
Δm^2_{32} (NO)/Δm^2_{31} (IO)	$(2.521^{+0.037}_{-0.050})10^{-3}\text{eV}^2/\text{c}^4$	$(-2.486^{+0.043}_{-0.044})10^{-3}\text{eV}^2/\text{c}^4$
$\sin^2(\theta_{23})$	$0.568^{+0.024}_{-0.125}$	$0.567^{+0.021}_{-0.048}$
-2 ln L	649.06	651.013
-2 Δln L	0.	1.953

against simulations so the favored hypothesis so far is a statistical fluctuation, especially since the POT collected in RHC mode (anti-neutrino beam) is significantly lower than that in FHC mode. That hypothesis is re-enforced by plots such as the ones in figure 3.16 which represent the distribution of fit results for 50 000 toy experiments produced at the global best fit oscillation parameters values and with systematic parameters thrown from the post ND fit covariance matrix. The part of the distribution containing 68% of the toys is shown in blue, and the one for 95% is shown in orange. The median is drawn in a black dotted line. This type of plots is traditionally called Brazil plots in reference to the usual colors used (green and yellow). Here the colors have been modified to be colorblind-friendly. The data result is superimposed in a red solid line. The left plot is for true inverted ordering (IO), fitted as such, and the right one for true normal ordering, fitted as such. It allows to see that, in particular for normal ordering, which is the favored scenario by T2K data, the data curve does not correspond to the median which explains that its sensitivity is slightly different than that of the Asimov simulated data at best fit. Indeed, the experiment (T2K) is only done once! Thus, this type of statistical behavior is perfectly expected. Additionally, the IO plot allows to get a sense of our sensitivity to mass ordering as the data curve is still in the 95% band of the toys in that case.
Concerning $\sin^2\theta_{23}$, the increase in sensitivity that is due to the new SK matrix is particularly strong in the sensitivity at best fit result. It can also be seen that the best fit point does not correspond to the minimum of the $\chi^2 = -2\Delta lnL$. This can happen since the global fit with Minuit includes many parameters and is specifically difficult for $\sin^2\theta_{23}$ which has two minima. The best fit is performed separately in the two octants but this slight shift could still come from a converging difficulty. It could also explain this likelihood curve difference between the data fit and the sensitivity. The main constraints extracted from the analysis are from the standard analysis and not the global best fit

anyway so this is not a major issue. Finally, as Δm^2 is very correlated with $\sin^2\theta_{23}$, this shift in best fit values could explain the small shift observed in the likelihood curves between data and sensitivity.

Due to the uncertainty on the choice of neutrino interaction cross-sections and nuclear model, as well as some other additional effect, the Δm^2 curve is smeared by a gaussian. This allows to account for an additional uncertainty. The computation of the width (sigma) of such a Gaussian is the topic of Chapter 4. Here the value applied is $3.1 \times 10^{-5}\ eV^2$.

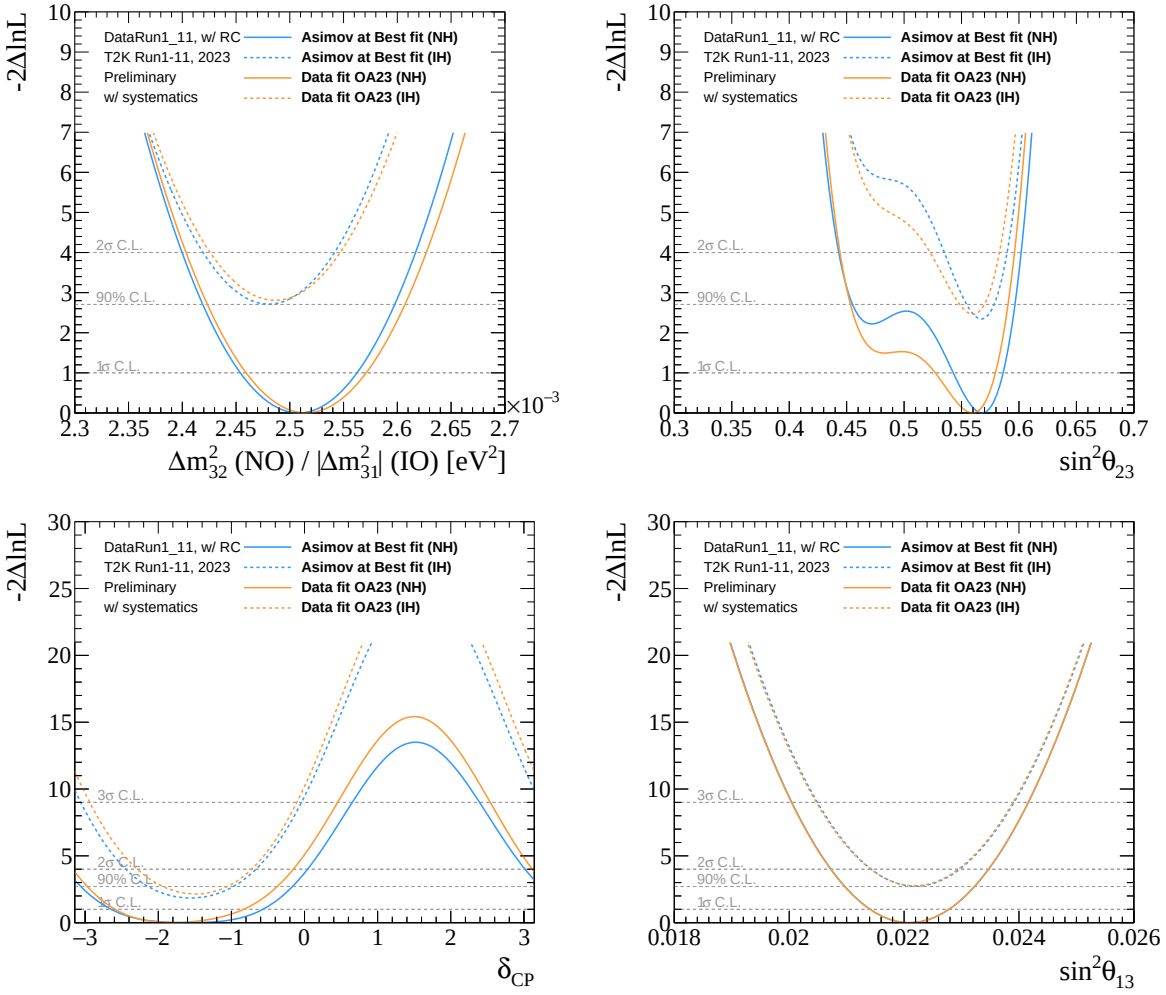

Figure 3.15. *1-D likelihood surfaces for Δm^2 (top left), $\sin\theta_{23}$ (top right), δ_{CP} (bottom left), and $\sin\theta_{13}$ (bottom right) with the reactor constraint on $\sin\theta_{13}$, for both normal (solid line) and inverted (dashed) ordering, for the data fit (orange) and sensitivity at best fit (blue). Smearing is applied on Δm^2.*

Finally, P-Theta also performs analyses in 2D likekihood surfaces and the results are displayed in figure 3.17: $\Delta m^2/\sin\theta_{23}$ (left) and $\sin\theta_{13}$ /δ_{CP}(right). This allows to observe the correlations between parameters. Contours are shown for different levels of confidence (C.L.) depending on the line style (refer to the legend of plots). The best fit point shown

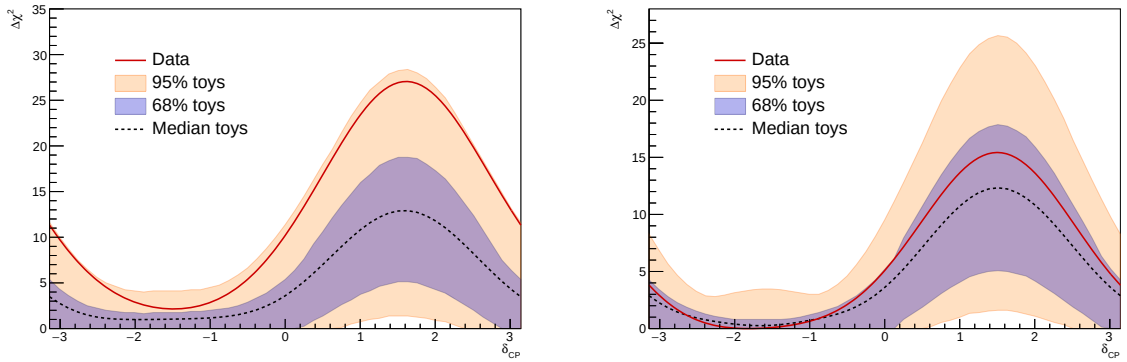

Figure 3.16. *So-called 'Brazil plots' for the data (red line) and 50 000 toy experiments at the global best fit points for true inverted ordering, fitted assuming inverted ordering (left) and true normal ordering fitted assuming normal ordering (right)*

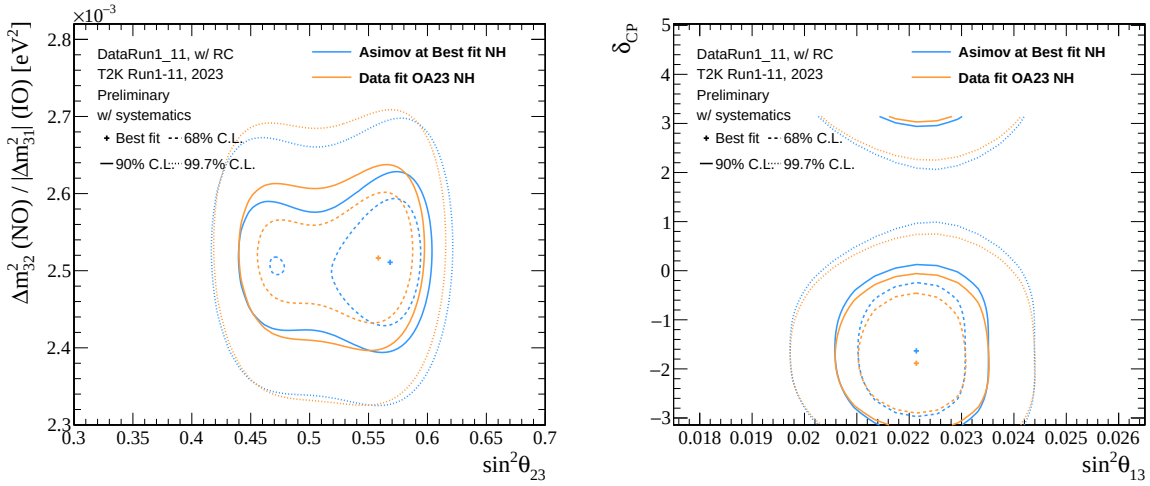

Figure 3.17. *2D likelihood surfaces in the Δm^2/ $\sin\theta_{23}$ (left) and $\sin\theta_{13}$ /δ_{CP} (right) planes with the reactor constraint on $\sin\theta_{13}$, for both normal (solid line) and inverted (dashed) ordering, for the data fit (orange) and sensitivity at best fit (blue). Smearing is applied on Δm^2.*

here is actually not the best fit point from the global fit but the point in the 2D space that has the lowest χ^2. Only normal ordering is presented and the color code is the same as for the 1D curves. One thing to notice on the left plot is the strong correlation between $\sin\theta_{13}$ and δ_{CP} which illustrates the importance of external constraints on $\sin\theta_{13}$ to be able to perform a precise measurement of the CP violation in neutrino oscillations. The second thing to notice is that the sensitivity and the constraints from the data fit are very similar except for $\sin\theta_{23}$ which is consistent with the 1D results. For the 68% C.L., the contours for sensitivity is splitting in two areas. This is a result of the shifted best fit point and the higher sensitivity to exclude values around 0.5 discussed previously and is a limitation of this 2D representation of the analysis results. As for the 1D curves, a

gaussian smearing is applied to the likelihood surface involving Δm^2.

As a conclusion on these results, it can be said that overall the data fit is consistent with expectations. Better constraints are still needed to discover the octant of $\sin\theta_{23}$ at 5σ as it can be seen from the standard gaussian confidence levels drawn on the 1D plots. Similarly, better constraints are still needed to exclude CP conservation at the discovery level of 5σ. More precise constraints on δ_{CP} will be extracted from Feldman-Cousins studies and reported in section 3.3.2.7.

Without the Reactor constraints

As said before, the analysis was also performed without applying the reactor constraints on $\sin^2 2\theta_{13}$. The best fit values found in that case are reported for both mass orderings in Table 3.9. The asymmetric errors are computed from the standard analysis (with marginalization), using the best fit point distance to the 1σ interval limits in most cases, except for $\sin^2(\theta_{23})$ where the 90% C.L. interval is used because the 1σ intervals are split in two regions. We do not perform Feldman-Cousins studies without the reactor constraints so these errors are computed from intervals built with classical critical values of χ^2.

Table 3.9. *Best fit values for the OA23 analysis* ***without*** *reactor constraints, global best fit is in normal ordering*

	Normal ordering	Inverted ordering
$\sin^2(\theta_{13})/10^{-3}$	$(27.8^{+1.8}_{-6.9})$	$(31.0^{+1.8}_{-7.4})$
δ_{CP}	$-2.21^{+1.62}_{-0.75}$	$-1.29^{+0.63}_{-0.99}$
Δm^2_{32} (NO)/Δm^2_{31} (IO)	$(2.521^{+0.039}_{-0.050})10^{-3}\mathrm{eV}^2/\mathrm{c}^4$	$(-2.489^{+0.042}_{-0.046})10^{-3}\mathrm{eV}^2/\mathrm{c}^4$
$\sin^2(\theta_{23})$	$0.458^{+0.130}_{-0.021}$	$0.458^{+0.127}_{-0.021}$
-2 ln L	648.837	649.655
-2 Δln L	0.	0.818

The standard analysis is performed with 10^5 throws for both systematic and oscillation parameters but, without the reactor constrains, more throws are necessary to obtain reliable results since more freedom is given into the analysis. As a result, 10^6 throws are used here. The 1D likelihood curves obtained for the data fit are shown in figure 3.18. It illustrates the crucial role that these constraints have as the sensitivity to δ_{CP} (upper left plot) is very reduced: the χ^2 difference between the most favored and most disfavored

values in normal ordering is around 6 instead of 15. In the same way, the octant favored for $\sin\theta_{23}$ (upper right plot) is the lower one instead of the upper one and the preference is very mild compared to the fit with reactor constraints. Finally, the poor sensitivity of T2K to $\sin^2 2\theta_{13}$ (bottom plot) can be seen as the obtained likelihood distribution is very wide.

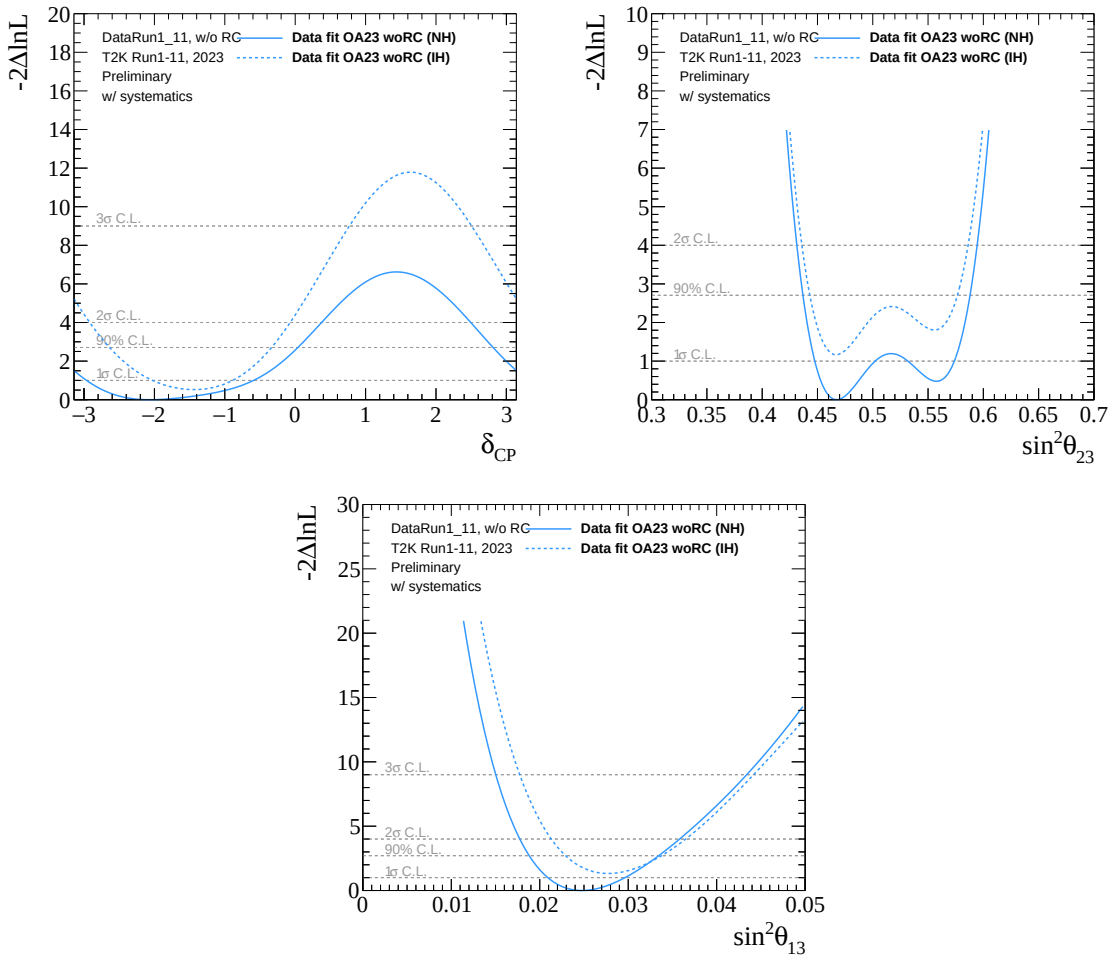

Figure 3.18. *Data fit results,* ***without*** *reactor constraints and with systematic parameters, for δ_{CP} (left), $\sin^2\theta_{23}$ (right), and $\sin^2\theta_{13}$ (bottom).*

Statistical-only analysis

As an illustration of the importance of systematic parameters in the T2K analysis, a data fit is performed without throwing them, fixing them to their best post ND fit values if they are constrained by the near detector, or their nominal value otherwise (for SK detector parameters for instance). That analysis was performed with the reactor constraints and the 1D curve results (orange) can be seen in figure 3.19 for two main parameters for which the effect is the largest: δ_{CP} (left) and $\sin^2\theta_{23}$ (right). The standard data fit with

systematics is shown in blue for comparison. The minimal χ^2 for δ_{CP} is displaced in comparison with the full analysis even-though the χ^2 values (thus the sensitivity) are more or less similar. The systematic parameters are pulling δ_{CP} towards maximal CP violation. Indeed, introducing systematic parameters aims at both suppressing biases of the analysis and adding a sensible uncertainty by providing targeted freedom in the fit, motivated by Physics (e.g.: interaction models), especially on the CP violation in order to perform the best possible measurement. Similarly, the minimal χ^2 point for $\sin^2\theta_{23}$ is slightly shifted toward lower values (0.55) and the constraint on the octant is weaker which is expected since adding systematics means adding uncertainties on the measurement.

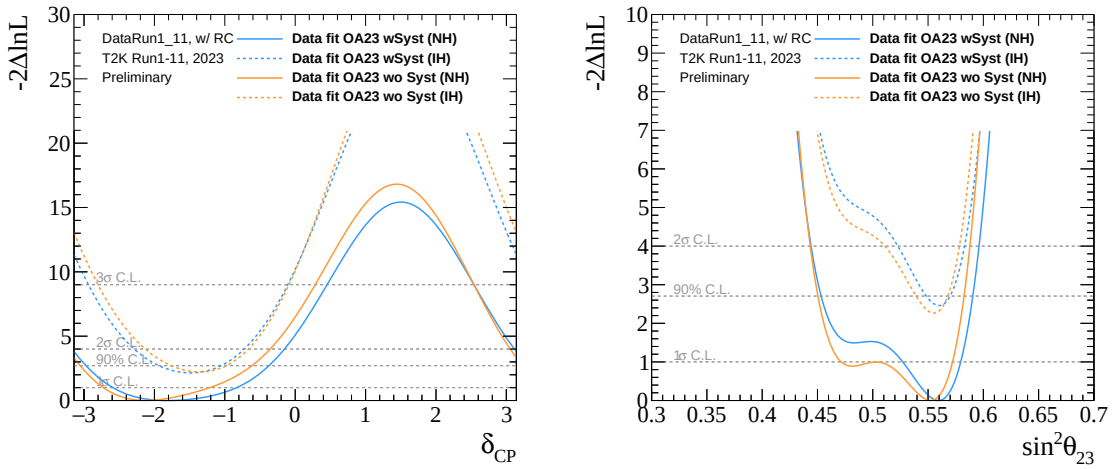

Figure 3.19. *Data fit results, with reactor constraints but* ***without*** *systematic parameters (orange), for δ_{CP} (left) and $\sin^2\theta_{23}$ (right). The blue curve is the standard data fit with systematics for comparison.*

Bi-probability plot

Another way to study the constraints we obtain on δ_{CP} and $\sin^2\theta_{23}$ is to draw so-called bi-probability plots. It simply consists in plotting the number of e-like anti-neutrino candidates as a function of the number of e-like neutrino candidates. In figure 3.20, this has been done with MC events oscillated at the OA23 best fit values (normal ordering) except for δ_{CP} and $\sin^2\theta_{23}$ which have been fixed at 4 specific values each. Each marker style represents a value of δ_{CP} and each color represents a value of $\sin^2\theta_{23}$. All points with the same value of $\sin^2\theta_{23}$ belong to an ellipse since the dominant term in δ_{CP} (when varied) is in $\sin(\delta_{CP})$ (see Chapter 1). Ellipses have been drawn to join the points. The Run 1-11 data point is also shown in fuchsia with statistical error bars (Poisson). Electron-like neutrino candidates number is computed as the sum of the events in samples 1Re and 1Re1de. This type of plot illustrates the degeneracy between CP violation and

the value of other oscillation parameters such as $\sin^2\theta_{23}$ as well as the fact that with current data, this degeneracy can not be lifted. It is therefore very important to constrain well all oscillation parameters in order to be able to perform a meaningful measurement of δ_{CP}. In addition to the bi-probability plot, actual numbers of events broken down

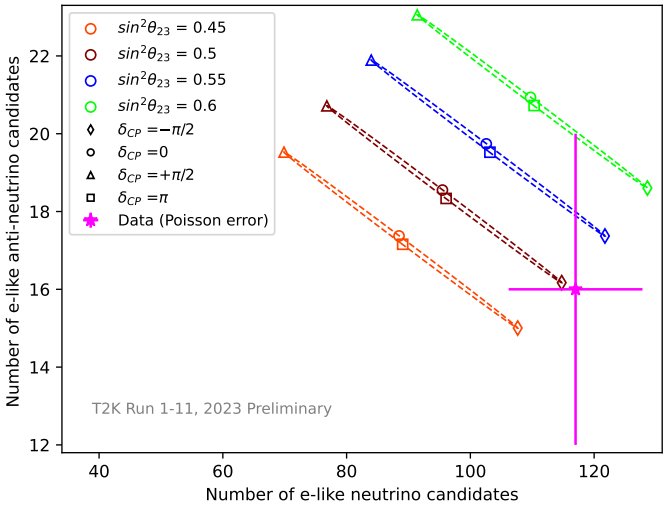

Figure 3.20. *Bi-probability plot: number of electron-like anti-neutrino candidates as a function of the number of electron-like neutrino candidates for data (fuchsia) and for Asimov at best fit predictions (Normal ordering) for various values of* $\sin^2\theta_{23}$ *(colors) and* δ_{CP} *(marker types).*

by samples can be found in Table 3.10 for various values of δ_{CP} including the best fit point $\delta_{CP} = -2.08$, other oscillation parameters at their best fit values, and systematic parameters at their best ND fit values. The last column shows the numbers of observed event in the data for comparison. It can be observe that less events than predicted have been recorded in most samples, except for the samples with a pion. This is consistent with the statistical fluctuations discussed with Figure 3.16. However, the excess in the pion samples might suggest a bias in the selection of these samples and needs to be carefully monitored and investigated by the working groups in charge.

Table 3.10. *Predicted event rates for different values of δ_{CP} including the Best fit point of this analysis, other oscillation parameters at their best fit values, and systematic parameters at their pos ND best fit values. The last column shows the numbers of observed event in the data for comparison.*

	$\delta_{CP} = -\pi/2$	$\delta_{CP} = 0$	$\delta_{CP} = \pi/2$	$\delta_{CP} = \pi$	$\delta_{CP} = -2.08$	Data
FHC 1Rμ	417.175	416.263	417.13	418.176	419.535	357
RHC 1Rμ	146.65	146.278	146.653	147.053	146.979	137
FHC 1Re	113.168	95.4898	78.3118	95.99	112.053	102
RHC 1Re	17.6271	20.0327	22.1536	19.7481	18.0458	16
ν_e1R1de	10.0463	8.78564	7.15618	8.41697	9.89284	15
$\nu_\mu$cc1π	123.889	123.349	123.863	124.411	123.318	140

3.3.2.6 Impact of the $\nu_\mu$cc1π sample

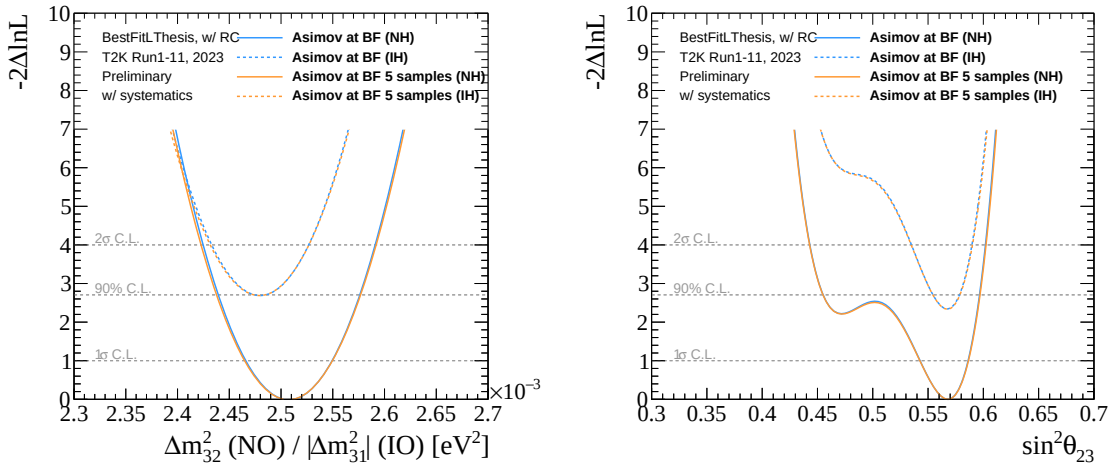

Figure 3.21. *Sensitivity at best fit, with reactor constraints and with systematic parameters, for Δm^2 (left, no smearing) and $\sin^2\theta_{23}$ (right). Comparison with (blue) and without (orange) the $\nu_\mu cc1\pi$ sample. In the legend, BF stands for Best Fit.*

An additional study was performed, using Asimov at best fit so as to assess the sensitivity performance. The analysis was run with (blue) and without (orange) the new sample from OA21: $\nu_\mu$cc1π. All other features were standard: with reactor constraints and with systematic parameters varied. The 1D likelihood curves overlaid are visible in figure 3.21 for Δm^2 (left, no smearing) and $\sin^2\theta_{23}$ (right) since these two parameters showed a small difference in the same study for OA21 [112]. As expected, no impact is observed on δ_{CP} as this sample is a so-called disappearance sample, which is not what leads the sensitivity to δ_{CP}. A very small shift in the most favored value is observable for Δm^2 and the sensitivity around 0.5 for $\sin^2\theta_{23}$ is slightly better with the $\nu_\mu$cc1π sample.

The sensitivity for Δm^2 is also very mildly improved. Even if the difference is small, it is beneficial to have this sample in order to have more muon-like events (40% increase) and to constrain associated systematic parameters. The small impact is expected as most of the reconstructed distribution for this sample is above the oscillation maximum (0.6 GeV) as it can be seen for the Asimov A22 set in figure 3.22.

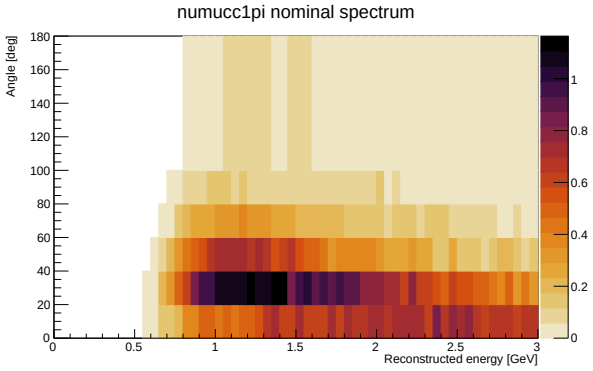

Figure 3.22. *Distribution in neutrino reconstructed energy and lepton/beam θ angle of a nominal $\nu_\mu cc1\pi$ sample oscillated with the Asimov A22 set of oscillation parameter values. The color scale indicates the number of events.*

In figure 3.23, the impact of that same $\nu_\mu$cc1π sample is assessed on the data fit. It can be observed that in that case, the impact is slightly larger compared to what has been observed on the sensitivity study. The addition of this sample improves in particular the constraint on the Δm^2 parameter.

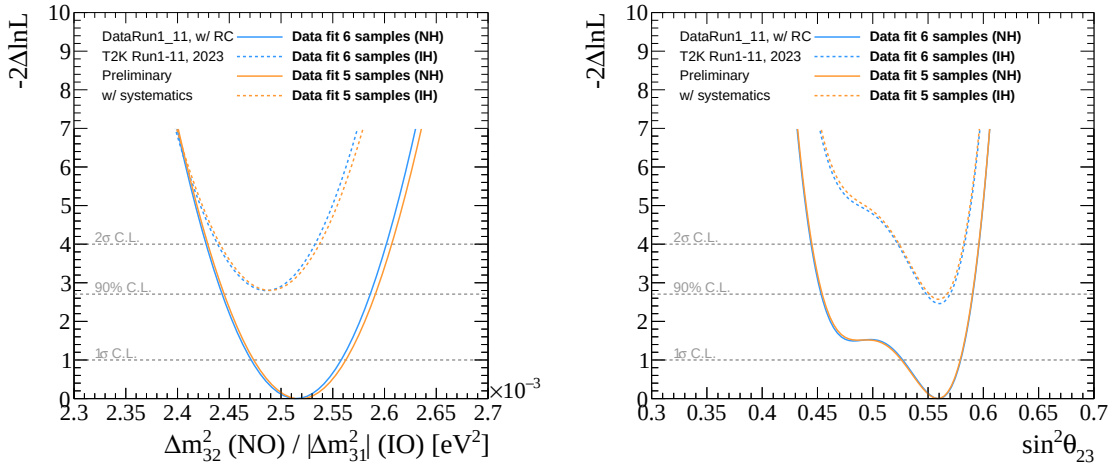

Figure 3.23. *Data fit, with reactor constraints and with systematic parameters, for Δm^2 (left, no smearing) and $\sin^2\theta_{23}$ (right). Comparison with (blue) and without (orange) the numucc1π sample*

3.3.2.7 Feldman-Cousins results

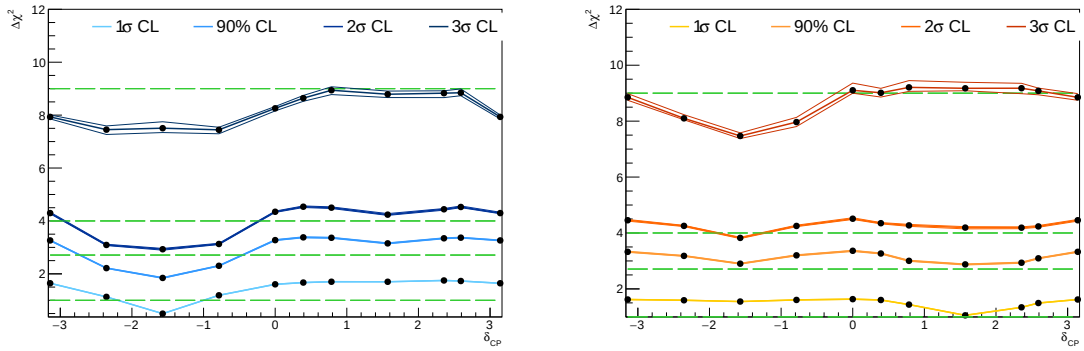

Figure 3.24. *Critical χ^2 values as a function of true δ_{CP} computed with 50000 toy experiments, for 10 values of δ_{CP}, and 4 levels of confidence. Multiple lines represent statistical error bands. Green dotted lines show the standard levels of confidence under the Gaussian assumption. Results are given for Normal (left) and Inverted (right) orderings.*

As it was introduced in 3.1.2.11, a more refined study is performed for the δ_{CP} parameter so as to interpret as accurately as possible the obtained confidence intervals. Indeed, mostly due to the cyclic nature of δ_{CP}, the Gaussian assumption for the χ^2 distribution fails and can not be used to build the confidence intervals with enough precision. This is why Feldman-Cousins (FC) studies are performed in order to compute more precise critical χ^2 values to use to build the intervals.
The results presented here were obtained with 50000 toy experiments, all other oscillation parameters were set to the data best fit value. Only the global best fit (which is in normal mass ordering) was used.
Figure 3.24 shows the critical χ^2 values as a function of δ_{CP} computed with 50000 toy experiments, for 10 values of δ_{CP}, and 4 levels of confidence . Multiple lines represent statistical error bands in relation with the number of toy experiments used. Green dotted lines show the standard levels of confidence under the Gaussian assumption. Results are given for Normal (left-hand plot) and Inverted (right-hand plot) orderings. As an illustration of the motivation for these studies, it can be seen that for most true values of δ_{CP}, the gaussian assumption (in green) for the critical values of χ^2 would be more conservative than the results from the FC studies.

The computed confidence intervals with the Feldman-Cousins studies results are summarized in Table 3.11 in terms of interval edges for the following levels of confidence: 1σ, 90%, 2σ, 3σ. It can be read that the CP conservation is still compatible with the T2K data at 3σ, but not at a bit less than 2σ, this is why, in combination with the best fit value obtained, it can be said that T2K favors a maximal violation of CP, without having yet discovered it. A full representation of results can be found in figure 3.25 where the χ^2

Table 3.11. *δ_{CP} interval edges for the 2023 data fit, computed using the Feldman-Cousins critical χ^2 values for the following levels of confidence: 1σ, 90%, 2σ, 3σ.*

Confidence level	Interval (NH)	Interval (IH)
1σ	[-2.69,-0.75]	
90%	[-3.04,-0.34]	[-2.07,-0.91]
2σ	$[-\pi,-0.13] \cup [3.06,\pi]$	[-2.34,-0.67]
3σ	$[-\pi,0.43] \cup [2.54,\pi]$	[-2.92,-0.08]

of the data fit for δ_{CP} for both normal (blue) and inverted (orange) orderings are shown together with the obtained confidence intervals. One thing that can be noticed is that there is not any 1σ interval in the inverted ordering. This is because at 1σ, T2K data rejects this ordering, the intervals being built from the global best-fit point. In the same idea, it is important to understand that narrower intervals in inverted ordering do not mean that the constraint on δ_{CP} is better in that scenario but only that it is not favored and should only be interpreted alongside the normal ordering results.

As a conclusion, FC studies are a necessary subtlety in the statistical interpretation of T2K data, in particular for the very interesting δ_{CP} parameter, in order to make the best use of the data without artificially degrading the sensitivity of the quoted results.

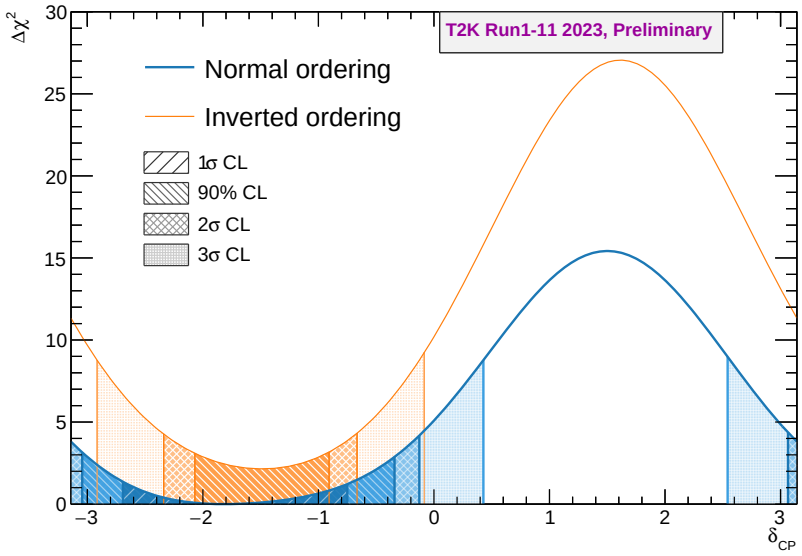

Figure 3.25. *χ^2 of the data fit for δ_{CP} for both normal (blue) and inverted (orange) orderings. The computed confidence intervals are displayed in different textures.*

Feldman-Cousins studies were also performed for $\sin^2(\theta_{23})$ as this parameter has a non-Gaussian χ^2 curve due to the fact that μ-like events constrain $\sin^2(2\theta_{23})$ whereas e-like events constrain $\sin^2(\theta_{23})$ (at 1^{st} order).

3.4 Conclusion

In this chapter, the overall oscillation analysis strategy in T2K has been described before going into the details of one particular far detector fitter: P-Theta which I have used as a main analyzer for the OA23 analysis. A small analysis on a new treatment of the removal energy systematic parameters was conducted before the main statistical update of the oscillation analysis. This extensive work on the T2K main analysis has illustrated the high level of complexity of such an analysis. The obtained results are highlighting the necessary improvements both in statistics and in reducing uncertainties so as to perform an accurate δ_{CP} measurement as well as a full characterization of neutrino oscillations. The role, impact and sophistication of the uncertainty models in T2K will be further discussed in Chapter 4. Moreover, the future experiments such as Hyper-Kamiokande, which will be introduced in Chapter 5, will aim at providing both a better understanding of uncertainties and a massive increase in collected statistics.

Chapter 4

Pushing the analysis limits: Fake data studies

This chapter will focus on the studies and actions taken in the T2K analysis to test the robustness of the analysis method and models when pushed to their limits. As it will be demonstrated, this allows to assess the behavior of the analysis with respect to some experimental or theoretical unknowns. Such studies are internally called fake data studies, based on how they are performed.

Contents

4.1 Goal and growing importance

As it has been detailed in chapter 3, the analysis relies on a flux and most importantly a cross-section model. The choice of the model, although it is a highly motivated and careful one and results from the constant work of dedicated working groups, is not absolute. There is not any unique fully satisfactory neutrino interaction model available. However, the analysis needs to be robust against the model choice so that the results are not biased by it. In particular, the systematic parameters introduced in the analysis must provide enough flexibility to 'absorb' any bias that would be due to the choice of model. This is why, in T2K, we perform a specific analysis process to quantify the impact of some model choices as well as additional effects that were not included in the model. It is a test of robustness of the analysis against alternative interaction models. As we gain more and more statistics, going into T2K-II era and preparing HK, understanding how our systematic parameters behave in case of mis-modelling and whether they are sufficient to cover all possible neutrino interaction effects that are not yet well known, is becoming more and more crucial. T2K uncertainty budget is statistically dominated for now but of course, more data is giving more importance to the systematic uncertainties.

4.2 Method

To assess this robustness, we perform Fake Data Studies (FDS). It consists in producing fake data from MC events as if the 'true' model was the alternative one we want to test. Then, these fake data are analyzed as real data, with a near detector fit passing on constraints to the far detector fit which leads to contours on oscillation parameters. The BANFF is used for the near detector fit with a cross-check with MaCh3. The far detector fit is performed by P-Theta because it has the ability to run several analyses in a reasonable time frame. In general, the fake data is produced by reweighting the MC events, weights being produced by the neutrino interaction experts, and accessed with the dedicated T2KReweight software. The general flow of the process is represented in Figure 4.1.

For each fake data study, two sets of Asimov points, meaning for oscillation parameter values, is used to create the fake data: Asimov A22 and Asimov B22 which have both been described in chapter 3. The exact value used can be found in table 3.7. This is so as to fully test the robustness of the analysis, avoiding biases from previous results as much as possible.

One technical detail to note on the method is that for some studies, some systematic parameters interfering with what is being tested need to be set to specific values in order for the study to make sense.

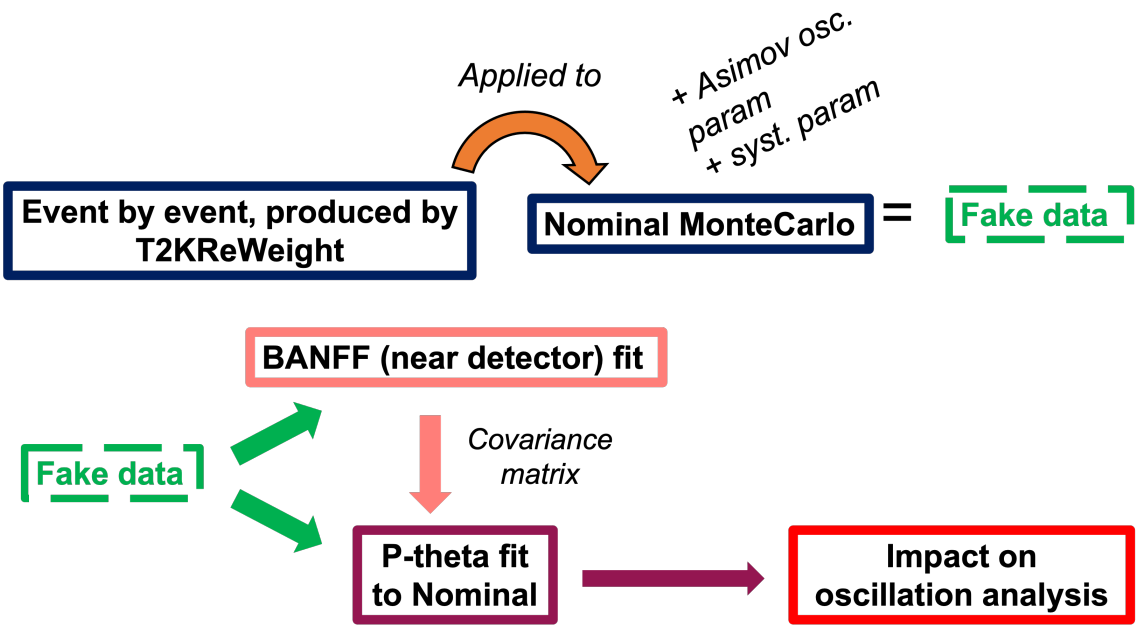

Figure 4.1. *Flow chart of the fake data studies process*

A second round of analyses was performed for each identified FDS. For this, each predicted spectra was reweighted to the total number of events inside the fake data instead of performing the standard fit of the fake data against the usual nominal spectra whose statistics depend on the POT and oscillation and systematic parameters. In the collaboration jargon, we call this "scaled Asimov fits". The idea here is that the reweighting of events to produce the fake data can in some cases change the total number of events. This change of statistics will affect the oscillation analysis results but this is not the effect we are trying to quantify here. This is why re-scaling the predicted spectra in the fit allows to isolate the impact of the studied item. Both standard and scaled fits were performed for each FDS. However, it is not relevant to use scaled Asimov in the case that the ND fit predictions do not reproduce well the fake data because in that case discrepancies in statistics can also come from that disagreement and should not be re-scaled.
The Fake Data Studies were run for the so-called OA 2021/22 analysis, meaning before the statistical update and were not rerun when the Run 11 data was added as the cross-section model was not modified at all in between. I ran about half of the established list of FDS on the far detector side with P-Theta.

4.3 List of studies

The FDS that were performed for OA 2021 can be divided into several categories: alternative nuclear models, alternative interaction model, processes involved in presence of a pion in the final state, radiative corrections and data driven studies. Moreover, I performed a fake data study to test the consequences of using a different value for the α parameter discussed in section 3.2.3. Here is the full list of primary study names, each of them will be explained in following subsections, not always in details as producing the fake data studies is the work of neutrino cross-section experts and was not one of my tasks for my thesis work.

- Low Q^2
- Data driven 1 pion: SPP Adversarial
- Radiative corrections
- Pion kinematics = 2 studies
- Extremal removal energy value
- Non-QE
- Continuous Random Phase Approximation (CRPA) model
- Local Fermi Gas (LFG) model
- Alternative Form factors (Z-expansion and 3-components) = 6 studies
- Martini model
- Interpolation for removal energy value

The work was shared with another analyser whom I thank, and as a result I ran myself the studies for the 7 first items of the above list and participated in two additional studies which will be mentioned at the end of this chapter. The following subsections will provide a description and motivation for each FDS except the two that will be detailed in the next section: CRPA and Radiative corrections.
A full summary of the obtained final results will be given in section 4.4.3. A detailed T2K internal technical note (TN441) presents a comprehensive list of all results for all studies.

4.3.1 Low Q^2

Q^2 is the squared 4-momentum transfer in the neutrino/nucleon interaction. This study introduces a suppression of order 20% of single pion production in the final state for low values of Q^2 ($<$1 GeV^2). This correction would address the data/model discrepancy observed in the MINERVνA experiment [113]. However, they had been using the event generator GENIE [114] whereas T2K uses, for its MC production, a dedicated generator called NEUT [115] which was developed by collaborators. It was later shown that NEUT and even more recent versions of GENIE do not produce such a discrepancy in pion production at low Q^2 [116]. This study is still performed as an extreme check of whether our analysis would be able to deal with such unlikely anomalies.

4.3.2 Data driven 1 pion: SPP Adversarial

It consists in taking into account the pion kinematics in the final state for the 1 electron-like ring and 1 decay electron (1Re1de) sample at the far detector. This study is data-driven as it is motivated and constructed from an observed discrepancy in the ND280 data. Indeed the selection for this sample does not take into account the kinematics of the pion, but the efficiency of the selection does depend on it. This study is not a new one but has been updated since the previous analysis. The weights to produce the fake data, which are therefore a function of the pion momentum, have now been calculated from the ND280 data/MC differences in a refined way, separating the pions detected in TPC, FGD or those for which the decay electron (Michel electron) was successfully tagged.

4.3.3 Pion kinematics

This is a new study. A specific care is given to studying pion related effects in this new analysis because of the introduction of the new Numucc1pi analysis sample. Motivated by this sample, a new systematic parameter was introduced in the analysis, representing the uncertainty on the shape of the pion and nucleon kinematics in pion production, leaving the lepton kinematics unchanged. However, there are two ways to introduce this uncertainty, either playing on the ejection mechanism, meaning the way the resonance state produces the pion/nucleon system in the final state, or changing the matrix element values for the $^{1232}\Delta$ resonance. It was chosen to implement the first systematic uncertainty, which does not fix the resonance to a specific state. These fake data studies however explore the other solution of using instead different matrix elements with uncertainties fixed to $+3\sigma$ and -3σ, turning off the chosen uncertainty in the regular analysis.

4.3.4 Extremal removal energy value

This study simply consists in changing the removal energy (E_b) of Oxygen value to an extreme value of 15 MeV instead of the nominal 27 MeV. In that sense, there is no reweighting produced by T2KReWeight software but only the change of value at the level of producing the fake data spectra in reconstructed variable as this is where the removal energy plays a role, as it has been explained in section 3.2.3. The simple goal of this study is to check that the current uncertainties on E_b can cover even an extremal variation of E_b without inferring strong biases in the oscillation analysis. From previous analysis it is expected to indeed not have a large impact on the oscillation parameters constraints.

4.3.5 Non-QE

In the analysis, we have systematic parameters that give a fair amount of freedom to the 4-momentum value (Q^2) in the case of CCQE interaction for CC0π samples in order to cover observed data/model differences in the near detector fit. However, subdominant non quasi-elastic (non-QE) interaction modes (such as 2p2h or pion absorption) participate to populating the CC0π samples but do not possess specific associated systematic parameters giving this type of freedom on the Q^2 value. This is because of a lack of theoretical knowledge on those processes. As a result, there is a possibility that the CCQE Q^2 systematic parameters absorb some variations of the non-QE processes, biasing the analysis. This study aims at quantifying this possibility and testing the robustness of the analysis against it by attributing all of the necessary freedom to reconcile data and model to the non-QE contributions instead of the CCQE ones. This is once again an extreme test which is the idea of FDS: pushing the limits of the analysis.

4.3.6 Local Fermi Gas (LFG) model

The CCQE interaction is the dominant one and as expected the systematic uncertainty on this interaction is also the dominant cross-section uncertainty. The model for the nucleus in its initial state, before neutrino interaction, that is used in the regular analysis is Spectral Functions (SF). It takes individual nucleon-nucleon interactions into account, using a shell model for the nucleus. However, there is no satisfactory model to match all the different types of existing data and the choice of model can impact the dependence of the cross-section on the neutrino energy, and cross-sections differences between neutrino/antineutrinos, carbon/oxygen, and electron/muon. A simpler but still very common alternative model for CCQE is the Local Fermi Gas model which parameterizes a local nuclear matter density depending on the distance to the center of the nucleus. It has been established with electron scattering data. It can include an overall nuclear

screening accounting for long range nucleon-nucleon interaction, through the Random Phase Approximation (RPA) method, in which case the model can be called LFG+RPA [117]. This FDS is therefore assessing the bias on oscillation analysis if the "true" model should be LFG+RPA, since we are fitting data to the Spectral function model.

4.3.7 Alternative Form factors (Z-expansion and 3-components)

One element that plays an important role in the calculation of cross-sections are the form factors of the interacting nucleon which basically represent the charge distribution of the nucleon; in particular vector form factors account for the electric and magnetic charge distribution and are a probe for the nucleon radius whereas axial form factors account for weak charge distribution and as such are crucial to neutrino interaction. In general, based on theoretical assumptions and due to lack of data, axial form factors are considered to have a simple dipole distribution. Because this does not allow to account for the experimental uncertainty observed, systematic parameters have been introduced separately at low and high Q^2 values. To test the robustness of those parameters against different axial form factor distributions, those fake data studies are performed, reweighting the data to other than dipole-like distributions, namely Z-expansion and 3-components model. Both are tested at 3 value points, raising the total number of such FDS to 6.

4.3.8 Martini model

This fake data study is similar to the LFG one in the sense that it consists in testing an alternative CCQE cross-section model: the Martini et al. model [118]. This model is the most complete available as it allows, through the nuclear response functions and RPA approach, to include both quasi elastic mechanism and delta resonance so that it can also predict pion production and npnh processes (ie: processes with several (n) bound nucleons interacting).

4.3.9 Interpolation for removal energy value

To extract the weights associated with removal energy variations at the near detector fit (BANFF), both linear or cubic interpolation can be used. To ensure that this choice does not introduce any major bias as the removal energy plays a crucial role in reconstructing the neutrino energy, two fake data studies were performed. One is using the best fit points for oscillation parameters found with linear interpolation and is fitting it with cubic interpolation and the other way around. This is done only at the near detector side and then simply propagated at the far detector, meaning that the far detector treatment of E_b is not modified at any point in those studies. The standard interpolation used in

the analysis is the linear one. This study is therefore testing the impact of a technical implementation choice, not a physics model choice: this is another use that FDS can have.

4.4 Results and applied biases

In this section, we will go through a typical FDS that I ran, step by step, describing all results that can be shown, then a slightly different FDS will be presented before a full summary of all results.

4.4.1 A typical FDS: detailed results for CRPA

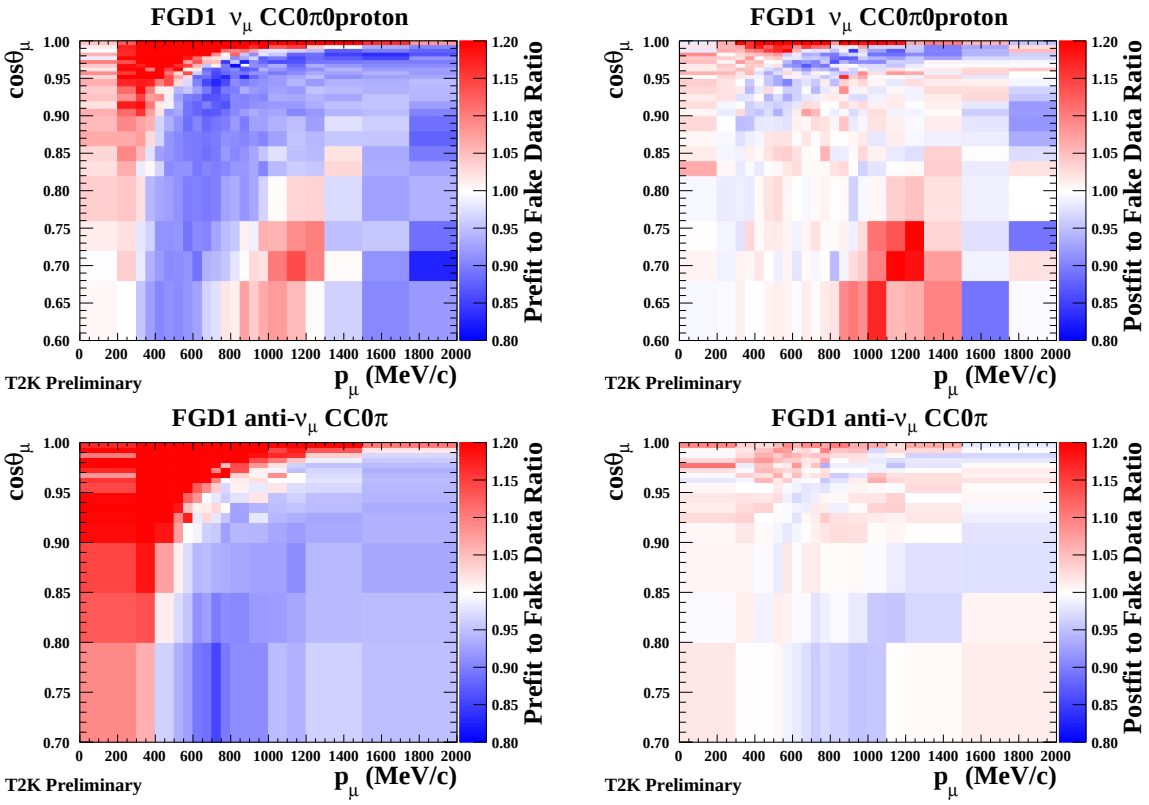

Figure 4.2. *Pre- and post-fit ratios to the CRPA FDS for the FGD1 ν_μ CC0π0p0γ (top row) and $\bar{\nu}_\mu$CC0π (bottom row) samples.*

This study is also testing an alternative cross-section model to Spectral functions: the Hartree-Fock Continuous Random Phase Approximation (HF + CRPA) model [119]. This model predicts significantly different cross-sections at low Q^2 and momentum compared to SF or LFG models and is successful in reproducing electron scattering data. In particular, it treats the final state nucleon wave function with distortions which is a significant difference to other models which use plane waves. This is of course a strong motivation to perform a fake data study, reweighting the fake data as if that alternative model were the

"true" one in Nature.

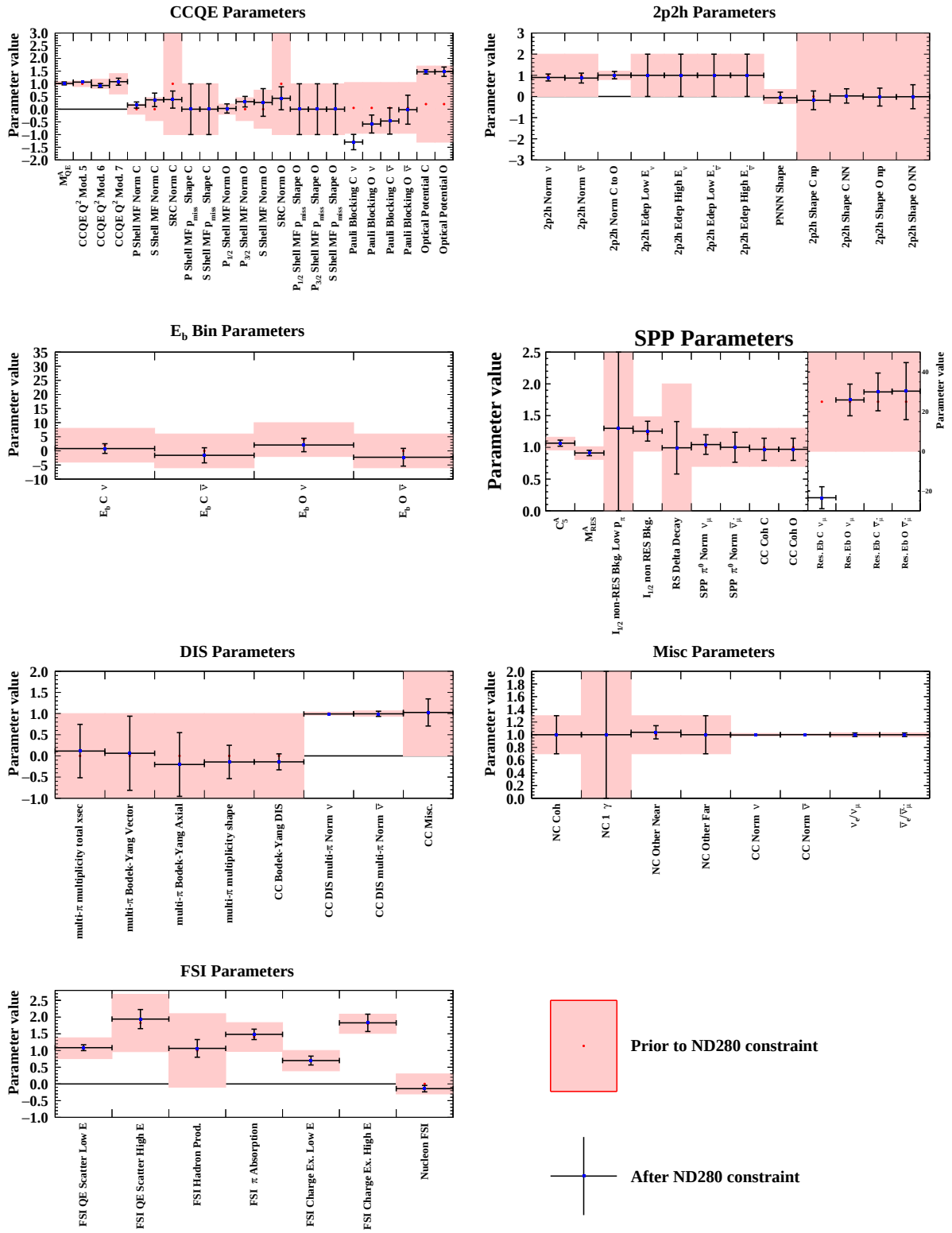

Figure 4.3. *Pre- (red band) and post-fit (blue dots and black error bars) cross-section parameters from the* `BANFF` *fit to CRPA FDS.*

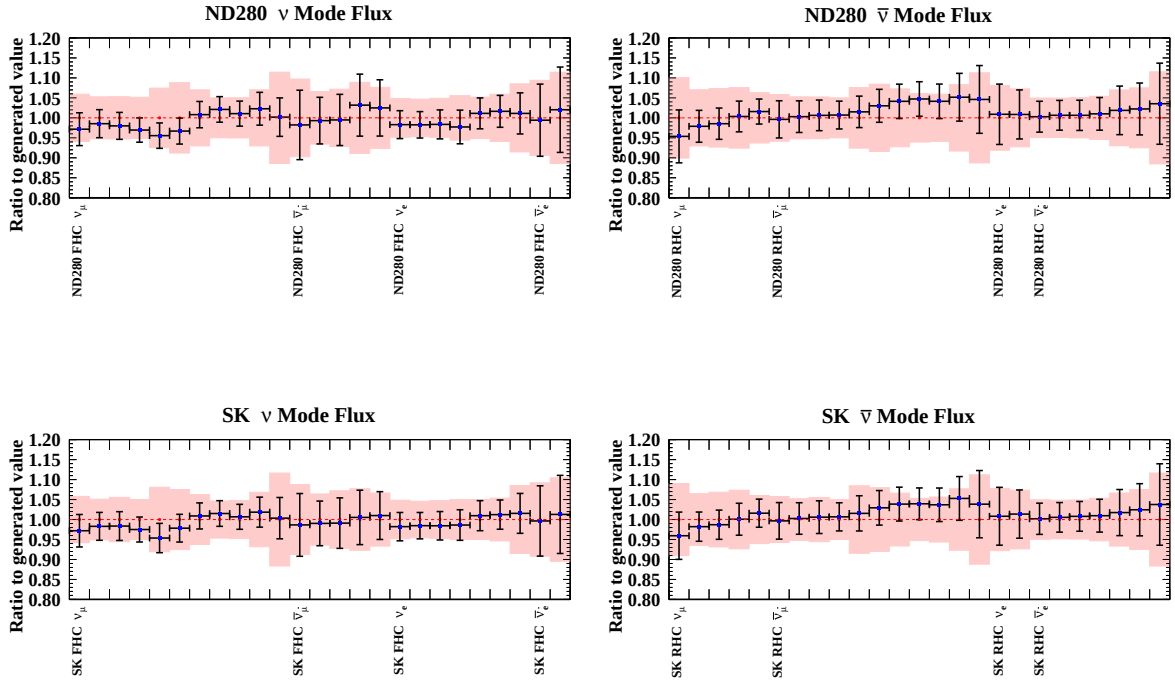

Figure 4.4. *Pre- (red band) and post-fit (blue dots and black error bars) flux parameters from the* ***BANFF*** *fit to CRPA FDS. Inside each sample category, the parameters are ordered from left to right by increasing energy range. Legend in 4.3.*

As a reminder the fake data is first produced and fitted at the near detector.
The effect of the reweighing on the near detector side on the FGD1 ν_μ CC0π0p0γ sample can be seen in figure 4.2 which presents the 2D distribution of events in the muon cos(θ) versus muon momentum plane. More precisely, the color scale shows the ratio of the fit result over the fake data. The top plots show the results for neutrinos and the bottom plots for anti-neutrinos. The left plots show the ratio between pre-BANFF fit and reweighted data and the right plots the ratio between the post-fit distribution and that of the reweighted data. It can be seen in the pre-fit plots that the effect of the reweight is to increase the number of events (as a result of increasing the cross-section) at high momentum and decrease it at low momentum. It is also possible to see that after the fit, the effect of the reweight seems to have been mostly absorbed by the systematic parameters.
A bit more in detail, the result of the ND fit shows in figure 4.3 that the systematic cross-section parameters that have an impact on the CCQE cross-section at low Q^2, namely Optical Potential and Pauli Blocking, are the ones that have absorbed the differences between the fake data model and the fit model as their post fit best value (blue dot) is displaced from the prior central value (red dot). Moreover, the flux parameters impacting

the lower energies have been moved a bit by the fit from their prior value so as to absorb the differences as can be seen in figure 4.4.

As a partial conclusion, it can be said from the near detector fit results that T2K systematics model seem to be able to cope with the CRPA alternative CCQE cross-section model. The next step is to apply those ND fit results and the fake data at the far detector to confirm the conclusion and quantify the bias on the oscillation parameters constraints. The first step of the far detector analysis is to produce the fake data spectra as a function of the neutrino reconstructed energy for each of the 6 SK analysis samples. It can be reminded here that the fit is performed for two sets of oscillation parameters A22 and B22 (see table 3.7). In figure 4.5, the comparison between fake data spectra in green, the nominal ones in blue (Asimov data, non reweighted fake data) and the BANFF prediction with error bands in red is shown for the Asimov set A22. Figure 4.6 is the same for the B22 set. As expected by the cross-section model experts, the most impacted part of the spectra is the one around 0.5 GeV for the muon one ring samples [**CRPA1**, **CRPA2**]. Full agreement is not observed between BANFF prediction and the fake data at the FD, possibly due to a change in the total number of events by the reweighting or the complexity of the reweighting for that particular study. Those conclusions apply to both A22 and B22 Asimov sets.

The fit at the far detector, by P-Theta, allows to obtain constraints on the oscillation parameters, in particular δ_{CP}, Δm^2 and $\sin^2\theta_{23}$, for both sets of oscillation parameters and for both standard and 'scaled' Asimov FDS fits as explained in section 4.2, applying reactor constraints in all cases. The 1D likelihood χ^2 distributions are shown in figure 4.7 for A22 and 4.8 for B22. The dotted lines are for the inverted hierarchy case, the solid ones for the normal hierarchy. Light blue represents the results for nominal (= Asimov data, non reweighted fake data) for comparison, the orange is the standard fake data fit and the dark blue is scaled Asimov fake data fit. The confidence levels are the standard one under Gaussian assumption, not the ones computed from the Feldman-Cousins procedure. It can be observed that without re-scaling the model to the new reweighted statistics (ie performed scaled Asimov fits), the shift is very large. This study is in fact specifically sensitive to this effect. This illustrates the need for scaled Asimov fits to disentangle the change of overall statistics with the effect of the reweighting in the shape of spectra. The shift in Δm^2 and $\sin\theta_{23}$ is however still visible in the dark blue curve and will be quantified as one of the last steps of the fake data analysis. Another visualization is given by 2D contours at 68%, 90% and 99.7% in figures 4.9 and 4.10 for Asimov A22 and B22 respectively.

Once those fit results are obtained, the effect of the FDS on $\sin^2\theta_{23}$, Δm^2_{32} and δ_{CP} can be quantified by computing the shifts in confidence intervals lengths and centers. The fits have actually all been performed in both "statistics only" mode and "full systematics"

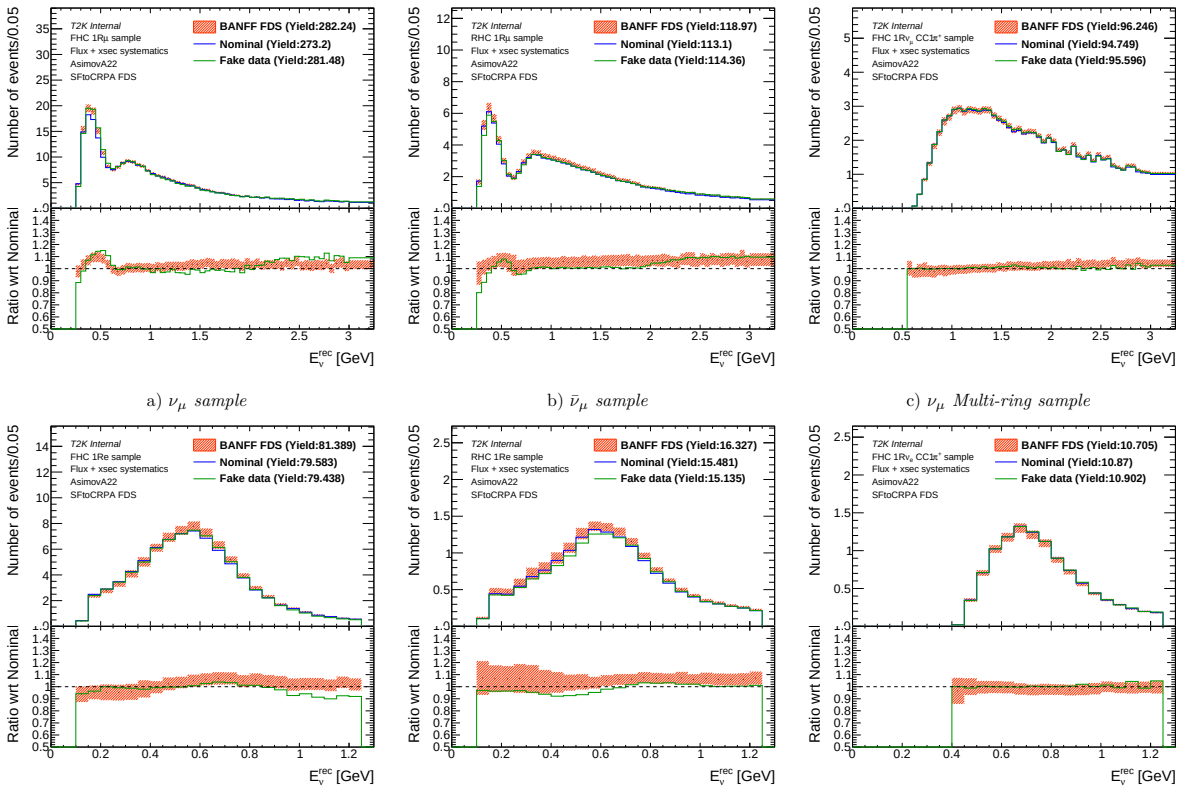

a) ν_μ *sample* b) $\bar{\nu}_\mu$ *sample* c) ν_μ *Multi-ring sample*

d) ν_e *sample* e) $\bar{\nu}_e$ *sample* f) ν_e *1 d.e. sample*

Figure 4.5. *Comparison between the nominal SK samples (blue solid line), the SK fake data for Asimov A22 (green solid line), and the prediction from the* **BANFF** *fit to the CRPA FDS (red band).*

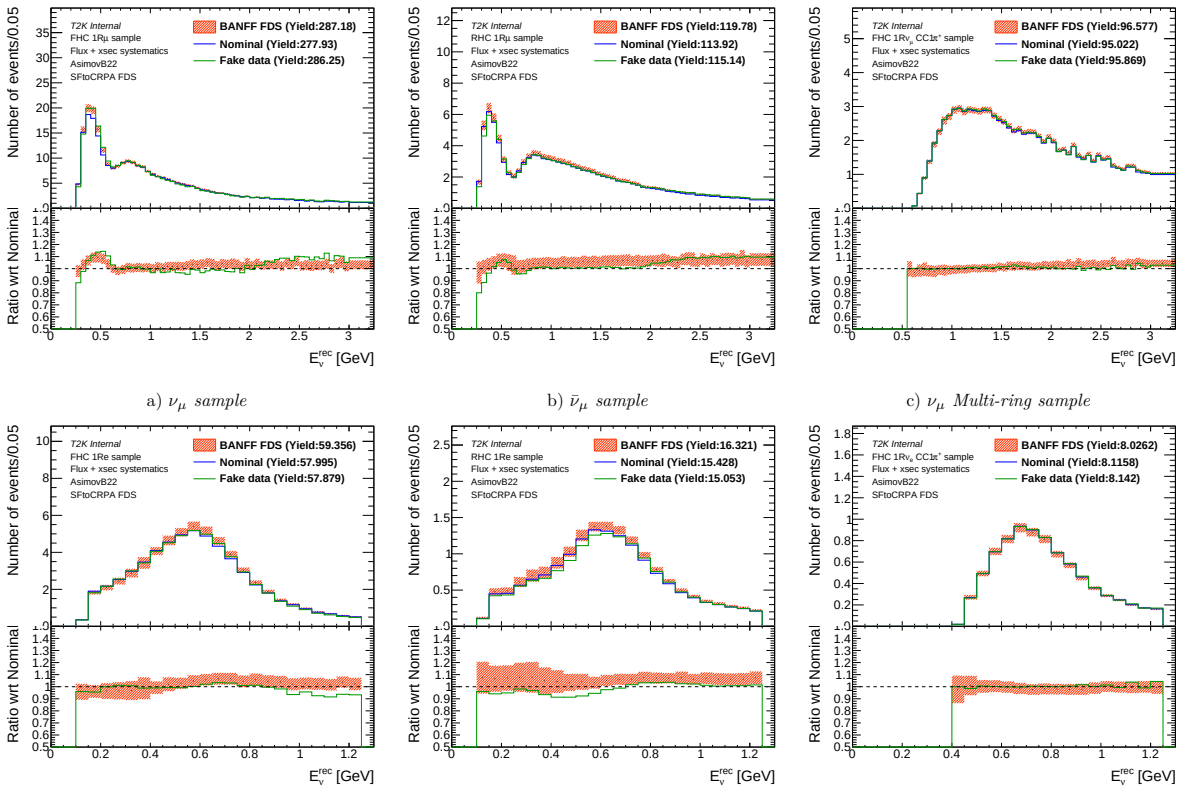

a) ν_μ *sample* b) $\bar{\nu}_\mu$ *sample* c) ν_μ *Multi-ring sample*

d) ν_e *sample* e) $\bar{\nu}_e$ *sample* f) ν_e *1 d.e. sample*

Figure 4.6. *Comparison between the nominal SK samples (blue solid line), the SK fake data for Asimov B22 (green solid line), and the prediction from the* **BANFF** *fit to the CRPA FDS (red band).*

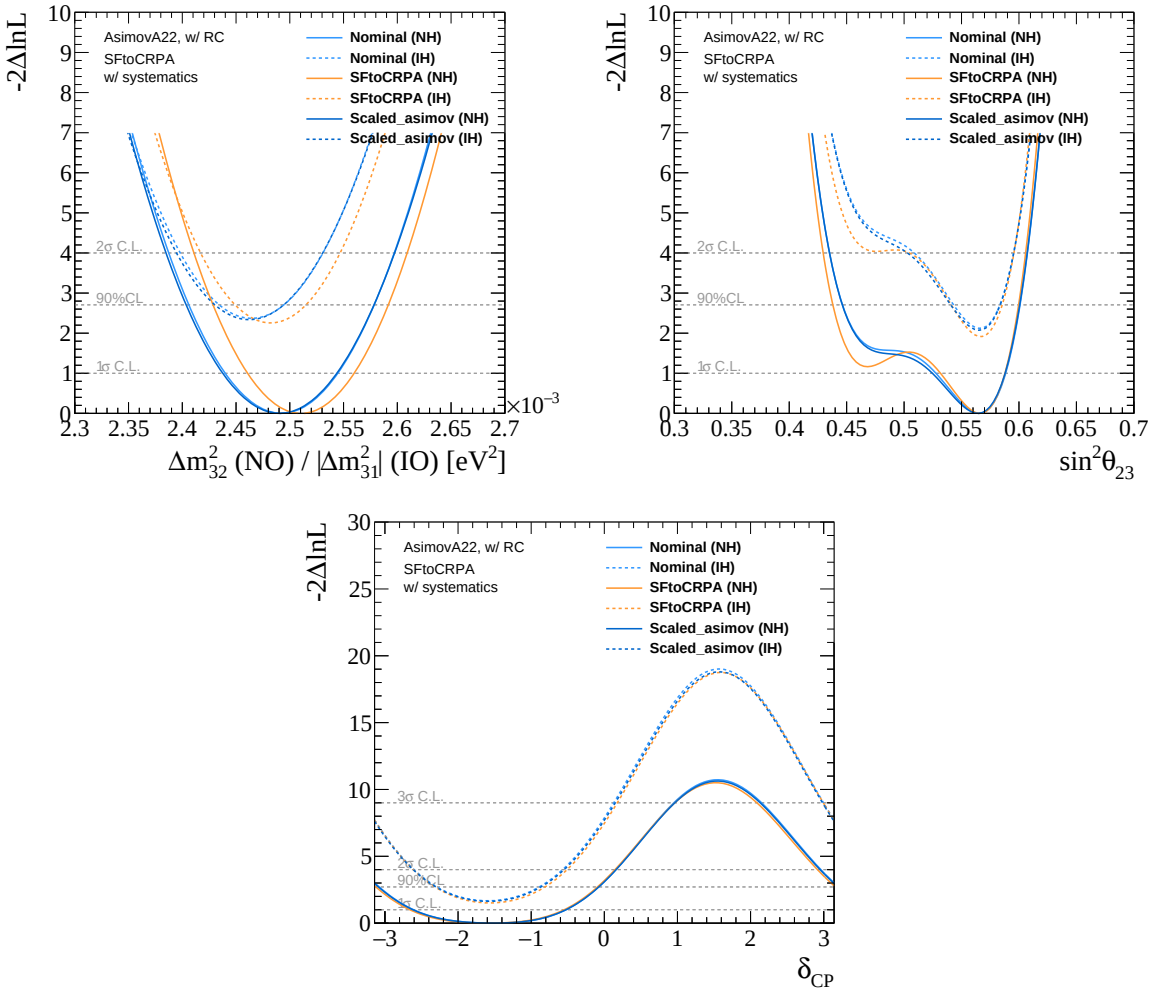

Figure 4.7. *1-D likelihood surfaces for* Δm^2 *(top left),* $\sin^2\theta_{23}$ *(top right) and* δ_{CP} *(bottom), with the reactor constraint on* $\sin^2\theta_{13}$*, for both normal (solid line) and inverted (dashed) ordering, for the CRPA FDS and Asimov A22. The* $\Delta\chi^2$ *curves of the Asimov fit, FDS and scaled Asimov are reported in blue, orange and dark blue respectively.*

mode meaning with and without applying the systematic parameters. This allows to perform subtractions to cancel out the effect of the statistical uncertainty since we are trying to test the systematic model limits and robustness. All possible quantification of the FDS effect are summarized in table 4.1 for the standard fit and 4.2 for the scaled Asimov fit with the values of interest, which will be presented in section 4.4.3, written in blue.

The conclusions to draw from those values will be detailed in the next section 4.4.3. Because the intervals on δ_{CP} are the most critical in terms of result and present a likelihood which is non Gaussian and so very sensitive to shape shifts, an additional analysis of the FDS fit result is done in the case of normal hierarchy and Asimov A22 for the fake data (as it is the most favored scenario). The results presented before were compared to a nominal spectra, meaning an Asimov fit, not a data fit. For δ_{CP}, we compare the interval

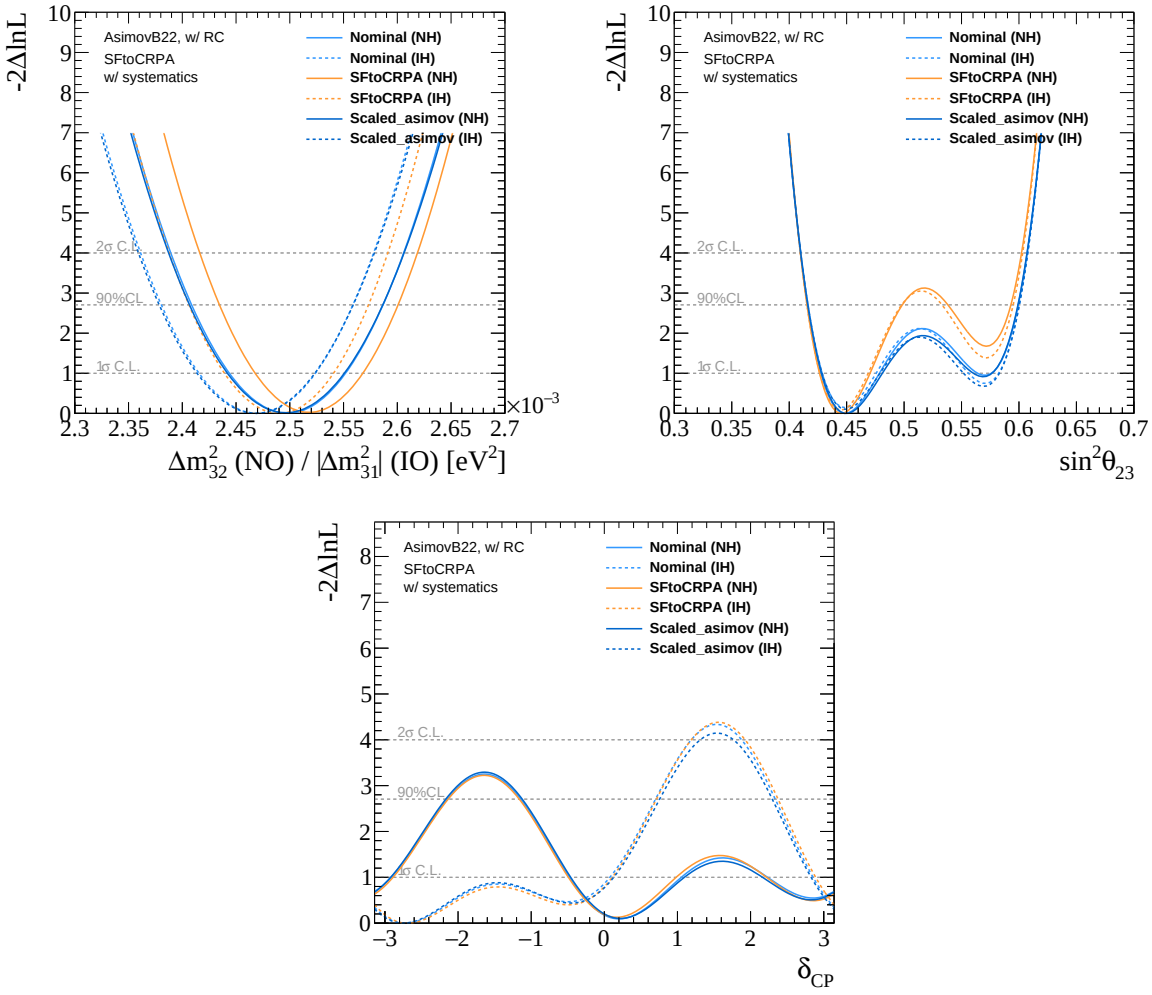

Figure 4.8. *1-D likelihood surfaces for* Δm^2 *(top left),* $\sin^2\theta_{23}$ *(top right) and* δ_{CP} *(bottom), with the reactor constraint on* $\sin^2\theta_{13}$*, for both normal (solid line) and inverted (dashed) ordering, for the CRPA FDS and Asimov B22. The* $\Delta\chi^2$ *curves of the Asimov fit, FDS and scaled Asimov are reported in blue, orange and dark blue respectively.*

edges with the one found for the data fit as can be seen in tables 4.3 and 4.4 for standard and scaled Asimov fits.

For δ_{CP}, because it is our main result and because, being a cyclic parameter, its quoted intervals can be more sensitive to shifts, the effect of the FDS on data is estimated by applying the computed $\Delta\chi^2$ shift to the data. The $\Delta\chi^2$ distributions of the official data fit and data fit with the FDS shift applied are also plotted against each other, together with the critical χ^2 values extracted from the Feldman-Cousins study in the left plots of figures 4.11 and 4.12 for respectively standard and scaled Asimov FDS fits; while in the right plots, the computed FDS shift $\chi^2_{Nom} - \chi^2_{FDS}$ for the CRPA study is plotted as a visual representation of the tables 4.3 and 4.4. No significant shift was found to change our conclusions on δ_{CP}.

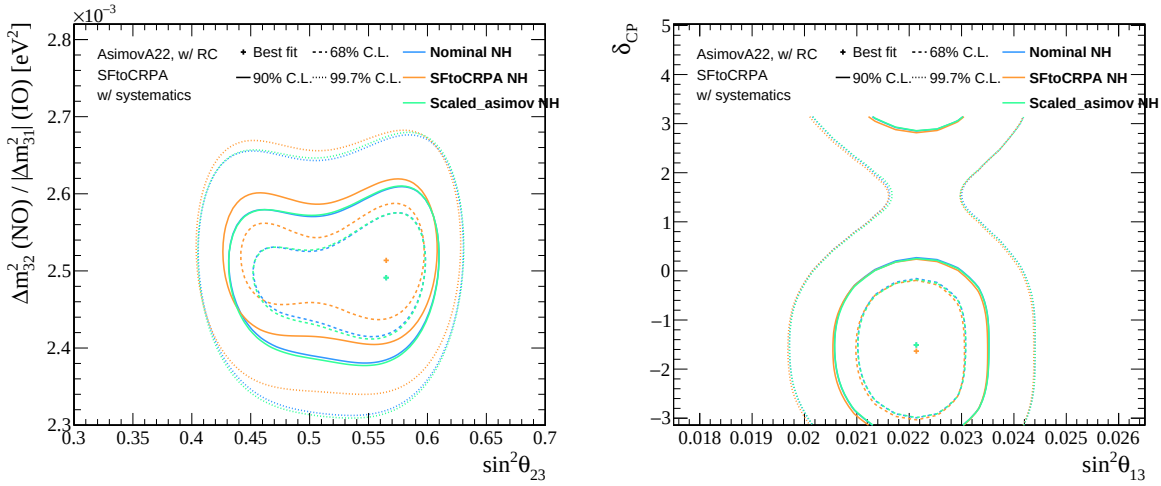

Figure 4.9. *2D likelihood surfaces in the $\Delta m^2/\sin^2\theta_{23}$ (left) and $\sin^2\theta_{13}$ /δ_{CP}(right) planes with the reactor constraint on $\sin\theta_{13}$, for normal ordering, for the CRPA FDS and Asimov A22. The contours of the Asimov fit, FDS and scaled Asimov are reported in blue, orange and green respectively.*

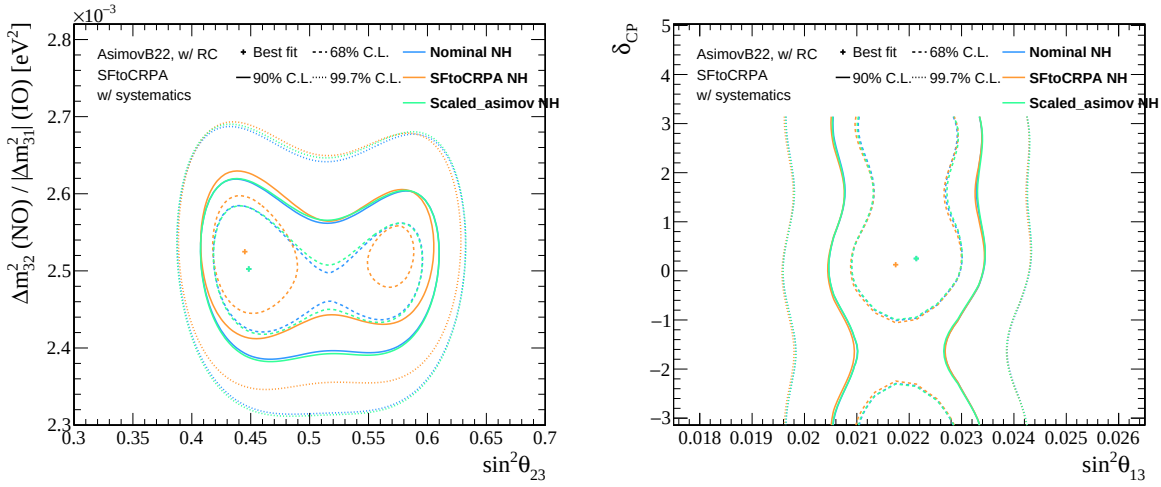

Figure 4.10. *2D likelihood surfaces in the $\Delta m^2/\sin^2\theta_{23}$ (left) and $\sin^2\theta_{13}$ /δ_{CP}(right) planes with the reactor constraint on $\sin\theta_{13}$, for normal ordering, for the CRPA FDS and Asimov B22. The contours of the Asimov fit, FDS and scaled Asimov are reported in blue, orange and green respectively.*

Table 4.1. *Table of the bias for the CRPA FDS for both Asimov sets. For Asimov B22, results at the lower and upper octant minima are shown.*

		$\sin^2\theta_{23}$	Δm^2_{32}	δ_{CP}
AsimovA22	Middle of the 1σ interval	0.5597	0.0025103	-1.604
	1σ interval size: 1σ	0.028	4.96e-05	1.06
	1σ interval ratio to Nominal	0.924	0.946	1.01
	Fractional change in the 1σ interval size wrt the syst interval: $\left(1\sigma^{\text{FDS}}_{\text{tot.}} - 1\sigma^{\text{ref}}_{\text{tot.}}\right)/1\sigma^{\text{ref}}_{\text{syst.}}$	-16.3%	-13.5%	5.1%
	Bias in the middle of 1σ interval wrt the size of the $1\sigma^{\text{ref}}_{\text{tot.}}$ interval	5.52%	34.4%	-3.65%
	Bias in the middle of 1σ interval wrt the size of the $1\sigma^{\text{ref}}_{\text{syst.}}$ interval	11.9%	86.4%	-14.7%
	Middle of the 2σ interval	0.5177	0.00251	-1.611
	2σ interval size: 2σ	0.0881	9.92e-05	1.76
	2σ interval ratio to Nominal	1.02	0.946	1.01
	Fractional change in the 2σ interval size wrt the syst interval: $\left(2\sigma^{\text{FDS}}_{\text{tot.}} - 2\sigma^{\text{ref}}_{\text{tot.}}\right)/2\sigma^{\text{ref}}_{\text{syst.}}$	6.91%	-13.6%	3.7%
	Bias in the middle of 2σ interval wrt the size of the $2\sigma^{\text{ref}}_{\text{tot.}}$ interval	-4.11%	16.9%	-1.66%
	Bias in the middle of 2σ interval wrt the size of the $2\sigma^{\text{ref}}_{\text{syst.}}$ interval	-12.1%	42.3%	-6.2%
	Bias in the middle of 2σ interval wrt the size of the $1\sigma^{\text{ref}}_{\text{tot.}}$ interval	-11.7%	33.8%	-2.78%
	Bias in the middle of 2σ interval wrt the size of the $1\sigma^{\text{ref}}_{\text{syst.}}$ interval	-25.1%	84.9%	-11.2%
AsimovB22	Middle of the 1σ interval	0.4484	0.0025178	0.2676 and 2.784
	1σ interval size: 1σ	0.022	5.09e-05	0.812 and 0.678
	1σ interval ratio to Nominal	0.863	0.936	0.987 and 1.06
	Fractional change in the 1σ interval size wrt the syst interval: $\left(1\sigma^{\text{FDS}}_{\text{tot.}} - 1\sigma^{\text{ref}}_{\text{tot.}}\right)/1\sigma^{\text{ref}}_{\text{syst.}}$	-35.6%	-15.8%	-4.49% and 29.6%
	Bias in the middle of 1σ interval wrt the size of the $1\sigma^{\text{ref}}_{\text{tot.}}$ interval	-18.5%	36.9%	-4.66% and 0.358%
	Bias in the middle of 1σ interval wrt the size of the $1\sigma^{\text{ref}}_{\text{syst.}}$ interval	-48%	91.6%	-15.9% and 1.77%
	Middle of the 2σ interval	0.506	0.0025175	0
	2σ interval size: 2σ	0.0963	0.000102	3.14
	2σ interval ratio to Nominal	0.975	0.937	1
	Fractional change in the 2σ interval size wrt the syst interval: $\left(2\sigma^{\text{FDS}}_{\text{tot.}} - 2\sigma^{\text{ref}}_{\text{tot.}}\right)/2\sigma^{\text{ref}}_{\text{syst.}}$	-8.09%	-15.6%	
	Bias in the middle of 2σ interval wrt the size of the $2\sigma^{\text{ref}}_{\text{tot.}}$ interval	-2.52%	18.3%	0%
	Bias in the middle of 2σ interval wrt the size of the $2\sigma^{\text{ref}}_{\text{syst.}}$ interval	-8.26%	45.6%	
	Bias in the middle of 2σ interval wrt the size of the $1\sigma^{\text{ref}}_{\text{tot.}}$ interval	-9.75%	36.6%	0%
	Bias in the middle of 2σ interval wrt the size of the $1\sigma^{\text{ref}}_{\text{syst.}}$ interval	-25.3%	90.8%	0%

Table 4.2. *Table of the bias for the CRPA FDS for both Asimov sets when the* ***scaled Asimov method*** *is used. For Asimov B22, results at the lower and upper octant minima are shown.*

		$\sin^2\theta_{23}$	Δm^2_{32}	δ_{CP}
AsimovA22	Middle of the 1σ interval	0.5597	0.0025103	-1.604
	1σ interval size: 1σ	0.028	4.96e-05	1.06
	1σ interval ratio to Nominal	0.886	0.934	1.01
	Fractional change in the 1σ interval size wrt the syst interval: $\left(1\sigma^{\mathrm{FDS}}_{\mathrm{tot.}} - 1\sigma^{\mathrm{ref}}_{\mathrm{tot.}}\right)/1\sigma^{\mathrm{ref}}_{\mathrm{syst.}}$	-22.5%	-16.9%	3.44%
	Bias in the middle of 1σ interval wrt the size of the $1\sigma^{\mathrm{ref}}_{\mathrm{tot.}}$ interval	11%	36.9%	-3.15%
	Bias in the middle of 1σ interval wrt the size of the $1\sigma^{\mathrm{ref}}_{\mathrm{syst.}}$ interval	21.6%	94.3%	-12.4%
	Middle of the 2σ interval	0.5177	0.00251	-1.611
	2σ interval size: 2σ	0.0881	9.92e-05	1.76
	2σ interval ratio to Nominal	1.02	0.933	1.01
	Fractional change in the 2σ interval size wrt the syst interval: $\left(2\sigma^{\mathrm{FDS}}_{\mathrm{tot.}} - 2\sigma^{\mathrm{ref}}_{\mathrm{tot.}}\right)/2\sigma^{\mathrm{ref}}_{\mathrm{syst.}}$	7.53%	-17.1%	2.04%
	Bias in the middle of 2σ interval wrt the size of the $2\sigma^{\mathrm{ref}}_{\mathrm{tot.}}$ interval	-4%	17.7%	-1.45%
	Bias in the middle of 2σ interval wrt the size of the $2\sigma^{\mathrm{ref}}_{\mathrm{syst.}}$ interval	-12.4%	45.1%	-5.37%
	Bias in the middle of 2σ interval wrt the size of the $1\sigma^{\mathrm{ref}}_{\mathrm{tot.}}$ interval	-10.9%	35.4%	-2.42%
	Bias in the middle of 2σ interval wrt the size of the $1\sigma^{\mathrm{ref}}_{\mathrm{syst.}}$ interval	-21.4%	90.5%	-9.52%
AsimovB22	Middle of the 1σ interval	0.4484	0.0025178	0.2676 and 2.784
	1σ interval size: 1σ	0.022	5.09e-05	0.812 and 0.678
	1σ interval ratio to Nominal	0.83	0.925	0.963 and 0.999
	Fractional change in the 1σ interval size wrt the syst interval: $\left(1\sigma^{\mathrm{FDS}}_{\mathrm{tot.}} - 1\sigma^{\mathrm{ref}}_{\mathrm{tot.}}\right)/1\sigma^{\mathrm{ref}}_{\mathrm{syst.}}$	-40.2%	-18.9%	-12.6% and -0.313%
	Bias in the middle of 1σ interval wrt the size of the $1\sigma^{\mathrm{ref}}_{\mathrm{tot.}}$ interval	-23.5%	39%	-8.68% and 6.48%
	Bias in the middle of 1σ interval wrt the size of the $1\sigma^{\mathrm{ref}}_{\mathrm{syst.}}$ interval	-55.4%	97.9%	-29.6% and 26.3%
	Middle of the 2σ interval	0.506	0.0025175	0
	2σ interval size: 2σ	0.0963	0.000102	3.14
	2σ interval ratio to Nominal	0.977	0.926	1
	Fractional change in the 2σ interval size wrt the syst interval: $\left(2\sigma^{\mathrm{FDS}}_{\mathrm{tot.}} - 2\sigma^{\mathrm{ref}}_{\mathrm{tot.}}\right)/2\sigma^{\mathrm{ref}}_{\mathrm{syst.}}$	-8.18%	-18.8%	
	Bias in the middle of 2σ interval wrt the size of the $2\sigma^{\mathrm{ref}}_{\mathrm{tot.}}$ interval	-2.53%	18.8%	0%
	Bias in the middle of 2σ interval wrt the size of the $2\sigma^{\mathrm{ref}}_{\mathrm{syst.}}$ interval	-9.04%	47.5%	
	Bias in the middle of 2σ interval wrt the size of the $1\sigma^{\mathrm{ref}}_{\mathrm{tot.}}$ interval	-9.42%	37.6%	0%
	Bias in the middle of 2σ interval wrt the size of the $1\sigma^{\mathrm{ref}}_{\mathrm{syst.}}$ interval	-22.2%	94.3%	0%

Table 4.3. *δ_{CP} interval edges from the data and CRPA FDS fits and the changes to the edges due to CRPA FDS.*

	1σ		90% CL		2σ		3σ	
Data	-2.754	-0.943	-3.097	-0.451	-3.259	-0.206	-3.735	0.387
FDS edges	-2.787	-1.005	-3.132	-0.485	-3.289	-0.233	-3.767	0.374
Shift	-0.0329	-0.0618	-0.0348	-0.0336	-0.0302	-0.0263	-0.0325	-0.0134

Table 4.4. *δ_{CP} interval edges from the data and CRPA FDS fits and the changes to the edges due to CRPA FDS when the* ***scaled Asimov method*** *is used.*

	1σ		90% CL		2σ		3σ	
Data	-2.754	-0.943	-3.097	-0.451	-3.259	-0.206	-3.735	0.387
FDS edges	-2.780	-0.997	-3.123	-0.483	-3.281	-0.232	-3.757	0.369
Shift	-0.0254	-0.0539	-0.0258	-0.0313	-0.0221	-0.0262	-0.0228	-0.0181

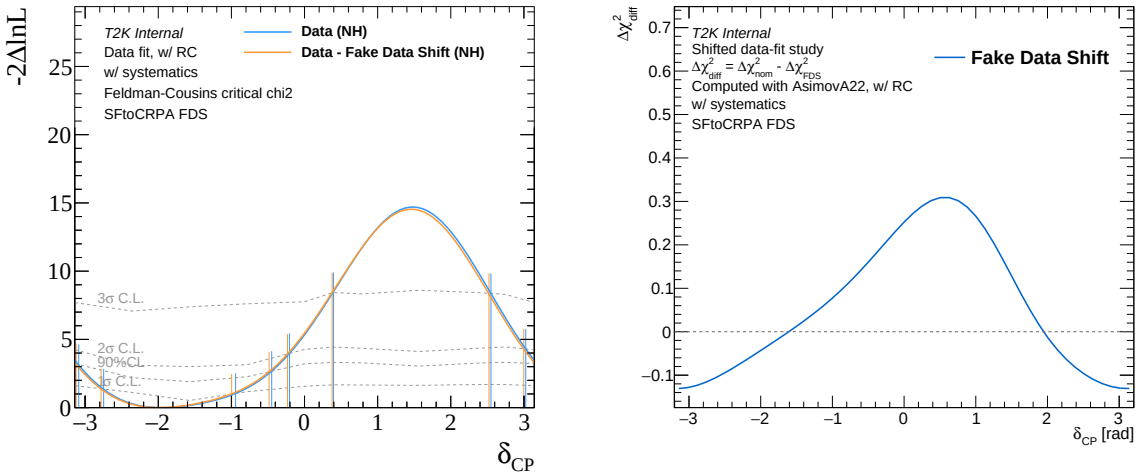

Figure 4.11. *Comparison of the δ_{CP} 1D $\Delta\chi^2$ from the data and CRPA FDS (left) and the difference between $\Delta\chi^2_{nom.}$ and $\Delta\chi^2_{FDS}$ (right). The Feldman-Cousins critical χ^2 are reported as well in the left plot.*

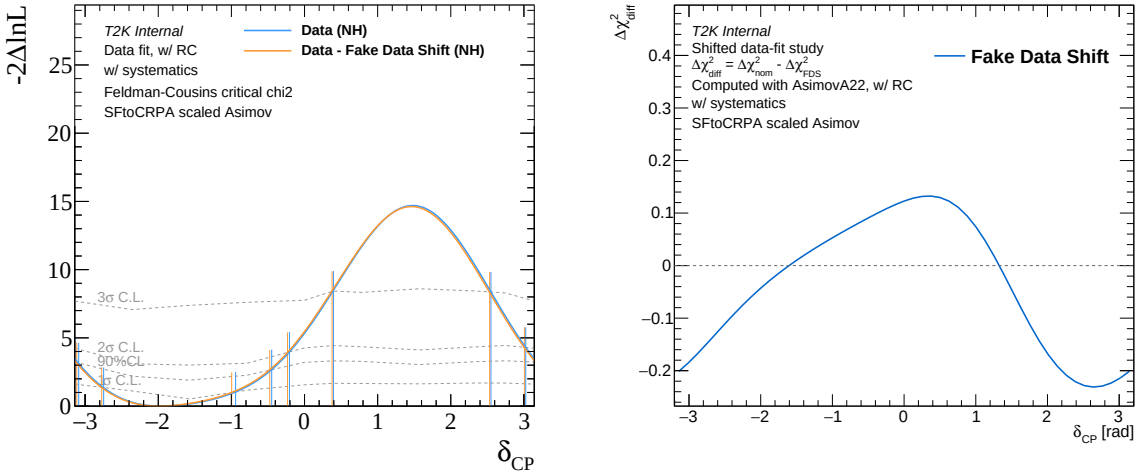

Figure 4.12. *Comparison of the Δ_{CP} 1D $\Delta\chi^2$ from the data and CRPA FDS (left) and the difference between $\Delta\chi^2_{nom.}$ and $\Delta\chi^2_{FDS}$ (right) when the* ***scaled Asimov method*** *is used. The Feldman-Cousins critical χ^2 are reported as well in the left plot.*

4.4.2 A different implementation for Radiative corrections

The final FDS that has not been described yet is the radiative corrections one. It concerns the possibility of having a visible photon emitted in the final state through radiations of the outgoing lepton in case of a CCQE interaction. This is mainly for muon radiative processes. These processes are not taken into account in the cross-section uncertainty very much so a FDS is necessary. This photon can impact the analysis in different ways. The photon can account for a significant part of the cross-section and differ between muon and electron. It can also lead to mis-categorization of an event in three different cases. If the event is muon-like and the photon is colinear with the muon, two rings will be superimposed and mimic a single electron-like ring. If the event is muon-like also but the photon carries an important part of the energy, the muon energy might fall below the Cherenkov threshold leading to only one visible electron-like ring produced by the muon. Finally, if the photon is non-colinear, it will produce a second ring that will be interpreted as a decay electron since the photon identification is not possible with the current Cherenkov ring pattern recognition performance.
To produce the corresponding fake data, weights were not produced by T2KReWeight Software and I had to implement this in P-Theta at the level of sample selection. The way it was implemented came from simulation studies by the neutrino interaction group, using a particle gun. Although the simulation study was performed on CCQE events only, it was assumed that the fake data weights could be applied to all charged current interaction modes as a first approximation.

The weights to apply to 1-ring samples, displayed in table 4.5, were identified to be linear functions of the true lepton energy. This is to account for the loss of events in all samples in case of mis-identification due to radiative corrections. In addition, it has just been explained that those radiative corrections can lead to an increase of events in the 1Re1de sample when the photon mimics the decay electron signal. It was recommended to us to model this by a Landau distribution in reconstructed neutrino energy (Erec) using the TMath::Landau(Erec., 537, 48.6) with parameters in MeV. This being done the full process of analysis described for the CRPA FDS can follow. Some key results only will be shown here. As it can be seen in figure 4.13, the reweighting, as expected

Table 4.5. *Linear weights to apply to all charged-current interactions in each far detector sample to build the radiative corrections fake data set.*

Sample	Weighting function
FHC 1Rμ	$w\,(E_\ell/\mathrm{MeV}) = 0.982 - 7\times10^{-6}\cdot E_\ell$
RHC 1Rμ	$w\,(E_\ell/\mathrm{MeV}) = 0.984 - 11\times10^{-6}\cdot E_\ell$
FHC 1Re	$w\,(E_\ell/\mathrm{MeV}) = 0.989 - 19\times10^{-6}\cdot E_\ell$
RHC 1Re	$w\,(E_\ell/\mathrm{MeV}) = 0.985 - 13\times10^{-6}\cdot E_\ell$

from the mis-identification of the rings it represents, leads to a decrease of about 2% of events in 1Rμ and 1Re samples (neutrino and anti-neutrino) and an increase of 0.18% in the 1Re1de sample. On those spectra, the error bands from BANFF fit are not present as this fake data study only concerns an effect in the far detector, which does not need any reweighting from nominal spectra at the near detector fit. For brevity, only plots for Asimov A22 oscillation parameters set is shown. This fake data study proved to not have

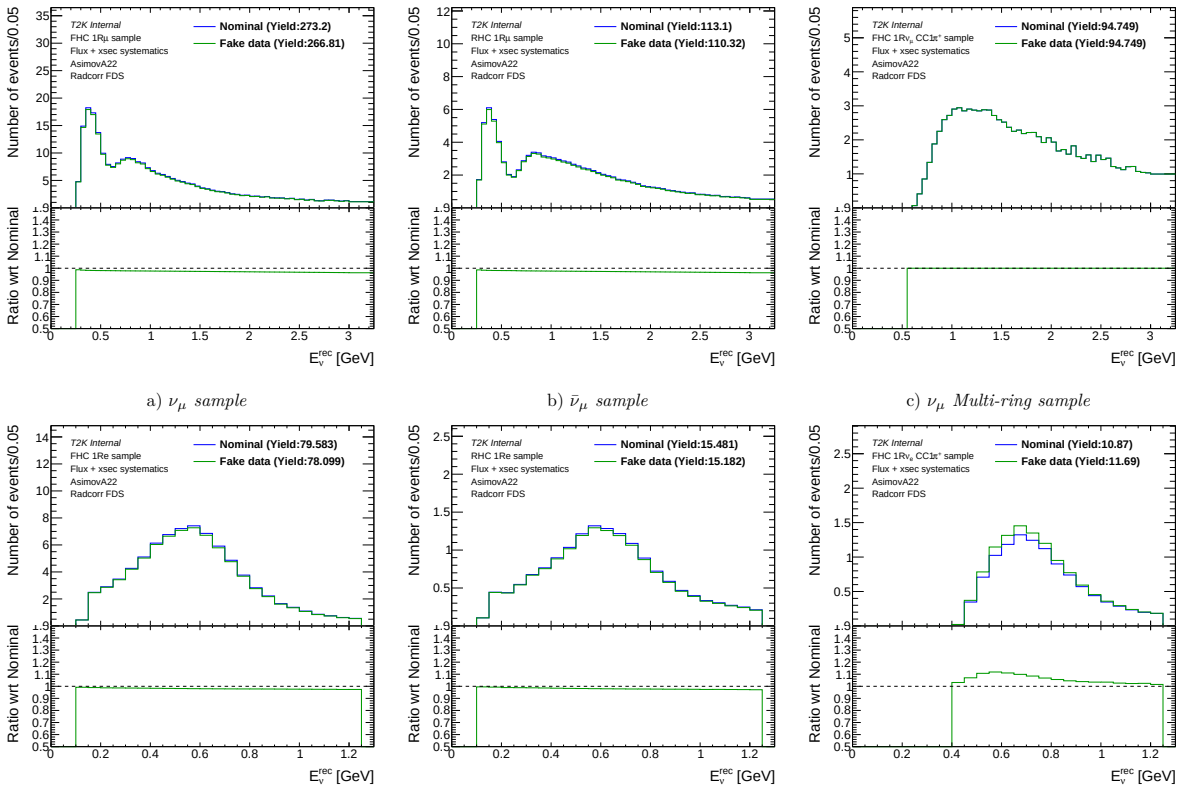

a) ν_μ *sample* b) $\bar{\nu}_\mu$ *sample* c) ν_μ *Multi-ring sample*

d) ν_e *sample* e) $\bar{\nu}_e$ *sample* f) ν_e *1 d.e. sample*

Figure 4.13. *Comparison between the nominal SK samples (blue solid line), the SK fake data for Asimov A22 (green solid line).*

a large impact on oscillation parameters (16% maximum on Δm^2). The 1D contours for Asimov A22 can be found in figure 4.14 and the overall summary of biases that can be computed is reported in table 4.6 for standard FDS fit and in 4.7 for scaled Asimov fits.

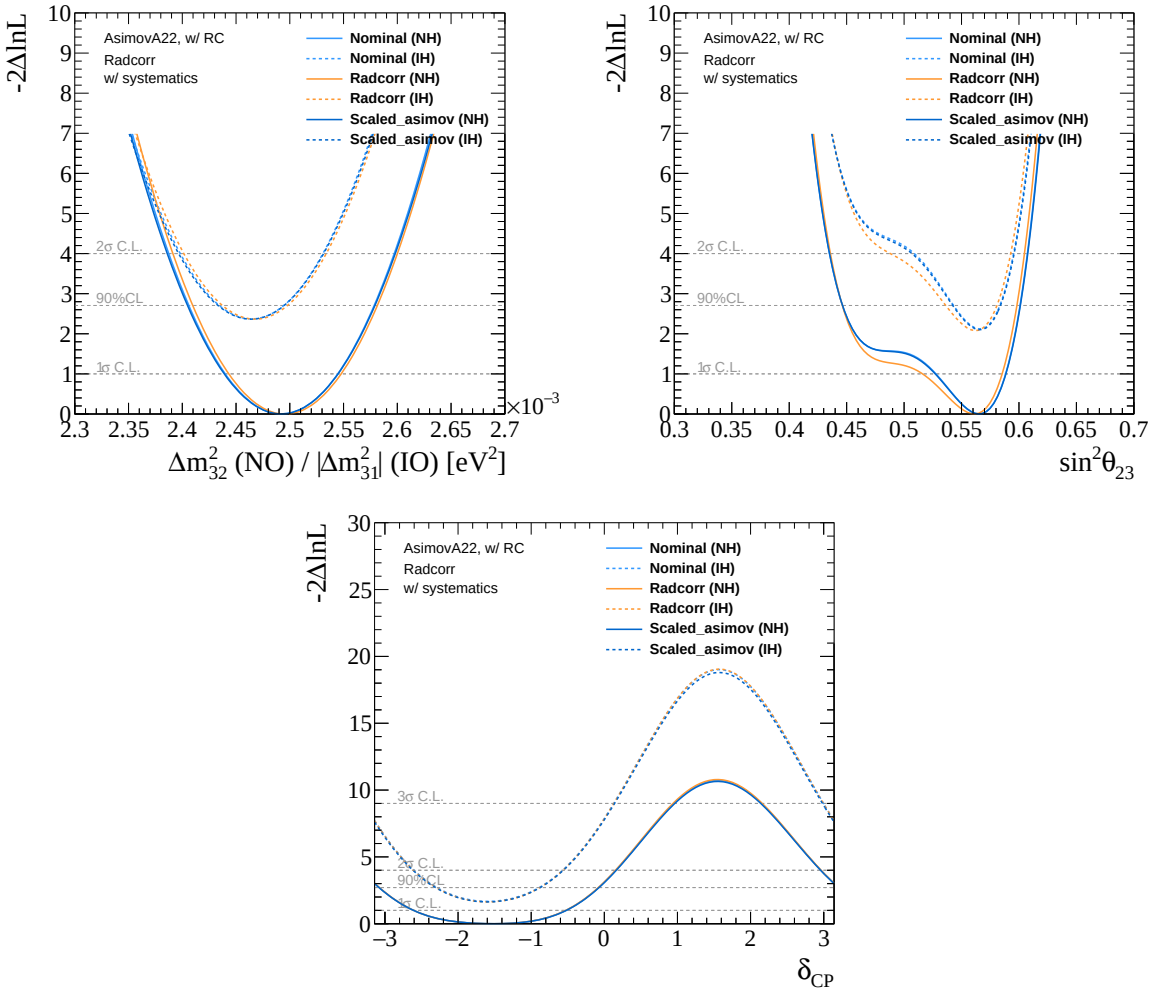

Figure 4.14. *1-D likelihood surfaces for Δm^2_{32} (top left), $\sin^2\theta_{23}$ (top right) and δ_{CP} (bottom), with the reactor constraint on $\sin^2\theta_{13}$, for both normal (solid line) and inverted (dashed) ordering, for the Radiative corrections FDS and Asimov A22. The $\Delta\chi^2$ curves of the Asimov fit, FDS and scaled Asimov are reported in blue, orange and dark blue respectively.*

Table 4.6. *Table of the bias for the Radiative corrections FDS for both Asimov sets. For Asimov B22, results at the lower and upper octant minima are shown.*

		$\sin^2\theta_{23}$	Δm^2_{32}	δ_{CP}
AsimovA22	Middle of the 1σ interval	0.5507	0.0024955	-1.567
	1σ interval size: 1σ	0.0346	5.23e-05	1.04
	1σ interval ratio to Nominal	1.14	0.998	0.998
	Fractional change in the 1σ interval size wrt the syst interval: $\left(1\sigma^{\text{FDS}}_{\text{tot.}} - 1\sigma^{\text{ref}}_{\text{tot.}}\right)/1\sigma^{\text{ref}}_{\text{syst.}}$	30.4%	-0.493%	-0.707%
	Bias in the middle of 1σ interval wrt the size of the $1\sigma^{\text{ref}}_{\text{tot.}}$ interval	-24.2%	6.23%	-0.126%
	Bias in the middle of 1σ interval wrt the size of the $1\sigma^{\text{ref}}_{\text{syst.}}$ interval	-52.1%	15.6%	-0.505%
	Middle of the 2σ interval	0.5203	0.0024957	-1.583
	2σ interval size: 2σ	0.0845	0.000104	1.74
	2σ interval ratio to Nominal	0.981	0.996	0.998
	Fractional change in the 2σ interval size wrt the syst interval: $\left(2\sigma^{\text{FDS}}_{\text{tot.}} - 2\sigma^{\text{ref}}_{\text{tot.}}\right)/2\sigma^{\text{ref}}_{\text{syst.}}$	-5.69%	-1.12%	-0.841%
	Bias in the middle of 2σ interval wrt the size of the $2\sigma^{\text{ref}}_{\text{tot.}}$ interval	-1.07%	3.21%	-0.0602%
	Bias in the middle of 2σ interval wrt the size of the $2\sigma^{\text{ref}}_{\text{syst.}}$ interval	-3.16%	8.05%	-0.224%
	Bias in the middle of 2σ interval wrt the size of the $1\sigma^{\text{ref}}_{\text{tot.}}$ interval	-3.04%	6.42%	-0.1%
	Bias in the middle of 2σ interval wrt the size of the $1\sigma^{\text{ref}}_{\text{syst.}}$ interval	-6.54%	16.1%	-0.404%
AsimovB22	Middle of the 1σ interval	0.4565	0.0025012	0.3113 and 2.78
	1σ interval size: 1σ	0.0266	5.39e-05	0.817 and 0.644
	1σ interval ratio to Nominal	1.05	0.992	0.993 and 1.01
	Fractional change in the 1σ interval size wrt the syst interval: $\left(1\sigma^{\text{FDS}}_{\text{tot.}} - 1\sigma^{\text{ref}}_{\text{tot.}}\right)/1\sigma^{\text{ref}}_{\text{syst.}}$	12%	-2.01%	-2.43% and 3.38%
	Bias in the middle of 1σ interval wrt the size of the $1\sigma^{\text{ref}}_{\text{tot.}}$ interval	13.6%	6.32%	0.652% and -0.297%
	Bias in the middle of 1σ interval wrt the size of the $1\sigma^{\text{ref}}_{\text{syst.}}$ interval	35.3%	15.7%	2.22% and -1.46%
	Middle of the 2σ interval	0.5079	0.0025011	0
	2σ interval size: 2σ	0.096	0.000108	3.14
	2σ interval ratio to Nominal	0.973	0.994	1
	Fractional change in the 2σ interval size wrt the syst interval: $\left(2\sigma^{\text{FDS}}_{\text{tot.}} - 2\sigma^{\text{ref}}_{\text{tot.}}\right)/2\sigma^{\text{ref}}_{\text{syst.}}$	-8.85%	-1.44%	
	Bias in the middle of 2σ interval wrt the size of the $2\sigma^{\text{ref}}_{\text{tot.}}$ interval	-0.612%	3.28%	0%
	Bias in the middle of 2σ interval wrt the size of the $2\sigma^{\text{ref}}_{\text{syst.}}$ interval	-2.01%	8.15%	
	Bias in the middle of 2σ interval wrt the size of the $1\sigma^{\text{ref}}_{\text{tot.}}$ interval	-2.37%	6.54%	0%
	Bias in the middle of 2σ interval wrt the size of the $1\sigma^{\text{ref}}_{\text{syst.}}$ interval	-6.16%	16.2%	0%

Table 4.7. *Table of the bias for the Radiative corrections FDS for both Asimov sets when the* ***scaled Asimov method*** *is used. For Asimov B22, results at the lower and upper octant minima are shown.*

		$\sin^2\theta_{23}$	Δm^2_{32}	δ_{CP}
AsimovA22	Middle of the 1σ interval	0.5507	0.0024955	-1.567
	1σ interval size: 1σ	0.0346	5.23e-05	1.04
	1σ interval ratio to Nominal	1.13	0.987	0.995
	Fractional change in the 1σ interval size wrt the syst interval: $\left(1\sigma^{\text{FDS}}_{\text{tot.}} - 1\sigma^{\text{ref}}_{\text{tot.}}\right)/1\sigma^{\text{ref}}_{\text{syst.}}$	27.1%	-3.26%	-1.93%
	Bias in the middle of 1σ interval wrt the size of the $1\sigma^{\text{ref}}_{\text{tot.}}$ interval	-23.3%	6.74%	-0.313%
	Bias in the middle of 1σ interval wrt the size of the $1\sigma^{\text{ref}}_{\text{syst.}}$ interval	-49.6%	16.8%	-1.24%
	Middle of the 2σ interval	0.5203	0.0024957	-1.583
	2σ interval size: 2σ	0.0845	0.000104	1.74
	2σ interval ratio to Nominal	0.979	0.985	0.995
	Fractional change in the 2σ interval size wrt the syst interval: $\left(2\sigma^{\text{FDS}}_{\text{tot.}} - 2\sigma^{\text{ref}}_{\text{tot.}}\right)/2\sigma^{\text{ref}}_{\text{syst.}}$	-6.36%	-3.82%	-1.9%
	Bias in the middle of 2σ interval wrt the size of the $2\sigma^{\text{ref}}_{\text{tot.}}$ interval	-1.23%	3.39%	-0.135%
	Bias in the middle of 2σ interval wrt the size of the $2\sigma^{\text{ref}}_{\text{syst.}}$ interval	-3.68%	8.46%	-0.503%
	Bias in the middle of 2σ interval wrt the size of the $1\sigma^{\text{ref}}_{\text{tot.}}$ interval	-3.45%	6.78%	-0.225%
	Bias in the middle of 2σ interval wrt the size of the $1\sigma^{\text{ref}}_{\text{syst.}}$ interval	-7.36%	16.9%	-0.892%
AsimovB22	Middle of the 1σ interval	0.4565	0.0025012	0.3113 and 2.78
	1σ interval size: 1σ	0.0266	5.39e-05	0.817 and 0.644
	1σ interval ratio to Nominal	1.03	0.982	0.986 and 0.997
	Fractional change in the 1σ interval size wrt the syst interval: $\left(1\sigma^{\text{FDS}}_{\text{tot.}} - 1\sigma^{\text{ref}}_{\text{tot.}}\right)/1\sigma^{\text{ref}}_{\text{syst.}}$	9.13%	-4.55%	-4.77% and -1.66%
	Bias in the middle of 1σ interval wrt the size of the $1\sigma^{\text{ref}}_{\text{tot.}}$ interval	13%	6.17%	0.427% and -0.375%
	Bias in the middle of 1σ interval wrt the size of the $1\sigma^{\text{ref}}_{\text{syst.}}$ interval	34%	15.3%	1.48% and -2.12%
	Middle of the 2σ interval	0.5079	0.0025011	0
	2σ interval size: 2σ	0.096	0.000108	3.14
	2σ interval ratio to Nominal	0.971	0.984	1
	Fractional change in the 2σ interval size wrt the syst interval: $\left(2\sigma^{\text{FDS}}_{\text{tot.}} - 2\sigma^{\text{ref}}_{\text{tot.}}\right)/2\sigma^{\text{ref}}_{\text{syst.}}$	-9.62%	-3.94%	
	Bias in the middle of 2σ interval wrt the size of the $2\sigma^{\text{ref}}_{\text{tot.}}$ interval	-0.511%	3.11%	0%
	Bias in the middle of 2σ interval wrt the size of the $2\sigma^{\text{ref}}_{\text{syst.}}$ interval	-1.71%	7.72%	
	Bias in the middle of 2σ interval wrt the size of the $1\sigma^{\text{ref}}_{\text{tot.}}$ interval	-1.96%	6.2%	0%
	Bias in the middle of 2σ interval wrt the size of the $1\sigma^{\text{ref}}_{\text{syst.}}$ interval	-5.14%	15.3%	0%

4.4.3 Biases applied on final contours

4.4.3.1 Conclusions from the above Fake data studies

Once the impact of all the chosen items (FDS) on the oscillation analysis results has been quantified, it is taken into account in the reported results in the following way: a smearing is applied on the $\sin^2\theta_{23}$ likelihood curve (1D) and $\sin^2\theta_{23}$ /Δm^2_{32} 2D contours. The impact on CP conservation conclusion is also checked in the way that was described in section 4.4.1 for the CRPA study. None of the studies suggested any change in the CP conservation/exclusion conclusion of the analysis.
The impact of each FDS on $\sin^2\theta_{23}$ or Δm^2_{32} was quantified by using two different metrics. The first one is the bias B_x^{syst} on the mean of the 2σ interval with respect to the systematic uncertainty $\sigma_{syst}^{Nominal}$. That uncertainty was computed thanks to the fact that all studies were performed both with and without systematics applied so that σ^2_{syst} can be computed as $\sigma^2_{syst} = \sigma^2_{tot} - \sigma^2_{stat}$ although it might not be exact for bounded parameters. The bias was computed this way, x denoting either one of the two oscillation parameters:

$$B_x^{syst} = \frac{\overline{x^{2\sigma}_{Nominal}} - \overline{x^{2\sigma}_{FDS}}}{1\sigma_{syst}^{Nominal}} \tag{4.1}$$

The second metric is the ratio $R_x^{2\sigma}$ of the 2σ interval widths between nominal and FDS intervals.

$$R_x^{2\sigma} = \frac{2\sigma_{tot}^{FDS}}{2\sigma_{tot}^{Nominal}} \tag{4.2}$$

The collaboration worked to provide criteria for when a bias is significant and should be taken into account and reported it in an internal dedicated technical note: TN441 [120]. The criteria is that, so as to be acceptable without taking any action, the bias B_x^{syst} in the mean of intervals should be less than 50% and the width of the 2σ should never change by more than 10% so that we should have $|R_x^{2\sigma} - 1| < 10\%$. If not, a smearing should be applied on the reported confidence intervals to take into account that additional uncertainty.
Both those metrics, for both $\sin^2\theta_{23}$ and Δm^2_{32} are reported for each FDS in table 4.8 for standard FDS fits and in table 4.9 for the scaled Asimov fits.

As it can be read from these tables, no action is required for $\sin^2\theta_{23}$. However, the CRPA, non-QE and removal energy interpolation FDS have results beyond the criteria for Δm^2_{32}. In the end, because the difference was small and the collaboration preferred to stay conservative, the smearing factor to apply was computed not only from the studies exceeding the criteria, but from all of them. When studies were the same but evaluated at different value points, only the most impactful one was included in the smearing factor

calculation. That factor, noted S_{All}^{A22}, was computed from the results with Asimov A22 oscillation parameters values because it is the closest to data set of values. Its formula is:

$$S_{All}^{A22} = \sigma_{syst}^{Nominal} \sqrt{\sum_{All\ FDS} (B_{\Delta m^2_{32}}^{syst,FDS})^2} \tag{4.3}$$

Table 4.8. *Summary of all biases computed for Δm^2_{32} and $\sin^2\theta_{32}$ from the standard FDS fits for both Asimov sets. Values in this table are truncated and those that are negligible are removed for ease of reading.*

	A22				B22			
Fake Data Study	$B^{\text{syst.}}_{\Delta m^2_{32}}$	$R^{2\sigma}_{\Delta m^2_{32}}$	$B^{\text{syst.}}_{sin^2\theta_{32}}$	$R^{2\sigma}_{sin^2\theta_{32}}$	$B^{\text{syst.}}_{\Delta m^2_{32}}$	$R^{2\sigma}_{\Delta m^2_{32}}$	$B^{\text{syst.}}_{sin^2\theta_{32}}$	$R^{2\sigma}_{sin^2\theta_{32}}$
Z-exp Lower	-6%	0.99	—	0.99	-6%	0.99	—	—
Z-exp CV	—	0.98	—	0.99	1%	0.98	—	0.99
Z-exp Upper	-26%	0.95	-1%	0.98	-23%	0.95	-1%	0.98
3Comp Lower	-3%	0.95	1%	0.97	-1%	0.95	—	0.98
3Comp CV	-6%	0.95	1%	0.98	-3%	0.95	-1%	0.98
3Comp Upper	-10%	0.94	7%	0.97	-9%	0.94	3%	0.99
LFG	-46%	0.99	—	0.97	-48%	0.99	1%	0.98
CRPA	85%	0.95	-25%	1.02	91%	0.94	-25%	0.98
Extremal Removal Energy	-17%	—	-2%	0.99	-18%	—	-1%	0.99
Removal Energy cubic interpolation	-40%	0.83	5%	0.92	-37%	0.83	5.8%	0.96
Removal Energy linear interpolation	-29%	0.83	1%	0.92	-24%	0.83	3%	0.94
1π Low Q^2	19%	0.98	14%	1.02	23.1%	0.98	13%	1.04
1π Kin. -3σ	7%	—	-6%	0.99	7%	—	-4%	0.98
1π Kin. $+3\sigma$	-8%	—	1%	1.01	-7%	—	3%	1.01
Martini 1π	-19%	0.99	-5%	—	-16%	0.99	1%	—
Radiative Corrections	16%	—	-8%	0.98	15%	0.99	-7%	0.97
Data-driven non-QE	-76%	0.99	10%	1.03	-71%	0.99	5%	1.04
Data-driven 1π	-8%	—	-2%	—	-10%	—	-3%	—

This factor was found to be $S_{All}^{A22} = 2.7 \times 10^{-5}\ eV^2$. At this precision level, the same value was found for standard and scaled Asimov fits, due to small differences compensating each other. This is to be compared to the error on Δm^2 in the data fit. For example from the global best fit that error was $3.4 \times 10^{-5}\ eV^2$. This is therefore the same order of magnitude.

The smearing factor is then applied to the reported intervals in the following way. The likelihood space (not χ^2), for either 1D likelihood as a function of Δm^2 (Δm^2_{32} for normal hierarchy or Δm^2_{31} for inverted hierarchy) or 2D including Δm^2, is binned. For each bin, a Gaussian function with its mean equal to the likelihood value in that bin and with its standard deviation the smearing value S_{All}^{A22} is built. The integral of that Gaussian is computed and added to the nearby bins with a loop. The integral added represents a

potential migration from one bin to another because of uncertainty, directly at the level of likelihood values.

Table 4.9. *Summary of all biases computed for* Δm^2_{32} *and* $\sin^2\theta_{32}$ *from the* ***scaled Asimov*** *FDS fits for both Asimov sets. Values in this table are truncated and those that are negligible are removed for ease of reading.*

	A22				B22			
Fake Data Study	$B^{\text{syst.}}_{\Delta m^2_{32}}$	$R^{2\sigma}_{\Delta m^2_{32}}$	$B^{\text{syst.}}_{sin^2\theta_{32}}$	$R^{2\sigma}_{sin^2\theta_{32}}$	$B^{\text{syst.}}_{\Delta m^2_{32}}$	$R^{2\sigma}_{\Delta m^2_{32}}$	$B^{\text{syst.}}_{sin^2\theta_{32}}$	$R^{2\sigma}_{sin^2\theta_{32}}$
Z-exp Lower	-6%	1.00	2%	1.0	-7%	1.00	—	1.00
Z-exp CV	—	1.00	—	1.0	-0.803%	0.996	0.367%	0.999
Z-exp Upper	-20%	1.0	—	1.00	-20%	1.0	-2%	1.00
3Comp Lower	2%	1.0	—	1.00	3%	1.0	-2%	1.0
3Comp CV	-4%	1.00	2%	1.00	-1%	1.00	—	1.00
3Comp Upper	-6%	1.01	8%	1.01	-4%	1.01	3%	1.02
LFG	-44%	1.00	—	0.98	-46%	1.00	-1%	1.0
CRPA	90%	0.93	-21%	1.02	94%	1.0	-22%	0.98
Removal Energy	-1%	1.0	-1%	1.0	—	1.00	—	1.0
Removal Energy cubic interpolation	-17%	1.01	6%	1.02	-16.6%	1.01	2%	1.03
Removal Energy linear interpolation	-5%	1.01	4%	1.02	-0.1%	1.01	3%	1.02
1π Low Q^2	20%	0.99	17%	1.02	22%	1.0	10%	1.04
1π Kin. -3σ	19%	1.00	-3%	1.00	19%	1.00	-3%	1.0
1π Kin. $+3\sigma$	-8%	1.0	2%	1.01	-5%	1.0	3%	1.01
Martini 1π	-18%	1.0	-3%	1.0	-16%	1.0	-2%	0.99
Radiative Corrections.	17%	0.98	-7%	0.98	15%	1.0	-5%	0.97
Data-driven non-QE	-76%	0.99	7%	1.02	-71%	0.99	2%	1.03
Data-driven 1π	-7%	1.01	-2%	1.00	-9%	1.01	-3%	1.0

When the smearing is applied on 2D spaces such as $\sin^2\theta_{23}$ /Δm^2 contours , the gaussian integral computed in a bin with a $\sin^2\theta_{23}$ value should only be added to bins with the same $\sin^2\theta_{23}$ value. The final results are then, in general, reported in terms of χ^2, not likelihood.

Ideally, when a fake data study has a large impact (defined by the criteria above), a new systematic parameter should be included in the analysis to account for that uncertainty that is not yet taken care of by the other parameters. When it concerns a flux or cross-section model that is more complete than the one currently used in the T2K analysis, it can also be considered to implement that model in the future analyses. Of course, those implementations take a lot of work and might not always be the best solution or might not be technically possible in the analyses software as they are. But, more than adding additional uncertainty through smearing, investigating all those studies and especially looking at which have the largest impact on the oscillation analysis serves an important purpose in designing the future analysis strategies. It provides clues as to which new features would be the most useful in the future analyses or to which parallel studies are the most critical to improve our understanding of neutrino interactions occurring in our

detectors.

4.4.3.2 Additional smearing from the pion FSI bug

In the previous oscillation analysis, a bug was introduced at the level of the NEUT software used to model all interactions. Specifically, the bug concerned the pion final state interactions, whose reweights were all applied as if the target was Oxygen, whereas, in the near detector fit there are other materials to take into account such as Carbon. For this new analysis, the bug was thought to be fixed but actually it was only partially fixed. From previous studies it was known that the impact was not major on the final extracted oscillation parameters constraints.
It was decided to, instead of redoing all analysis steps, perform a fake data study to evaluate the impact of the remaining bug. From the result of this study, an additional smearing was counted and so the final smearing value applied was $3.1 \times 10^{-5}\ eV^2$ on Δm^2.

4.4.4 Additional study on the α parameter for the new removal energy treatment

I also lead an additional fake data study that was not to be included in the smearing computation but was to try and understand the effect of the α parameter introduced in section 3.2.3 for a more refined removal energy treatment. This study consists in using the extreme value $\alpha = 1$ to produce fake data and then fit them with the decided standard fixed $\alpha = 0$ value. Because the α parameter was in the end set to 0 in the analysis, which is equivalent to not being used, there is no reason to include whatever bias will be computed from that study in the smearing budget. The motivation for this study is to get clues as to why the near detector data is strongly constraining α to 0 in contradiction with electron scattering data; and also for the sake of completion to conclude on the implementation of this feature.
The same process as described in detail previously for standard FDS was followed. Figure 4.15 shows the comparison of fake data against the nominal ones and the BANFF predictions. The good agreement with BANFF error-bands is yet another validation of the implementation of this feature in P-Theta as the implementation in BANFF is different. Moreover, the impact of the α parameter on the spectra seem very small. When results from the near detector fits are propagated to the far detector fit and the oscillation analysis results are plotted, as in figure 4.16 for the A22 Asimov set, a strong bias in Δm^2 and $\sin^2\theta_{32}$ is observed. It is indeed quantified in table 4.10 and reaches more than 90% bias in Δm^2 for both Asimov sets. The explanation for this strong bias is the

tension between the value 1 for the fake data and the near detector favored value 0. That being said, the reason for this disagreement between external data and ND data is not understood. As mentioned in section 3.2.3, the freedom given by α parameter might be absorbed by other interfering systematic parameters, constraining by the same process the α parameter to not being used.

No scaled Asimov fit was performed for this study because there is no need for precision on this point. Further investigation on that matter would be necessary by cross-section experts to understand the behaviour of the parameter in order to use it in T2K and conclude on the physical value it should have.

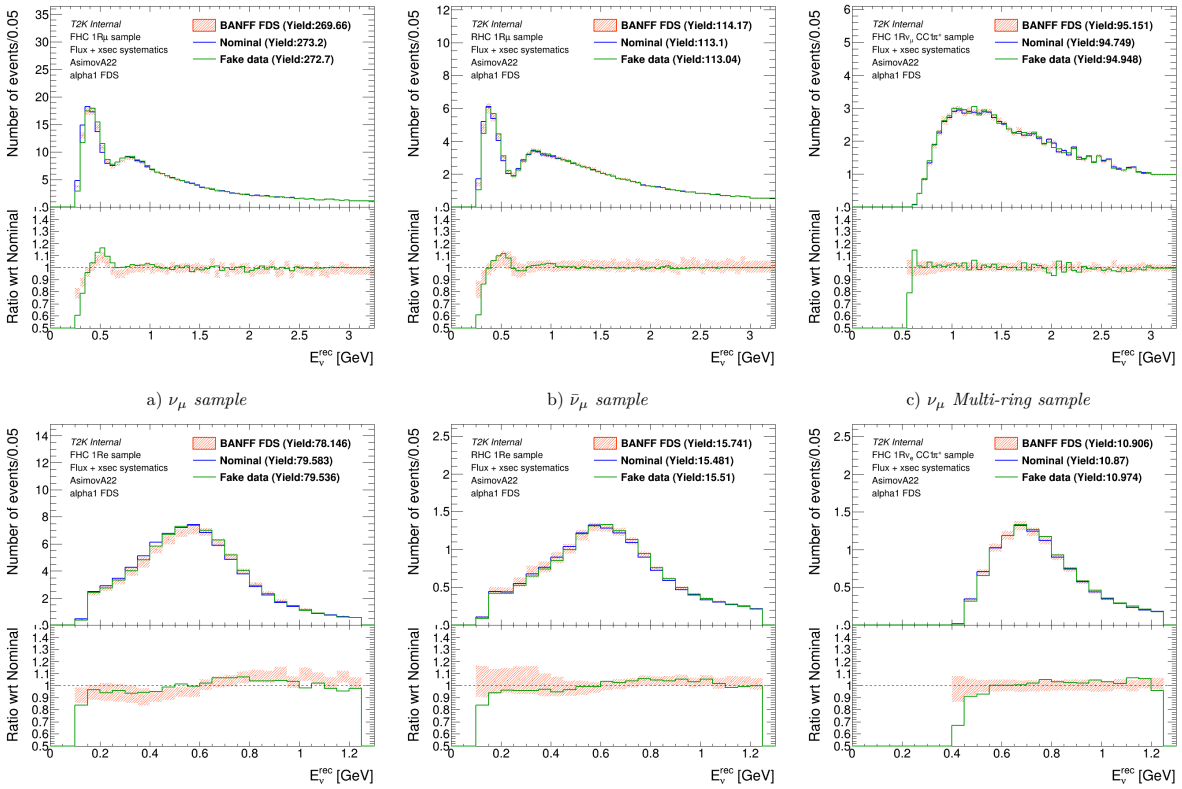

a) ν_μ *sample* b) $\bar{\nu}_\mu$ *sample* c) ν_μ *Multi-ring sample*

d) ν_e *sample* e) $\bar{\nu}_e$ *sample* f) ν_e *1 d.e. sample*

Figure 4.15. *Comparison between the nominal SK samples (blue solid line), the SK fake data for Asimov A22 (green solid line).*

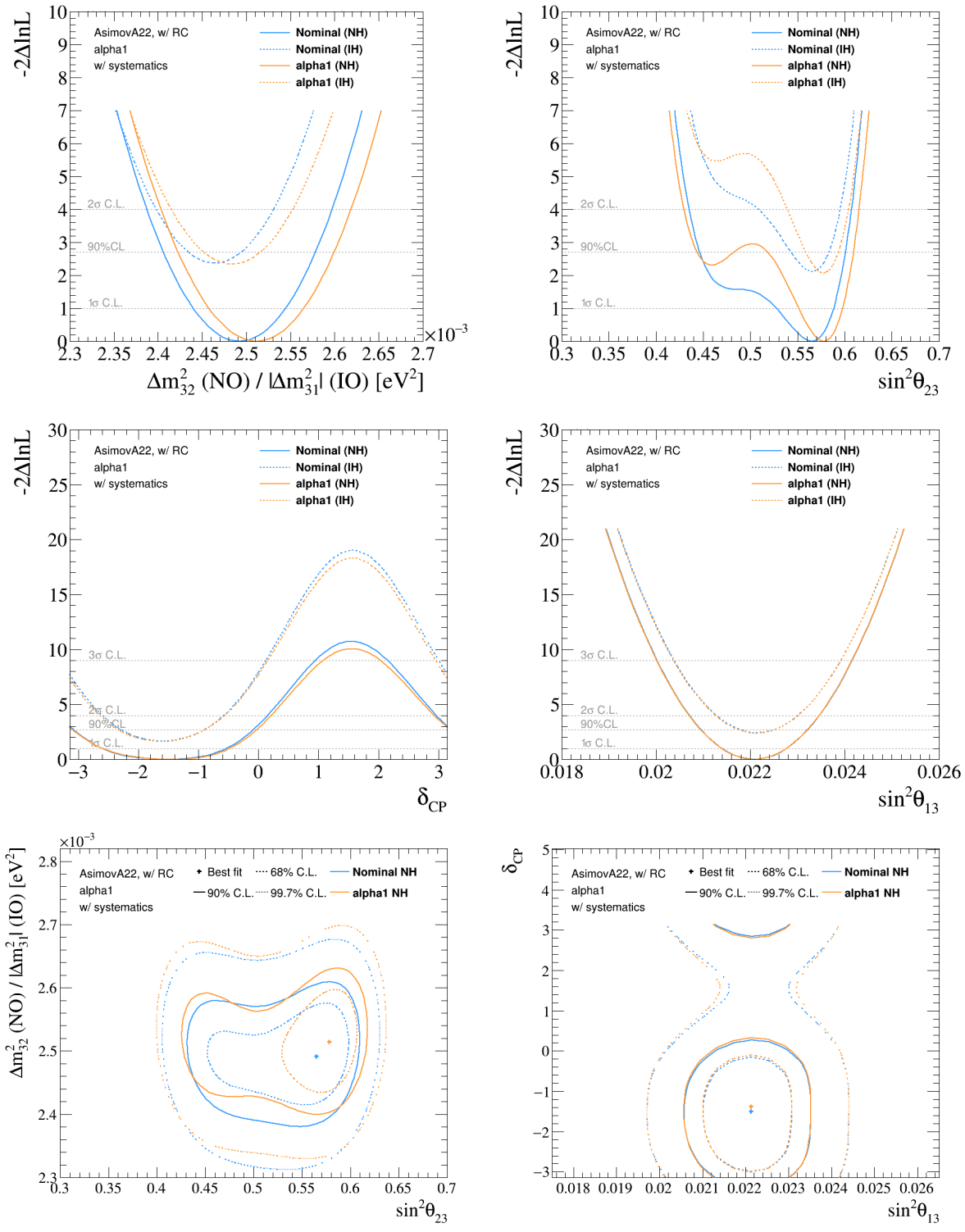

Figure 4.16. *1-D likelihood surfaces for Δm^2_{32} (top left), $\sin^2\theta_{23}$ (top right) and δ_{CP} (bottom), with the reactor constraint on $\sin^2\theta_{13}$, for both normal (solid line) and inverted (dashed) ordering, for the $\alpha = 1$ FDS and Asimov A22. The contours of the Asimov fit and FDS are reported in blue and orange respectively.*

Table 4.10. *Table of the bias for the Alpha = 1 FDS for both Asimov sets. For Asimov B22, results at the lower and upper octant minima are shown.*

		$\sin^2\theta_{23}$	Δm^2_{32}	δ_{CP}
AsimovA22	Middle of the 1σ interval	0.5747	0.0025115	-1.535
	1σ interval size: 1σ	0.0233	5.38e-05	1.06
	1σ interval ratio to Nominal	0.768	1.03	1.02
	Fractional change in the 1σ interval size wrt the syst interval: $\left(1\sigma^{\text{FDS}}_{\text{tot.}} - 1\sigma^{\text{ref}}_{\text{tot.}}\right)/1\sigma^{\text{ref}}_{\text{syst.}}$	-49.9%	6.55%	8.59%
	Bias in the middle of 1σ interval wrt the size of the $1\sigma^{\text{ref}}_{\text{tot.}}$ interval	54.7%	36.8%	2.99%
	Bias in the middle of 1σ interval wrt the size of the $1\sigma^{\text{ref}}_{\text{syst.}}$ interval	118%	92.4%	12%
	Middle of the 2σ interval	0.5225	0.0025111	-1.57
	2σ interval size: 2σ	0.0928	0.000108	1.79
	2σ interval ratio to Nominal	1.08	1.03	1.03
	Fractional change in the 2σ interval size wrt the syst interval: $\left(2\sigma^{\text{FDS}}_{\text{tot.}} - 2\sigma^{\text{ref}}_{\text{tot.}}\right)/2\sigma^{\text{ref}}_{\text{syst.}}$	23%	6.44%	10.2%
	Bias in the middle of 2σ interval wrt the size of the $2\sigma^{\text{ref}}_{\text{tot.}}$ interval	1.49%	17.9%	0.685%
	Bias in the middle of 2σ interval wrt the size of the $2\sigma^{\text{ref}}_{\text{syst.}}$ interval	4.39%	45%	2.55%
	Bias in the middle of 2σ interval wrt the size of the $1\sigma^{\text{ref}}_{\text{tot.}}$ interval	4.22%	35.9%	1.14%
	Bias in the middle of 2σ interval wrt the size of the $1\sigma^{\text{ref}}_{\text{syst.}}$ interval	9.09%	90.3%	4.6%
AsimovB22	Middle of the 1σ interval	0.4399	0.0025183	0.2328 and 2.851
	1σ interval size: 1σ	0.021	5.54e-05	0.83 and 0.518
	1σ interval ratio to Nominal	0.826	1.02	1.01 and 0.811
	Fractional change in the 1σ interval size wrt the syst interval: $\left(1\sigma^{\text{FDS}}_{\text{tot.}} - 1\sigma^{\text{ref}}_{\text{tot.}}\right)/1\sigma^{\text{ref}}_{\text{syst.}}$	-45.3%	5.08%	2.98% and -93.4%
	Bias in the middle of 1σ interval wrt the size of the $1\sigma^{\text{ref}}_{\text{tot.}}$ interval	-51.6%	37.7%	-8.89% and 10.8%
	Bias in the middle of 1σ interval wrt the size of the $1\sigma^{\text{ref}}_{\text{syst.}}$ interval	-134%	93.5%	-30.2% and 53.4%
	Middle of the 2σ interval	0.5089	0.0025176	0
	2σ interval size: 2σ	0.106	0.000111	3.14
	2σ interval ratio to Nominal	1.08	1.02	1
	Fractional change in the 2σ interval size wrt the syst interval: $\left(2\sigma^{\text{FDS}}_{\text{tot.}} - 2\sigma^{\text{ref}}_{\text{tot.}}\right)/2\sigma^{\text{ref}}_{\text{syst.}}$	25.9%	5.15%	
	Bias in the middle of 2σ interval wrt the size of the $2\sigma^{\text{ref}}_{\text{tot.}}$ interval	0.421%	18.4%	0%
	Bias in the middle of 2σ interval wrt the size of the $2\sigma^{\text{ref}}_{\text{syst.}}$ interval	1.38%	45.8%	
	Bias in the middle of 2σ interval wrt the size of the $1\sigma^{\text{ref}}_{\text{tot.}}$ interval	1.63%	36.8%	0%
	Bias in the middle of 2σ interval wrt the size of the $1\sigma^{\text{ref}}_{\text{syst.}}$ interval	4.24%	91.2%	0%

4.5 Conclusion

In this Chapter, the procedure of fake data studies has been introduced and detailed through a few examples. A full list of fake data studies performed for the oscillation analysis 2021/2022 has been provided together with all final biases computed from them. Fake data studies are a powerful test of robustness of the analysis which relies on nuclear and interaction models of processes that are not yet fully understood and modelled. It is therefore essential to quantify the biases it can infer on the final results. As any systematic uncertainty, it has a growing importance as more and more statistics are accumulated

in the experiment. It is considered a necessary step towards publishing our results on oscillation parameters constraints with confidence that all systematic errors have been monitored carefully. For this particular round of analysis, the smearing to apply to Δm^2 has been found to be of $3.1 \times 10^{-5}\ eV^2$.

However, the FDS tool can also be used to answer other questions than computing an uncertainty, such as making a decision about a bug fix or assessing the impact of a feature that is not yet used in the analysis such as the α parameter ruling the potential Q_3 dependence of the removal energy. FDS can be used to investigate any cross-section related physics question that might impact the analysis. Moreover, it is interesting to stress out that these procedures are a specificity of the T2K collaboration but a lot of thinking is given to extending them to other experiments in the context of joint fits with SK and NOνA.

Chapter 5

The Hyper-Kamiokande experiment

This Chapter will introduce the next generation Hyper-Kamiokande detector in terms of its new characteristics, its scientific goals and its expected performance. This is both the background and motivation for the studies presented afterwards in Chapters 6 and 7.

Contents

5.1 Overview

In Chapters 3 and 4, it has been extensively discussed that the current constraints obtained by T2K on oscillation parameters are not as precise as we want them to be, and in particular do not allow us to claim the discovery of CP violation in the leptonic sector. To that end, it has been shown that the analysis can become even more sophisticated and need to give a great care to systematic parameters. Nonetheless, the analysis is currently statistically dominated and will still be at the end of T2K around 2026, meaning that the largest errors on the measurement come from the lack of statistics. The number of neutrino events that are detected at the far detector, specifically beam neutrino events in the context of T2K, has to be massively increased to reduce the uncertainty and improve our measurements. In that perspective, as stated in Chapter 2, the beam power is currently being upgraded. The off-axis ND280 set of near detectors is also being upgraded in order to have more near detector data and more accurate cross-section measurements. The NA61/SHINE experiment at CERN, mentioned before in Chapter 3 has also been recently upgraded and has taken new data to constrain T2K flux. But the most substantial foreseen improvement is the construction of a new far detector: Hyper-Kamiokande. Increased detection efficiency and volume at the far detector will not only allow for more statistics for the accelerator neutrinos but improve performance for the whole far detector physics program as it will be described in section 5.4.

5.2 Hyper-Kamiokande detector

Hyper-Kamiokande will be based on the same technology and principles as Super-Kamiokande: it will consist in a large water Cherenkov detector instrumented with PMTs. The Japanese government gave the final approval for the project in 2019 and since then the excavation of tunnels to access the mine where the detector will be placed has started. The beginning of the experiment with the first data taking run with the full tank is planned for 2027. The water Cherenkov detector will be located in the Tochibora mine, Gifu prefecture, in Japan. It will be symmetric to SK with respect to the beam axis, thus at the same off-axis angle of 2.5°, as it can be seen in figure 5.1. This corresponds to 8 km South of the current SK detector. The mine is located under Mont Nijugo under a rock overburden of about 650 m. This is useful to shield the detector from cosmic/atmospheric muons. However, it is a little bit less deep than SK which is at about 1000 m deep under the rock. Therefore a more careful management of background at the analysis level will be needed. To help with this task, just like at SK, the water tank will be separated into an inner (ID) and an outer detector (OD). The full tank will be a cylinder of 68 m of diameter and 71 m of height. The outer detector will be the outer-layer with a width

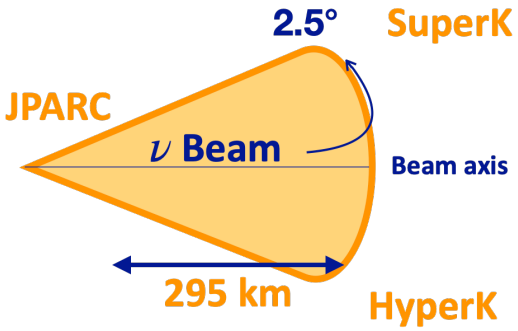

Figure 5.1. *Schematic of HK position with respect to the beam axis*

of 1 to 2 m. When an event includes hits in the OD, it can be identified as either a partially contained event or vetoed as an event coming from outside the detector instead of a neutrino interaction in the detector. Both the OD and ID will be filled with ultra pure water. A general scheme of the water tank can be found in figure 5.2.

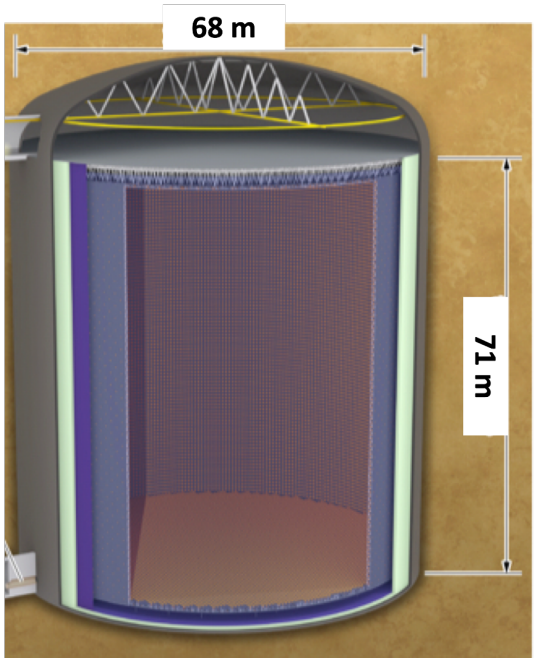

Figure 5.2. *Schematic of the Hyper-Kamiokande water tank*

Because the tank will be much larger (∼5x) than that of SK, the target mass of water will also be. HK's tank will be filled with 237 kton of water instead of the 50 kton of SK. This is one of the main reasons why the fiducial volume, which is the volume of detector that can actually be used to detect interactions, will be about 8 times larger, allowing for the increase in statistics that we seek. The other main reason for this increase of fiducial volume is that new photo-multipliers (PMT) have been designed for HK, in collaboration with

the company Hamamatsu Photonics K.K. (R12860-HQE), to have a better photo-coverage.

Indeed, the walls of the inner detector will be covered with at least 20 000 PMTs. Those will have a 50 cm diameter, similarly to SK's PMTs. However, the structure of their cathode and dynode have been modified in order to optimize the photon detection efficiency. It has been estimated [121] that this improvement is sufficient to compensate for having a larger detector (hence more light scattering and attenuation). In addition, this new design provides a two-times better time resolution and a reduced dark rate. The OD PMTs will be 20 cm diameter PMTs with improved quantum efficiency as well. The possibility to add another type of PMTs is also considered. Those would be so-called multi-PMTs (mPMT), meaning that one module would contain 19 small PMTs of 8 cm diameter each. Different scenarii are envisioned, from 1000 mPMTs to 5000 mPMTs. mPMTs provide a higher spatial resolution especially on short distances for events close to the wall, which allows to increase the fiducial volume by 5-10%. The fact that each 8 cm PMT in a module is facing the detection volume with a different angle provides more accurate directionnality. Smaller PMTs have better time resolution and lower dark rate. Finally, having a second type of PMT allows for cross-validation of the main PMTs calibration. As a conclusion, this configuration including mPMT would further improve the detection efficiency of HK and will hopefully be implemented, at least partially.

Since the collaboration is building a brand new detector from scratch, even-though it is based on the same technologies as SK, every single element will be more recent and potentially improved. This is for instance the case of the timing system that is being developed as it will be the topic of the next two chapters.

5.3 IWCD detector and the WCTE experiment

In parallel to improving the analysis, the detector (HK) technologies and performance and accumulating more statistics, a continuous effort is being made to reduce the systematic uncertainties on flux and cross-sections. This effort takes place at the level of dedicated measurements including with new detectors.

In addition to the near detectors currently upgraded at J-PARC towards HK, it is planned to build a new near detector at a slightly different site further along the beamline. It is called Intermediate Water Cherenkov detector (IWCD) [122]. The idea is to be able to detect and characterize the beam in the same way as at the far detector, with a water Cherenkov detector, but before flavor oscillations occur. The detector will be placed at a distance of about 1 km downstream the production target. It will bring a characterization of the beam composition as well as detection effects with the exact

same technology and target material (water) as the far detector. This is very valuable because some detector and cross-section systematic parameters can, if not monitored or measured properly, modify the observed ratios of neutrinos and anti-neutrinos and of muon and electron neutrinos, mimicking the effect of CP violation on reconstructed spectra and observed asymmetry. A schematic of the initial design can be found in figure 5.3. It will consist in a water tank of about 1 kton, being a cylinder of 10 m high

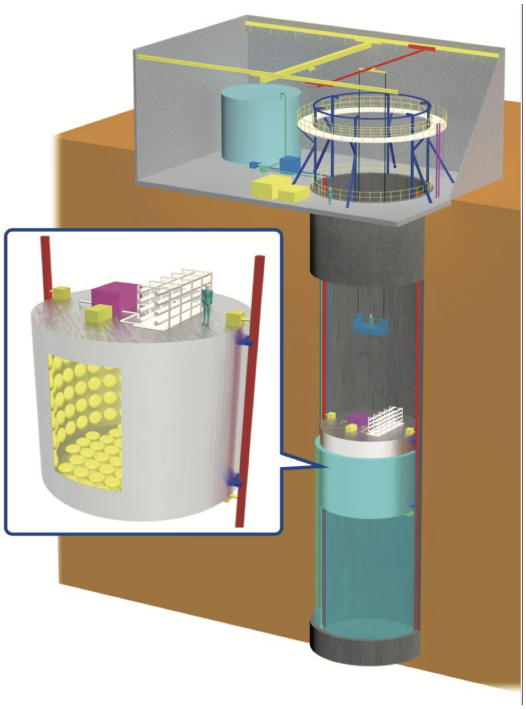

Figure 5.3. *Schematic of the Intermediate Water Cherenkov Detector (IWCD)*

and 10 m of diameter. Just as HK, it will be separated between an outer and an inner detection volumes. It will be filled with pure water at first, with the possibility to add dissolved encapsulated Gadolinium later on for neutron tagging, as it has been done in Super-Kamiokande. The inner part of the tank will be 6 m high with an 8 m diameter. It will use an array of about 500 multi-PMTs equally spaced by 60 cm for detection, the same as the one potentially added to HK. Initially, it was designed to move on a vertical axis along a pit of 50 m in order to span different off-axis angles of the neutrino beam this different neutrino energies, following the NUPRISM design [123]. This would allow to disentangle some systematic and calibration effects from energy differences and measure and study the relationship between true and reconstructed energy. It would also allow for more energy dependent characterizations of the neutrino flux. In the end, this would reduce uncertainties mainly on $\nu/\bar{\nu}$ and ν_e/ν_μ ratios which are crucial to extrapolate constraints on CP violation after oscillation. Even though this might not be the final design, having a water Cherenkov near detector, with same mPMTs and off-axis angle

will be very useful to reduce flux systematic errors and to perform additional cross-section measurements on water, especially for electron neutrinos. It is planned to be ready by 2025.

In order to prepare for IWCD as well as other next generation experiments relying on water Cherenkov detectors such as THEIA in the U.S [124] and ESSnuSB in Sweden [72], a small version of state of the art water Cherenkov detector is being built at CERN. It is called WCTE for Water Cherenkov Test Experiment [125]. It will be a tank of pure water of about half of IWCD size with a diameter of 4.1 m and height of 4 m. Multi-PMTs will also be used. This test experiment will allow for independent calibration and performance evaluation of the detector and its components before being used in neutrino experiments, using a beamline of muons, electrons, pions and protons with an energy range containing those expected at IWCD and HK. For hadrons, this will be achieved by placing a small secondary target together with a spectrometer to monitor the production of low momentum hadrons. It is scheduled to start taking data at the end of 2023, before a secondary run phase including Gadolinium loading.

5.4 Physics program and expected sensitivity

As said before, the operation of HK will allow to collect much more data with a greater efficiency. For the accelerator neutrinos, it is foreseen that, after 10 years of operation, the beam will have delivered 2.7×10^{22} protons on target (POT) which is more than 10 times the accumulated POT so far by T2K. Thanks to the larger and improved HK detector, this is estimated to result in a massive statistics increase. For instance in 10 years, it is expected to detect about 9000 muon neutrinos and 2000 electron neutrinos instead of the about 400 muon neutrinos and 110 electron neutrinos detected so far in 10 years of T2K. This consists in 18 to 25 times more data. Longer exposure with a larger detector will also allow to collect more data for non-accelerator neutrinos. The physics program and expected sensitivities following those improvements will be detailed in the next subsections.

5.4.1 Oscillations with accelerator neutrinos

The main medium-term goal of the long baseline neutrino oscillation (LBNO) program of HK is to discover CP violation in the leptonic sector. Being for now on track for a starting date in 2027, HK has the potential to make that discovery before other experiments such as DUNE. Figure 5.4 shows the sensitivity in $\sqrt{\Delta\chi^2}$ to exclude conservation of CP (which is equivalent to discovering CP violation) as a function of years of operation of HK. It has been estimated with the oscillation analysis of 2018. In particular, the systematic

error model has been adapted to take into account the increase of statistics by scaling errors with a factor $\sqrt{N}$ where N is the relative expected statistics increase after 10 years of HK and to take into account the increased performance of the near detector following ND280 upgrade, as well as the addition of IWCD. This last point resulted in:

- a factor 3 reduction of uncertainties on non quasi-elastic (QE) interactions
- a factor 2.5 reduction of uncertainties on QE interactions
- a factor 2 reduction of uncertainties on $\bar{\nu}$ interactions
- a 10% reduction of uncertainties on neutral current interactions

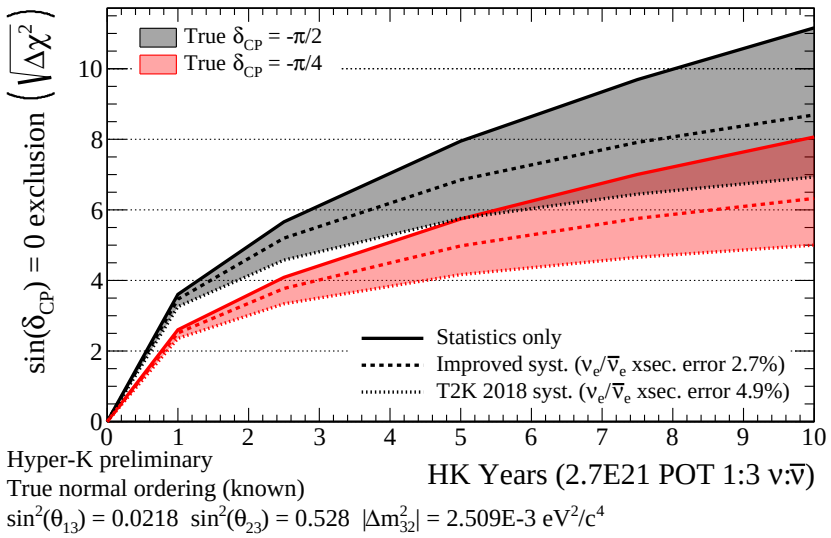

Figure 5.4. *Sensitivity to exclude $sin(\delta_{CP}) = 0$ for true $\delta_{CP} = -\pi/2$ (grey) and $\delta_{CP} = -\pi/4$ (red), as a function of HK years of operation. The shaded areas show the span of possible values, depending on the systematic error models, source: HK collaboration*

Figure 5.4 is also assuming that the true value of δ_{CP} is either the currently favored maximal violation value of $-\pi/2$ (grey) or $-\pi/4$ (red), with normal mass ordering. It is also assumed that the beam operation is such that the ratio between modes $\nu/\bar{\nu}$ is 1 to 3. From this plot it is possible to see that HK has the potential to discover CP violation at the level of 5σ (more or less equivalent to $\sqrt{\Delta\chi^2} = 5$) within just a few years of being online, depending on the true value of the CP phase. It is also important to notice that the systematic parameters grow in importance quite fast as the experiment collects data. In particular, an improvement on the ratio $\nu_e/\bar{\nu_e}$ from the 2018 systematics model as shown by the two dashed lines can have a significant impact on sensitivity. With newer models and dedicated study including with IWCD, it is possible to expect an even greater sensitivity to δ_{CP}.

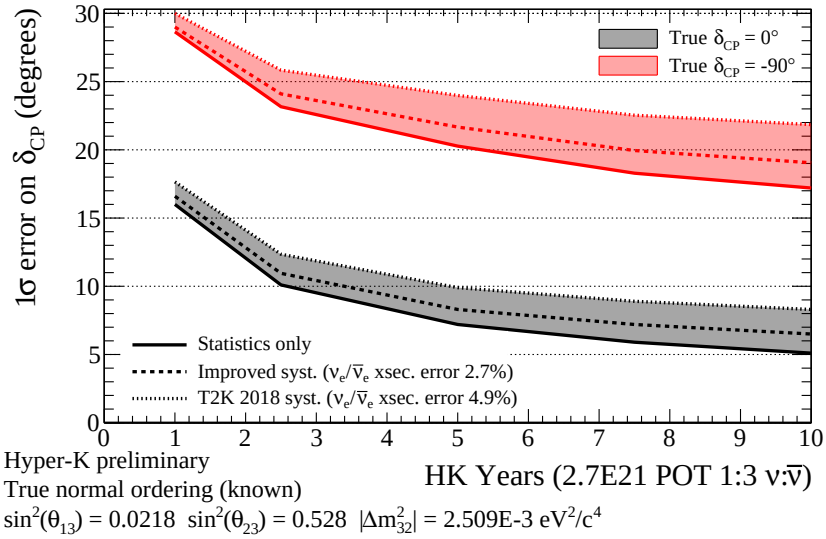

Figure 5.5. *1σ errors on the measurement of δ_{CP} for true $\delta_{CP} = -\pi/2$ (red) and $\delta_{CP} = 0$(grey), as a function of HK years of operation. The shaded areas show the span of possible values, depending on the systematic error models, source: HK collaboration*

After the discovery of δ_{CP}, the next goal will be to measure as precisely as possible its value. Figure 5.5 shows the 1σ errors on the measurement of δ_{CP} for two true values: $\delta_{CP} = -\pi/2$ (red) and $\delta_{CP} = 0$ (grey). It can be seen after ten years of operation, if the value is the favored maximal violation, the precision of HK is expected to be around 20°. This is comparable with what is expected for 10 years of operation of DUNE [126] but will come earlier. Moreover, a potential combination of both experiments results could lead to an even more precise measurement. This is especially interesting in the context of leptogenesis models as they can be distinguished by knowing the value.

As T2K, HK LBNO program will also have sensitivity to the atmospheric oscillation parameters and might, depending on the value of $sin^2(\theta_{23})$, determine the octant. Because a lot of parameters are entangled as explained in Chapter 1, HK will, for precision measurements, benefit from the determination of mass hierarchy that could be done by other experiments with a longer baseline or by its atmospheric neutrino program. For that reason as well, it has been proposed to build a second detector identical to HK in Korea, using the same beam and at a baseline of more than 1000 km. Although this project is ambitious, it would definitely be valuable for the oscillation parameter sensitivity to be able to observe the second maximum of oscillation with the same beam and detector technology, cancelling out some of the flux and detector systematic errors.

Taking more data with the near detector will also allow to greatly improve neutrino cross-section measurements, thus reducing systematic errors on the oscillation analysis.

5.4.2 Atmospheric neutrinos

5.4.2.1 Atmospheric only analyses

Atmospheric neutrinos, which are neutrinos produced by interactions of cosmic rays with the atmosphere, as explained in Chapter 1, are a very abundant source of neutrinos detectable by HK. From models of such production of neutrinos, it is possible to perform oscillation analysis of atmospheric neutrinos. It can bring on lot of information and help disentangle some effects as those neutrinos can have traveled very different distances from 10 km to 13 000 km depending on whether they are coming from above the detector (down-going) or below (up-going), traversing the Earth. Moreover, down-going neutrinos will have essentially oscillated in vacuum whereas up-going ones have gone through different layers of the Earth of various densities as schematized in figure 5.6. As discussed in section 1.2.2, a model of Earth density profile is then needed. Finally, atmospheric neutrinos

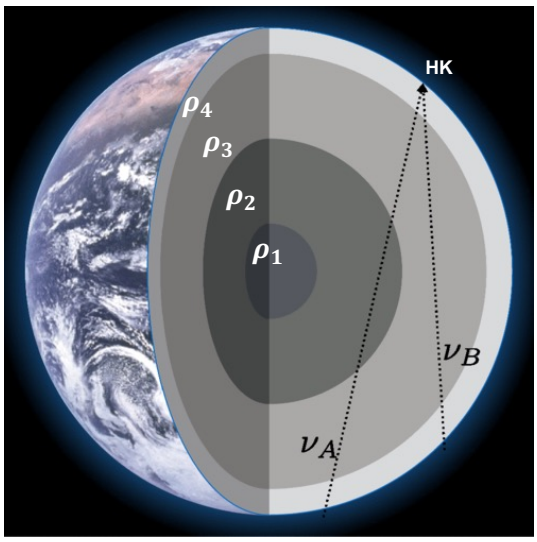

Figure 5.6. *Schematic of the different layers of density in Earth that atmospheric neutrinos can travel through before reaching the HK detector, adapted from [127]*

energies can range from a few MeV to several GeV. However, since the sign of particles can not be identified in a water Cherenkov detector, atmospheric neutrino interactions can not be directly distinguished from anti-neutrino interactions. This can only be done statistically within the analysis. Nevertheless, the cleanest signature of mass hierarchy in the HK detector will come from $\nu/\bar{\nu}$ asymmetry in electron appearance in the up-going high energy atmospheric neutrino flux. Figure 5.7 shows the sensitivity of HK to mass ordering with atmospheric neutrinos only. It can be seen that after 10 years of data taking, for most values of $sin^2(\theta_{23})$ (>0.48) the hierarchy can be determined without any other input. Atmospheric neutrinos are also a great source to better constrain the systematics parameters related to the detector.

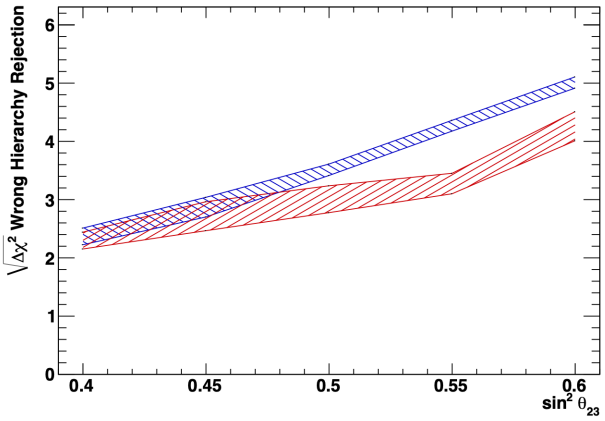

Figure 5.7. *HK's power to reject the wrong mass ordering after 10 years with atmospheric neutrino-only analysis, blue (red) refers to the normal (inverted) ordering, as a function of the true value of $sin^2(\theta_{23})$. The wide band represents the uncertainty on δ_{CP}, figure from [121]*

It is also beneficial to characterize precisely the atmospheric flux with such a larger and highly performing detector since it is a background to many other searches, in particular proton decay measurements and new physics searches.

5.4.2.2 Joint analyses

Because atmospheric neutrinos would bring a lot of statistics and a variety of energies and travelled distances, it is foreseen to perform HK's oscillation studies as joint analyses with beam and atmospheric data. Since a few years people have tried to do a posteriori combinations of both analyses (e.g. [127]) to enhance the sensitivity. However, since SK and T2K, though two separate collaborations, share the far detector Super-Kamiokande, a true joint oscillation analysis is currently being performed. In that context, I have worked on a project studying detector systematic uncertainties. At the moment, the detector systematics are estimated in different ways for the two collaborations. The idea of the project was to try to find a unified method to produce a consistent systematic model for the joint fit. Currently, the far detector uncertainty model for T2K is built from samples of data independent of the analysis such as atmospheric neutrinos and cosmic muons. The estimation of MonteCarlo/data differences, as well as dedicated studies (for instance for Michel electrons) are used to assess systematic parameters values. The construction of the model also relies on a Markov Chain Monte Carlo (MCMC) algorithm on likelihoods to estimate parameters concerning the number of rings or the particle identification. The MCMC outputs systematic parameters constraints from the likelihood computation of spectra after applying the sample selection cuts for different values of parameters. SK can not use atmospheric data/MC differences to estimate the uncertainties as it would

not be independent from their analysis, so they use an MCMC for all of their parameters. The research work I performed aimed at demonstrating a proof of feasibility to use an MCMC for all parameters in both experiments. The idea was also to simplify the method by, instead of having parameters on computed secondary variables used as a figure of merit for selection, only having parameters on the underlying raw variables such as position, visible energy, etc. Only two types of parameters were applied to these variables in that study: shifting (multiplicative) and smearing (additive) parameters. I wrote a Metropolis-Hastings MCMC for that purpose. However, since the number of parameters was very high and the chosen parameters were not targeted at specific physical effects but were very generic, the acceptance rate and run time of the algorithm were not satisfying. This very long term project, not being a priority, was not pursued and the joint fit group chose to do a posteriori combinations of both systematic models moving forward.
As stated before, the future analyses in HK aim at always being joint analyses and it was evaluated [121] to not only constrain better the mass ordering but improve also δ_{CP} for instance. It can be seen in the left-hand side of figure 5.8, that mainly in normal ordering

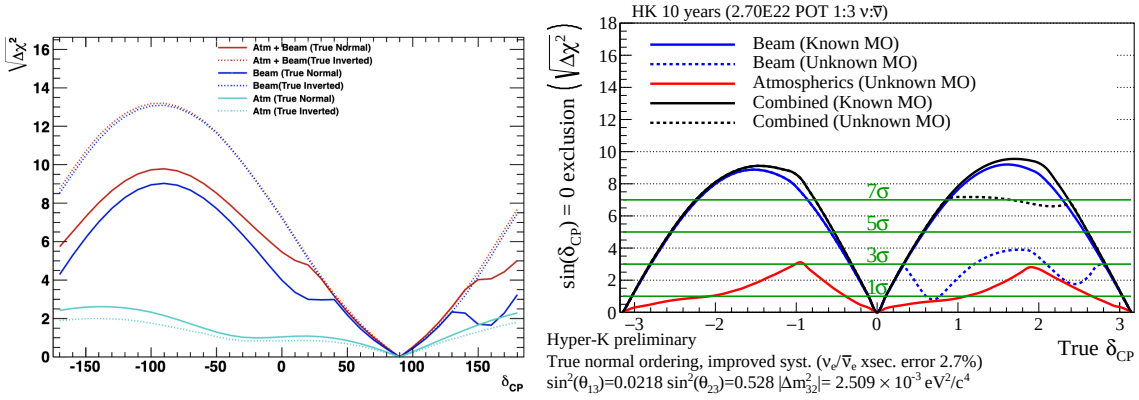

Figure 5.8. *Expected gain in δ_{CP} sensitivity with beam/atmospheric joint oscillation analyses in HK. Left: δ_{CP} in degrees °, assuming 10 years of HK operation and the true value $\delta_{CP} = -\pi/2$, from [121]. Right: CP conservation exclusion as a function of true δ_{CP}, for true normal mass ordering and 10 years of HK, source: HK collaboration*

(solid lines), the gain in sensitivity can be substantial for a joint fit (red curve) compared to an accelerator neutrino only study (blue curve). This is the case even-though the accelerator neutrinos are clearly leading the sensitivity to δ_{CP} compared to atmospheric neutrinos only (cyan curve), having a separation between neutrinos and anti-neutrinos, having a peaked energy spectrum and a fixed baseline at the first oscillation maximum. Similarly, the right plot of figure 5.8 shows the power to exclude CP conservation as a function of the true value δ_{CP}, for true normal mass ordering and 10 years of HK. It can be seen that for some values of non-maximal violation, the combined analysis (black

curve) offers a better sensitivity than the beam-only analysis (blue curve). It is even more the case if the mass ordering is assumed unknown (dashed curves).

5.4.3 Solar neutrinos

Hyper-Kamiokande can also become an observatory for solar neutrinos, in particular distinguishing them by their low energy and the day-night asymmetry. Due to the low energy of solar neutrinos (a few MeV), only electron neutrinos from the Sun can be detected as the Cherenkov kinematic threshold is about 0.8 MeV for electrons but 160 MeV for muons. The detection threshold in the detector is 5 MeV, taking into account the PMTs performance. The large HK detector will be able to collect a lot of solar data in short times, giving the possibility to study the variability of temperature of the Sun for instance. HK could also participate in precision measurement of solar fluxes and solar oscillation studies even if this is not its primary physics goal. Once again, the gain in statistics will compensate for the higher spallation background (neutrinos, electrons, photons or hadrons produced by nuclear decays induced by cosmic muons) due to a shallower site.

5.4.4 Astrophysical neutrinos

Being an astrophysical observatory, and, in particular, participating in the global effort of multi-messengers astronomy is the main secondary physics goal of HK. Since the detection of neutrinos from a supernovae burst by the precursor Kamiokande in 1987 [43], such detectors are being prepared to detect the next close-by explosion efficiently. The larger detector as well as the new PMT technology offering lower dark rate and energy threshold, improves the sensitivity to such transitory fast signals (high event rate during about 10 s). From figure 5.9, it can be seen that HK will be able to detect between 50 000 and 90 000 events in case of a galactic supernova (within 10 kpc) and still 3000 for an explosion at 50 kpc which was the distance for the 1987 supernova. Such large statistics will allow us to reconstruct and study energy spectra of the burst of neutrinos. This is very valuable because from them it is possible to rule out models of supernovae explosions as discussed in [128] since the exact mechanisms are not yet known. The design of HK took into account that goal by choosing a data acquisition system (DAQ) that can handle a high rate of data (up to 10^8Hz for a supernova at 0.2 kpc). The design of the timing system as it will be extensively discussed in the next two chapters, aims at time-tagging each event with a universal time in order to perform coincidence studies with other neutrino detectors and in particular in the context of the supernova global alert system SNEWS [129]. Moreover, a precise internal timing will allow to study the distribution of events as a function of time, which can help discriminate between explosion

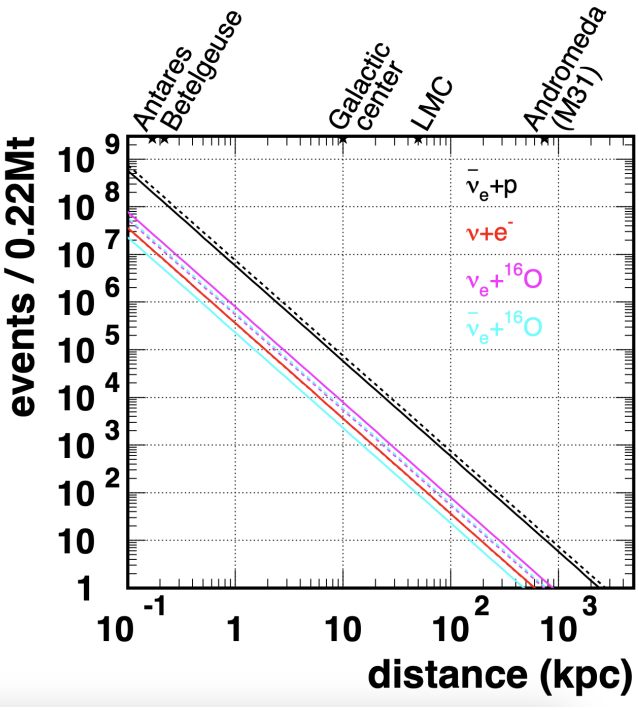

Figure 5.9. *Expected number of detected events at HK as a function of supernova distance for different detection channels (colors), solid (dashed) lines assume normal (inverted) ordering , from [128]*

models predicting various neutrino burst lengths.

As said previously, it is also very interesting to study neutrinos from the diffuse supernova neutrino background (DSNB) or so-called relic neutrinos. They have never been detected so far. They are low energy but, because the event rates in HK are dominated by the spallation background below 16 MeV and the atmospheric neutrinos above 30 MeV, such relic neutrinos can only be observed in that restricted energy range. It has been estimated [121] that after 10 years of HK about 70 relic neutrinos could be detected with a statistical error of 17 events. This corresponds to a significance of 4.2σ, just below the 5σ threshold for DSNB discovery. Running the experiment for longer could allow for its discovery. Moreover, the addition of Gadolinium as in SK would allow to tag neutrons from inverse beta decay. The threshold for relic neutrinos search could be lowered to 10 MeV with that specific signal, including more potential detected events.

A last example of multi-messengers astrophysical neutrino searches is to look for neutrino counterparts to gravitational waves detection. This would also involve timing coincidence. Three cosmic events could lead to such events: supernovae, gamma-ray bursts and mergers that contain at least one neutron star. This has also never been detected and might give very similar signals as for relic neutrinos.

5.4.5 Nucleon decay searches

The first large Water Cherenkov detector built in Japan was for KamiokaNDE which stands for Kamioka (the nearest village to the experimental site) Nucleon Decay Experiment. Indeed, this was the primary goal of the detector when it was designed and started taking data in 1983. It went through an upgrade in 1985 to be able to study solar and atmospheric neutrinos as well and given its success in these areas, it was shortly after renamed Kamioka Neutrino Detection Experiment. However, its primary goal always remained in the physics program, including for its successor Super-Kamiokande. It will naturally be a physics goal of Hyper-Kamiokande as well and has been designed accordingly.

Nucleon decay, and in particular proton decay are processes beyond the Standard Model that violate the Lepton (L) and Baryon (B) numbers conservation. Those processes are predicted by most Grand Unified Theories (GUT) that aim at unifying strong and weak interactions at a scale of $10^{14} - 10^{16}$ GeV. Most of these theories conserve the difference between leptonic and baryonic numbers B-L. Hints of decay of a proton or a neutron are not only a probe to New Physics but would allow to discriminate between different GUT models predicting different values for lifetimes. Proton decay is predicted in the two following favoured channels:

$$p \rightarrow e^{+}\pi^{0} \tag{5.1}$$

and

$$p \rightarrow K^{+}\bar{\nu} \tag{5.2}$$

but Cherenkov detectors are suited to look for various modes. The first favoured mode in Eq. 5.1 is easier to detect as it involves two visible final state particles. The second favored mode (Eq. 5.2) detection relies on the Kaon decay with a lifetime of 12 ns. The kaon decay mostly either in $K \rightarrow \mu\nu$ or $K \rightarrow \pi\pi$ which can be identified in a water Cherenkov detector. The main background for such measurements are the atmospheric neutrino interactions but those often involve a neutron. For that reason, the addition of Gadolinium in water as in SK can enhance the decay search sensitivity, identifying more background events thanks to neutron capture delayed signals. Figure 5.10 shows HK's expected 3σ potential for discovery as a function of years of exposure [121]. Lifetimes (τ) are expressed in years divided by the branching ratio (β) of the specific channel as they are partial decay measurements. The expected performance of HK can be compared to current limits obtained by SK [130, 131] in table 5.1 that presents HK's 90% CL sensitivity for various channels of proton and neutron decays assuming 10 years of exposure. It can clearly be seen that HK will have the potential to improve current limits by a factor 5 to 10.

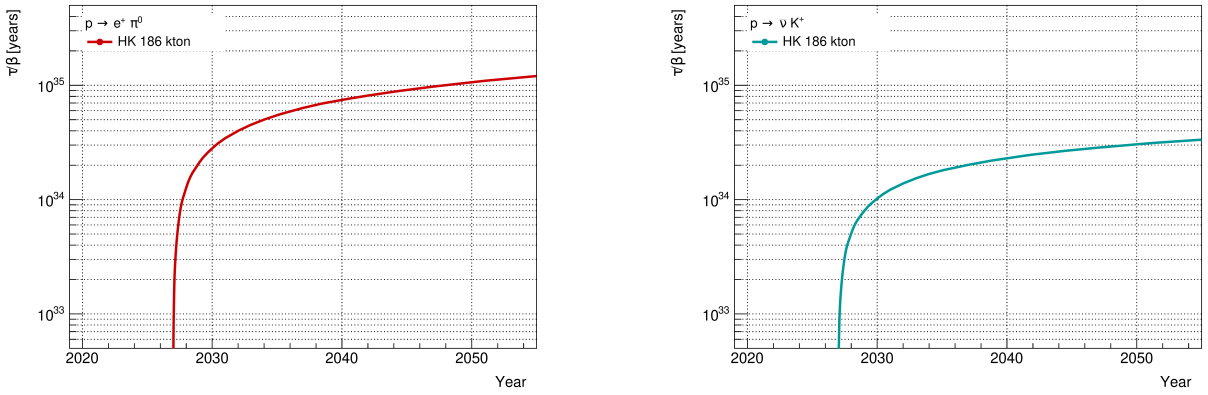

Figure 5.10. *3 σ discovery potential for partial decay lifetime (τ/β) of a proton in HK as a function of years of exposure for the $p \to e^+\pi^0$ channel (left) and the $p \to K^+\bar{\nu}$ channel (right), source: HK collaboration*

Table 5.1. *HK predicted proton and neutron lifetime sensitivity [121] for various channels (assuming 1.9 Mton exposure) compared to current limits from SK (0.316 Mton exposure for π^0 channel and 0.26 Mton for K^+ channel) ([130, 131])*

Mode	Sensitivity (90% CL) [years]	Current limit [years]
$p \to e^+\pi^0$	7.8×10^{34}	1.6×10^{34}
$p \to \bar{\nu}K^+$	3.2×10^{34}	0.7×10^{34}
$p \to \mu^+\pi^0$	7.7×10^{34}	0.77×10^{34}
$p \to e^+\eta^0$	4.3×10^{34}	1.0×10^{34}
$p \to \mu^+\eta^0$	4.9×10^{34}	0.47×10^{34}
$p \to e^+\rho^0$	0.63×10^{34}	0.07×10^{34}
$p \to \mu^+\rho^0$	0.22×10^{34}	0.06×10^{34}
$p \to e^+\omega^0$	0.86×10^{34}	0.16×10^{34}
$p \to \mu^+\omega^0$	1.3×10^{34}	0.28×10^{34}
$n \to e^+\pi^-$	2.0×10^{34}	0.53×10^{34}
$n \to \mu^+\pi^-$	1.8×10^{34}	0.35×10^{34}

5.4.6 Other searches

Hyper-Kamiokande can also be used to perform extra studies which are not the main goals of HK but are carried out of opportunity. These studies include searches for so-called exotic oscillations suggesting the presence of heavy and/or sterile neutrinos or non-standard neutrino interactions. Within the oscillation program, it is also possible to perform tests of the CPT and Lorentz invariance (details in [132]). Finally, HK can be used to probe geophysics of the Earth. This can mean studying the natural radioactivity background for the composition of the nearby rock. More importantly, atmospheric oscillation analyses can probe the whole Earth density model thanks to matter effects in neutrino propagation as discussed in Chapter 1.

5.5 Conclusion

As a conclusion, the Hyper-Kamiokande collaboration has planned a very rich, diverse and exciting physics program. It is mainly focused on two aspects. One is the neutrino oscillation program to constrain oscillation parameters, including mass ordering with both accelerator and atmospheric neutrinos. The other one is multi-messenger astrophysics and in particular the prospect to detect the next supernovae burst in the Galaxy. However, HK will be the worthy successor of KamiokaNDE and SK, keeping the original plan to search for nucleon decay and study solar neutrinos. Finally, one can take the opportunity of HK's large set of data to perform additional studies such as searches for anomalies in oscillations or geophysics studies.
The design of the detector takes into account all these physics possibilities and as a result will allow to have exciting sensitivities in all of them. The following chapters will illustrate this intention to not leave any physics goal aside, with the example of the timing system design, aiming at the best precision possible, beyond the minimal requirements.

Chapter 6

Keeping time in neutrino experiments

The two final chapters of this thesis will focus on one item that needs to be carefully designed and maintained in neutrino detectors: time keeping. To be more precise, each experiment needs to develop a clock generation and time distribution system according to its detection principle and physics goals. This chapter aims at introducing time keeping methods, including the usual figure of merit for time signal stability: The Allan Variance.

Contents

6.1 Requirements and constraints

In the frame-work of HK, within which I have performed the R&D work that will be presented in Chapter 7, there are two types of timing requirements as shown in figure 6.1.

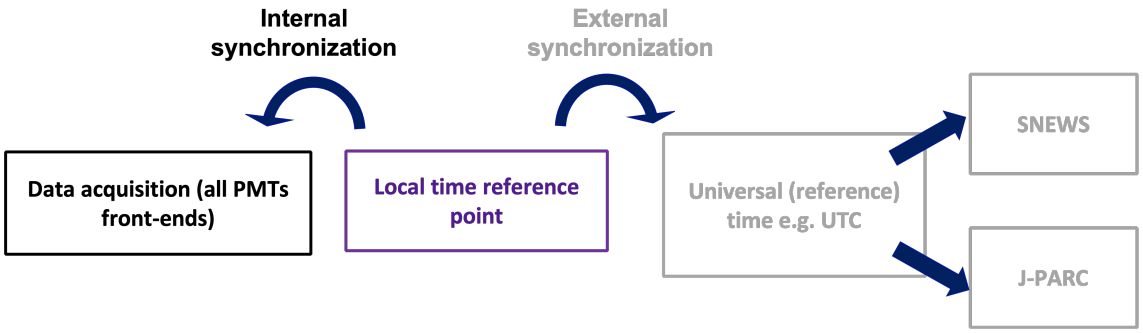

Figure 6.1. *Scheme of the two types of synchronization needed*

The first one can be referred to as internal synchronization. As presented before, HK's far detector is a water Cherenkov detector and the indirect detection of neutrinos relies on the detection of the emitted charged lepton's Cherenkov light. More precisely, the 3D Cherenkov rings have to be reconstructed using signal coincidence between all the photo-multipliers on the walls of the detector so that the lepton flavour can be identified and the lepton energy can be measured. To achieve good precision for this reconstruction, all the photo-multipliers must be synchronized between themselves very accurately. This has been quantified to a requirement of a stability or jitter under 100 ps at the end points of the distribution system [121].

In addition, an external synchronization is needed. It allows to time tag each detected event with respect to the coordinated universal time UTC. This is a necessary feature of the HK detector for two main reasons. One is that T2HK will be a long-baseline oscillation experiment where the neutrino beam from the J-PARC accelerator facility will be detected at both the near and far detectors. Windows of data taking need to be opened when the beam bunches are expected, hence the need for a universal time-tagging of the events between the detectors and the accelerator. Moreover, outside of beam time, HK will be an astrophysical neutrino observatory and in that context time-tagging the neutrino candidates with respect to UTC will allow for comparison with other experiments and detectors. This is very valuable as part of a multi-messengers astronomy physics program. For instance, in case of a supernova explosion burst, UTC synchronization can allow different neutrino observatories to point out to the right region of the sky if the timing precision is sufficient for efficient triangulation; this is the SuperNova Early Warning System (SNEWS) project [129]. To achieve this, it is required to monitor HK's

timing with respect to UTC within 100 ns at least [121].

Once those requirements are met, it is possible to optimize the timing system with the chosen equipment and take advantage of the obtained time precision to perform additional physics studies such as a time of flight measurement that can lead to an upper limit on the neutrino mass as in [133].
A number of constraints and specificities have to be considered when building HK's future timing system. First, the far detector site will be in a valley in a mountain area, 295 km from the near detector. This makes physical links for timing data propagation unfeasible and it also means that satellite signals reception will be limited. The detector is underground which makes the signal distribution a little bit more complex with a necessity to have parts of the system at different locations and as a consequence, a need to monitor all possible delays at each step carefully. Finally, collaboration with the Japanese official time keeping lab has to be established as the experiment is located in Japan and such official input will be needed as explained in the next sections.

6.2 Review of existing systems in the community

Many neutrino experiments have run previously to Hyper-Kamiokande with similar need for precise timing of the detected events. Though the work that will be presented in Chapter 7 is an R&D for a new timing system, it benefits from previous designs and knowledge in the community. This section will give a quick overview of some known existing systems, without entering into details and without being exhaustive.
MINOS, NOνA, OPERA, DUNE and of course T2K are all former, running or future long-baseline neutrino oscillation (LBNO) experiments. IceCube is slightly different neutrino detector but needing time synchronization for the same reasons. All these selected experiments are based on a 'master clock' from which all clock signals are derived. The different frequency signals derived from it are then distributed through mostly custom distribution schemes to the detector end-points, following a layer hierarchy. In most cases, this timing signal is either embedded in or completed with additional information such as calibration delays, time tags from a link to UTC, or even data.
MINOS (Main Injector Neutrino Oscillation Search) was a long-baseline neutrino experiment than ran from 2005 to 2016 in the U.S. The beam and near detectors were at the Fermilab facility (Batavia, Illinois) and the far detector 735 km away in the Soudan mine (Minnesota). Its timing system was built upon Caesium atomic clocks to measure timing precisely and GPS antennas and receivers to perform time transfer (monitoring the alignment) with its near detector [134]. More recently, the NOνA (NuMI Off-Axis Electron Neutrino Appearance) experiment was built and runs since 2013 as the successor

of MINOS. It also uses the neutrino beam from Fermilab but the far detector is a little bit further away (810 km) in Ash River (Minnesota). Its timing system [135] is based on GPS antennas and receivers from which, through a PLL (Phase Locked Loop), is derived the master clock. The signal is then distributed in several stages as said before, through active time distribution modules. An extensive campaign of calibration was made through portable atomic clocks (Rubidium clocks) time transfer [136] to measure delays between near and far detectors with respect to the GPS signals. The MINOS site was used as an intermediate point of comparison in the journey. The idea is to use the portable clock as a reference against which each local time signals are computed.

The OPERA (Oscillation Project with Emulsion-tRacking Apparatus) experiment was specifically designed to detect tau neutrinos from muon neutrinos oscillations over a baseline of 730 km between CERN (France/Switzerland) and the Gran Sasso site (Italie). It was running as a fully completed experiment between 2010 and 2012. Its timing system was originally based, at the far detector, on free-running Rubidium clocks and GPS receivers, but an additional system was designed carefully and installed with the purpose of achieving a great precision to perform a time of flight study. For this, two identical systems were installed at both the near and far detector sites. They relied on free-running Caesium clocks producing a reference clock signal that was then given as an input to a GPS receiver [137]. The obtained timing data were then passed on to the data acquisition system through a custom distribution scheme. Common-view time transfer through GPS was performed to compare timing at the near and far detectors. Calibration campaigns using portable atomic clocks were also performed. Unfortunately, in 2011, the experiment encountered hardware issues that lead to measure a neutrino time of flight shorter than that of the light [138], which was then retracted. Nevertheless, its timing system was designed to achieve a precision of the order of a few tenths of nanoseconds and can be a base model to build new timing systems.

DUNE (Deep Underground Neutrino Experiment) is a future long-baseline neutrino experiment in the U.S., of the same generation as Hyper-Kamiokande but based on liquid argon technology. It aims at starting data taking in 2030, a few years after HK. Its baseline will be of 1300 km between the Fermilab and the Sanford Underground Research Facility (South Dakota). Its primary clock signal is coming from a GPS-disciplined oscillator [139]. Its master clock is also composed of a Rubidium clock to detect instabilities. It is interesting to note that the requirements for DUNE are very similar to those for HK, with a link to UTC within 10 to 100 ns and jitter between end-points of the order of 10 ps.

IceCube is a neutrino observatory installed deep inside the ice of the South pole in Antarctica since 2010. Though it is not a long-baseline experiment which needs to align timing between two sites, it requires very good timing precision to coordinate multi-messenger astrophysics searches and to reconstruct Cherenkov light signals as in HK. To this end, it

uses as well GPS-disciplined oscillators [140] and performs calibration between detectors modules thanks to two-way signal exchanges.
Finally, the true sister experiment of Hyper-Kamiokande, T2K uses both a local clock and a GPS-disciplined Rubidium clock to build the master clock signal on both the J-PARC and SK sides [133, 141]. The current system at SK will be further discussed in section 7.2.2.

All these experiments also include redundancy, hot-spare items and calibration procedure to ensure the robustness of the system. Despite some specificities and different choices depending on the scientific goals of the experiments, it can be noticed that there are a lot of similarities in the architecture of the distribution process for the timing signals and in the use of recurrent items: atomic clocks and GPS-type satellites antennas and receivers. Those elements will be further explained in the next two sections.

6.3 Generalities on atomic clocks

One thing that can be noticed from the previous section is that atomic clocks are a popular part of timing systems. This is because they are the most precise source of frequency signal (under certain conditions as it will be seen) and are used as official standards. The second, for instance, is currently officially defined as 9 192 631 770 periods of the radiation corresponding to the transition between the two hyperfine levels of the unperturbed ground state of the ^{133}Cs atom [142], with an uncertainty of order of 1 part per 10^{16}. Moreover, the international atomic time (TAI) is produced through a combination of atomic clocks maintained by expert timing laboratories (referred to as national time-service laboratories) in such experimental conditions that the frequencies are unperturbed (no electric or magnetic fields, no movement, monitored temperature, etc). Many corrections are also taken into account such as relativistic effects and non-uniformity of the gravitational field. The coordinated universal time (UTC) is then built from TAI, differing only by an integer number of seconds, called leap seconds, to keep UTC in phase with the rotation of the Earth [143]. Those universal times are maintained by the *Bureau International des Poids et Mesures* (BIPM) in Paris, France. In more details, each time-service lab creates local realizations of UTC known as UTC(k) from their ensemble of clocks and the offset with respect to the global UTC is published monthly by a BIPM circular called Circular T [144].
There exist different types of atomic clocks using different atoms, all alkalines. As said before, one source of uncertainty comes from the relativistic corrections that need to be applied. To this end, the velocity of the atom has to be assumed given the temperature. This effect can be reduced by cooling of the atoms for the most accurate clocks (cold atoms fountains). However, the velocity will always be higher for a lighter atom. This is

one argument to choose which are the relevant atoms to build a clock. Another one is the frequency of the transition, a higher one leading to more accurate measurements. Those two main arguments make the Caesium 133 the best candidate. It is indeed used a lot by time-service labs and has the best overall stability. However, hydrogen masers show a better stability at short terms thanks to a narrower width of the resonance. A very common and widely commercially available frequency standard is the Rubidium clock. Its working principle will be detailed here so as to describe how atomic clocks work in general, taking the example of the clock mostly used in the work presented in Chapter 7.

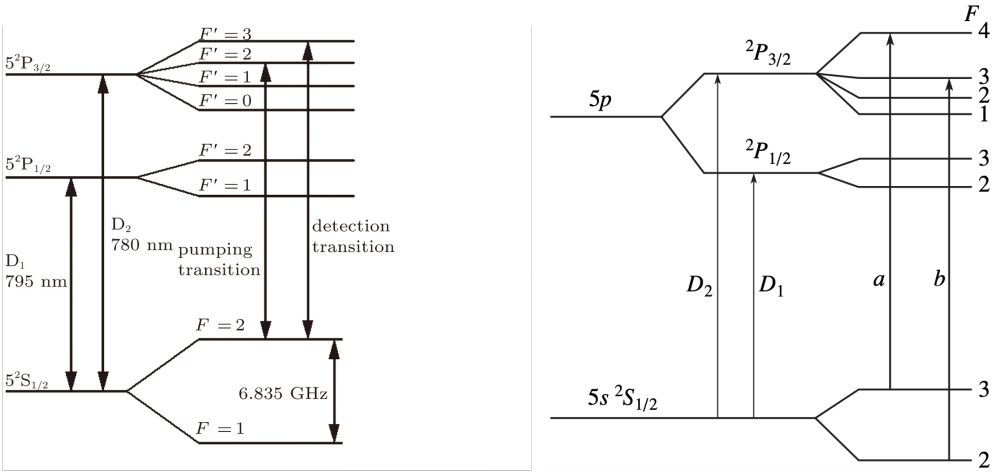

Figure 6.2. *Schematic of energy levels and relevant transitions for Rubidium 87 [145] (left) and for Rubidium 85 [146] (right)*

Lets start by noticing that the energy levels of Rubidium 87 are split into hyperfine sub-levels in figure 6.2 (*on the left*). The hyperfine structure is due to the coupling of the isospin of the nucleus with the magnetic field created by the movement of the electrons 'around' it. Overall, the Rubidium clock is composed of a ^{87}Rb lamp, a Rubidium 85 buffer gas, a resonant cavity filled with ^{87}Rb and a system of frequency generator disciplined by the photon absorption observed in the resonant cavity, as can be seen in figure 6.3. The working principle is based on a careful selection of the emitted photons by the initial lamp so as to only trigger one transition (with one specific frequency) in the resonant cavity and obtain optical pumping. The output frequency is then disciplined by injecting it inside the cavity and monitoring the effect.
In more details, the ^{87}Rb lamp where the atoms experience several possible transitions will radiate photons of several energies towards the ^{85}Rb buffer gas. Those photons belong to either the D1 = 795 nm spectral line or the D2 = 780 nm one. They come from the de-excitation of either $P_{3/2}$ or $P_{1/2}$ towards the fundamental level $S_{1/2}$. An interference filter is placed before the buffer gas to select only the D2 line (the filter is not sensitive to

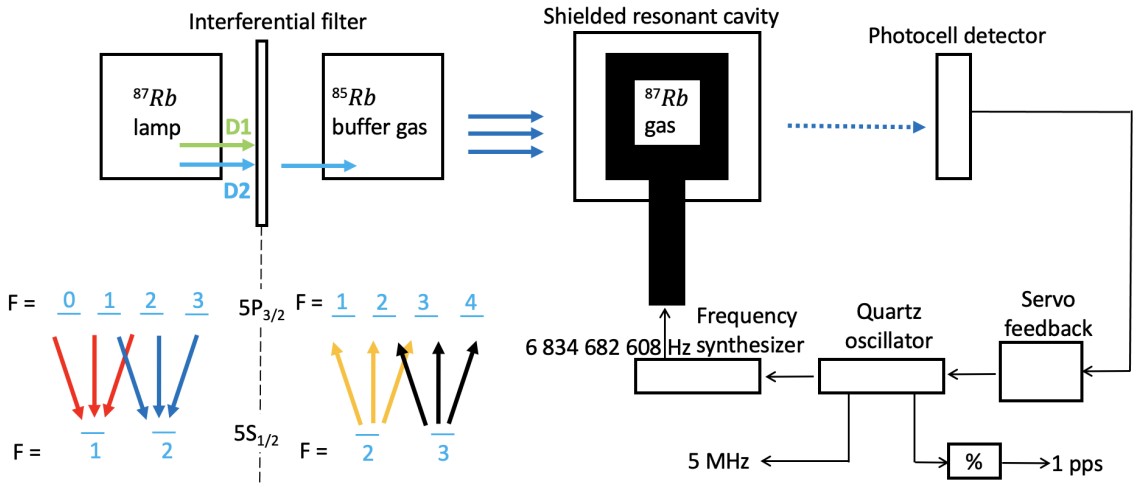

Figure 6.3. *Schematic of the components of a Rubidium clock adapted from [147]*

the hyperfine structure because of the energy proximity of the split levels). From atomic physics we know that only transitions with $\Delta F = -1,0,1$ are allowed, F being the quantum number associated with hyperfine interactions. As a result, photons reaching the ^{85}Rb gas necessarily come from the following 6 possible transitions:

$$
\begin{aligned}
&(1) \quad 5P_{3/2}(F=0) \rightarrow 5S_{1/2}(F=1)\\
&(2) \quad 5P_{3/2}(F=1) \rightarrow 5S_{1/2}(F=1)\\
&(3) \quad 5P_{3/2}(F=2) \rightarrow 5S_{1/2}(F=1)\\
&(4) \quad 5P_{3/2}(F=1) \rightarrow 5S_{1/2}(F=2)\\
&(5) \quad 5P_{3/2}(F=2) \rightarrow 5S_{1/2}(F=2)\\
&(6) \quad 5P_{3/2}(F=3) \rightarrow 5S_{1/2}(F=2)
\end{aligned}
$$

The first 3 transitions correspond to the red arrows in figure 6.3 and the three last to the blue arrows. Referring to the right part of figure 6.2, we notice that the structure of ^{85}Rb is similar to that of ^{87}Rb, with D1 and D2 lines at the same energies but with a different hyperfine structure. There is a degeneracy in energies for certain levels between both Rubidium isotopes. This way, the ^{85}Rb gas buffer, originally in its ground state $S_{1/2}$ can absorb photons coming from the D2 line in the following way:

$$
\begin{aligned}
&(7) \quad 5S_{1/2}(F=3) \rightarrow 5P_{3/2}(F=2)\\
&(8) \quad 5S_{1/2}(F=3) \rightarrow 5P_{3/2}(F=3)\\
&(9) \quad 5S_{1/2}(F=3) \rightarrow 5P_{3/2}(F=4)\\
&(10) \quad 5S_{1/2}(F=2) \rightarrow 5P_{3/2}(F=1)\\
&(11) \quad 5S_{1/2}(F=2) \rightarrow 5P_{3/2}(F=2)\\
&(12) \quad 5S_{1/2}(F=2) \rightarrow 5P_{3/2}(F=3)
\end{aligned}
$$

Transitions (7),(8) and (9) will not occur in our case since there is not a F=3 level on the fundamental $5S_{1/2}$ state of ^{87}Rb. Photons coming from the ^{87}Rb lamp through transitions (4), (5) and (6) (in blue in figure 6.3) will respectively be absorbed by the buffer gas through transitions 10, 11 and 12 (in orange in figure 6.3). Only photons from transitions (1), (2) and (3) towards the fundamental state of hyperfine level F = 1 will go through (in red in figure 6.3). The next component of the clock is a shielded resonant cavity filled with ^{87}Rb gas. Thanks to the careful selection explained before, photons arriving at this step can only stimulate the fundamental level with F = 1. The following de-excitation can be towards F = 1 or F = 2 fundamental levels without preference. However, after several cycles of excitation of F = 1 and de-excitation, one can understand that the cavity becomes saturated in F = 2 states and no longer has atoms in the F = 1 state. This is the optical pumping phenomena that was described by Alfred Kastler in the 50's. Photons from the initial lamp can no longer be absorbed and the cavity becomes transparent to those. The frequency of the full process from $5S_{1/2}(F = 1)$ to $5S_{1/2}(F = 2)$ is $f_0 = 6\ 834\ 682\ 610.904$ Hz. So as to build a frequency standard from this, a frequency f close to f_0 is injected to the cavity and the luminosity after the cavity is monitored. Thanks to a servo feedback from the luminosity measurement, f can be maintained as close as possible to f_0, corresponding to a maximal luminosity. The output signals of the clock are then built from f.

To specify a term used in the previous section 6.2, some atomic clocks can be disciplined by an external reference. For instance for the Rubidium clock, this means that the output frequency can be adjusted, through a small variable magnetic field and a PLL in order to follow the external input. This was the example of a Rubidium clock, other atomic clocks rely on similar atomic physics and optical pumping items.

As a side note, atomic clocks are based on micro-wave transitions. Optical clocks are more and more studied nowadays to improve even further the stability that can be achieved. They are generally based on induced forbidden electronic transitions of certain atoms (Ca, Yb, Sr,...) in the range of optical frequencies. Most of the uncertainties that can be reduced have been reduced in the most advanced atomic clocks and they are now limited by the width of the transition. Optical clocks present a narrower bandwidth; this is why they could become the most stable standard in the future.

6.4 Generalities on GNSS signals

As we have seen, GNSS (Global Navigation Satellite Systems) receivers and antenna are almost always a part of a timing system. We will discuss in this section about GNSS

to be more general; GNSS including the GPS (Global Positioning System) developed by the U.S. military but also any other satellite constellations available to the public.

6.4.1 Introduction to GNSS signals

The signals that can be received are based on common standards.
Satellite's signals are sent in codes modulating a carrier frequency in the order of GHz and a navigation message. For GPS, the two carrier frequencies are L1 = 1 575.42 MHz and L2 = 1 227.60 MHz. Some codes are available to the public (commercial receivers have the decryption key and firmware), some other, more precise, are restricted to authorized users such as the military of the provider's country. For GPS, the public code is referred to as C/A (coarse acquisition) and has a sequence rate of 1.023 Mbit/s and a period of 1 ms whereas the precision code P has a sequence rate of 10.23 Mbit/s and a period of 280 days. Navigation messages contain ephemeris (of both natural and artificial objects), and the almanach which gives the full status of the constellation, including ionospheric and tropospheric models to compute corrections, a UTC-driven time, etc. Data carried by the modulated signals provide mainly three types of information [148]. First, one can extract from the signal the pseudo-range, which is the satellite-receiver distance "seen" by the receiver, meaning computed from the speed of light, the time of arrival given in the receiver's time base and the time of emission of the signal, given in the satellite time base (transmitted in the navigation message). The second 'observable' is the carrier phase. The evolution of this phase also infers information on the pseudo-distance between the receiver and the satellite which would actually be more accurate as long as the receiver does not stop tracking the satellite. However, the phase contains a random integer number of wavelength that makes it more difficult to use in case of loss of lock on the satellite. The third information from the satellite data is the Doppler shift to consider in all measurement analyses. It is determined by the relative speed of the satellite with respect to the receiver (and an offset from clock errors) and is in practice the time derivative of the carrier phase. The standard raw output of the receiver is in the file format of RINEX (Receiver Independent EXchange) [149] where all necessary information and variables can be found.
When used to determine position, at least four satellites need to be tracked simultaneously by the receiver so that it can compute its 3-dimensional position by triangulation from the pseudo-range data, using the so-called navigation equations.

6.4.2 Principle of time transfer

In our case, the receiver is intended to be used as a timing receiver. To that end, the exact position of the antenna needs to be first determined. More precisely, the Antenna Phase Center (APC, [150]) for each carrier frequency is needed. It corresponds to the apparent source of radiation. In general, 24h of data are enough to determine the position of the antenna with a precision of tenth of mm. To obtain the GPS coordinates of both APC and ARP (Antenna Reference Point, frequency independent) of the antenna, the RINEX file for 24h of data can be submitted to specialized national institutes through free web applications that run navigation algorithms (precise point positionning (PPP) techniques). Governmental Institutes providing this service are for instance the National Resources Canada (nrCAN [151]) institute or the French Institut Géographique National (IGN [152]).

How can GNSS signals help in building a timing system ? Mostly because they provide a link to the UTC: they provide a comparison between the receiver's time base and the satellite's time base, as will be explained later, and the satellite's time base is regularly corrected to stay close to UTC. Moreover, satellites can be used to perform time transfer. Time transfer consists in comparing two time bases which are physically separated. In the case of linking the timing system of an experiment to UTC, the two time bases to compare are the reference frequency distributed to the experiment and the time base of the local expert lab. This would give the time differences between the experiment time and the local UTC(k), which can then be converted into global UTC if needed as described in section 6.3.

There are several time transfer techniques that can be employed. Ethernet can be used with Precision Time Protocol (PTP) but the precision of those cannot be monitored externally and thus cannot be known which is not ideal for very precise applications. It also implies a common network between the two time bases to compare. Signals can also be exchanged through optical links and compared with time interval or frequency counters. In that case, all propagation delays must be taken into account carefully. In order to do so, CERN has developed the White Rabbit protocol which is now widely used by the high energy physics community achieving sub-nanosecond accuracy. It combines PTP with phase delays measurements in both ways and synthonization [153] [154]. Nevertheless, its accuracy is guaranteed up to 10 km only in its initial design (even-though it has been used on longer distances) and once again it implies to draw optical fibers between the two sites. For a wireless time transfer, the best solution is to use GNSS satellites as intermediates. One technique that will be of particular interest in Chapter 7 is the common-view technique that is illustrated in figure 6.4. It consists in using satellites that were seen (in view) at the same time at both sites so that most common delays cancel

out [155]. This is ideal if both sites are sufficiently close (same region of the world) to each other. Otherwise, the all-in-view technique can be used. In consists in using all possible satellites visible at each site. The only components that do not cancel out are the satellite clock estimate and the ephemeris estimate and it has been showed [156] that with a proper averaging they do not degrade the performance of the transfer too much.

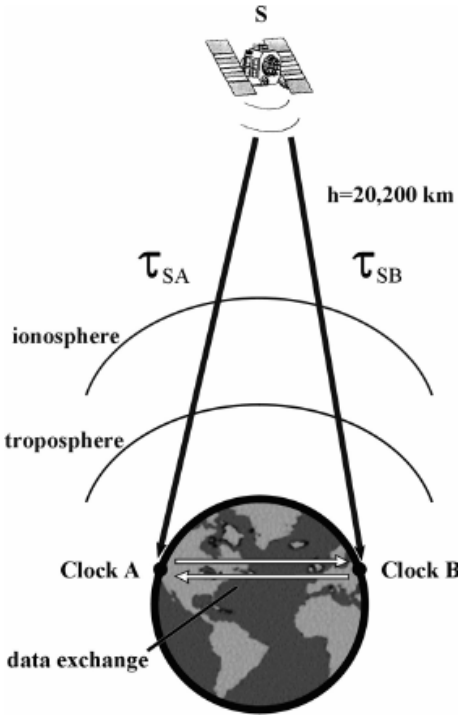

Figure 6.4. *Illustration of the common-view time transfer technique [155]*

6.4.3 Details of time transfer with GNSS signals

Let's come back in more details on the output of the GNSS receiver. As said before, it provides a comparison between the receiver's time base and the satellites' one. Indeed, the difference can be computed from the pseudo-range P (in meters) in that way:

$$P = \Delta D + \Delta d \tag{6.1}$$

with ΔD the physical distance between the receiver and the satellite and Δd the pseudo-distance due to the time bases difference. Let t_1 be the emission time of the signal from the satellite and t_2 the reception time at the receiver. In addition, let ^{r} and ^{s} indices

denote respectively the receiver and the satellite time base. We can then derive:

$$\begin{aligned} P &= \Delta D + \Delta d \\ &= c\,(\Delta T + \Delta\tau) \end{aligned} \tag{6.2}$$

with c the speed of light, ΔT the physical time of propagation and $\Delta\tau$ the contribution of the time base difference to the pseudo-range in the form of a time difference. Indeed, one can write, under the assumption that the frequencies of the two time bases are close enough:

$$\begin{aligned} \Delta T &= t_2^r - t_1^r \\ &= t_2^s - t_1^s \end{aligned} \tag{6.3}$$

and

$$\begin{aligned} \Delta\tau &= t_1^r - t_1^s \\ &= t_2^r - t_2^s \end{aligned} \tag{6.4}$$

One can note that the raw information that the receiver has are t_1^s the emission time in the satellite base time (included in the navigation message) and t_2^r the reception time in the receiver time base:

$$P = (t_2^r - t_1^s) \times c \tag{6.5}$$

From Eq. (6.3) and (6.4) and (6.5) , it can be inferred:

$$\begin{aligned} t_2^r - t_1^s &= 2\Delta T + t_1^r - t_2^s \\ &= 2\Delta T + t_1^r - t_2^s - t_1^s + t_1^s \\ &= 2\Delta T + \Delta\tau - \Delta T \\ \Rightarrow \Delta\tau &= t_2^r - t_1^s - \Delta T = \frac{P}{c} - \Delta T \end{aligned} \tag{6.6}$$

P is measured and the physical propagation time ΔT can be computed because the exact positions of the antenna are known as well as these of the satellites from navigation information. Thus, we have proved with Eq.(6.6) that $\Delta\tau$, the comparison between both time bases, can be inferred from the information gathered in the RINEX output files. In fact, many corrections and delays also have to be applied due to effects of the ionosphere and troposphere on the signal propagation, the rotation of the Earth, relativistic effects and so on. The necessary information is contained in navigation messages. In some receivers such as the Septentrio PolaRx5 [157], the whole calculation of delays to apply as well as the extraction of the time bases comparisons can be done and outputted in another

standard format called Common GNSS Generic Time Transfer Standard (CGGTTS [158]) format. In particular, the time differences between the receiver time and the satellite time is written in units of 0.1 ns; the full detail of the output format can be found in Appendix B.

The receiver makes that comparison every 30 s and tracks the satellite for 13 mn; there is for retro-compatibility reasons a 3 mn gap which leads to having in the output one point of comparison every 16 mn (the receivers makes regressions between all points of 30 s and applies the corrections mentioned before). Because the idea is to build a very precise time base, those receivers can also apply delays that need to be taken into account and measured before. Those are physical inherent delays of the components of the system such as cable delays which can be measured thanks to a vector network analyzer (VNA) or any internal delays [159]. Another thing to take into account to achieve a great precision is that GNSS signals are in the range of GHz which means that they can be reflected on thick metallic surfaces such as buildings and thus make the pseudo-range measurement incorrect. In urban area, an elevation filter that removes signals coming from low elevation can help overcome that effect. The GNSS signals can also be absorbed, meaning that the antenna has to have a clear view of the sky to receive signals. Mountains such as in the HK site area can block the signals as will be discussed in section 7.2.2.

How a GNSS receiver can compare its own time base to the GNSS has been extensively explained. Two questions remain: What is the receiver's time base and how exactly can one link it to a local UTC(k) ? The answer to the first question is that the receiver has an internal frequency but it is not very precise and so as to relate the output to the experiment's time base it would require yet another comparison. Fortunately, the most recent receivers can take into account an external frequency that will by-pass the internal one. For the external frequency, both a 1 pulse per second (PPS) signal and a 10 MHz frequency are needed as the 10 MHz signal will be used to measure time intervals between PPS signals. In particular, the external frequency can be the experiment's time base signal. This way the output of the receiver in the CGGTTS files will directly be the comparison between the experiment's time base and the satellites' ones. The last step is to perform time transfer with the local time-service laboratory. As it has been showed, in CGGTTS files computed time differences between the site of the receiver and the GNSS time (say, GPS if that is the used constellation) are stored. Using the common-view technique [155] as illustrated in figure 6.4, one can combine the time differences $\Delta\tau_A = t_A - t_{GNSS}$ and $\Delta\tau_B = t_B - t_{GNSS}$ by choosing the satellites seen at both sites at the same time in order to cancel out all satellite-specific uncertainties and the GNSS time in such a way that what remains is $t_A - t_B$. If site A is the experiment's site and site B is the local UTC (UTC_k) reference institute, this is $t_{experiment} - UTC_k$.

6.5 Estimating stability: the Allan Standard Deviation

As it has been stated in section 6.1, the requirements for HK's timing system are expressed in terms of stability. In this section, how stability can be measured and characterized will be detailed. In particular, we will describe the mathematical tool that will be used in the next chapter.

First of all, it is important to acknowledge that the measurement of a signal's stability can never be absolute. It will always be a relative characterization against a reference signal that is known to be more stable than the signal under test. Stability can be evaluated in both the time domain and the frequency domain [143]. In general, when the signal is a 1PPS signal the measurement is performed in the time domain. In that case, the data are the time intervals between the raising edges of the measured signal and of the reference signal for each pulse, using a time interval counter. The study of the evolution of this time offset will provide the information on the stability. Another common situation is that the signals in question are sinusoidal and of a higher frequency than the 1 Hz of PPS signals. In that case, the measurement will be performed in the frequency domain. The data will be the ratio of frequencies for each cycle of measurement using a frequency counter and, following the same idea as in the time domain, the evolution of this ratio defines the stability of the signal under test.

The precision of clock signals depends on the time scale and this needs to be characterized so as to collect all relevant information to the use of the clock signal. This is why it is not sufficient to look at the variations of the raw data (time intervals or frequency ratios) and a specific statistical tool has to be used. This is the Allan variance or Allan standard deviation (ASD). It was first introduced by Dr David Allan in 1966 [160] and became the standard analysis tool for timing stability. The idea is to not only compute the variance between all points of data which is the variance at the sampling rate of data taking τ_{data}, but compute it also at any other longer time scales τ up to half of the total length T of the data sample. To achieve this, one should take data at the highest frequency possible (this limit depends on the technical specifications of the counter used to make the measurement and the desired sensitivity which needs to be lower than the result of the measurement). Then, the computation of the Allan variance will do the following:

For each value of averaging or sampling τ, with $\tau_{\text{data}} < \tau \leq \frac{\text{T}}{2}$, one builds adjacent intervals of length τ in the data. An average value is then computed for each interval and the 2 by 2 variance is computed between interval. This gives a variance value different for each value of averaging time τ, so for different time scales. For each value of τ, all data points are used in the computation. A variant of Allan deviation was introduced: the

overlapping Allan Variance. Its specificity is only the way the different intervals are built: they are overlapping. This induces correlation between data points but in general the gain in statistics to compute the variance overcomes the correlation in terms of precision of the result [161]. In general, it is the deviation that is represented as a function of τ. This allows to visualize the stability performance of the signal at different time scales. It is not a representation of variations over the time of data taking because, as said before each point was computed with all the data.
The general formula for Allan variance is given by [162]:

$$\sigma_y^2(\tau) = \frac{1}{2}\langle\ (\overline{y}_{n+1} - \overline{y}_n)^2\ \rangle \tag{6.7}$$

where y is the raw data in the form of frequency ratios, $\bar{y}$ its averaged value on one interval, n is the index of the intervals, and where $\langle\rangle$ denotes an average over all intervals. If the data x_i are in the time domain, the formula is:

$$\sigma_y^2(\tau) = \frac{1}{2\tau^2}\langle\ (x_{n+1} - 2x_n + x_{n-1})^2\ \rangle \tag{6.8}$$

The overlapping Allan variance for frequency data is given by:

$$\sigma_y^2(\tau = m\tau_0) = \frac{1}{2\times(N-2m)} \times \sum_{i=1}^{N-2\times m} (\overline{y}_{i+m} - \overline{y}_i)^2 \tag{6.9}$$

and for phase/time data:

$$\sigma_y^2(\tau = m\tau_0) = \frac{1}{2\times(N-2m)\times\tau^2} \times \sum_{i=1}^{N-2\times m} (x_{i+2m} - 2x_{i+m} + x_i)^2 \tag{6.10}$$

where N is the total number of raw data points and τ_0 the data taking rate.

Looking at the dependence of this variance on the time scale, one can extract information on the noise types involved in the signal under test. Allan deviation can actually be related to the Power Spectral Density (PSD) $S_y(f)$ of the signal in the following way [162]:

$$\sigma_y^2(\tau) = \int_0^{+\infty} S_y(f)\ |H(f)|^2\ \frac{\sin^4(\pi f\tau)}{(\pi f\tau)^2}\, df \tag{6.11}$$

where $|H(f)|^2$ is the detector transfer function that can be considered independent of f and ignored in the case of a frequency measurement with a frequency counter. From this relation (6.11), one can derive the behavior in terms of Allan Standard Deviation (ASD) of typical relevant types of noise. For instance, for a frequency white noise, $S_y(f)$ will be

a constant h_0 [163], so the corresponding variance can be written from (6.11) as:

$$\sigma_y^2(\tau) = \int_0^{+\infty} h_0 \frac{\sin^4(\pi f \tau)}{(\pi f \tau)^2} \, df \tag{6.12}$$

with the following variable change:

$$\begin{aligned} x &= \pi f \tau \\ dx &= \pi \tau df \end{aligned} \tag{6.13}$$

One can obtain:

$$\sigma_y^2(\tau) = \frac{2h_0}{\pi\tau} \int_0^{+\infty} \frac{\sin^4(x)}{x^2} \, dx \tag{6.14}$$

The remaining integral in Eq.(6.14) converges and thus gives a constant. From Eq.(6.12) and Eq.(6.14), it can be deduced that the ASD for a frequency white noise will behave as:

$$\sigma_y(\tau) \propto \sqrt{\frac{1}{\tau}} \tag{6.15}$$

which is a slope of $-\frac{1}{2}$ in the usual log-log scale ASD plots. Let's note that this makes sense physically as averaging a white noise over a longer period of time indeed decreases the sensitivity to those variations, increasing the precision of the result.
For a random walk noise in frequency, like a Brownian noise, $S_y(f)$ will go as $h_{-2}f^{-2}$ [163], so the corresponding variance can be written from Eq.(6.11) as:

$$\sigma_y^2(\tau) = \int_0^{+\infty} h_{-2} \; f^{-2} \; \frac{\sin^4(\pi f \tau)}{(\pi f \tau)^2} \, df \tag{6.16}$$

With the same change of variable Eq.(6.13) and with the same logic, the variance can be found to be:

$$\sigma_y^2(\tau) = 2h_{-2}\pi\tau \int_0^{+\infty} \frac{\sin^4(x)}{x^2} \, dx \tag{6.17}$$

from which the deviation behavior can be inferred to be as follows:

$$\sigma_y(\tau) \propto \sqrt{\tau} \tag{6.18}$$

which is a slope of $+\frac{1}{2}$ in the usually represented log-log scale ASD plots.
With the same types of calculation for the most common noises in frequency and in phase, the summary of expected log-log slopes for ASD has been established and is represented in figure 6.5. As can be seen in this figure, Allan deviation do not allow to distinguish between Phase white noise and flicker phase noise; this is also the case of Overlapping Allan deviation. To remedy this, a more sophisticated way to compute Allan deviation

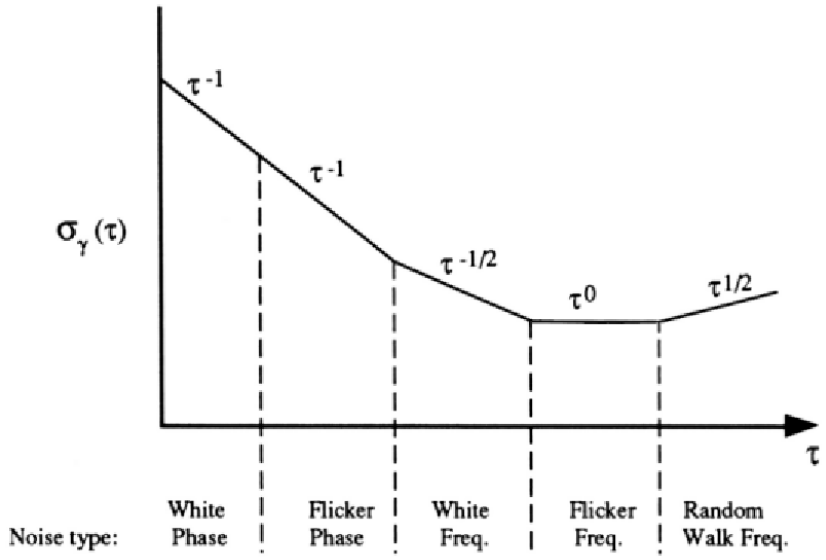

Figure 6.5. *Slopes expected on ASD curves for 5 most common noise types [143]*

given by Eq.(6.19), called Modified Allan deviation has been introduced in 1981 [164]. It involves an additional sum compared to Eq.(6.9):

$$Mod\sigma_y^2(\tau) = \frac{1}{2m^2} \left\langle \sum_{i=1}^{m} (\overline{y}_{i+m} - \overline{y}_i)^2 \right\rangle \tag{6.19}$$

with the same variables and notation as in (6.7) and (6.9).

In practice, in Chapter 7, the Overlapping Allan variance only will be used because there will not be any need to separate phase white noise and flicker phase noise for these studies.

6.6 Conclusion

This chapter has given an overview of time keeping and provided the reader with the prerequisite to understand the studies presented in Chapter 7. This overview included the timing requirements for HK, the standard time-keeping technologies and how they are used for neutrino experiments, as well as the statistical tools for clock signal analysis and interpretation.

Chapter 7

Development of clock generation for HK

This chapter will present the R&D work that was performed towards designing Hyper-Kamiokande's timing system. This work was both one of characterizing and choosing the elements and their connections for the system and of producing simulations in order to study relevant noise types and the different possible corrections that can be applied in the context of HK. Each chosen element will be separately characterized before the full system performance will be studied for two set-ups. On the analysis side, the simulations that have been developed so as to test and choose correction methods for the timing signal will be detailed together with the obtained results.

Contents

7.1 Our proposed solution

As it has been described in Chapter 6, the two key elements to timing systems in particle physics experiments, and in particular for long baseline neutrino experiments where time has to be transferred from one site to another, are atomic clocks and GNSS antenna and receivers. Still in the previous chapter, it has been explained that atomic clocks have demonstrated high stability performance to establish time standards and GNSS signals are commonly used to transfer time, meaning establishing a time link between two time bases, including providing a link to the official time UTC. This motivates the presence of both those elements at the heart of our proposed solution for HK. The process of design for this system included frequent discussions with SYRTE experts. The system will be built from a single point of reference. This point of reference will distribute to the whole system a clock signal built from an atomic clock, a rubidium clock, in the form of a 1 PPS (pulse per second) and several frequencies (125 MHz and 10 MHz have been picked at the moment). The system will also integrate GNSS antennas and receivers. The clock signals and the necessary information from the GNSS signals will then be distributed in two stages to the front ends, each front-ends being in charge of 24 PMTs. The full scheme (in its current form) is presented in figure 7.1.

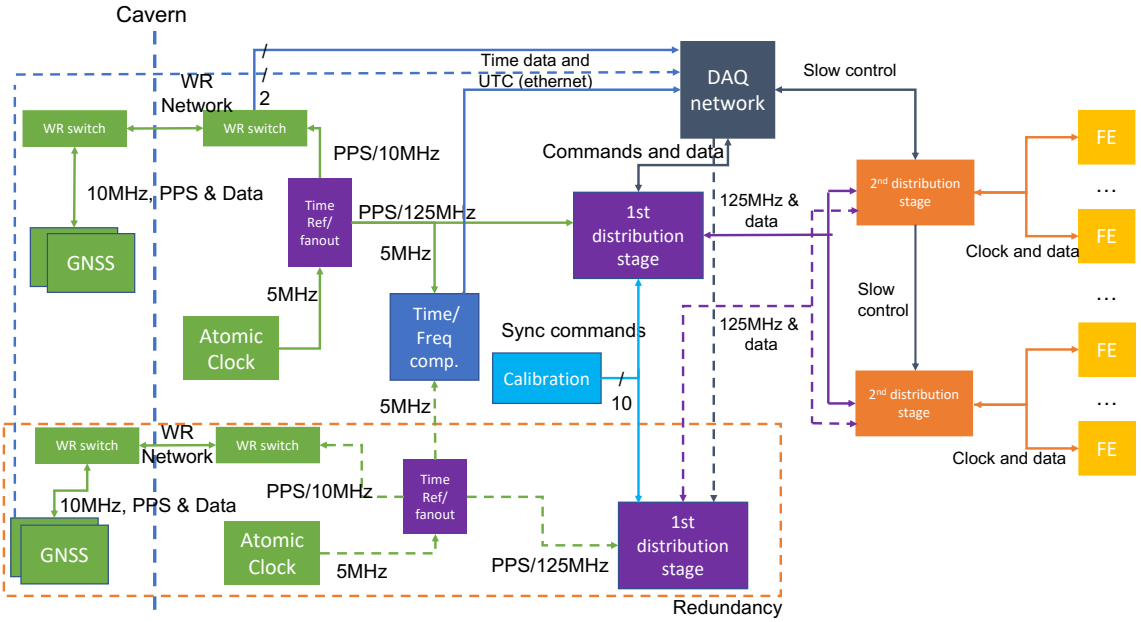

Figure 7.1. *Scheme of the overall foreseen timing system for HK. The green boxes correspond to the time generation part, the purple and orange ones to the first and second distribution stages and the yellow ones to the front-end electronics located in vessels under water*

Full redundancy of the system is foreseen, both with cold spares (clock and receivers turned off, out of the system) and hot spares, in particular for the GNSS receiver and antenna for which an online 3-body comparison is necessary to detect and identify any faulty behaviour. To this end, receiver and antenna of a different brand than the one chosen for the system will be included in case there is a malfunction specific to the chosen equipment or firmware version. A second atomic clock is also part of the hot spare system as the idea is to have a fully functional back-up system to which we can switch fast enough in case of failure of the principle system in the middle of a beam data run, without losing too much data. Of course, such a switch would imply to redo some quick calibration and initialization and such procedures will be prepared before the start of the experiment. Moreover, the scheme includes all links containing data and information for slow control even if the exact architecture for this has not yet been frozen.
As it has been shown in section 6.4, from the GNSS information, the time differences between the local time base and the GNSS time base can be inferred and so, to that end, the signal from the clock will be an input to the receiver. This choice is possible thanks to a specificity of the receiver we have picked: the Septentrio PolaRx5 [157] GNSS receiver. It indeed possesses a feature that enables it to handle an input frequency in the form of a 1 PPS signal and a 10 MHz signal. When both those signals are given as an input, they by-pass the receiver local oscillator, making the input frequency the time base that is compared to the GNSS. This means that the time differences outputted in the CGGTTS files by the receiver will directly be a comparison of the GNSS time base with the clock signal distributed through HK's timing system. This particular setup will be further discussed in section 7.2.2.

Among all the system described in figure 7.1, the R&D performed for this thesis was mostly about the time generation part as opposed to the distribution part. This includes the generation of the clock signal with the Rubidium clock as well as the management and integration of the information from GNSS such as time stamps and time base corrections.

7.2 Characterizations and performance evaluation

7.2.1 Characterization of each element

This section will detail the separate characterization of each element of the time generation part of the proposed system for HK.

7.2.1.1 At SYRTE

As it has been stated in section 6.5, a timing element can only be characterized against a reference signal. In order to have a starting point for our comparison and to build our test bench at the laboratory, our chosen equipment to test was first characterized at SYRTE (SYstème Reference Temps Espace) laboratory. This is the official time-service laboratory for France and it is located at Observatoire de Paris, about 3 km away from LPNHE. This allowed our equipment to be characterized against a very stable reference: one of the official clock signals from SYRTE (called UTC(OP)) and by the time keeping experts. Namely, the instruments chosen for our system that we brought were the following:

- One rubidium atomic clock FS725 from Standford Research [165]
- One Septentrio PolaRx5 [157] GNSS receiver
- One PolaNt B3E6 choke ring GNSS antenna [166]
- One 25 m antenna cable

The results of the characterization were given for the two main items: the stability performance of atomic clocks on one side and of the antenna + receiver system on the other side.

Atomic clocks

The Rubidium clock's stability has been assessed against the UTC(OP) reference signal after a few hours of warm-up, using a time interval and frequency counter. In the left plot of figure 7.2, provided by SYRTE, the overlapping Allan deviation of the comparison of 1 PPS signals every second is shown in blue. For longer time scales, a comparison of those signals every hour is shown in red. The performance are those expected for a rubidium clock from the manufacturer's specifications. It has a low-white noise level at 1s, of the order of a few 10^{-11} and presents a characteristic drift, dominated by frequency random-walk noise after 10^4 s. In addition, a deterministic quadratic phase drift[1] has been observed and the stability evaluation after removal of this drift is shown with the black curve. The effect of this correction is to decrease the slope of the longer time scale drift, since the deterministic component is removed and only the random walk is remaining.

[1] Inherent to all atomic clocks hence expected. It is coming from linear variations of frequency.

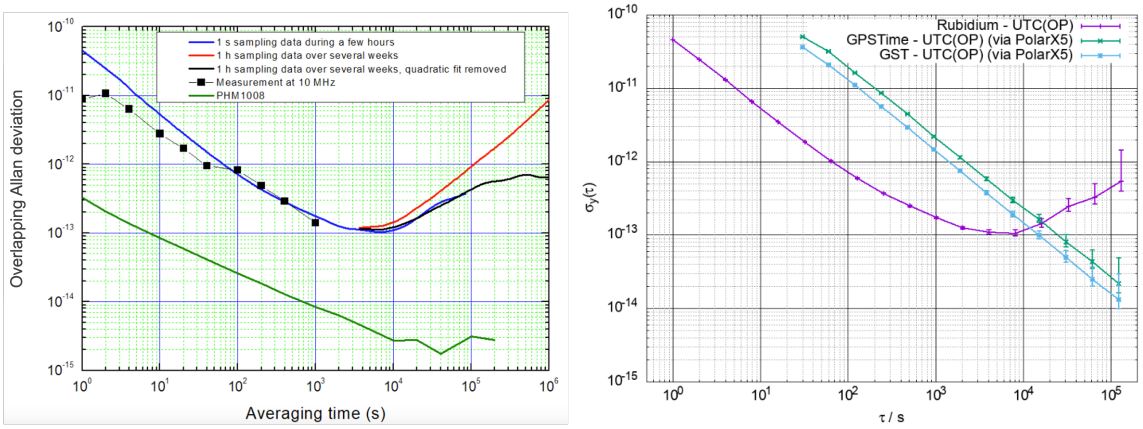

Figure 7.2. *Stability results provided by SYRTE for the FS725 Rb clock and the selected GNSS receiver+antenna pair*

Finally, the clock was characterized in the frequency domain, using the ratio of the 10 MHz signals of the clock and the reference signal. The result is shown in black squared markers in that same plot. It is consistent with the 1 PPS measurement but shows lower values, indicating a better stability of the clock. This is because using the 10 MHz signal allows for a higher sampling rate, decreasing the measurement's noise. The stability of an additional instrument was tested: a passive hydrogen maser (PHM). It is another atomic clock, more expensive and more precise. The one that was tested against UTC(OP) belongs to SYRTE. The overlapping Allan, deviation of this comparison is reported in green on the left plot of figure 7.2 and it can be noticed its white noise level at 1s is 2 orders of magnitude lower than that of the rubidium clock and the random walk noise becomes dominant later than for the rubidium clock (can not yet be clearly seen on that plot but is known to occur at a time scale of $\tau = 10^5$ s). Based on this confirmation of the performances, LPNHE bought a PHM (VCH 1008 T4Science) to use as a reference signal for tests with the rubidium clock.

GNSS antenna and receiver

In the right plot of figure 7.2, the overlapping frequency Allan deviation for the 1 PPS clock measurements is reported together with the results for the GNSS receiver+antenna system. The antenna we brought was placed on the roof of the SYRTE lab for a few weeks and connected to our receiver, using our cable. It is important to keep the antenna/cable/receiver system together for calibration as will be seen later. To assess the timing performance stability of the receiver+antenna pair, the UTC(OP) signal was given as an input to the receiver. Because the GNSS signals and UTC(OP) are aligned by definition (up to some fine tuning), the result of the comparison gives the level of noise of

the system in data taking conditions. The overlapping deviation is given in green using the GPS satellite constellations and in blue using the Galileo one. Both curves are similar and a pure $1/\tau$ (white-noise here) component is shown, at a level of a little more than an order of magnitude higher than the clock at 10^3 s for instance. The most crucial thing to see on this plot is that the rubidium clock drift at longer time scales but not the GNSS signal, even though, at short time scales the stability of the clock is better. This is yet another reason why it is necessary to combine the information of both those elements in our timing system so as to obtain the best timing performance possible at both short and long terms.

The main purpose of bringing our instruments to SYRTE was actually to calibrate the antenna-receiver-cable system. In fact, the procedure to calibrate equipment external to time-service labs is to do it by comparison with the already well-calibrated instruments of a time-service lab. As it can be seen in figure 7.3, the following delays need to be measured and taken into account during operation [159]. The calibration consists in measuring these:

- X_S: internal delay inside the antenna, frequency dependent
- X_C: delay caused by the antenna cable
- X_R: internal delay of the receiver for the antenna signal, frequency dependent
- X_P: in case an external signal is given in input, connection cable delay
- X_O: in case an external signal is given in input, internal receiver delay between external 1 PPS and internal clock

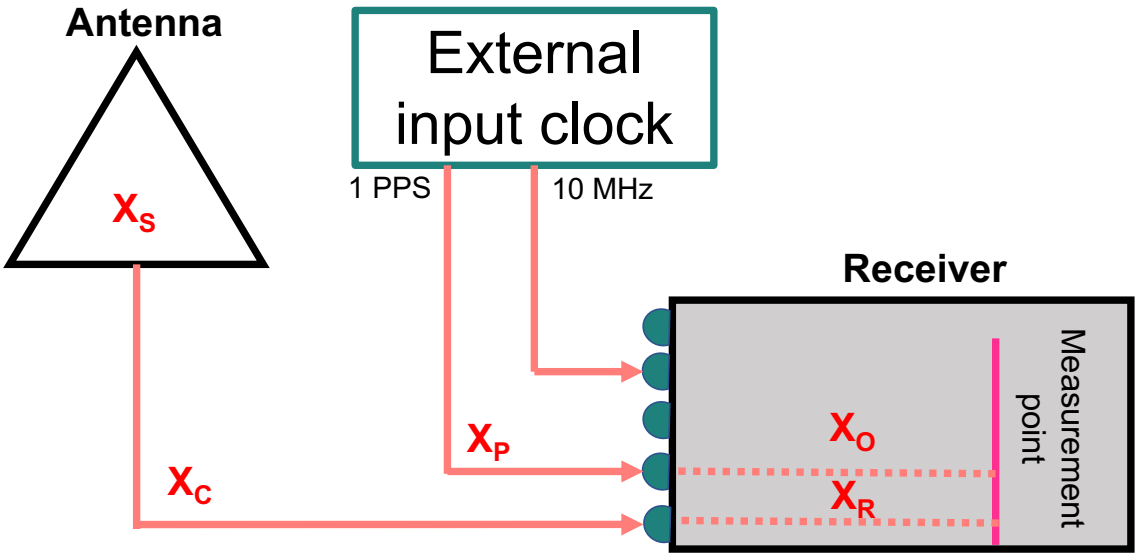

Figure 7.3. *Delays to consider for the selected GNSS receiver+antenna pair*

X_S and X_R depend on the GNSS frequency that is being read, meaning it is specific to each frequency of each constellation. The calibration was here performed for both GPS and Galileo constellation, each having two available frequencies. The cable delays X_C and X_P can be evaluated with specific equipment that measures the round-trip time of an injected signal. The dispersion can be measured with the same device. For this 25 m antenna cable in particular, all specifications were found in agreement with the data sheet and the delay X_C was found to be of 127 ns.
The internal delays of the antenna and receiver can only be measured together (for each frequency) as INTDLY $= X_S + X_R$ thanks to a comparison with OP73, one of the calibrated stations of SYRTE, and with UTC(OP) as an input to the receivers. The values of INTDLY found for the two most widely available frequencies of the GPS constellation (L1 and L2) and the Galileo constellation (E1 and E5a) are given in table 7.1:
Finally, X_O can be set to 0 thanks to an auto-calibration feature of the selected receiver.

Table 7.1. *Values of INTDLY in ns found for the first antenna+receiver+cable system calibrated at the SYRTE lab against the OP73 station*

GPS L1	GPS L2	Galileo E1	Galileo E5a
25.832	22.871	28.242	25.431

In that case, the cable delay X_P needs to be measured. In general, cable delays are of the order of 6 ns per meter. If auto-calibration is not used, the total delay REFDLY = X_P + X_O can be measured through a setup that compares the output 1 PPS of the receiver with the input external frequency. For that specific calibration, to report an order of

magnitude, a REFDLY delay of 88.3 ns was measured.
The delays X_C, INTDLY, and REFDLY can then be given as parameters of the receiver so that they are automatically handled in any further use of the receiver. Uncertainty on the measured delays were evaluated to 4 ns according to estimations fixed for the employed method. The calibration needs to be re-done for any new antenna+receiver+cable combination. To conclude on these calibrations, since the measured delays are of the order of several tenths of nano-seconds, they can not be ignored. Indeed, this first step is crucial to building HK's timing system as the requirement of accuracy with respect to UTC is 100 ns or less.

7.2.1.2 At LPNHE

These characterizations and calibrations at SYRTE were very important as a first approach to be able to build a test setup at LPNHE to perform the R&D. To that end, the calibrated antenna+cable+receiver system was installed, with the antenna on the roof of LPNHE (tower 13 of the Jussieu campus). A test bench was built, centralizing all the equipment: two time-interval/frequency counters Keysight 53230A [167] and an oscilloscope for measurements, two rubidium atomic clocks to test, the GNSS receiver, and the PHM and an optical link to SYRTE's UTC(OP) signal (transferred with a White Rabbit protocol) as references.

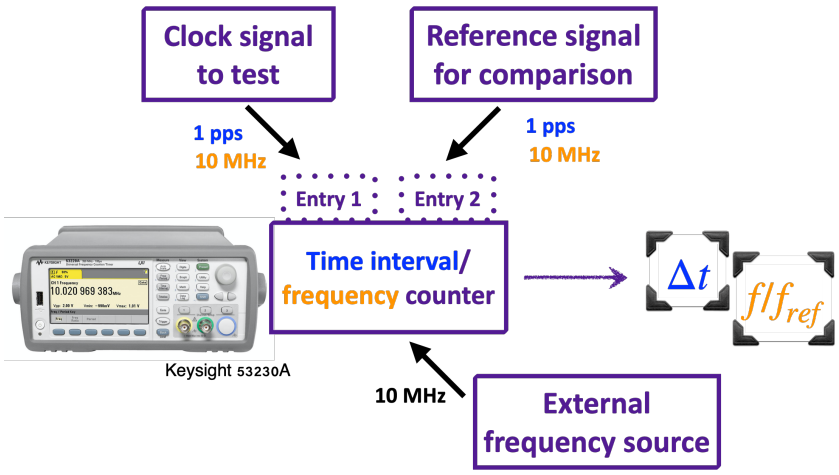

Figure 7.4. *Scheme of the two main use of the Keysight 53230A counter*

The counter, when used as a time interval counter will measure the interval between the pulse on the trigger entry, say entry 1, and the next pulse on entry 2. The counting can either be done by a fast frequency internal oscillator or an external input source frequency signal. When used as a frequency counter, it will, still thanks to either the internal oscillator or the external frequency source, measure the frequency of the signal

under test (single entry). The fastest rate at which the result of measurement is given is 1 s^{-1}, meaning that the counter averages measurements over many cycles, reducing the error on the measurement. The resolution of the measurement can be varied by adjusting the gate time of the measurement. In other words, longer measurements provide a better resolution. At analysis level, the ratio of the measured frequency over the theoretical frequency can be studied but the counter can also directly compute the frequency ratio between two entries. These two measurement methods are summarized in figure 7.4.
The first element to characterize is the atomic clock. It was first characterized against the PHM PPS signal, in the time domain, meaning that a time interval counter was used. The expected deterministic drift is observed in figure 7.5 (left). It seems linear on those 23 days of data but is actually slightly quadratic and corrected as such. The order of magnitude of the drift is proportional to the frequency difference between the rubidium clock output and the reference signal. However, as said before, this drift is deterministic and therefore can be removed. After this correction, the random walk component can clearly be seen in figure 7.5 (right). It can be seen that at the scale of a few hours, the time variations are smaller than the required 100 ns but can become much larger after a day or more. This is why this work will focus on monitoring and correcting for this random walk noise.

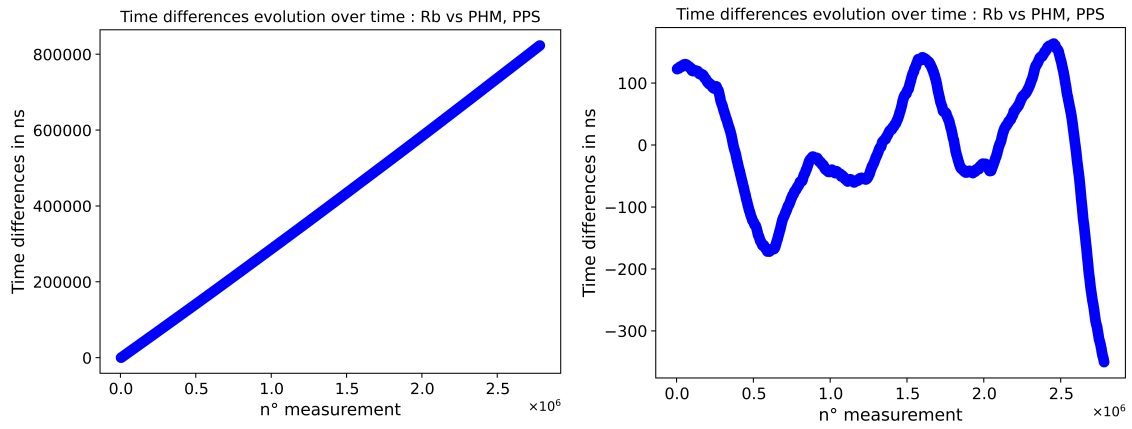

Figure 7.5. *Time differences between the Rubidium clock and the PHM PPS signals at LPNHE, deterministic drift not corrected (left) and corrected (right).*

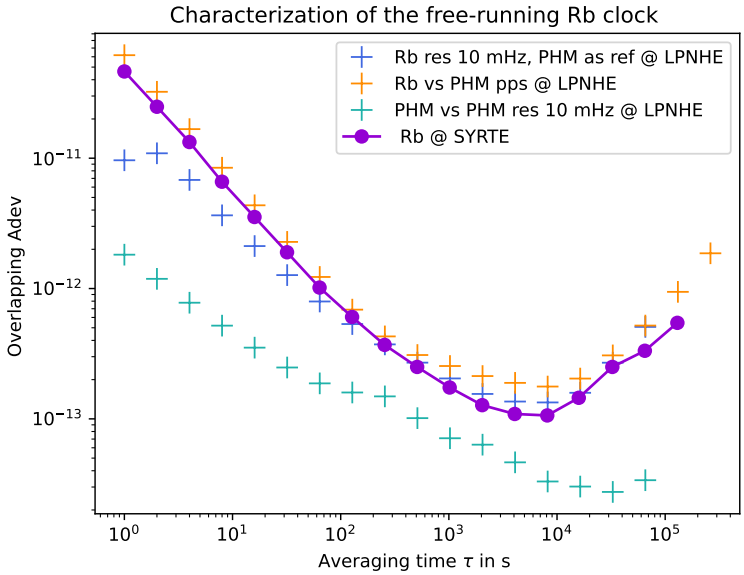

Figure 7.6. *Overlapping Allan standard deviations for the Rubidium clock characterization at LPNHE, the characterization of the clock at SYRTE (the right-hand side of figure 7.2) is reported in purple dots for reference.*

The Overlapping ASD (OASD) of these PPS time differences was computed and is displayed as the orange curve in figure 7.6. Uncertainty on the OASD in the form of error bars are not visible on the plot as in this Chapter OASD is used and the errors depend on the number of data intervals (N) that are made to compute the variance such that $error(\tau) = \frac{1}{\sqrt{N}}$. When using overlapping intervals, this error is very small. The agreement with the characterization done at SYRTE (reported in the purple curve) is quite good, validating the test bench setup. However, the agreement is not perfect. This is due to imperfections in the PPS signal production in both clocks (Rb and reference PHM) and the method of measurement. Indeed, time intervals are one-time measurements, reducing the resolution compared to measurements in the frequency domain where the frequency counter can make an average over many cycles. Such a measurement was performed with the 10 MHz signal from the Rubidium clock, comparing against the PHM 100 MHz signal. The result is given by the light blue curve in figure 7.6 and is indeed even closer to the SYRTE characterization, providing a definite validation of the setup. For this frequency measurement, the resolution of the counter can be set in a certain range. The better it is, the longer it is between two measurements so a trade-off has to be made here in order to be able to test the OASD along the whole range of values of averaging times. A resolution of 10 mHz for the measurement of the 10 MHz signal was found to be enough. Indeed, in figure 7.6 the cyan curve represents the ASD sensitivity of the counter for this particular resolution value, obtained by comparing the PHM signal against itself. It can be seen

that the sensitivity of the instrument in these conditions is at least around one order of magnitude better than the level of the signal under test (Rubidium clock).

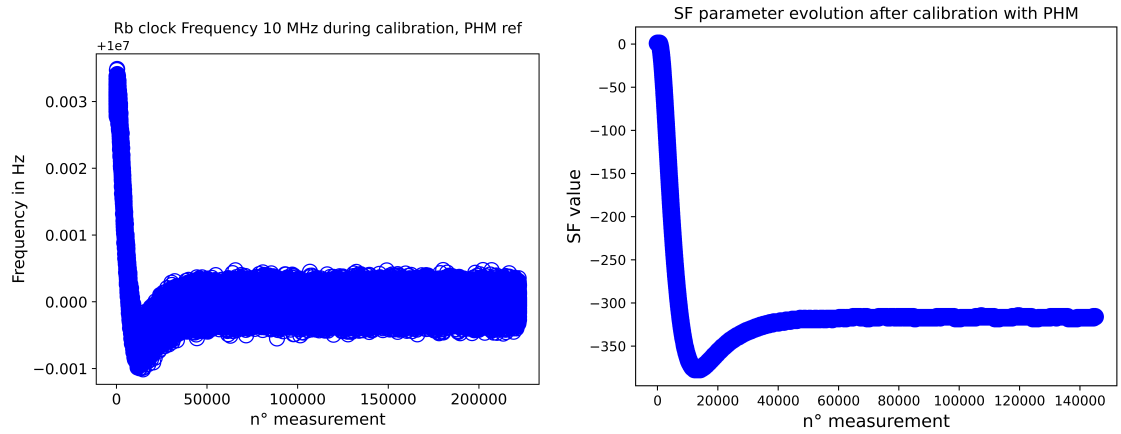

Figure 7.7. *Calibration of the Rubidium clock with the PHM PPS signal: frequency evolution (left) and SF parameter evolution (right)*

This was the characterization of the stability of the rubidium clock. This was made leaving the clock 'free running'. However, our model of Rb clock can take a PPS signal as an input. In that case, the output frequency signals of the clock will be adjusted to follow the input frequency. It is then said that the clock is driven by the external reference. The way it works is that a Phase locked loop (PLL) is incorporated into the clock's firmware and triggers a change of a parameter called SF which controls a small magnetic field that adjusts the frequency. The PLL has a flexible integration time, as will be seen later. This feature can primarily be used to calibrate the clock's frequency which is necessary as it can have drifted a little from the nominal value while it was turned off. As a note, the exact value of frequency is not important for the stability characterization. The action of the PLL on the frequency can be seen in the left plot of figure 7.7 where the frequency of the 10 MHz signal goes back to its value and remains, within variations due to the clock noise, around this value after calibration. In the right plot of the same figure, the same behaviour can be observed for the SF parameter, showing the direct correlation between this parameter and the output frequency.
Finally, the receiver was characterized at LPNHE so as to validate both the data taking with our setup and the analysis of output files. The UTC(OP) signal from SYRTE was given as an input to the receiver, meaning that the 1 PPS and 10 MHz signals provided by SYRTE through the White Rabbit switch at LPNHE were connected to the receiver as depicted in figure 7.3. It is important to note here that for all results presented in this thesis, the firmware version of the receiver was 5.3.2 and only the GPS constellation was

used, although Galileo was used for internal cross-checks. The time variations between GPS time and the UTC(OP) through the receiver were directly read from the CGGTTS files and are plotted in figure 7.8. As expected only white noise is observed with mean = -0.88 ns (close to 0, slight offset due to delays not taken into account and WR link not fully calibrated), with an amplitude of a few ns, $\sigma = 1.75$ ns. In figure 7.9, the OASD of these variations is plotted together with the results from the SYRTE calibration. The agreement is found to be very satisfying and can be seen as a green light to use our test bench for tests of the proposed system.

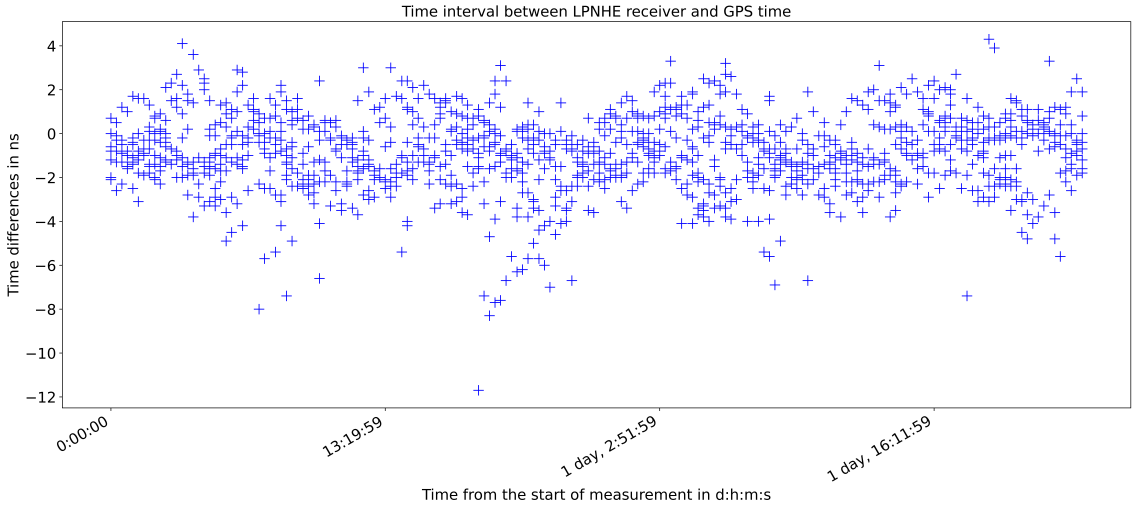

Figure 7.8. *Comparison of GPS time and the receiver's time (UTC(OP) as an input) at LPNHE: time differences*

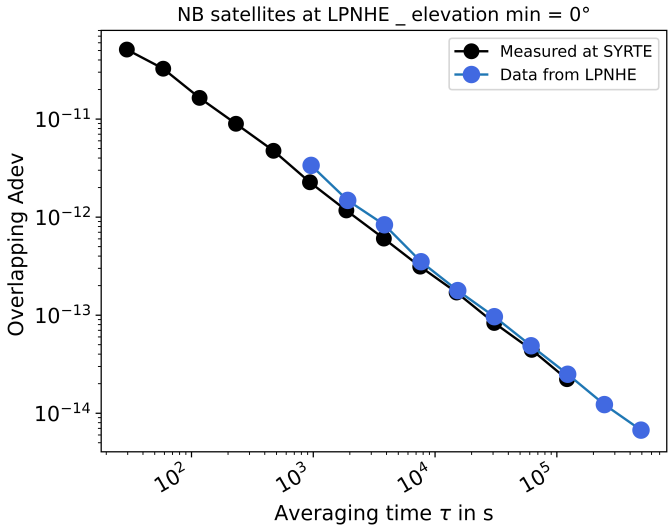

Figure 7.9. *Comparison of GPS time and the receiver's time (UTC(OP) as an input) at LPNHE, Overlapping ASD*

7.2.2 Characterization of the full system

On top of being able to obtain time tags for the events, there is another motivation for including a GNSS receiver in the HK's timing system. Based on their performance in Allan deviations, reported on the same plot in figure 7.10, it is preferable to combine the short term performance of the clock with the long term stability of the GNSS signals. In

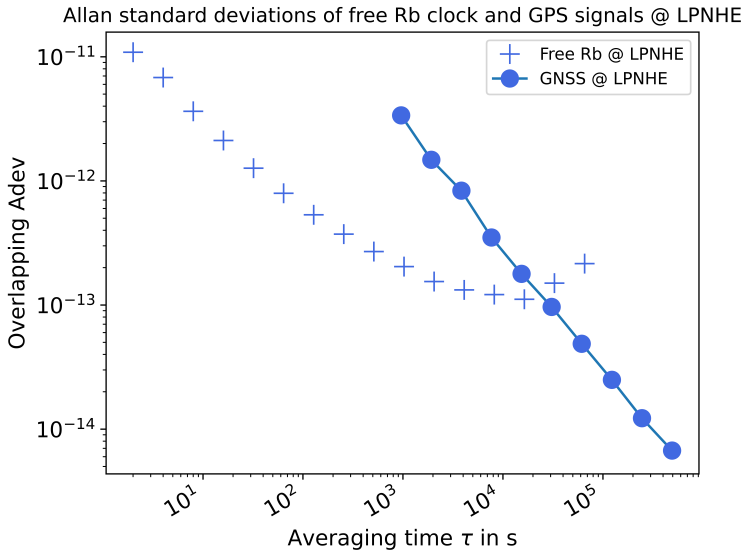

Figure 7.10. *Overlapping ASD for GPS signals and the free running rubidium clock measured at LPNHE*

other words, the GPS signals can be used to correct for the frequency random walk of the rubidium clock without degrading the clock's short term stability if the correction is applied at right time scale/rate.

Stability performance of the full foreseen system, without corrections

This is why it was decided to propose a configuration in which the rubidium clock PPS and 10 MHz signals (through the reference point) are given as inputs to the receiver. It allows for the output of the receiver (CGGTTS files) to directly give time differences between the clock time base and the GPS time base. From the monitoring of those differences, it is possible to compute the necessary corrections to apply to the signal that is distributed to the rest of the system. Figure 7.11 shows the observed time variations for a period of 19 days after removal of the quadratic drift of the rubidium clock. It can again be seen that the variations over even 1 day do not exceed a few ns, and stay well within the requirement of 100 ns. Actually, from figure 7.10, it can be deduced that the ideal time to apply corrections is around every 4h, where the two ASD curves cross. This is the time scale at which the rubidium clock starts drifting away from UTC. It is

important to remember that ASD curves show stability at different time scales, not over time, meaning that corrections should be applied periodically, integrating the information on time differences with GPS over these 4h. Corrections will be further discussed in section 7.3 where in particular simulations to choose the correction method will be presented.

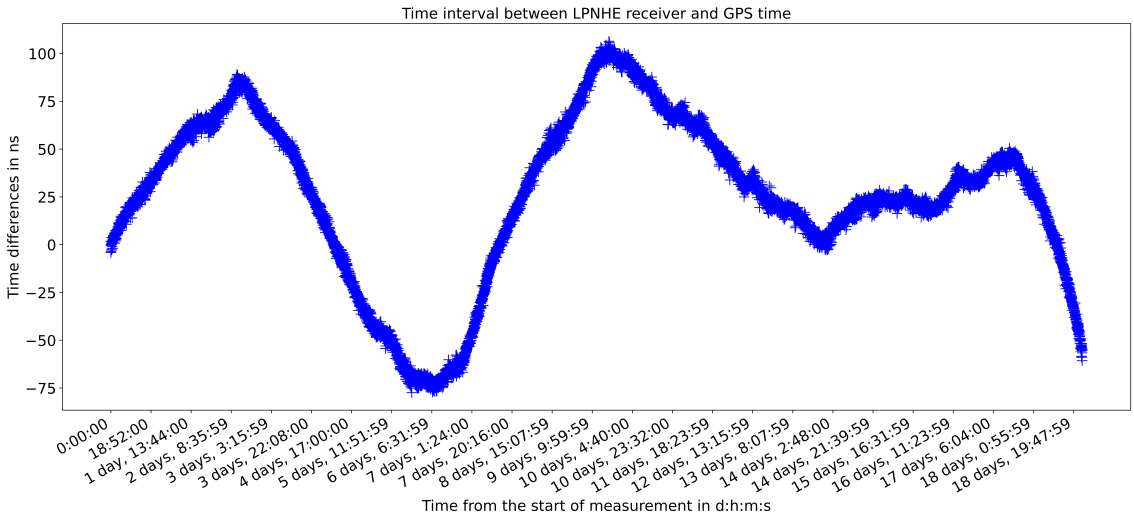

Figure 7.11. *Time differences between GPS time and the rubidium clock signals in the foreseen configuration of the system, measured over 19 days*

Study of the satellite reception

This was a first characterization of the proposed system and showed performances that are compatible with requirements providing the right corrections are applied, all as expected. Another thing that needed to be tested is the number of satellites that can be seen. It was first tested from LPNHE in Paris even though it will be tested on site in Japan later on. Those tests were performed with GPS only but it will be possible to use several constellations at the same time, so this is a kind of stress test of the minimum number of satellites we might have access to. In the left plot of figure 7.12, an histogram of the elevation in the sky of the satellites that were seen over 19 days is shown. The results were similar for shorter data taking periods. One concern is that the experiment's site will be located in a valley, in a mountain area. Because of their frequencies in GHz, the satellites' signals can be blocked by the mountains or reflected by metallic constructions in the cities. Once the position of the antenna is known, as explained in Chapter 6, one or two satellites can be enough for timing purpose but it increases the uncertainty. According to rough estimations at the SK site by our colleagues, the minimal elevation from ground (in degrees) for which the receiver can have a clear view of the sky is around 30°. The same can be expected at HK given this is the same mountain chain. The histogram

therefore shows that most satellites are above that minimal elevation. A filter is applied to remove all satellites below 15° as a standard procedure to reduce the probability of a signal to come from reflections. To visualize better the number of satellites to expect as a function of the elevation constraints from the mountains, a 2D histogram is plotted in the right-hand side of figure 7.12. It shows the number of satellites per 16 mn epochs, meaning per data point of the receiver, as a function of imposed minimal elevation angle. It is filled in color scale to represent the population of events for each case. With basic geometry, we computed an extreme case to be 50°. The 2D histogram shows that even in that case and with only the GPS constellation, it never happens that no GPS satellite is available and most of the times, 3 are available. This is an encouraging test, even if such measurements should be performed on site. The effect of loosing signal for a 16 mn epoch should still be studied as a precaution and a course of action should be defined in the future for data taking and analysis in that case.

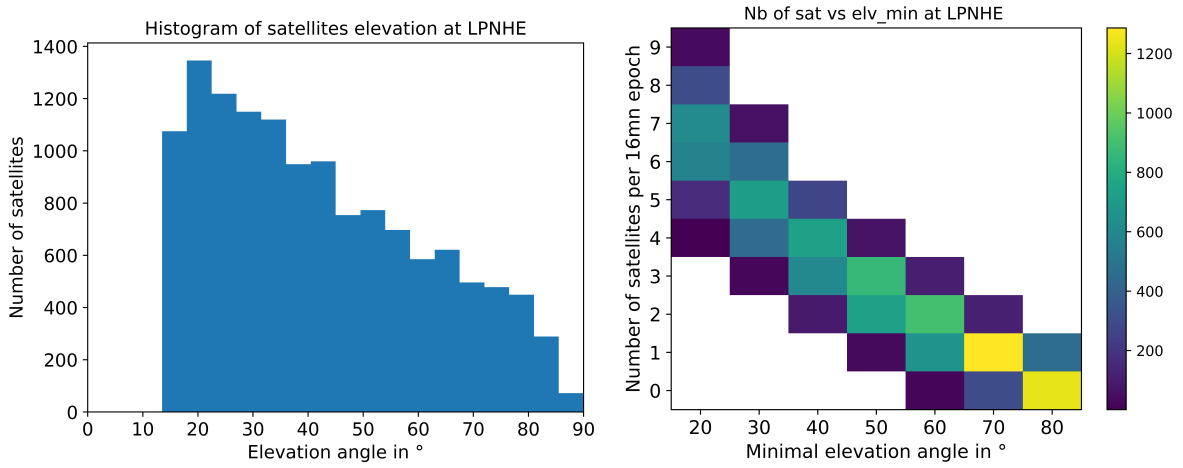

Figure 7.12. *Number of GPS satellites seen at LPNHE by the chosen receiver over 19 days, simple histogram (left) and 2D histogram (right)*

An alternative configuration for HK's timing system

Another configuration was studied. It is not preferred by our group for HK but is a possibility and more importantly, is the configuration currently deployed at SK. It consists in driving the rubidium clock by the GNSS 1 PPS signal instead of letting it run free and correcting for the long term drift. The two configurations are summarized in figure 7.13. This alternative solution displays advantages. In particular, it does not require any online or offline correction of the long-term clock drift as the output signal of the clock is already disciplined by the GNSS signals. However, one can not control how the clock signal is corrected to follow the GNSS signals since it is handled by the PLL within the

clock, and in particular if something goes wrong with the GNSS signals reception, the clock signal distributed to the experiment is directly impacted.

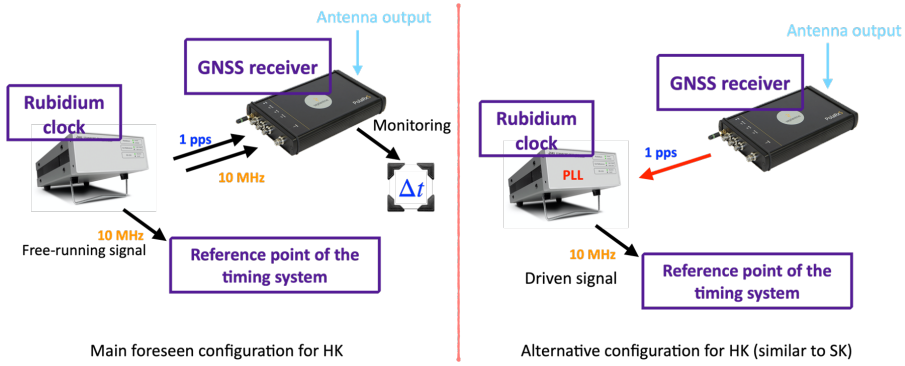

Figure 7.13. *Scheme of the proposed system for HK (left) and the alternative configuration similar to the current one at SK (right), for comparison*

Table 7.2. *Correspondence of PT parameter value and the PLL response time for the FS725 Rubidium clock [165]*

PT value	Response time of the PLL (hours)
0	0.14
1	0.20
2	0.28
3	0.40
4	0.56
5	0.80
6	1.12
7	1.59
8	2.25
9	3.18
10	4.50
11	6.36
12	8.99
13	12.72
14	17.99

This risk can be mitigated by choosing the appropriate time integration which is the time on which the PLL will integrate before applying a correction to the signal. Actually, it can also be seen as the rate at which there will be an effect on the output frequency of the clock. If this time is chosen to be long enough, a transitory issue with GNSS signals might be averaged and not impact significantly the output frequency. The effect of the PLL is not a sudden correction but a slow change of the value of the SF parameter described in section 7.2.1.2, resulting in a periodic (integration time) change of sign of the

frequency drift so as to bring it closer to the nominal value. The correspondence between the value of the parameter PT and the integration time is given by the clock's data sheet and is reported in table 7.2. This behavior of the clock's 10 MHz frequency under this configuration was characterized against the PHM reference signal and is shown in figure 7.14 where data has been taken for a value of PT = 5 which was then changed to PT = 10 after around 7500 data points. It can be seen that it results in periodic fluctuations of

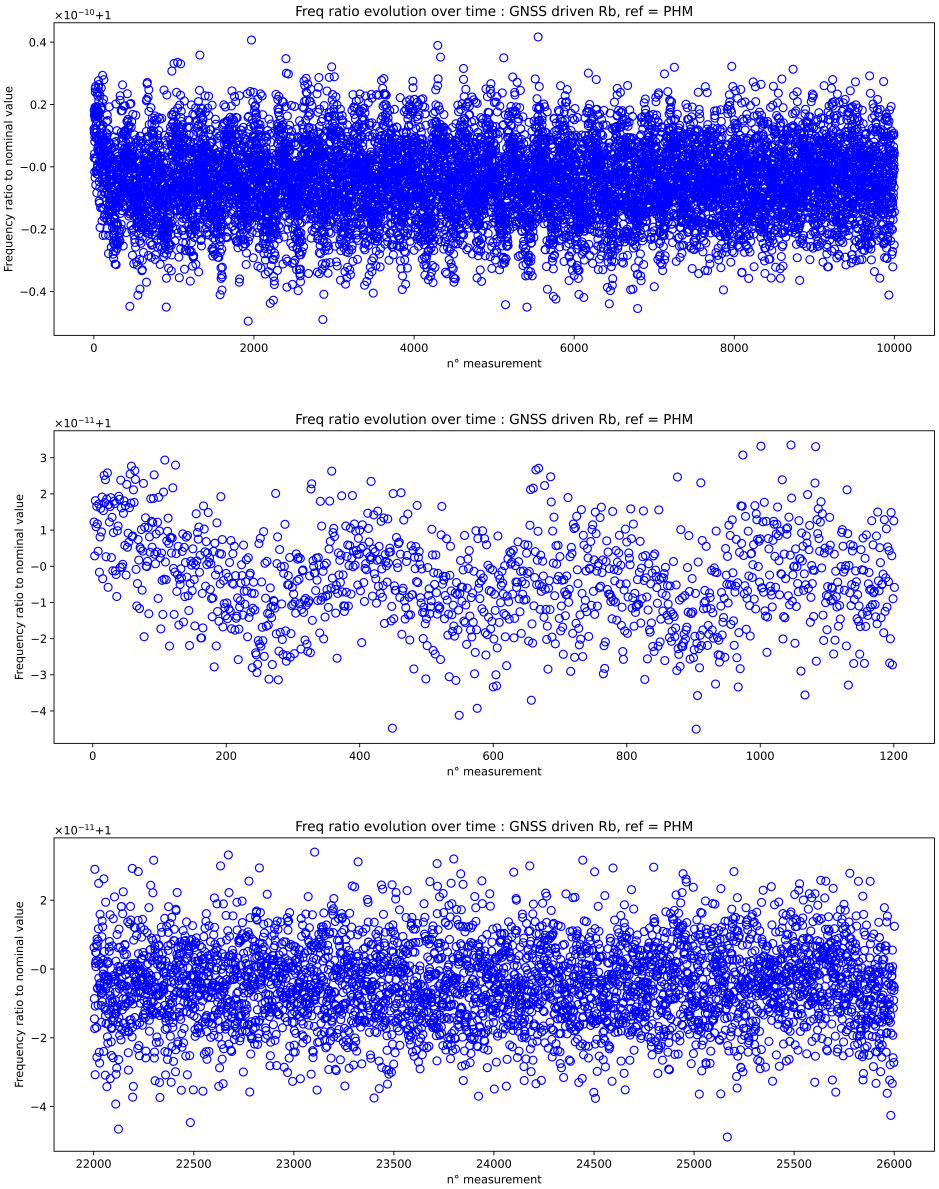

Figure 7.14. *Frequency ratios between PHM reference and GNSS-driven Rubidium clock for integration time parameter PT = 5 then 10 (top), PT = 5 part (middle) and PT = 10 part (bottom)*

the output frequency whose period is defined by the chosen integration time. Similarly, the corresponding effect on the intermediate parameter SF that is varied by the PLL is

plotted in figure 7.15. It can be noticed that the amplitude of variations is larger for the smaller integration time, which is expected as the clock drift with respect to the GNSS input is, in that case, averaged over a shorter period of time. Indeed, we know that the GNSS signals are very noisy at short term so making the clock follow them on short period of times adds noise to the clock signal.

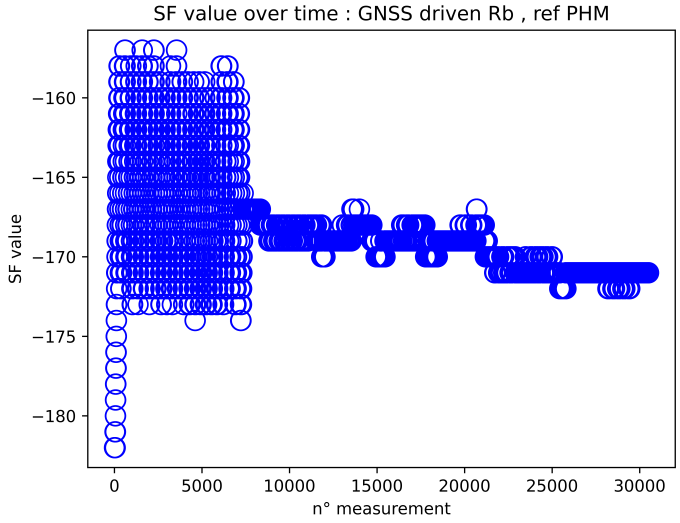

Figure 7.15. *SF parameter variations during GNSS-driven Rubidium clock operation for integration time parameter PT = 5 then 10*

Finally this alternative configuration (shown on the right-hand plot of figure 7.13) was studied in terms of OASD in figure 7.16 for different values of PT. As expected, when the integration time is short, the clock signal stability is very degraded and when it is too long, like for PT = 14, the clock signal drift can become dominant before the PLL correction kicks in. It can also be observed that at the scale of the integration time, in the OASD plot, when the averaging time τ is equal to the integration time, a "bump" is present denoting the instability engendered by the new correction starting, corresponding to the change of sign of the frequency drift as explained above. As a conclusion on this alternative configuration, it is not considered ideal for HK by our group because it does not allow the user to monitor the corrections applied or have access to the raw signal of the clock, uncorrected and it adds an additional instability due to periodic corrections. In other words, this configuration does not allow us to make the best use of each instruments performance regardless of the value of the integration time PT. However, this configuration is perfectly working and sufficient for beam neutrino window requirements, provided that no sudden large jumps in satellites's signals is observed. For HK, the idea is to build the most stable system possible with the chosen equipment and to reach levels of precision

that might bring new possibilities for studies such as astrophysical neutrinos detection in multi-messenger astronomy.

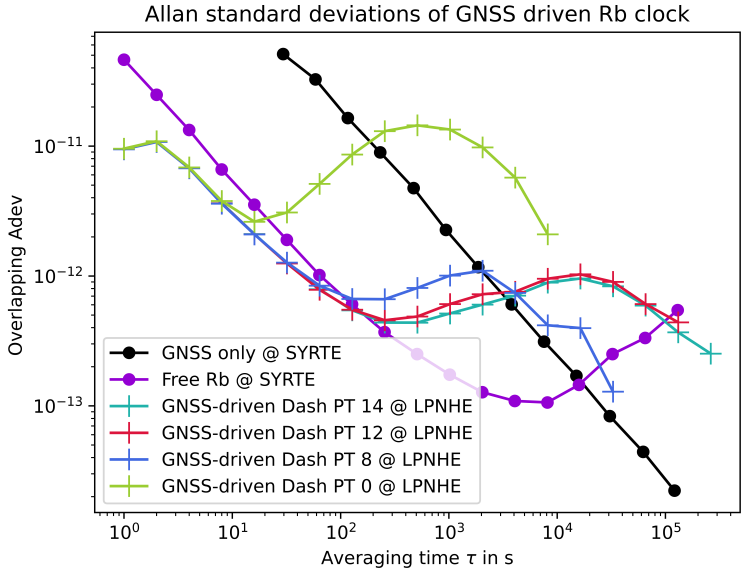

Figure 7.16. *Overlapping ASD of the comparison of GNSS-driven Rubidium clock with PHM reference for several integration time parameter PT values*

7.3 Timing corrections

7.3.1 Types and needs

In the proposed connection scheme (fig 7.1), the clock signal will be built from a free running rubidium clock. However, it was shown that on time scales of the order of 10^4 s the GNSS signal becomes more stable in terms of frequency than the Rubidium clock signal. To monitor the differences between both timing information, the proposed solution inputs to the receiver both the clock signal and the antenna output. In this configuration, the receiver acts as a time interval counter and outputs directly through the CGGTTS files, the time differences between the clock and the GNSS signals. With this information, it is possible to implement different types of corrections applied both to the clock signal and the time stamps. Different correction types at different levels and for different purposes will be needed:

- An online correction of the clock signal using the GNSS information will first be applied to remove the clock drift. This is important for the ring reconstruction by coincidence but mostly to allow the Data Acquisition system (DAQ) to open and close time windows for beam events. To this end, an estimated UTC tag needs to

be associated to each PPS. This correction does not need to be very precise as the time windows width are of about 10 μs.

- Then, an offline correction using also only the GNSS information will remove the clock drift with a better precision.

- Later, to obtain local UTC time tags, time transfer will be performed through common-view between the far detector site and the Japanese time-service National Institute for information and Communication Technology (NICT) [168]. This is needed for astrophysical events to perform multi-messenger astronomy by comparison to other experiments (such as supernovae explosion alerts with SNEWS). This correction can be performed as soon as the CGGTTS files from NICT are available, in general the next day. It is also needed for time-of-flight studies between the near and far detectors, although in that case it would be ideal to perform common view time transfer between the near and far detectors directly.

- To convert the local UTC time tags obtained at previous step into global UTC, the "circular T" document [144] published every month by the BIPM can then be used.

The next 3 subsections will describe the possible methods for offline and online corrections as well as time transfer; the conversion from local to global UTC being only a matter of applying given coefficients which does not necessitate any R&D studies. In particular the two next subsections will detail the simulations that were produced to test correction methods and evaluate the expected performance of the corrected signal.

7.3.2 Offline corrections: simulations and results on data

It has been shown in section 7.2.1 that the Rubidium clock has a deterministic quadratic drift in phase. Moreover, the frequency random walk is dominant at large time scales, meaning that it can, on shorter time ranges, be modeled as quadratic as well. The idea for an offline correction method is to divide the time differences between the Rubidium clock and the GNSS signals (computed by the receiver in the proposed configuration) into intervals of length L that we will optimize. Each interval is then fitted independently with a quadratic function (2^{nd} degree polynomial). The result of the fit is removed from the clock signal to correct for the drift. Those are offline corrections because the data of the total interval of length L need to have been collected before the correction can be computed.
Simulations were built in the following way. Phase series were simulated for PPS signals for simplicity. The quadratic drift was not included because it is deterministic and therefore does not require further study for being corrected. From the characterizations through

ASD, the dominant noise types of both the Rubidium clock and the GNSS signals were identified. At first order, the clock signal can be modeled by white noise in both phase and frequency as well as a random walk noise in frequency. The GNSS can be modeled as pure phase white noise. Therefore, the OASD the signals we want to simulate as a function of the averaging time τ can be written as:

$$OASD(\tau) \cong A_{WNp} \times \tau^{-1} + A_{WNf} \times \tau^{-1/2} + A_{RWf} \times \tau^{+1/2}. \tag{7.1}$$

The amplitudes of noise were computed from a fit of the OASD for data in order to obtain realistic simulations and were found to be of these orders for the Rubidium clock:

$$\begin{aligned} A_{WNf} &= 7 \times 10^{-12}, \\ A_{RWf} &= 1 \times 10^{-15}, \\ A_{WNp} &= 5 \times 10^{-11}, \end{aligned} \tag{7.2}$$

and for the GNSS signals

$$\begin{aligned} A_{WNf} &= 0, \\ A_{RWf} &= 0, \\ A_{WNp} &= 2 \times 10^{-9}, \end{aligned} \tag{7.3}$$

with WN for white noise, RW for random walk and the indices f and p for frequency and phase respectively. Those amplitudes are unit-less because throughout the work presented here we have been using Allan deviations in such a way that they do not have units: they are either variances of frequency ratios or variances of time differences divided by the square of the averaging time (see section 6.5).
To create phase series Φ_i of the involved noises, the following random realizations of frequencies (f_i) and phases (Φ_i) were computed successively for each simulated data point. In the following equations, $\mathcal{N}_{Gauss(0,1)}$ denotes generically a random number that is drawn each time and for each equation from a standard Gaussian distribution. First, the random walk component of the frequency, $f_{RW,i}$, which is cumulative point after point (denoted by $+=$) is computed:

$$f_{RW,i+1} = A_{RWf} \times \mathcal{N}_{Gauss(0,1)} + f_{RW,i}. \tag{7.4}$$

The total noise in frequency f_i is defined as the sum of the frequency random-walk and white noises:

$$f_i = f_{RW,i} + A_{WNf} \times \mathcal{N}_{Gauss(0,1)}. \tag{7.5}$$

The corresponding phase Φf_i, which is cumulative, can be computed as:

$$\Phi f_{i+1} = \Phi f_i + f_i \times \Delta t, \tag{7.6}$$

where Δt is equal to 1s because this phase series is designed to be applied on PPS signals. Finally, the total phase series Φ_i inferred by the noise types is deduced in this way:

$$\Phi_i = \Phi f_i + A_{WNp} \times \mathcal{N}_{Gauss(0,1)}. \tag{7.7}$$

Times series of simulated signals are then obtained by adding the corresponding phases computed from noise models to a "perfect" PPS signal t^i_{perf} (a series of integers): t^i_{Rb} and t^i_{ref} respectively for the clock and the GNSS PPS. The equivalent of 10^6 s of data was simulated. To mimic the output of the GNSS receiver, time differences between the simulated Rubidium PPS and the simulated GNSS PPS (Δt^i_{Rb-ref}) are computed every 16 mn[2], taking the average of differences between each signal for each pulse on the 16 mn. An example of obtained simulated time differences, which is equivalent to simulated receiver data is given in the left plot of figure 7.17. Since the deterministic drift was not added, the random walk component can be seen easily spotted on that curve. Initial differences between the simulated clock PPS and the perfect signal ($\Delta t^i_{Rb-perf}$) are also computed. Indeed, corrections will be computed from the simulated receiver's output and applied to the simulated clock signal. However, the corrected clock signal will then be compared to the perfect signal so as to isolate the effect and performance of the correction method without having cumulative effects of the noise on the GNSS signal. This is the reason why we use simulation and not data to validate the correction method. Those initial time differences between simulated clock and perfect PPS can be seen in the right plot of figure 7.17 and it can be noticed that they are very similar to the simulated data in the left plot.

The way correction coefficients are extracted is that a quadratic fit is performed on the initial differences with the simulated GNSS:

$$\begin{aligned} \Delta t^i_{Rb-ref} &= t^i_{Rb} - t^i_{ref} \\ &= ai^2 + bi + c, \end{aligned} \tag{7.8}$$

where a, b, and c are the quadratic coefficient of the correction and i is the 'perfect time' or number of the measurement. This quadratic trend is then removed from the simulated

[2]In principle, we should only use 13mn and discard 3 mn of data to perfectly mimic the receiver's process but this does not impact our results.

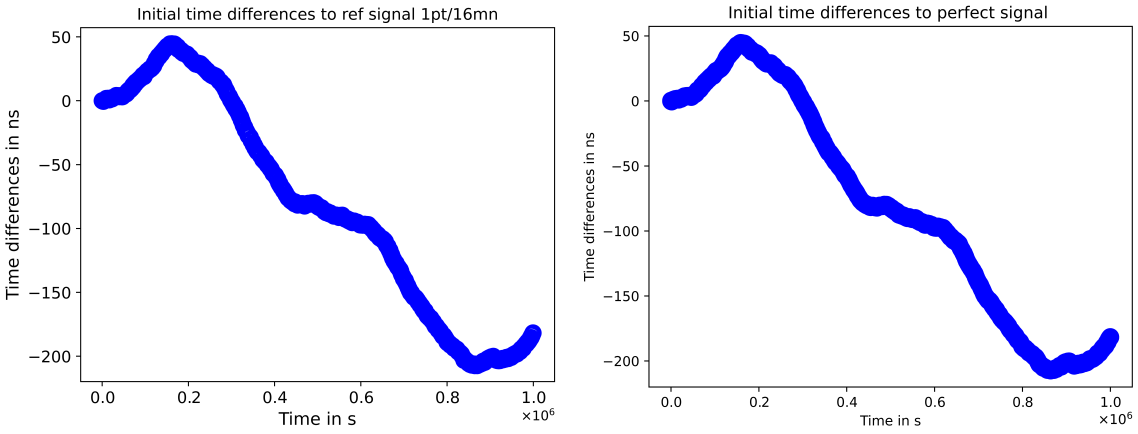

Figure 7.17. *Initial time differences between* 10^6 *s of simulated Rb clock data and GNSS reference signal (left) or perfect signal (right)*

rubidium time series so as to obtain a corrected time series t^i_{Rbcorr}:

$$t^i_{Rbcorr} = t^i_{Rb} - ai^2 - bi - c. \tag{7.9}$$

The remaining time differences between the corrected clock PPS and the perfect signal ($\Delta t^i_{Rbcorr-perf}$) are then computed in order to assess the stability performance of the corrected signal:

$$\Delta t^i_{Rbcorr-perf} = t^i_{Rbcorr} - t^i_{perf} \tag{7.10}$$

Or in one step:

$$\Delta t^i_{Rbcorr-perf} = \Delta t^i_{Rb-perf} - ai^2 - bi - c \tag{7.11}$$

The fit is performed independently for adjacent intervals of data of length L, giving each time different coefficients a, b, and c. Each set of coefficients is used to correct the corresponding interval of data. The length L of the intervals is a choice that can be optimized and can be seen as the rate of correction. As explained before and according to the characterization of both the clock and GNSS signals with real data as presented in figure 7.10, the ideal value for L was found to be 10^4 s. The performance of such offline corrections at this rate are given in figure 7.18. In the left plot, the remaining time differences with the perfect signal are shown and stay within a few ns of variations which is a very satisfying success of the method as the requirement of variations with respect to UTC, including distribution throughout the whole detector, is of 100 ns. This provides more than necessary margin for the distribution part. The right plots shows the OASD of these remaining time differences in red, together with the OASD of the simulated signals with respect to the perfect signal for comparison. The desired effect is obtained: the short term performance of the clock are perfectly combined with the long term stability of the

GNSS signals, with a smooth transition.

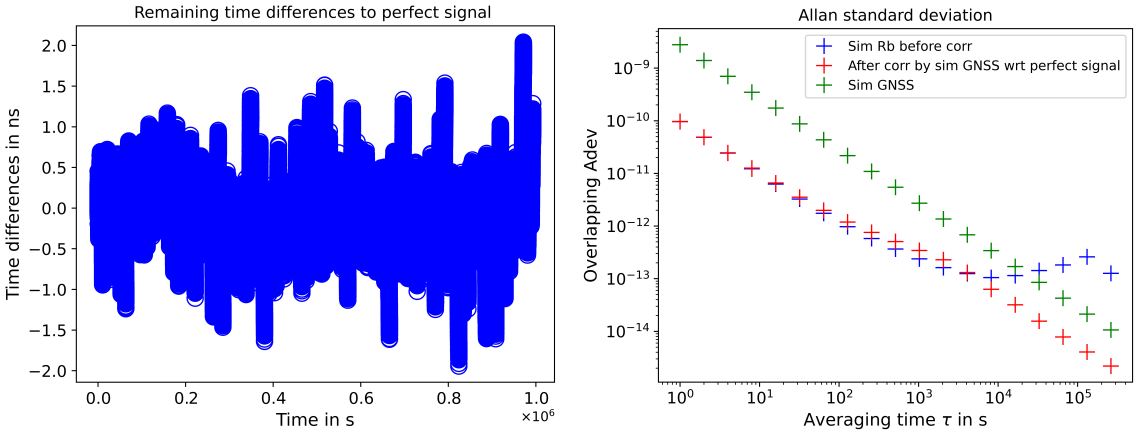

Figure 7.18. *After offline corrections at* 10^4 *s: remaining time differences between simulated Rb clock data and perfect signal (left) and Overlapping ASD of these (right)*

In figure 7.19, the OASD for simulated clock signals corrected with different interval lengths L are plotted to illustrate the optimization of L. The red stars represent the optimized length L of order 10^4 s, corresponding to 11 GNSS cycles of 16 mn. The orange stars are the case where the corrections are applied too often (order 10^3 s) which degrades the short term stability of the clock by adding the high white noise of the GNSS (since it is not averaged over a long enough period of time). On the opposite, the light blue stars show the results for corrections applied not often enough (order 10^5 s). In that case, the clock random walk impacts the stability of the obtained signals at time scale where it is dominant and below the correction time scale. This also degrades the potential stability of the corrected signal. It was therefore found, as expected, that an ideal correction rate value is more or less the time scale at which the GNSS signals become more stable than the clock signal.

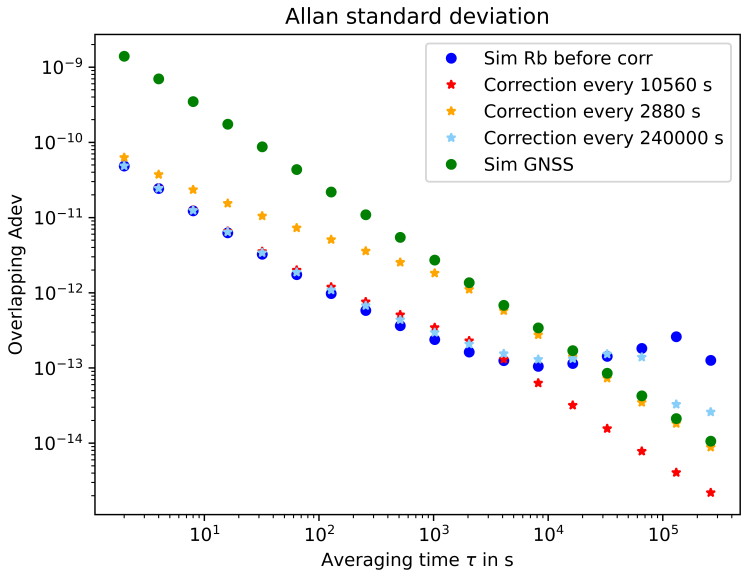

Figure 7.19. *Comparison of overlapping ASD for corrected signals at different time scales*

As a conclusion, this offline correction method with an optimized interval length of L = 10^4 s is validated by these simulations and seems to offer ideal combination of stabilities in a smooth way. However, those are corrections that can only be computed and applied a posteriori on already collected data. The next subsection will focus on how to apply a similar method online, so as to not propagate any strong clock drift to the system, as required for beam neutrinos identification.

7.3.3 Online corrections

The idea here is actually to apply the same method as described above for so-called offline corrections but instead applying the computed correction coefficients over a certain interval on the next interval, online, as it is being collected. Of course, this is less accurate but as it will be shown in this section, with simulations we have demonstrated that this is well within requirements for the first round of corrections that are the online corrections. Keeping the optimized length of intervals as 10^4 s to perform the fit and compute the corrections, we found that linear fits rather than quadratic fit were giving better results in that case. This is explained by the fact that over 10^4 s, the trend is generally mostly linear and a quadratic fit giving additional freedom, models small variations that are specific to the interval and end up being very wrong for the next interval. Linear corrections computed on the previous intervals of length $L = 10^4$ s, applied on the simulated Rb clock PPS and compared to a perfect signal gave the OASD performance shown in the left plot of figure 7.20. The obtained stability is very reasonable, eliminating the long term

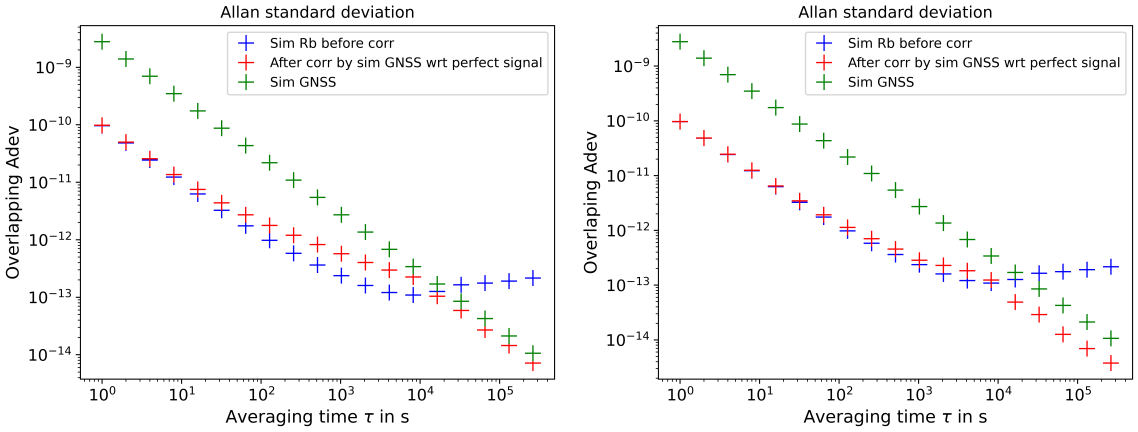

Figure 7.20. *After online corrections at* 10^4 *s: Overlapping ASD with respect to perfect signal without sliding intervals (left) and with sliding intervals (right)*

random walk drift of the clock and keeping a better stability at short term than GNSS signals alone. However, it is degraded compared to what can be obtained with offline corrections, up to 75% less stable at $\tau = 10^3$ s. Even-though it would still fall within the requirements, we developed a little bit more sophisticated method to improve this result. Corrections are now computed on an interval of same length L every time a new point of data is available, i.e. every 16 mn. This means that the correction to apply changes every 16 mn, being computed on an interval that is as close as possible to the data that is being corrected online which should improve the performance. We chose to call this method "online corrections with sliding intervals". The OASD of a simulated Rb signal corrected in such a way is shown in the right plot of figure 7.20. It can be seen that the middle term performance is much less degraded and the overall performance are very similar to that of the offline corrections. Actually, figure 7.21 is the overlayed plotting of remaining differences between the corrected clock signal and a perfect signal for both the offline corrections simulation (in blue) and the online corrections with sliding intervals (in pink). It can be observed that the remaining time variations are very similar for both methods, validating the online correction method, and well within requirements, with standard deviation of $\sigma_{Off} = 0.32$ ns for offline corrections and $\sigma_{On} = 0.53$ ns for online corrections with sliding intervals, for one simulation (very similar results for others).

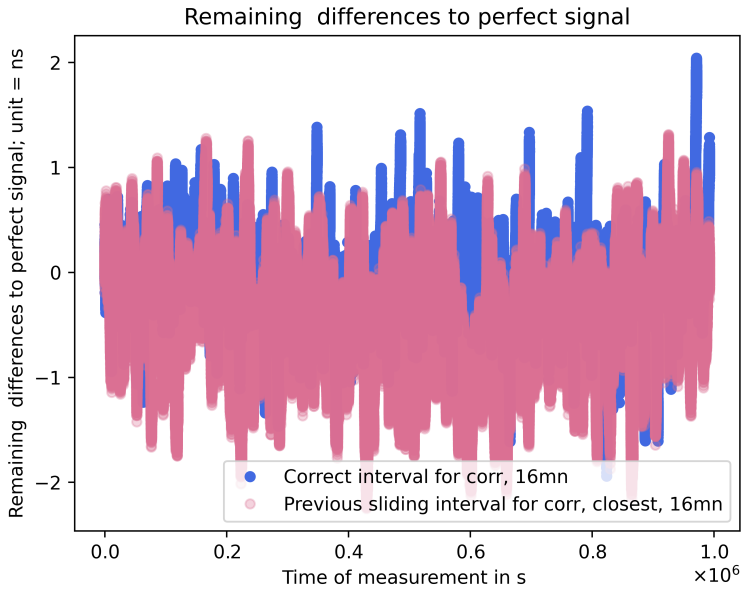

Figure 7.21. *Comparison of time variations for simulated signals corrected with the offline method (blue) or with the sliding interval online method (pink)*

7.3.4 Time transfer with common view in Paris

The previous detailed studies have demonstrated how to build a clock signal for HK's timing system that is as stable as possible and corrected in an ideal way, both online and a posteriori. Another requirement, as stated in Chapter 6, is to be able to time tag each potential neutrino event detected, at the level of the data acquisition, with UTC, or at least local UTC. Moreover, SK data acquisition needs to have a common time base, or a possibility of comparison with the J-PARC side, where the accelerator is producing the beam. Those two goals can be met by using time transfer through common-view. In particular, if one of the sites is the Japanese time-service lab (NICT) then the comparison through common-view directly gives a comparison with the local UTC. If the starting time is known, then local UTC time-tags can be attributed to each event. For comparison with J-PARC, either all times can be kept in each experiment's sites time bases and time transfer can be performed directly in between them to correct discrepancies (convert one into the other), or all time tags and beam trigger information can be converted into local UTC for comparison. Common-view is ideal in that case because the two sites are separated by only 300 km and the time-service lab is also not very far, in the same country. This conversion can only be made one day later as it consists in isolating the satellites seen at both sites at the same time, and for them subtract the time differences computed by the receivers, for instance through the CGGTTS files at both sites so as to be left with the comparison between the two sites. For example for common-view between HK and

NICT with GPS constellation:

$$\begin{aligned} \text{CGGTTS at HK} \rightarrow \quad & t_{HK} - t_{GPS} && = \tau_{HK} \\ \text{CGGTTS at NICT} \rightarrow \quad & UTC_{Japan} - t_{GPS} && = \tau_{NICT} \\ \text{Common view} \rightarrow \quad & \tau_{HK} - \tau_{NICT} && = t_{HK} - UTC_{Japan} \end{aligned} \tag{7.12}$$

In that case, it allows to monitor directly a time base with respect to local UTC. As said before, if greater precision is needed, a month later this local UTC can be converted into global UTC.

To acquire the knowledge to use this tool and test it with our setup, we performed common view between our proposed solution installed at LPNHE and the French time-service lab SYRTE, located about 3 km away. The software to make the common-view comparison used is the open source one developed by SYRTE [169]. The time variations with respect to French UTC over 19 days of real data are shown in figure 7.22, with the deterministic drift removed but no further correction. The random walk behaviour is possible to see and it is found that variations of more than 100 ns only occur after a few days, which means that with correction of the random walk online and correcting the time tags at the end of each day as planned, we will be able to achieve a ns precision with respect to UTC according to these first tests. The number of satellites in common was also studied and is displayed in figure 7.23. Using only GPS, 6 satellites at least are seen in common for most of the 16 mn points. This is more than enough and expected given the short distance between both sites.

As a conclusion, the common-view technique to monitor UTC time tags is easily integrated in our system and tests in Paris suggest the ability of this timing solution to provide high precision.

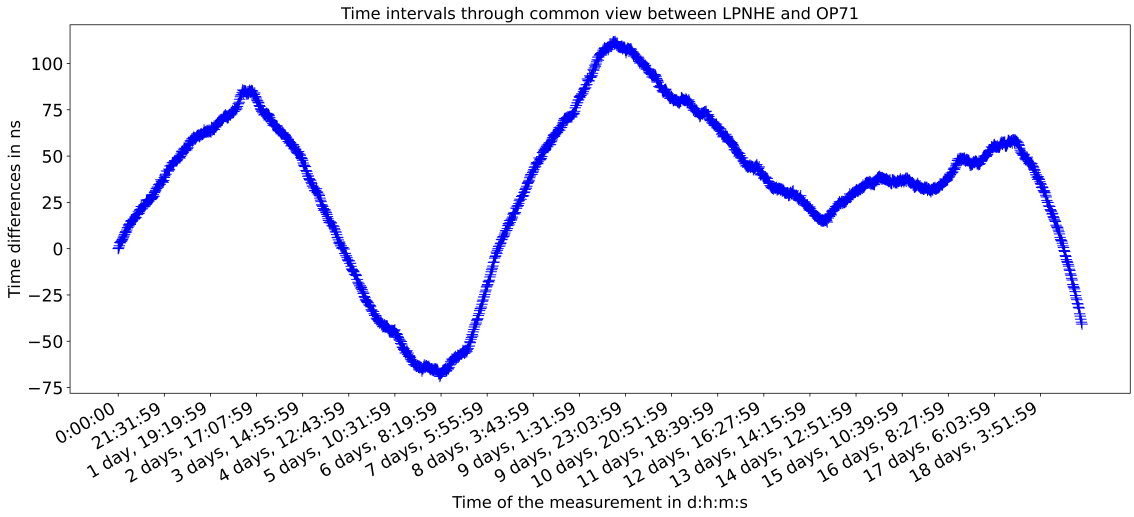

Figure 7.22. *Time variations between the tested setup at LPNHE and local French UTC through common view between LPNHE and SYRTE over 19 days of data*

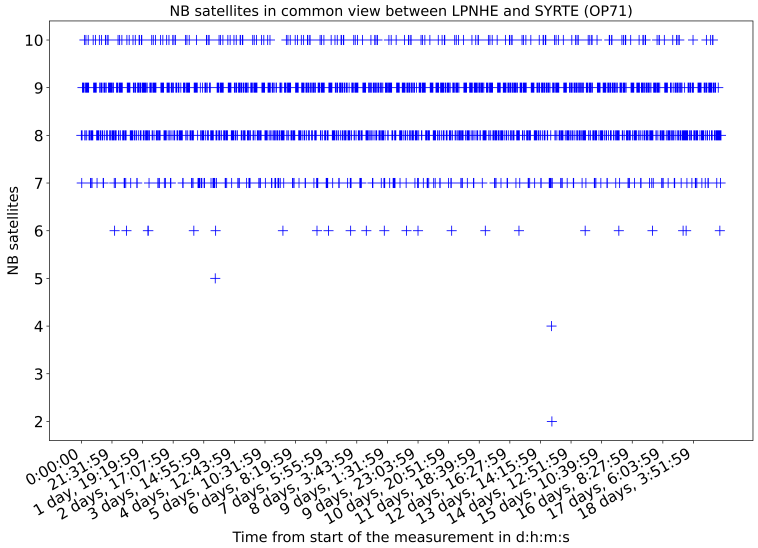

Figure 7.23. *Number of satellites seen in common view between LPNHE and SYRTE per 16 mn epoch, over 19 days of data*

7.4 Foreseen distribution scheme

The final main element of the timing system is the distribution part. It will not be detailed in this thesis as I was not directly involved in this part of the design of HK's timing system. The exact connection schemes and data stream are still under discussion, however figure 7.24 illustrates an overview of the foreseen architecture. TDM stands for time distribution module and PMT for Photo-Multiplier Tube in the scheme. The distribution will happen in two stages with electronic boards similar for both and currently prototyped and tested. The detection information from the front-ends needs to be associated with corrected time tags and sent back to the acquisition system. Feedback for calibration, reboot procedure and monitoring of the system will also be implemented. From first tests of the 2^{nd} stage distributor showed level of jitter of 40 ps which can be reduced to 2 ps with a PLL filter, which is well below the requirement of 100 ps, even multiplied by 2 to take into account a similar jitter from the 1^{st} stage distributor. Those results are encouraging. The R&D is still ongoing for the design of this part of the system.

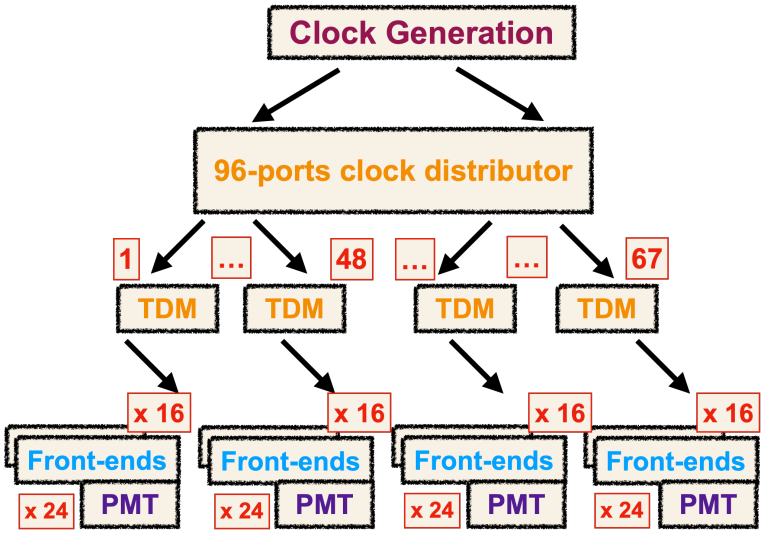

Figure 7.24. *Summarized scheme of the time distribution system foreseen for HK*

7.5 Conclusions and perspectives

To summarize this chapter on the work performed towards developing HK's timing system, and more specifically the clock generation part, the proposed solution from this work is to distribute in two stages a clock signal built from a free-running rubidium clock. This clock signal will constantly be compared to GNSS times being given as an input to GNSS receivers which can, in this configuration, act as time interval comparators.

The first study performed in this thesis allowed to acquire skills to characterize the time stability performance of this system and its component and establish that they meet HK's requirements. The same was done concerning time-tagging the events with a study on using the common-view time transfer technique with satisfying results. The final main part of this work was to produce simulation of signals based on data fits and study of the dominant noise types in order to choose and validate methods of correction. By correction it is meant correction to the clock signal so as to combine the short term performance of the clock with the long term stability of GNSS signals. It was found that offline quadratic corrections on interval of length 10^4 s, as well as online linear corrections with so-called sliding intervals at the same rate were ideal. This configuration for the timing system was compared to an alternative solution which also meets the requirements and has been used for neutrino experiments, including T2K. Nevertheless, this alternative configuration, using the same equipment does not provide as much control to the user to achieve the best possible precision.

The next steps for this development are mainly to test the full system, clock generation and distribution together taking into account distances between the data acquisition electronics inside the cavern, the clock system in a building on surface and the GNSS antennas on the roof of one of the nearby buildings, as well as making final test campaigns onsite, especially to check the satellite coverage. Towards installation of the system, the integration of automated corrections of the timing and comparisons with the redundancy system will have to be achieved as well as the integration of the timing information in the overall stream of data. Finally, to perform common view with NICT whose CGGTTS files are not public as SYRTE's ones are, solid collaboration with Japanese colleagues in HK and in NICT will have to be established.

Conclusion

Throughout this manuscript, the many challenges that come into play when studying neutrino flavor oscillations have been discussed. Those challenges can be classified in two categories. Some are related to the physics analysis and statistical frameworks and have been mainly described in the first part of this thesis, from Chapter 2 to Chapter 4. Some are technological and inherent in the elusive nature of neutrinos which has been introduced in Chapter 1. One of such challenges, obtaining the time precision needed in Hyper-Kamiokande, has been discussed in the second part of this thesis from Chapter 5 to Chapter 7.

It has been shown that the Tokai to Kamioka (T2K) experiment has needed huge infrastructures, cutting-edge detector technologies and hundreds of physicists and engineers in order to reach world-leading sensitivity to some of the neutrino oscillation parameters, especially δ_{CP}. Being able to observe flavor oscillations of weakly interacting particles within an artificially-produced beam over 300 km is already an impressive achievement. However, the current sensitivity is not enough to answer some of our questions about the Universe, for instance if the leptonic sector is involved in the matter/anti-matter asymmetry. Indeed, it can not yet be claimed that δ_{CP} is different from 0 (modulo π) and other correlated parameters such as $\sin^2(\theta_{23})$ whose octant is not determined, are not constrained well enough.

To go further in constraining these parameters, T2K and future similar experiments will have to both accumulate more statistics, T2K being currently statistically limited, and enhance their sensitivity with better detection and reconstruction performance as well as a more accurate way of treating systematic parameters. As it has been extensively discussed in Chapter 4, the oscillation analysis in T2K relies on interaction cross-section and nuclear models and, even-though the systematic uncertainty model is already very sophisticated, there are still unknowns. There is room for improvement in the way the model dependence is treated and on constraining better experimentally accessible values, in particular for cross-sections. To this end, the near detector ND280 is being upgraded this year (2023) to perform more accurate cross-section and flux measurements. The J-PARC neutrino beam-line is also upgraded this year in order to be able to accumulate

more data in similar time of exposures.

Looking even further towards the future, the next generation long-baseline neutrino oscillation experiments, namely HK and DUNE (and later maybe EssnuSB), will most probably allow us to discover CP violation in neutrino oscillations thanks to massive increase of statistics due to their planned increased target volumes. Even if we are most probably already close to this discovery, what will come next is a precision era for the measurement of the CP phase and that constitutes an additional challenge. To perform this, the complementarity between different experiments will be crucial and extremely beneficial. As it has been demonstrated in this thesis, a variety of neutrino energies, baselines, and matter densities offers sensitivity to different parameters and this is especially true for the determination of the mass hierarchy. Moreover, the entanglement of different systematic parameters and kinematic variables of particles can be lifted by studying the neutrino beam flux and interactions at various distances and energies. An additional intermediate detector IWCD for Hyper-Kamiokande as well as a potential movable near detector PRISM for DUNE can also help on this particular point. Having different target material (water for HK and liquid Argon for DUNE) will also allow us to track any bias in the interaction models that are used.
As promising and exciting as it is to perform all these measurements to refine the systematic models, one will have to be cautious not to add to much freedom to the analysis through new parameters that would make the final results less meaningful.

Finally, when building a brand new detector such as Hyper-Kamiokande, each element and sub-system performance matters. For the next generation experiments to be successful, each chosen technology will have to provide the best performance possible in order to not reduce the overall achievable precision and in order to remain relevant for the at least 10 or 15 years of planned operation. Pushing the abilities of each sub-system of the detector beyond requirements will also open the door to additional studies and measurements. The detector development work on HK's timing system that is reported in the second part of this manuscript is a perfect illustration of this.

Appendix A

Appendix Full list of cross-section parameters in P-theta

Table A.1. *Full list of cross-section parameters in P-theta*

Parameter	Interaction categories applied	Type
MAQE	CCQE	shape
Q^2 norm 5	CCQE	shape
Q^2norm 6	CCQE	shape
Q^2 norm 7	CCQE	shape
SF P1 2Shell MeanF Norm O	CCQE	norm
SF P3 2Shell MeanF Norm O	CCQE	norm
SF S Shell MeanF Norm O	CCQE	norm
SF SRC Norm O	CCQE	norm
SF P1 2Shell MeanF PMissShape O	CCQE	shape
SF P3 2Shell MeanF PMissShape O	CCQE	shape
SF S Shell MeanF PMissShape O	CCQE	shape
SF PBTwkDial Hybrid O16 nu	CCQE	shape
SF PBTwkDial Hybrid O16 nubar	CCQE	shape
SF OptPotTwkDial O16	CCQE	shape
2p2h norm. ν	2p2h	norm
2p2h norm. $\bar{\nu}$	2p2h	norm
2p2h norm. C to O	2p2h	norm
2p2h Edep lowEnu	2p2h	shape
2p2h Edep highEnu	2p2h	shape
2p2h Edep lowEnubar	2p2h	shape

2p2h Edep highEnubar	2p2h	shape
MECTwkDial PNNN Shape	2p2h	shape
2p2h shape O np	2p2h	shape
2p2h shape O NN	2p2h	shape
CA5	CC1πC, CC1π0, NC1πC,NC1π0	shape
MARES	CC1πC, CC1π0, NC1πC,NC1π0	shape
ISO BKG LowPPi	CC1πC, CC1π0, NC1πC,NC1π0	shape
ISO BKG	CC1πC, CC1π0, NC1πC,NC1π0	shape
Res Eb O numu	CC1πC, CC1π0, NC1πC,NC1π0	shape
Res Eb O numubar	CC1πC, CC1π0, NC1πC,NC1π0	shape
RS Delta decay	CC1πC, CC1π0, NC1πC,NC1π0	shape
SPP Pi0 Norm numu	$CC1\pi0$	norm
SPP Pi0 Norm numubar	$CC1\pi0$	norm
PionFSI QELowMomProb	All	shape
PionFSI QEHighMomProb	All	shape
PionFSI InelProb	All	shape
PionFSI AbsProb	All	shape
PionFSI CExLowMomProb	All	shape
PionFSI CExHighMomProb	All	shape
FateNucleonFSI	All	shape
CC coherent O norm	CC coherent	norm
CC MultiPi Multiplicity TotXSec	CC MPI	shape
CC MultiPi BY Vector	CC MPI	shape
CC MultiPi BY Axial	CC MPI	shape
CC MultiPi Multiplicity	CC MPI Shape	shape
CC BY DIS	CC DIS	shape
CC DIS MultiPi norm nu	CC DIS, CC MPI	norm
CC DIS MultiPi norm nubar	CC DIS, CC MPI	norm
CC Misc norm	CC MISC	norm
NC coherent	NC coherent	norm
NC 1γ	NC 1γ	norm
NC other (far)	NC other	norm
CC norm ν	All CC	norm
CC norm $\bar{\nu}$	All CC	norm
$\sigma_{\nu_e}/\sigma_{\nu_\mu}$	CC	norm
$\sigma_{\bar{\nu_e}}/\sigma_{\bar{\nu_\mu}}$	CC	norm
Eb O nu	CCQE	migration
Eb O nubar	CCQE	migration

Appendix B

Appendix CGGTTS format

SAT/PRN : Constellation code + satellite number / only satellite number
CL : Common-view hexadecimal class byte
MJD : Date in Modified Julian DAY
STTIME. : Date of the start time of the satellite tracking in h:m:s
TRKL : Track length in s
ELV : Satellite elevation at the date corresponding to the midpoint of the track in 0.1 °
AZTH : Satellite azimuth at the date corresponding to the midpoint of the track in 0.1 °
REFSV : the time difference between the laboratory reference clock and satellite time in .1ns
SRSV : the slope determined via the linear fit to produce REFSV in .0.1 ps/s
REFSYS :the time difference between the laboratory reference clock and GPS system time in .1ns
SRSYS : the slope determined via the linear fit to produce REFSYS in 0.1 ps/s
DSG : Root-mean-square of the residuals to previous linear fit
IOE : Three-digit decimal code indicating the ephemeris used for the computation
MDTR : Modeled tropospheric delay in .1 ns
SMDT : Slope of the modeled tropospheric delay in 0.1 ps/s.
MDIO : Modelled ionospheric delay in .1 ns
SMDI : Slope of the modelled ionospheric delay in 0.1 ps/s.
MSIO : Measured ionospheric delay in .1 ns
SMSI : Slope of the measured ionospheric delay in 0.1 ps/s.
ISG : Root-mean-square of the residuals of the fit on measured delays
FR : GLONASS transmission frequency channel number
HC : Receiver hardware channel number
FRC : GNSS observation code (band)
CK : Data line check-sum for columns 1 to 125: hexadecimal representation of the sum modulo 256, of the ASCII values of the characters which constitute the data line from

column 1 to column 125

PS1 : optional comments

PS2 : optional comments

Bibliography

[1] *Source of the Standard Model schematic*. 2023. URL: https://texample.net/tikz/examples/model-physics/.

[2] Ziro Maki, Masami Nakagawa, and Shoichi Sakata. "Remarks on the Unified Model of Elementary Particles". In: *Progress of Theoretical Physics* 28.5 (Nov. 1962), pp. 870–880. ISSN: 0033-068X. DOI: 10.1143/PTP.28.870. eprint: https://academic.oup.com/ptp/article-pdf/28/5/870/5258750/28-5-870.pdf. URL: https://doi.org/10.1143/PTP.28.870.

[3] V. Gribov and B. Pontecorvo. "Neutrino astronomy and lepton charge". In: *Physics Letters B* 28.7 (1969), pp. 493–496. ISSN: 0370-2693. DOI: https://doi.org/10.1016/0370-2693(69)90525-5. URL: https://www.sciencedirect.com/science/article/pii/0370269369905255.

[4] F. Englert and R. Brout. "Broken Symmetry and the Mass of Gauge Vector Mesons". In: *Phys. Rev. Lett.* 13 (9 1964), pp. 321–323. DOI: 10.1103/PhysRevLett.13.321. URL: https://link.aps.org/doi/10.1103/PhysRevLett.13.321.

[5] Peter W. Higgs. "Broken Symmetries and the Masses of Gauge Bosons". In: *Phys. Rev. Lett.* 13 (16 1964), pp. 508–509. DOI: 10.1103/PhysRevLett.13.508. URL: https://link.aps.org/doi/10.1103/PhysRevLett.13.508.

[6] W. Pauli. "Dear radioactive ladies and gentlemen". In: *Phys. Today* 31N9 (1978), p. 27.

[7] B. Pontecorvo. "Inverse beta processes and nonconservation of lepton charge". In: *Zh. Eksp. Teor. Fiz.* 34 (1957), p. 247.

[8] Y. Fukuda et al. "Evidence for Oscillation of Atmospheric Neutrinos". In: *Phys. Rev. Lett.* 81 (8 Aug. 1998), pp. 1562–1567. DOI: 10.1103/PhysRevLett.81.1562. URL: https://link.aps.org/doi/10.1103/PhysRevLett.81.1562.

[9] M. Aker et al. "Direct neutrino-mass measurement with sub-electronvolt sensitivity". In: *Nature Phys.* 18.2 (2022), pp. 160–166. DOI: 10.1038/s41567-021-01463-1. arXiv: 2105.08533 [hep-ex].

[10] Guillermo Franco Abellán et al. “Improved cosmological constraints on the neutrino mass and lifetime”. In: *Journal of High Energy Physics* 2022.8 (Aug. 2022). DOI: 10.1007/jhep08(2022)076. URL: https://arxiv.org/abs/2112.13862.

[11] S F King. “Neutrino mass models”. In: *Reports on Progress in Physics* 67.2 (Dec. 2003), pp. 107–157. DOI: 10.1088/0034-4885/67/2/r01. URL: https://iopscience.iop.org/article/10.1088/0034-4885/67/2/R01.

[12] Michelle J. Dolinski, Alan W.P. Poon, and Werner Rodejohann. “Neutrinoless Double-Beta Decay: Status and Prospects”. In: *Annual Review of Nuclear and Particle Science* 69.1 (2019), pp. 219–251. DOI: 10.1146/annurev-nucl-101918-023407. eprint: https://doi.org/10.1146/annurev-nucl-101918-023407. URL: https://doi.org/10.1146/annurev-nucl-101918-023407.

[13] J. A. Formaggio and G. P. Zeller. “From eV to EeV: Neutrino cross sections across energy scales”. In: *Reviews of Modern Physics* 84.3 (2012), pp. 1307–1341. DOI: 10.1103/revmodphys.84.1307. URL: https://arxiv.org/abs/1305.7513.

[14] *Coherent Pion Production*. URL: https://danielscully.uk/thesis/coherent.html.

[15] Luke Pickering. “Measurement of lead-target neutrino interactions using the whole T2K near detector”. In: 2017.

[16] In: (). DOI: 10.1103/physrevd.88.113007.

[17] Simon Bienstock. “Étude de la violation de CP dans le secteur leptonique avec l’analyse combinée d’oscillations de neutrinos et d’anti-neutrinos dans l’expérience T2K”. Thèse de doctorat dirigée par Giganti, Claudio et Dumarchez, Jacques Physique de l’univers Sorbonne université 2018. PhD thesis. 2018. URL: http://www.theses.fr/2018SORUS415.

[18] Mario Pecimotika. “Transmittance Simulations for the Atmosphere with Clouds”. PhD thesis. Nov. 2018. DOI: 10.13140/RG.2.2.34140.95361/1.

[19] G. Danby et al. “Observation of High-Energy Neutrino Reactions and the Existence of Two Kinds of Neutrinos”. In: *Phys. Rev. Lett.* 9 (1 July 1962), pp. 36–44. DOI: 10.1103/PhysRevLett.9.36. URL: https://link.aps.org/doi/10.1103/PhysRevLett.9.36.

[20] F.J. Hasert et al. “Search for elastic muon-neutrino electron scattering”. In: *Physics Letters B* 46.1 (1973), pp. 121–124. ISSN: 0370-2693. DOI: https://doi.org/10.1016/0370-2693(73)90494-2. URL: https://www.sciencedirect.com/science/article/pii/0370269373904942.

[21] F.J. Hasert et al. “Observation of neutrino-like interactions without muon or electron in the gargamelle neutrino experiment”. In: *Physics Letters B* 46.1 (1973), pp. 138–140. ISSN: 0370-2693. DOI: https://doi.org/10.1016/0370-2693(73)90499-1. URL: https://www.sciencedirect.com/science/article/pii/0370269373904991.

[22] F. Reines and C. L. Cowan. “Detection of the Free Neutrino”. In: *Physical Review* 92.3 (Nov. 1953), pp. 830–831. DOI: 10.1103/PhysRev.92.830.

[23] Jr. Cowan C. L. et al. “Detection of the Free Neutrino: A Confirmation”. In: *Science* 124.3212 (July 1956), pp. 103–104. DOI: 10.1126/science.124.3212.103.

[24] “The Reines-Cowan Experiments, Detecting the Poltergeist”. In: *Los Alamos Science* 25 (1997). URL: https://library.lanl.gov/cgi-bin/getfile?00326606.pdf.

[25] K. Abe et al. “First gadolinium loading to Super-Kamiokande”. In: *Nucl. Instrum. Meth. A* 1027 (2022), p. 166248. DOI: 10.1016/j.nima.2021.166248. arXiv: 2109.00360 [physics.ins-det].

[26] K. Kodama et al. “Observation of tau neutrino interactions”. In: *Physics Letters B* 504.3 (Apr. 2001), pp. 218–224. DOI: 10.1016/s0370-2693(01)00307-0. URL: https://arxiv.org/pdf/hep-ex/0012035.pdf.

[27] N. Agafonova et al. “Observation of a first ν_τ candidate in the OPERA experiment in the CNGS beam”. In: *Physics Letters B* 691.3 (Sept. 2010), pp. 138–145. DOI: 10.1016/j.physletb.2010.06.022. URL: https://arxiv.org/abs/1006.1623.

[28] Raymond Davis. “Solar Neutrinos. II. Experimental”. In: *Phys. Rev. Lett.* 12 (11 Mar. 1964), pp. 303–305. DOI: 10.1103/PhysRevLett.12.303. URL: https://link.aps.org/doi/10.1103/PhysRevLett.12.303.

[29] Raymond Davis. “A review of the homestake solar neutrino experiment”. In: *Progress in Particle and Nuclear Physics* 32 (1994), pp. 13–32. ISSN: 0146-6410. DOI: https://doi.org/10.1016/0146-6410(94)90004-3. URL: https://www.sciencedirect.com/science/article/pii/0146641094900043.

[30] Lawrence M. Krauss, Sheldon L. Glashow, and David N. Schramm. “Anti-neutrinos Astronomy and Geophysics”. In: *Nature* 310 (1984), pp. 191–198. DOI: 10.1038/310191a0.

[31] G. Bellini et al. “Geo-neutrinos”. In: *Progress in Particle and Nuclear Physics* 73 (Nov. 2013), pp. 1–34. DOI: 10.1016/j.ppnp.2013.07.001. URL: https://arxiv.org/abs/1310.3732.

[32] K. Way and E. P. Wigner. "The Rate of Decay of Fission Products". In: *Phys. Rev.* 73 (11 June 1948), pp. 1318–1330. DOI: 10.1103/PhysRev.73.1318. URL: https://link.aps.org/doi/10.1103/PhysRev.73.1318.

[33] G. Bak et al. "Measurement of Reactor Antineutrino Oscillation Amplitude and Frequency at RENO". In: *Physical Review Letters* 121.20 (Nov. 2018). DOI: 10.1103/physrevlett.121.201801. URL: https://arxiv.org/abs/1806.00248.

[34] Z. Djurcic and M. C. Goodman. "Double Chooz theta13 measurement via total neutron capture detection". In: *Nature Physics* 16.5 (May 2020). DOI: 10.1038/s41567-020-0831-y. URL: https://www.osti.gov/biblio/1674943.

[35] F. P. An et al. "New measurement of θ_{13} via neutron capture on hydrogen at Daya Bay". In: *Phys. Rev. D* 93.7 (2016), p. 072011. DOI: 10.1103/PhysRevD.93.072011. arXiv: 1603.03549 [hep-ex]. URL: https://inspirehep.net/literature/1427291.

[36] and H. Almazán et al. "STEREO neutrino spectrum of 235U fission rejects sterile neutrino hypothesis". In: *Nature* 613.7943 (Jan. 2023), pp. 257–261. DOI: 10.1038/s41586-022-05568-2. URL: https://doi.org/10.1038%2Fs41586-022-05568-2.

[37] JUNO Collaboration et al. *TAO Conceptual Design Report: A Precision Measurement of the Reactor Antineutrino Spectrum with Sub-percent Energy Resolution.* 2020. arXiv: 2005.08745 [physics.ins-det].

[38] Wick Haxton, R. Robertson, and Aldo Serenelli. "Solar Neutrinos: Status and Prospects". In: *Annual Review of Astronomy and Astrophysics* 51 (Aug. 2012). DOI: 10.1146/annurev-astro-081811-125539.

[39] J. N. Bahcall et al. "Solar Neutrino Flux." In: *Astrophysical Journal* 137 (Jan. 1963), pp. 344–346. DOI: 10.1086/147513.

[40] "How the Sun and stars shine". In: *The Cern Courrier* (Dec. 2021). URL: https://cerncourier.com/a/how-the-sun-and-stars-shine/.

[41] Stirling A. Colgate and Richard H. White. "The Hydrodynamic Behavior of Supernovae Explosions". In: *Astrophysical Journal* 143 (Mar. 1966), p. 626. DOI: 10.1086/148549.

[42] Maria Cristina Volpe. "Core-collapse supernovae and neutrino properties". In: *10th Symposium on Large TPCs for Low-Energy Rare Event Detection.* Paris, France, Dec. 2021. URL: https://hal.science/hal-03693138.

[43] K. Hirata et al. "Observation of a neutrino burst from the supernova SN1987A". In: *Phys. Rev. Lett.* 58 (14 Apr. 1987), pp. 1490–1493. DOI: 10.1103/PhysRevLett.58.1490. URL: https://link.aps.org/doi/10.1103/PhysRevLett.58.1490.

[44] R. M. Bionta et al. “Observation of a neutrino burst in coincidence with supernova 1987A in the Large Magellanic Cloud”. In: *Phys. Rev. Lett.* 58 (14 Apr. 1987), pp. 1494–1496. DOI: 10.1103/PhysRevLett.58.1494. URL: https://link.aps.org/doi/10.1103/PhysRevLett.58.1494.

[45] E. N. Alexeyev et al. “Detection of the neutrino signal from SN 1987A in the LMC using the INR Baksan underground scintillation telescope”. In: *Physics Letters B* 205.2-3 (Apr. 1988), pp. 209–214. DOI: 10.1016/0370-2693(88)91651-6.

[46] M. Aglietta et al. “LOW-ENERGY NEUTRINO DETECTION WITH THE MONT BLANC LSD EXPERIMENT”. In: *International Symposium on Weak and Electromagnetic Interactions in Nuclei*. 1986, pp. 741–744.

[47] Alekseev E.N., Alekseeva L.N., and Volchenko I.V. Krivosheinaand V.I. In: *PLB* (205 1988).

[48] and M. G. Aartsen et al. “Detection of a particle shower at the Glashow resonance with IceCube”. In: *Nature* 591.7849 (Mar. 2021), pp. 220–224. DOI: 10.1038/s41586-021-03256-1. URL: https://arxiv.org/pdf/2110.15051.pdf.

[49] E.W. Grashorn et al. “The atmospheric charged kaon/pion ratio using seasonal variation methods”. In: *Astroparticle Physics* 33.3 (Apr. 2010), pp. 140–145. DOI: 10.1016/j.astropartphys.2009.12.006. URL: https://doi.org/10.1016%2Fj.astropartphys.2009.12.006.

[50] Y. Ashie et al. “A Measurement of atmospheric neutrino oscillation parameters by SUPER-KAMIOKANDE I”. In: *Phys. Rev. D* 71 (2005), p. 112005. DOI: 10.1103/PhysRevD.71.112005. arXiv: hep-ex/0501064.

[51] K. Abe et al. “T2K neutrino flux prediction”. In: *Physical Review D* 87.1 (Jan. 2013). DOI: 10.1103/physrevd.87.012001. URL: https://arxiv.org/abs/1211.0469.

[52] Ubaldo Dore, Pier Loverre, and Lucio Ludovici. “History of accelerator neutrino beams”. In: *The European Physical Journal H* 44.4-5 (Oct. 2019), pp. 271–305. DOI: 10.1140/epjh/e2019-90032-x. URL: https://doi.org/10.1140%2Fepjh%2Fe2019-90032-x.

[53] S. Abe et al. “Precision Measurement of Neutrino Oscillation Parameters with KamLAND”. In: *Physical Review Letters* 100.22 (June 2008). DOI: 10.1103/physrevlett.100.221803. URL: https://arxiv.org/pdf/0801.4589.pdf.

[54] L. Wolfenstein. “Neutrino oscillations in matter”. In: *Phys. Rev. D* 17 (9 May 1978), pp. 2369–2374. DOI: 10.1103/PhysRevD.17.2369. URL: https://link.aps.org/doi/10.1103/PhysRevD.17.2369.

[55] L. Wolfenstein. “Neutrino oscillations in matter”. In: *PhysRevD* 17.9 (May 1978), pp. 2369–2374. DOI: 10.1103/PhysRevD.17.2369.

[56] S. P. Mikheyev and A. Yu. Smirnov. "Resonance Amplification of Oscillations in Matter and Spectroscopy of Solar Neutrinos". In: *Sov. J. Nucl. Phys.* 42 (1985), pp. 913–917.

[57] Adam M. Dziewonski and Don L. Anderson. "Preliminary reference Earth model". In: *Physics of the Earth and Planetary Interiors* 25.4 (1981), pp. 297–356. ISSN: 0031-9201. DOI: https://doi.org/10.1016/0031-9201(81)90046-7. URL: https://www.sciencedirect.com/science/article/pii/0031920181900467.

[58] Andrea Donini, Sergio Palomares-Ruiz, and Jordi Salvado. "Neutrino tomography of Earth". In: *Nature Physics* 15.1 (Nov. 2018), pp. 37–40. DOI: 10.1038/s41567-018-0319-1. URL: https://arxiv.org/abs/1803.05901.

[59] R. L. Workman and Others. "Review of Particle Physics". In: *PTEP* 2022 (2022), p. 083C01. DOI: 10.1093/ptep/ptac097.

[60] C. Jarlskog. "Commutator of the Quark Mass Matrices in the Standard Electroweak Model and a Measure of Maximal CP Nonconservation". In: *Phys. Rev. Lett.* 55 (10 Sept. 1985), pp. 1039–1042. DOI: 10.1103/PhysRevLett.55.1039. URL: https://link.aps.org/doi/10.1103/PhysRevLett.55.1039.

[61] A. Alekou et al. *The ESSnuSB design study: overview and future prospects*. Tech. rep. 19 pages, 11 figures; Corrected minor error in alphabetical ordering of the authors: the author list is now fully alphabetical w.r.t. author surnames as was intended. Corrected an incorrect affiliation for two authors per their request. 2023. arXiv: 2303.17356. URL: https://cds.cern.ch/record/2855605.

[62] K. Abe et al. "The T2K Experiment". In: *Nucl. Instrum. Meth. A* 659 (2011), pp. 106–135. DOI: 10.1016/j.nima.2011.06.067. arXiv: 1106.1238 [physics.ins-det].

[63] Yuichi Oyama. *K2K (KEK to Kamioka) neutrino-oscillation experiment at KEK-PS*. 1998. arXiv: hep-ex/9803014 [hep-ex].

[64] I. Ambats et al. "The MINOS Detectors Technical Design Report". In: (Oct. 1998). DOI: 10.2172/1861363.

[65] E. Aliu et al. "Evidence for Muon Neutrino Oscillation in an Accelerator-Based Experiment". In: *Physical Review Letters* 94.8 (Mar. 2005). DOI: 10.1103/physrevlett.94.081802. URL: https://doi.org/10.1103%2Fphysrevlett.94.081802.

[66] D. S. Ayres et al. "The NOvA Technical Design Report". In: (Oct. 2007). DOI: 10.2172/935497.

[67] K. Abe et al. “Indication of Electron Neutrino Appearance from an Accelerator-Produced Off-Axis Muon Neutrino Beam”. In: *Physical Review Letters* 107.4 (July 2011). DOI: 10.1103/physrevlett.107.041801. URL: https://arxiv.org/abs/1106.2822.

[68] M. Apollonio et al. “Search for neutrino oscillations on a long base-line at the CHOOZ nuclear power station”. In: *The European Physical Journal C* 27.3 (Apr. 2003), pp. 331–374. DOI: 10.1140/epjc/s2002-01127-9. URL: https://arxiv.org/abs/hep-ex/0301017.

[69] Tsunayuki Matsubara. *First result from the Double Chooz reactor-neutrino experiment*. 2012. arXiv: 1205.6685 [hep-ex].

[70] and K. Abe et al. “Constraint on the matter–antimatter symmetry-violating phase in neutrino oscillations”. In: *Nature* 580.7803 (Apr. 2020), pp. 339–344. DOI: 10.1038/s41586-020-2177-0. URL: https://doi.org/10.1038%2Fs41586-020-2177-0.

[71] B. Abi et al. *Deep Underground Neutrino Experiment (DUNE), Far Detector Technical Design Report, Volume I: Introduction to DUNE*. 2020. arXiv: 2002.02967 [physics.ins-det]. URL: https://arxiv.org/abs/2002.02967.

[72] A. Alekou et al. “Updated physics performance of the ESSnuSB experiment”. In: *The European Physical Journal C* 81.12 (Dec. 2021). DOI: 10.1140/epjc/s10052-021-09845-8. URL: https://doi.org/10.1140%2Fepjc%2Fs10052-021-09845-8.

[73] K. Abe et al. “Measurements of the T2K neutrino beam properties using the INGRID on-axis near detector”. In: *Nuclear Instruments and Methods in Physics Research Section A: Accelerators, Spectrometers, Detectors and Associated Equipment* 694 (Dec. 2012), pp. 211–223. DOI: 10.1016/j.nima.2012.03.023. URL: https://https://arxiv.org/pdf/1111.3119.pdf.

[74] K. Abe et al. *T2K ND280 Upgrade – Technical Design Report*. 2020. arXiv: 1901.03750 [physics.ins-det]. URL: https://arxiv.org/abs/1901.03750.

[75] K. Abe et al. “Measurement of the single π^0 production rate in neutral current neutrino interactions on water”. In: *Phys. Rev. D* 97 (3 2018), p. 032002. DOI: 10.1103/PhysRevD.97.032002. URL: https://link.aps.org/doi/10.1103/PhysRevD.97.032002.

[76] *Passage of Particles Through Matter, PDG2022*. 2022. URL: https://pdg.lbl.gov/2022/reviews/rpp2022-rev-passage-particles-matter.pdf.

[77] S. Aoki et al. "The T2K Side Muon Range Detector (SMRD)". In: *Nuclear Instruments and Methods in Physics Research Section A: Accelerators, Spectrometers, Detectors and Associated Equipment* 698 (Jan. 2013), pp. 135–146. DOI: 10.1016/j.nima.2012.10.001. URL: https://arxiv.org/abs/1206.3553.

[78] Pintaudi Giorgio. "T2K-WAGASCI: First physics run of the WAGASCI-BabyMIND detector with full setup". In: *PoS* LeptonPhoton2019 (2019), p. 142. DOI: 10.22323/1.367.0142.

[79] A. Blondel et al. "The WAGASCI experiment at JPARC to measure neutrino cross-sections on water". In: *PoS* EPS-HEP2015 (2015), p. 292. DOI: 10.22323/1.234.0292.

[80] M. Antonova et al. *Baby MIND: A magnetised spectrometer for the WAGASCI experiment*. 2017. arXiv: 1704.08079 [physics.ins-det].

[81] K. Abe et al. *T2K ND280 Upgrade – Technical Design Report*. 2020. arXiv: 1901.03750 [physics.ins-det].

[82] D. Attié et al. "Characterization of resistive Micromegas detectors for the upgrade of the T2K Near Detector Time Projection Chambers". In: *Nucl. Instrum. Meth. A* 1025 (2022), p. 166109. DOI: 10.1016/j.nima.2021.166109. arXiv: 2106.12634 [physics.ins-det].

[83] R. Diener et al. "The DESY II test beam facility". In: *Nuclear Instruments and Methods in Physics Research Section A: Accelerators, Spectrometers, Detectors and Associated Equipment* 922 (Apr. 2019), pp. 265–286. DOI: 10.1016/j.nima.2018.11.133. URL: https://arxiv.org/abs/1807.09328.

[84] D. Attié et al. "Analysis of test beam data taken with a prototype of TPC with resistive Micromegas for the T2K Near Detector upgrade". In: *Nucl. Instrum. Meth. A* 1052 (2023), p. 168248. DOI: 10.1016/j.nima.2023.168248. arXiv: 2212.06541 [physics.ins-det].

[85] D. Attié et al. "Performances of a resistive Micromegas module for the Time Projection Chambers of the T2K Near Detector upgrade". In: *Nuclear Instruments and Methods in Physics Research Section A: Accelerators, Spectrometers, Detectors and Associated Equipment* 957 (Mar. 2020), p. 163286. DOI: 10.1016/j.nima.2019.163286. URL: https://arxiv.org/abs/1907.07060.

[86] A. Blondel et al. "The SuperFGD Prototype charged particle beam tests". In: *Journal of Instrumentation* 15.12 (Dec. 2020), P12003–P12003. DOI: 10.1088/1748-0221/15/12/p12003. URL: https://arxiv.org/abs/2008.08861.

[87] X.-G. Lu et al. “Measurement of nuclear effects in neutrino interactions with minimal dependence on neutrino energy”. In: *Physical Review C* 94.1 (July 2016). DOI: 10.1103/physrevc.94.015503. URL: https://arxiv.org/abs/1512.05748.

[88] S. Dolan et al. “Sensitivity of the upgraded T2K Near Detector to constrain neutrino and antineutrino interactions with no mesons in the final state by exploiting nucleon-lepton correlations”. In: *Physical Review D* 105.3 (Feb. 2022). DOI: 10.1103/physrevd.105.032010. URL: https://arxiv.org/abs/2108.11779.

[89] Thorsten Lux. “The Upgrade of the T2K ND280 Detector”. In: *Journal of Physics: Conference Series* 2374.1 (2022), p. 012036. DOI: 10.1088/1742-6596/2374/1/012036. URL: https://dx.doi.org/10.1088/1742-6596/2374/1/012036.

[90] Y. Fukuda et al. “The Super-Kamiokande detector”. In: *Nucl. Instrum. Meth. A* 501 (2003). Ed. by V. A. Ilyin, V. V. Korenkov, and D. Perret-Gallix, pp. 418–462. DOI: 10.1016/S0168-9002(03)00425-X.

[91] S Fukuda et al. “Constraints on neutrino oscillations using 1258 days of Super-Kamiokande solar neutrino data”. In: *Physical Review Letters* 86.25 (2001), p. 5656.

[92] A. Bellerive et al. “The Sudbury Neutrino Observatory”. In: *Nuclear Physics B* 908 (July 2016), pp. 30–51. DOI: 10.1016/j.nuclphysb.2016.04.035. URL: https://arxiv.org/abs/1602.02469.

[93] C. Regis et al. “Search for proton decay via $p \to \mu + K^0$ in Super-Kamiokande I, II, and III”. In: *Physical Review D* 86.1 (Feb. 2012). DOI: 10.1103/physrevd.86.012006. URL: https://arxiv.org/abs/1205.6538.

[94] H. Nishino et al. “Search for nucleon decay into charged antilepton plus meson in Super-Kamiokande I and II”. In: *Physical Review D* 85.11 (June 2012). DOI: 10.1103/physrevd.85.112001. URL: https://arxiv.org/abs/1203.4030.

[95] M Jiang et al. “Atmospheric neutrino oscillation analysis with improved event reconstruction in Super-Kamiokande IV”. In: *Progress of Theoretical and Experimental Physics* 2019.5 (2019). DOI: 10.1093/ptep/ptz015. URL: https://arxiv.org/abs/1901.03230.

[96] S. Berkman et al. *fiTQun: A New Reconstruction Algorithm for Super-K*. https://t2k.org/docs/tech 2013.

[97] M. Shiozawa. “Reconstruction algorithms in the Super-Kamiokande large water Cherenkov detector”. In: *Nucl. Instrum. Meth. A* 433 (1999). Ed. by A. Breskin, R. Chechik, and T. Ypsilantis, pp. 240–246. DOI: 10.1016/S0168-9002(99)00359-9.

[98] R.B. Patterson et al. "The extended-track event reconstruction for MiniBooNE". In: *Nuclear Instruments and Methods in Physics Research Section A: Accelerators, Spectrometers, Detectors and Associated Equipment* 608.1 (Sept. 2009), pp. 206–224. DOI: 10.1016/j.nima.2009.06.064. URL: https://arxiv.org/abs/0902.2222.

[99] Ll. Marti et al. "Evaluation of gadolinium's action on water Cherenkov detector systems with EGADS". In: *Nuclear Instruments and Methods in Physics Research Section A: Accelerators, Spectrometers, Detectors and Associated Equipment* 959 (2020), p. 163549. ISSN: 0168-9002. DOI: https://doi.org/10.1016/j.nima.2020.163549. URL: https://www.sciencedirect.com/science/article/pii/S0168900220301315.

[100] *SK official website*. 2023. URL: https://www-sk.icrr.u-tokyo.ac.jp/en/news/detail/309.

[101] N. Abgrall et al. "Measurements of $\pi^{\pm}$, $K^{\pm}$ and proton double differential yields from the surface of the T2K replica target for incoming 31 GeV/c protons with the NA61/SHINE spectrometer at the CERN SPS". In: *The European Physical Journal C* 79.2 (Jan. 2019). DOI: 10.1140/epjc/s10052-019-6583-0. URL: https://arxiv.org/abs/1808.04927.

[102] C. L. McGivern et al. "Cross sections for ν_μ and $\overline{\nu}_\mu$ induced pion production on hydrocarbon in the few-GeV region using MINERvA". In: *Phys. Rev. D* 94 (5 Sept. 2016), p. 052005. DOI: 10.1103/PhysRevD.94.052005. URL: https://link.aps.org/doi/10.1103/PhysRevD.94.052005.

[103] A. Mislivec et al. "Measurement of total and differential cross sections of neutrino and antineutrino coherent $\pi^{\pm}$ production on carbon". In: *Phys. Rev. D* 97 (3 Feb. 2018), p. 032014. DOI: 10.1103/PhysRevD.97.032014. URL: https://link.aps.org/doi/10.1103/PhysRevD.97.032014.

[104] A. A. Aguilar-Arevalo et al. "Measurement of neutrino-induced charged-current charged pion production cross sections on mineral oil at $E_\nu \sim 1$ GeV". In: *Phys. Rev. D* 83 (5 Mar. 2011), p. 052007. DOI: 10.1103/PhysRevD.83.052007. URL: https://link.aps.org/doi/10.1103/PhysRevD.83.052007.

[105] K. Abe et al. "Measurement of neutrino and antineutrino oscillations by the T2K experiment including a new additional sample of ν_e interactions at the far detector". In: *Physical Review D* 96.9 (Nov. 2017). DOI: 10.1103/physrevd.96.092006. URL: https://doi.org/10.1103/physrevd.96.092006.

[106] C. Wilkinson et al. "Testing charged current quasi-elastic and multinucleon interaction models in the NEUT neutrino interaction generator with published datasets from the MiniBooNE and MINERνA experiments". In: *Phys. Rev. D* 93 (7 Apr. 2016), p. 072010. DOI: 10.1103/PhysRevD.93.072010. URL: https://link.aps.org/doi/10.1103/PhysRevD.93.072010.

[107] *Minuit reference manual version 94.1*. URL: https://root.cern.ch/download/minuit.pdf.

[108] Rene Brun and Fons Rademakers. "ROOT — An object oriented data analysis framework". In: *Nuclear Instruments and Methods in Physics Research Section A: Accelerators, Spectrometers, Detectors and Associated Equipment* 389.1 (1997). New Computing Techniques in Physics Research V, pp. 81–86. ISSN: 0168-9002. DOI: https://doi.org/10.1016/S0168-9002(97)00048-X. URL: https://www.sciencedirect.com/science/article/pii/S016890029700048X.

[109] M.P. Decowski. "KamLAND's precision neutrino oscillation measurements". In: *Nuclear Physics B* 908 (2016). Neutrino Oscillations: Celebrating the Nobel Prize in Physics 2015, pp. 52–61. ISSN: 0550-3213. DOI: https://doi.org/10.1016/j.nuclphysb.2016.04.014. URL: https://www.sciencedirect.com/science/article/pii/S0550321316300529.

[110] Gary J. Feldman and Robert D. Cousins. "A Unified approach to the classical statistical analysis of small signals". In: *Phys. Rev. D* 57 (1998), pp. 3873–3889. DOI: 10.1103/PhysRevD.57.3873. arXiv: physics/9711021. URL: https://arxiv.org/pdf/physics/9711021.pdf.

[111] P.A. Zyla et al. "Review of Particle Physics". In: *PTEP* 2020.8 (2020). and 2021 update, p. 083C01. DOI: 10.1093/ptep/ptaa104.

[112] Kenji Yasutome et al. *Six Sample Joint Oscillation Analysis with T2K Run1–10 Data including a new multi-ring μ like sample*. https://t2k.org/docs/technotes/430. 2022.

[113] P. Stowell et al. "Tuning the genie pion production model with MINERvA data". In: *Phys. Rev. D* 100 (7 Oct. 2019), p. 072005. DOI: 10.1103/PhysRevD.100.072005. URL: https://link.aps.org/doi/10.1103/PhysRevD.100.072005.

[114] Costas Andreopoulos et al. *The GENIE Neutrino Monte Carlo Generator: Physics and User Manual*. 2015. DOI: 10.48550/ARXIV.1510.05494. URL: https://arxiv.org/abs/1510.05494.

[115] Yoshinari Hayato and Luke Pickering. "The NEUT neutrino interaction simulation program library". In: *The European Physical Journal Special Topics* 230.24 (Oct. 2021), pp. 4469–4481. DOI: 10.1140/epjs/s11734-021-00287-7. URL: https://arxiv.org/pdf/2106.15809.pdf.

[116] M. Buizza Avanzini et al. *Comparisons and challenges of modern neutrino-scattering experiments (TENSIONS 2019 report)*. 2021. DOI: 10.48550/ARXIV.2112.09194. URL: https://arxiv.org/abs/2112.09194.

[117] A. Nikolakopoulos et al. "Mean-field approach to reconstructed neutrino energy distributions in accelerator-based experiments". In: *Phys. Rev. C* 98 (5 Nov. 2018), p. 054603. DOI: 10.1103/PhysRevC.98.054603. URL: https://link.aps.org/doi/10.1103/PhysRevC.98.054603.

[118] M. Martini et al. "Unified approach for nucleon knock-out and coherent and incoherent pion production in neutrino interactions with nuclei". In: *Physical Review C* 80.6 (Dec. 2009). DOI: 10.1103/physrevc.80.065501. URL: https://arxiv.org/pdf/0910.2622.pdf.

[119] N. Jachowicz et al. "Continuum random phase approximation approach to charged-current neutrino-nucleus scattering". In: *Phys. Rev. C* 65 (2 Jan. 2002), p. 025501. DOI: 10.1103/PhysRevC.65.025501. URL: https://link.aps.org/doi/10.1103/PhysRevC.65.025501.

[120] Ciro Riccio et al. *Fake Data Studies for 2021 Oscillation Analyses*. https://t2k.org/docs/technotes/ 2022.

[121] Hyper-Kamiokande Proto-Collaboration. *Hyper-Kamiokande Design Report*. 2018. DOI: 10.48550/ARXIV.1805.04163. URL: https://arxiv.org/abs/1805.04163.

[122] Hyper-Kamiokande collaboration. *Technical Design Report of the Hyper-K Intermediate Water Cherenkov Detector,"Internal Technical Note 17*. 2022. URL: https://wiki.hyperk.org/do/view/HyperK/TechNote0017.

[123] S. Bhadra et al. *Letter of Intent to Construct a nuPRISM Detector in the J-PARC Neutrino Beamline*. 2014. arXiv: 1412.3086 [physics.ins-det].

[124] M. Askins et al. "Theia: an advanced optical neutrino detector". In: *The European Physical Journal C* 80.5 (May 2020). DOI: 10.1140/epjc/s10052-020-7977-8. URL: https://doi.org/10.1140%2Fepjc%2Fs10052-020-7977-8.

[125] M Barbi et al. *Proposal for A Water Cherenkov Test Beam Experiment for Hyper-Kamiokande andFuture Large-scale Water-based Detectors*. Tech. rep. Geneva: CERN, 2020. URL: https://cds.cern.ch/record/2712416.

[126] DUNE Collaboration et al. "Long-baseline neutrino oscillation physics potential of the DUNE experiment". In: (June 2020).

[127] K. Abe et al. “Atmospheric neutrino oscillation analysis with external constraints in Super-Kamiokande I-IV”. In: *Phys. Rev. D* 97 (7 2018), p. 072001. DOI: 10.1103/PhysRevD.97.072001. URL: https://link.aps.org/doi/10.1103/PhysRevD.97.072001.

[128] K. Abe et al. “Supernova Model Discrimination with Hyper-Kamiokande”. In: *The Astrophysical Journal* 916.1 (July 2021), p. 15. DOI: 10.3847/1538-4357/abf7c4. URL: https://arxiv.org/abs/2101.05269.

[129] S Al Kharusi et al. “SNEWS 2.0: a next-generation supernova early warning system for multi-messenger astronomy”. In: *New Journal of Physics* 23.3 (Mar. 2021), p. 031201. DOI: 10.1088/1367-2630/abde33. URL: https://dx.doi.org/10.1088/1367-2630/abde33.

[130] K. Abe and SK collaboration. “Search for proton decay via $p \to \bar{\nu}K^+$ using 260 kiloton.year data of Super-Kamiokande”. In: *Physical Review D* 90.7 (Oct. 2014). DOI: 10.1103/physrevd.90.072005. URL: https://arxiv.org/abs/1408.1195.

[131] K. Abe et al. “Search for Proton Decay via $p \to e^+\pi^0$ and $p \to \mu\pi^0$ in 0.31 megaton.years exposure of the Super-Kamiokande Water Cherenkov Detector”. In: *Phys. Rev. D* 95 (1 Jan. 2017), p. 012004. DOI: 10.1103/PhysRevD.95.012004. URL: https://link.aps.org/doi/10.1103/PhysRevD.95.012004.

[132] Benjamin Quilain. “Measurement of the muon neutrino cross section through charged-current interactions and search for Lorentz invariance violation at the T2K experiment”. PhD thesis. Ecole Polytechnique, 2014.

[133] T2K Collaboration. “Upper bound on neutrino mass based on T2K neutrino timing measurements”. In: *Physical Review D* 93 (2016), p. 012006. DOI: 10.1103/PhysRevD.93.012006. URL: https://arxiv.org/abs/1502.06605.

[134] P. Adamson et al. “Measurement of the Velocity of the Neutrino with MINOS”. In: 2012. arXiv: 1408.6267 [physics.acc-ph]. URL: https://arxiv.org/pdf/1408.6267.pdf.

[135] A Norman et al. “The NOvA Timing System: A system for synchronizing a long baseline neutrino experiment”. In: *Journal of Physics: Conference Series* 396.1 (Dec. 2012), p. 012034. DOI: 10.1088/1742-6596/396/1/012034. URL: https://dx.doi.org/10.1088/1742-6596/396/1/012034.

[136] A. Norman, E. Niner, and A. Habig. “Timing in the NOvA detectors with atomic clock based time transfers between Fermilab, the Soudan mine and the NOvA Far detector”. In: *Journal of Physics: Conference Series* 664.8 (Dec. 2015), p. 082040. DOI: 10.1088/1742-6596/664/8/082040. URL: https://dx.doi.org/10.1088/1742-6596/664/8/082040.

[137] Giulia Brunetti. “Neutrino velocity measurement with the OPERA experiment in the CNGS beam”. Theses. Université Claude Bernard - Lyon I, May 2011. URL: https://theses.hal.science/tel-00843100.

[138] The OPERA Collaboration et al. “Measurement of the neutrino velocity with the OPERA detector in the CNGS beam”. In: (2011). DOI: 10.48550/ARXIV.1109.4897. URL: https://arxiv.org/abs/1109.4897.

[139] A. Barcock et al. *Timing and Synchronization of the DUNE Neutrino Detector*. 2022. DOI: 10.48550/ARXIV.2210.15517. URL: https://arxiv.org/abs/2210.15517.

[140] The IceCube collaboration. “The IceCube data acquisition system: Signal capture, digitization, and timestamping”. In: *Nuclear Instruments and Methods in Physics Research Section A: Accelerators, Spectrometers, Detectors and Associated Equipment* 601.3 (Apr. 2009), pp. 294–316. DOI: 10.1016/j.nima.2009.01.001. URL: https://www.phys.hawaii.edu/~idlab/taskAndSchedule/ARA/0810.4930.pdf.

[141] S. Fukuda et al. “The Super-Kamiokande detector”. In: *Nuclear Instruments and Methods in Physics Research Section A: Accelerators, Spectrometers, Detectors and Associated Equipment* 501.2 (2003), pp. 418–462. ISSN: 0168-9002. DOI: https://doi.org/10.1016/S0168-9002(03)00425-X. URL: https://www.sciencedirect.com/science/article/pii/S016890020300425X.

[142] BIPM. *The International System of Units*. 2019. URL: https://www.bipm.org/en/publications/si-brochure/.

[143] Michael Lombardi. “Fundamentals of Time and Frequency”. In: Jan. 2002. ISBN: 978-0-8493-6358-0. DOI: 10.1201/9781420037241.ch10.

[144] BIPM. *Circular T*. URL: https://www.bipm.org/en/time-ftp/circular-t.

[145] Chang Liu et al. “Rubidium-beam microwave clock pumped by distributed feedback diode lasers*”. In: *Chinese Physics B* 26.11 (Oct. 2017), p. 113201. DOI: 10.1088/1674-1056/26/11/113201. URL: https://dx.doi.org/10.1088/1674-1056/26/11/113201.

[146] Pavel Chapovsky. “Spectral characteristics of cold rubidium atoms in a dark magneto-optical trap”. In: *Journal of Experimental and Theoretical Physics* 103 (Jan. 2006), pp. 711–719. DOI: 10.1134/S1063776106110069.

[147] NIST. *Time and Frequency from A to Z*. URL: https://www.nist.gov/pml/time-and-frequency-division/popular-links/time-frequency-z/time-and-frequency-z-re-ru.

[148] J.M. Juan Zornoza J. Sanz Subirana and Spain M. Hernández-Pajares Technical University of Catalonia. "GNSS Basic Observables". In: *ESA, Navipedia* (2011). URL: https://gssc.esa.int/navipedia/index.php/GNSS_Basic_Observables.

[149] Ignacio Romero. "The Receiver Independent Exchange Format Version 4.00". In: *International GNSS Service* (Dec. 2021). URL: https://files.igs.org/pub/data/format/rinex_4.00.pdf?_ga=2.170453346.394728173.1669807490-635132764.1669807490&_gl=1*rex5v5*_ga*NjM1MTMyNzY0LjE2Njk4MDc0OTA.*_ga_Z5RH7R682C*MTY2OTgxNjU1OS4yLjEuMTY2OTgxODAwOS42MC4wLjA..

[150] J.M. Juan Zornoza J. Sanz Subirana and Spain M. Hernández-Pajares Technical University of Catalonia. "Antenna Phase Centre". In: *ESA, Navipedia* (2011). URL: https://gssc.esa.int/navipedia/index.php/Antenna_Phase_Centre.

[151] URL: https://webapp.csrs-scrs.nrcan-rncan.gc.ca/geod/tools-outils/ppp.php?locale=fr&_gl=1*15ectfn*_ga*NjAxMzIwODIxLjE2Njk4MjMxMzU.*_ga_C2N57Y7DX5*MTY2OTgyMzEzNC4xLjEuMTY2OTgyMzcyMS4wLjAuMA..

[152] URL: https://rgp.ign.fr/SERVICES/ppp_online.php.

[153] J Serrano et al. "The White Rabbit project". In: (2013). URL: https://cds.cern.ch/record/1743073.

[154] *White Rabbit open hardware depository*. URL: https://ohwr.org/project/white-rabbit/wikis/home.

[155] Michael Lombardi et al. "Time and Frequency Measurements Using the Global Positioning System". In: *Cal Lab: The International Journal of Metrology* 8 (July 2001), pp. 26–33.

[156] Marc Weiss, Gérard Petit, and Z. Jiang. "A comparison of GPS common-view time transfer to all-in-view". In: Sept. 2005, 5 pp. ISBN: 0-7803-9053-9. DOI: 10.1109/FREQ.2005.1573953.

[157] *Septentrio polarx5tr gnss receiver web page*. 2021. URL: https://www.septentrio.com/en/products/gnss-receivers/reference-receivers/polarx-5tr.

[158] P Defraigne and G Petit. "CGGTTS-Version 2E : an extended standard for GNSS Time Transfer". In: *Metrologia* 52.6 (Oct. 2015), G1. DOI: 10.1088/0026-1394/52/6/G1. URL: https://metrologia.bipm.org/guides-stds-conventions/2015/G1.pdf.

[159] John Plumb et al. "Absolute calibration of a geodetic time transfer system". In: *Ultrasonics, Ferroelectrics and Frequency Control, IEEE Transactions on* 52 (Dec. 2005), pp. 1904 –1911. DOI: 10.1109/TUFFC.2005.1561658.

[160] D.W. Allan. “Statistics of atomic frequency standards”. In: *Proceedings of the IEEE* 54.2 (1966), pp. 221–230. DOI: 10.1109/PROC.1966.4634. URL: https://tf.nist.gov/general/pdf/7.pdf.

[161] D. Howe, D.U. Allan, and J.A. Barnes. “Properties of Signal Sources and Measurement Methods”. In: Feb. 1981, pp. 669–716. DOI: 10.1109/FREQ.1981.200541. URL: https://tf.nist.gov/general/pdf/554.pdf.

[162] T.J. Witt. “Using the Allan variance and power spectral density to characterize DC nanovoltmeters”. In: *IEEE Transactions on Instrumentation and Measurement* 50.2 (2001), pp. 445–448. DOI: 10.1109/19.918162. URL: https://xdevs.com/doc/_Metrology/witt2001.pdf.

[163] James A. Barnes et al. “Characterization of Frequency Stability”. In: *IEEE Transactions on Instrumentation and Measurement* IM-20.2 (1971), pp. 105–120. DOI: 10.1109/TIM.1971.5570702. URL: https://tf.nist.gov/general/tn1337/Tn146.PDF.

[164] D.W. Allan and J.A. Barnes. “A Modified "Allan Variance" with Increased Oscillator Characterization Ability”. In: *Thirty Fifth Annual Frequency Control Symposium*. 1981, pp. 470–475. DOI: 10.1109/FREQ.1981.200514. URL: https://tf.nist.gov/general/pdf/560.pdf.

[165] *Stanford research system FS725 rubidium atomic clock*. https://www.thinksrs.com/products/fs725.html. Accessed: 2023-03-10. 2021.

[166] *Septentrio choke ring antenna*. https://www.septentrio.com/en/products/antennas/chokering-b3-e6. Accessed: 2023-03-10.

[167] *Keysight 53220A/53230A 350 MHz Universal Frequency Counter/Timer*. 2023. URL: https://www.keysight.com/us/en/assets/9018-03351/user-manuals/9018-03351.pdf.

[168] *NICT website*. 2023. URL: https://www.nict.go.jp/en/.

[169] *Link to SYRTE common-view software, open source*. 2023. URL: https://syrte.obspm.fr/tfc/temps/outgoing_data/gnss/softs/.

[170] V. Pandey et al. “Low-energy excitations and quasielastic contribution to electron-nucleus and neutrino-nucleus scattering in the continuum random-phase approximation”. In: *Physical Review C* 92.2 (Aug. 2015). DOI: 10.1103/physrevc.92.024606. URL: https://arxiv.org/pdf/1412.4624.pdf.

[171] *Septentrio PolaRx5TR User Manual Revision 2.4*. 2022. URL: https://www.septentrio.com/system/files/support/polarx5tr_user_manual_v2.4.pdf.

Abstracts

Résumé

Les neutrinos sont les particules du Modèle Standard dont les propriétés posent le plus d'interrogations non résolues. Malgré leur abondance dans l'Univers, ils sont très difficiles à détecter. Pourtant, ils semblent être une des clefs pour comprendre les questions majeures qui demeurent sur notre Univers et pour découvrir de la Physique au-delà du Modèle Standard. En particulier, la phase de Dirac de violation de la symétrie CP, qui paramétrise l'asymétrie entre neutrinos et anti-neutrinos dans le phénomène d'oscillation de saveurs, est un des paramètres les plus étudiés de nos jours. Si cette phase est non-nulle (modulo pi), cela signifierait que les neutrinos, et le secteur leptonique en général, pourraient participer à l'asymétrie matière/anti-matière de l'Univers, inexpliquée à ce jour. Le programme d'étude des oscillations de neutrinos sur longue distance du Japon offre pour l'instant la meilleure sensibilité à la mesure de violation de CP dans ce contexte. Plus précisément, l'expérience Tokai to Kamioka (T2K) quantifie la disparition de neutrinos muoniques et l'apparition de neutrinos électroniques dans un faisceau de (anti-)neutrinos muoniques de 600 MeV en moyenne, sur une distance de 295 km. Ses performances sont basées sur un ensemble de détecteurs proches à la fois sur l'axe et hors-axe du faisceau, ainsi que sur le détecteur lointain hors-axe Super-Kamiokande (SK) utilisant la détection par lumière Cherenkov dans l'eau. Même si les incertitudes de l'analyse d'oscillation des neutrinos dans T2K sont pour l'instant dominées par les erreurs statistiques, l'impact des effets systématiques gagne en importance au fur et à mesure que des nouvelles données sont collectées. Ceci est particulièrement vrai du fait que l'analyse dépend de modèles pour les sections efficaces d'interaction des neutrinos et les effets nucléaires. Prendre en compte les effets systématiques de la manière la plus complète possible est crucial pour préparer le futur de T2K et de SK: l'expérience Hyper-Kamiokande (HK). C'est dans cette direction que ce manuscrit présente une analyse d'oscillation dans T2K avec les nouvelles données du Run 11, ainsi qu'une étude détaillée de l'impact de l'utilisation d'un modèle incorrect ou incomplet pour l'estimation des sections efficaces et des effets nucléaires sur les contraintes extraites sur les paramètres d'oscillation. De plus, HK sera surtout un nouveau détecteur lointain, basé sur la même technologie que SK mais plus grand et avec

de meilleures performances de détection. La prise de données doit commencer en 2027. Tout comme son prédécesseur SK, HK sera non seulement un détecteur lointain pour les expériences de neutrinos d'accélérateurs, mais aussi un observatoire pour les neutrinos de source solaire, atmosphérique, et astrophysique. Chaque élément de ce détecteur sera neuf, y compris le système de synchronisation en temps. Cette thèse porte donc également sur le développement de la génération du signal d'horloge pour un tel système reposant sur des horloges atomiques et des antennes et récepteurs GNSS, en suivant un cahier des charges prenant en compte tous les buts scientifiques de HK. Des simulations de ses performances attendues en stabilité avec une optimisation des méthodes de correction du signal sont aussi discutées dans ce manuscrit.

Mots-clefs: Neutrinos, Violation de CP, Horloges atomiques, GNSS, analyse, oscillations de saveur

Abstract

Neutrinos are Standard Model particles whose observed properties lead us to many open questions. Very abundant yet challenging to detect, they are a key towards physics beyond the Standard Model and they play a major role in the understanding of our Universe. In particular, the Dirac phase of CP symmetry violation that parameterizes the asymmetry in flavor oscillation probabilities between neutrino and anti-neutrinos is one of the most studied parameters nowadays. If this phase is non-zero (modulo pi), this would mean that neutrinos, and the leptonic sector in general, may participate in the unexplained matter/anti-matter asymmetry of the Universe via yet-to-be-discovered leptogenesis mechanisms. The long-baseline neutrino oscillation program in Japan is currently leading the sensitivity to CP violation in neutrino oscillations. More specifically, the Tokai to Kamioka (T2K) experiment measures muon neutrino disappearance and electron neutrino appearance in a beam of 600 MeV (anti-) neutrinos with a baseline of 295 km. Its sensitivity is based on a complex set of near detectors, both on- and off-axis, as well as the off-axis water Cherenkov far detector Super-Kamiokande (SK). Even-though the oscillation analysis of T2K data is currently statistically limited, the importance of systematic parameters is growing as we are accumulating data and since the analysis depends, among others, on neutrino interaction cross-section and nuclear models. Taking into account systematic parameters in the most accurate way possible will be crucial in preparing the future of T2K and SK: the Hyper-Kamiokande (HK) experiment. In that direction, this thesis presents a T2K oscillation analysis with the new Run 11 data as well as a detailed study of the impact of potential mis-modelling or imperfect systematic error model on the oscillation parameter constraints. Moreover, HK will consist mostly of a new far detector based on the same technology as SK but larger and with better performance. It will start taking data in 2027. Just like its predecessor SK, HK will not only be a far detector for accelerator-based experiments, but also a standalone astrophysical, solar, and atmospheric neutrino observatory. Each element of the detector will be new, including the time synchronization system. The development of the time signal generation of such a system following requirements related to all of HK's Physics goals and involving atomic clocks, GNSS antenna and receiver, is reported. Simulations of its stability performance with optimized signal correction methods are discussed as well.

Keywords: Neutrinos, CP violation, atomic clocks, GNSS, analysis, flavor oscillations